

# **Biomimetic Materials for Bone Regeneration**

**Shuyi Li**

VRIJE UNIVERSITEIT

## **Biomimetic Materials for Bone Regeneration**

ACADEMISCH PROEFSCHRIFT

ter verkrijging van de graad Doctor of Philosophy

aan de Vrije Universiteit Amsterdam,

op gezag van de rector magnificus

prof.dr. J.J.G. Geurts,

in het openbaar te verdedigen

ten overstaan van de promotiecommissie

van de Faculteit der Tandheelkunde

op woensdag 28 september 2022 om 9.45 uur

in een bijeenkomst van de universiteit,

De Boelelaan 1105

Biomimetic Materials for Bone Regeneration

ISBN: 978-94-6421-807-7

Cover design: Shuyi Li

Layout & printing production: Proefschrift All In One (AIO)

The printing of this book was kindly supported by:

Academisch Centrum Tandheelkunde Amsterdam (ACTA), Vrije Universiteit

Amsterdam



Copyright © 2022 by Shuyi Li, Amsterdam, the Netherlands.

All rights reserved. No part of this book may be reproduced, stored in retrievable system, or transmitted in any form or by any means, mechanical, photocopying, recording, or otherwise, without the prior written permission of the holder of copyright.

door

Shuyi Li

geboren te Jiangsu, China

promotoren: prof.dr. T. Forouzanfar

copromotoren: dr. G. Wu  
dr. M. Zhou

promotiecommissie: prof.dr. R.T. Jaspers  
prof.dr. S. van Vlierberghe  
dr. M.N. Helder  
dr. A.D. Bakker  
dr. J.J.J.P. van den Beucken

*Great things are not done by impulse, but by a series of small things brought together; and great things are not something accidental, but must certainly be willed.*

-Vincent van Gogh

## CONTENTS

<b>CHAPTER 1</b>	General introduction	9
<b>CHAPTER 2</b>	A novel method to improve the osteogenesis capacity of hUCMSCs with dual-directional pre-induction under screened co-culture conditions	27
<b>CHAPTER 3</b>	Decellularized periosteum-derived hydrogels promote the proliferation, migration, and osteogenic differentiation of human umbilical cord mesenchymal stem cells	61
<b>CHAPTER 4</b>	Highly efficient biphasic calcium-phosphate coating procedure with an enhanced coating yield and protein incorporation rate	85
<b>CHAPTER 5</b>	3D printed TCP scaffolds functionalized with polydopamine-immobilized BMP2 to construct prefabricated biomimetic bone grafts	107
<b>CHAPTER 6</b>	Development and fabrication of co-axially electrospun biomimetic periosteum with a decellularized periosteal ECM shell/PCL core structure to promote the repair of critical-sized bone defects	129
<b>CHAPTER 7</b>	General discussion	175
<b>CHAPTER 8</b>	General summary	195
<b>APPENDICES</b>	Contributing authors	199
	Acknowledgments	203
	Curriculum vitae	207



**CHAPTER 1**

General Introduction

## Clinical background

Large-volume bone defects (LVBDs) resulting from trauma, infection, or tumor resection exceed the intrinsic self-healing capacity of bone tissue and will result in bone non-union if no surgical interventions are involved [1]. LVBDs can cause compromised functions and aesthetic outcomes, which severely affect the quality of life and health of patients. To date, the repair of LVBDs has been challenging for clinicians. Autografts are considered the gold standard, as they bear excellent biocompatibility, osteoconductivity, osteoinductivity, and osteogenesis-related cells [1, 2]. However, the usage of autografts is associated with a series of drawbacks, such as limited availability, donor site morbidity, uncontrollable resorption, and difficulty in fitting the irregular shape of bone defects [1, 3, 4]. Alternatives that bear similar structures and compositions to bone tissue, such as allografts (e.g., Maxgraft®) [5], xenografts (e.g., Bio-Oss Collagen®) [6], and artificial bone grafts (e.g., Nanobone®) [7], have been widely used in clinics. Nevertheless, most of these bone grafts have no intrinsic osteoinductive elements. Their geometries also do not match the anatomy of bone defects. Thus, the grafts need to be trimmed during surgery, which results in time-consuming processes [4, 8].

As a fibrous connective tissue membrane covering most of the bone surface, periosteum can significantly promote the healing of bone fractures [9] and the re-union of segmental bone defects [10] by intramembranous and endochondral ossification. However, LVBDs are often accompanied by damaged or absent periosteum [11], which will remarkably attenuate the healing efficacy [12]. To address this issue, Masquelet et al. develop an induced membrane technique, which uses a cement spacer to induce the formation of a periosteum-like membrane *in situ*. This technique dramatically promotes bone regeneration when combined with bone grafts [13]. However, the usage of this technique is limited by additional two-staged surgeries and a long incubation time of over 6 weeks [14]. Due to their excellent biocompatibility, biodegradability, and mechanical properties, collagen membranes (e.g., Bio-Gide®) have been widely used as barrier membranes to prevent the invasion of soft tissues [15]. However, they cannot provide the periosteum-specific niches to regulate osteogenesis in recipient sites. As a result, continuous efforts have been made to develop new bone and

periosteum substitutes to enhance bone regeneration.

## Bone tissue engineering

Bone tissue engineering (BTE) is an advanced and interdisciplinary technique that synergistically combines osteoconductive scaffolds, osteoinductive growth factors, and osteogenic stem cells to manufacture biomimetic and tissue-specific constructs to expedite bone regeneration [16]. Scaffolds in BTE bear biocompatibility with hierarchical porous structures to facilitate cell adhesion, migration, proliferation, and differentiation during bone growth [17]. They also serve as biological carriers of growth factors to realize an effective control over bioactivities and release patterns [2, 18]. Besides, the scaffolds may gradually degrade in the recipient site until they are completely replaced by new bone tissue [19]. Furthermore, a suitable mechanical strength is required for scaffolds to resist external pressure and tissue collapse [20], thus ensuring a relatively stable microenvironment for new bone formation. The rapid development of novel biomaterial science and manufacturing technology over the past decades has enabled the fabrication of advanced BTE constructs with customized geometries, hierarchical microstructures, biomimetic compositions, and tissue-specific properties.

## Advanced fabrication technologies to make biomimetic BTE constructs

Biomimetics is synonymous with biomimicry or bionics [21]. “Bio” means life, and “mimesis” refers to imitation [22]. Biomimetics is a new discipline and creatively uses natural ideas and interdisciplinary methods to design and fabricate constructs that imitate the structures and functions of native biological systems [23]. Biomimetic constructs closely reproduce the three-dimensional (3D) architecture, chemical compositions, and physical properties of native tissues, thus providing environmental instructive cues to elicit tissue-specific cellular responses and guide tissue regeneration [22, 24]. Biomimetic BTE constructs can be fabricated by various advanced techniques, such as 3D printing [25], self-assembly [26], electrospinning [16], and surface modification [27].

## 3D printing

With the development of computer-aided design (CAD) and computer-aided

manufacturing (CAM) technologies, 3D printing (also known as additive manufacturing (AM), rapid prototyping (RP), and free form fabrication (FFF)) has shown a promising application potential in tissue engineering and provides a great impetus for regenerative medicine [28]. Through digital control and operation, 3D printing produces scaffolds from CAD models in a layer-by-layer approach for material laying [29]. As a result, 3D printing offers a powerful, customizable, and additive platform for manufacturing, which is fundamentally different from conventional fabrication methods (e.g., gas foaming processes and emulsion freeze-drying) [29-31]. Additionally, 3D printing allows for the fabrication of anatomically-shaped and customized scaffolds based on the 3D imaging data of patients. It also offers precise control over internal microstructures, thus making the scaffolds with a well-defined, interconnected, and porous architecture to facilitate cellular infiltration, vascularization, and bone ingrowth [4]. Furthermore, 3D bioprinting offers the layer-by-layer assembling of multiple types of cells and associated matrices in a highly organized 3D way to generate a tissue-analogous structure [31]. A variety of materials can currently be printed into 3D shapes using specific 3D printing techniques [29].

With a similarity to inorganic compositions of bone tissue, calcium phosphate (CaP) (e.g., tricalcium phosphate (TCP) and hydroxyapatite (HA)) are extensively used biomaterials in BTE [32, 33]. Robocasting, as one of the 3D printing techniques, enables the fabrication of CaP-based biomimetic constructs with controlled and customized structures [34]. The printed scaffolds bear excellent mechanical properties and osteoconductivity, and the slowly degraded calcium and phosphate ions can contribute to bone metabolism and regeneration [34].

### **Self-assembly**

Self-assembly refers to the spontaneous arrangement of molecules with a disordered distribution to an ordered structure by non-covalent interactions [35]. The self-assembly process can be controlled or triggered by adjusting factors, such as the concentration, pH, temperature, and ionic strength, to modulate electrostatic interactions between peptides or proteins [36]. As a major protein in extracellular matrix (ECM), collagen type I bears a multi-hierarchical self-assembly process, which begins with the interactions of peptide chains, resulting in the triple helix

structures. These helices further assemble into fibrils, and finally, a hydrogel network [37]. The presence of heparin and decorin in ECM influence the diameter and density of fibril [38]. This spontaneity and versatility make self-assembly a broad range of applications in biomedical sciences and manufacturing [35].

ECM is produced by resident cells and has tissue-specific components and complex organizations [39]. It's mainly composed of fibrous proteins (e.g., collagen type I, II, III, IV, VI, X, and elastin) and glycoproteins (e.g., proteoglycans, fibronectin, and laminin), which provide structural support and bear abundant cell-recognition sites and various protein-adhesive domains to localize and deliver growth factors (e.g., bone morphogenetic protein-2 (BMP2), vascular endothelial growth factor (VEGF), and transforming growth factor- $\beta$  (TGF- $\beta$ )), thus regulating cellular behaviors and phenotypic expression [39, 40]. Building a biomimetic BTE construct with ECM molecules and niches will provide a highly favorable microenvironment to trigger and sustain bone regeneration and remodeling. ECM-derived hydrogels are formed by the collagen-based self-assembly process [38]. They have the tissue-specific functions of ECM and the structural and biological properties of hydrogels [41]. For example, ECM hydrogels from decellularized periosteum resemble the functions of periosteum, which significantly promote the osteogenic differentiation of mouse bone marrow mesenchymal stem cells (BMSCs) than pure collagen hydrogels [42]. Besides, ECM hydrogels from decellularized nucleus pulposus (NP) induce human BMSCs to differentiate into NP-like cells, while the hydrogels from decellularized annulus fibrosus (AF) induce the formation of AF-like cells [43].

### **Electrospinning**

Electrospinning is a classical manufacturing technique that uses electrostatic forces to generate continuous polymeric fibers with diameters ranging from micro- to nano-scale [44]. It shows superiority in fabricating periosteum-like membranes with controllable and individualized shape and size [45], which bear hierarchically-porous structures and high surface area to volume ratios to facilitate cell adhesion, migration, proliferation, and the transportation of nutrients and oxygen [45, 46]. Electrospinning provides a versatile platform that allows the processing of a broad range of polymeric materials into varied microstructures with different properties.

To confer electrospun tissue-engineered periosteum (TEP) a biomimetic surface and certain mechanical properties, natural polymeric materials (e.g., collagen) and bioceramic materials (e.g., HA) are often blended with synthetic materials (e.g., poly( $\epsilon$ -caprolactone) (PCL)) [47-49]. Though these composite membranes have improved physicochemical properties and osteoconductivity, they lack the periosteum-specific niches to regulate cellular activities and are hard to realize genuine biomimetic periosteum in composition. As previously mentioned, periosteal decellularized extracellular matrix (dECM) preserves the ultrastructure and biological compositions of periosteum [50, 51]. These biological compositions are capable of accelerating the healing efficacy of critical-sized bone defects [52] and can also induce bio-mineralization of seeded mesenchymal stem cells (MSCs) ectopically in nude mice [53]. Given its weak mechanical properties and fast degradation rate, the dECM from skeletal muscle [54], cartilage [55], cornea [56], etc. is often blended with PCL, which bears tunable mechanical strength, biodegradability, and biocompatibility [26], to electrospun tissue-engineered grafts with enhanced mechanical properties and tissue-specific niches. However, due to the different characteristics of ECM and synthetic polymeric materials, phase separation of PCL and ECM compositions occurs in blended electrospinning, leading to deteriorated fiber morphology, non-uniform structure, and weakened strength [57-59]. These drawbacks adversely influence cellular activities [60]. In contrast, co-axial electrospinning offers two separate channels for the core and shell materials, thus avoiding the immiscibility of different compositions. Besides, the electrospun fibers bear a core-shell layered structure, which allows each fiber to exhibit characteristics from both the core and shell materials [60].

### **Surface modification**

The physicochemical properties and topography of implants directly affect the cellular behaviors in recipient sites, including cell adhesion, migration, and differentiation as well as the final success of the implants [61]. Surface modification has been widely used to confer implants various functions in regenerative medicine [27]. For example, as the commonly used metallic implants in clinics, titanium and its alloys are considered inert biomaterials [62]. Surface modification technologies, such as plasma spray and biomimetic coating, can significantly increase the

osteoconductivity and osseointegration of titanium-based implants [27, 63]. Moreover, growth factors can be immobilized on the scaffolds to increase osteoinductivity and reduce the burst release [64].

Among the biomimetic coating methods, biomimetic biphasic CaP-coating is a promising surface modification technique for functionalizing various endosseous biomaterials [63]. In 2000, Prof. Dr. Klaas de Groot and his colleagues developed the following biphasic biomimetic coating protocol: an amorphous CaP seeding layer is formed through incubation in a 5 $\times$  simulated body fluid (SBF) solution, and a subsequent CaP crystalline layer is formed through incubation in a supersaturated calcium-phosphate solution (SCPS) [65, 66]. This biphasic biomimetic method enables the formation of a crystalline CaP-coating within 3 days. This BioCaP coating can confer BTE constructs an osteoconductive surface, which can significantly improve cell adhesion, proliferation, and ECM formation to support bone regeneration [32, 67, 68]. Compared with HA, the precipitated BioCaP layers bear highly similar structures to those of bone minerals [69] and can significantly promote the osseointegration of host bone and implants [70]. Besides, the coating process is conducted at physiological temperature, during which the osteogenic growth factors co-precipitate simultaneously into the 3D crystalline CaP network, thus realizing a controlled release of the incorporated growth factors and continuously promoting osteogenic differentiation of MSCs and bone regeneration [71, 72]. This BioCaP coating has increased surface bioactivity of various materials, including titanium [63], Bio-Oss<sup>®</sup> [72], and polymeric materials [73].

As another viable approach to immobilize growth factors, polydopamine (pDA)-mediated surface modification has been widely applied to increase surface bioactivity and osteoinductivity of various biomaterials, such as titanium, polymeric, composite, and CaP-based scaffolds [64, 74-76]. As a precursor of pDA, dopamine (DA) with functional groups of catechol and phenethylamine can self-polymerize in a weak alkaline environment to form the pDA coating, thus covalently or non-covalently bonding to various matrices [77]. The pDA coating is biocompatible and can immobilize growth factors via Michael addition and Schiff-base reactions [78]. The total amount of pDA coating-immobilized BMP2 is significantly higher than the directly adsorbed one on poly(lactic-co-glycolic acid) (PLGA)/HA scaffolds [79].

Besides, pDA can significantly increase cell adhesion to the hydrophobic matrix by adjusting surface energy [80].

Prefabrication technique bears a promising potential to repair LVBDs for patients [81]. It can construct biomimetic bone grafts with mandibular curvatures by implanting superficially adsorbed BMP2-functionalized bone-filling materials in *in-vivo* ectopic bioreactors, such as latissimus dorsi muscle [81]. However, thereby delivered BMP2 may result in a burst release, causing various side effects and compromising its osteoinductive efficacy [82-84]. Whether 3D printed TCP scaffolds functionalized by pDA-immobilized BMP2 are superior in prefabricating biomimetic bone grafts than the 3D printed TCP scaffolds functionalized by the superficially adsorbed one in latissimus dorsi muscle remains to be proved.

### **Biomimetic functionalization with MSCs**

MSCs are the most commonly used stem cells in preclinical and clinical studies on bone diseases [85, 86]. MSCs are “fibroblast-like” cells adherent to plastic culture plates, expressing typical mesenchymal specific surface markers (e.g., CD73, CD90, and CD105) but no hematopoietic markers (e.g., CD34 and CD45) [87]. MSCs are multipotent stem cells and can differentiate into diverse cell types, such as osteoblasts, chondrocytes, and adipocytes under specific stimuli from culture media or biomaterials [87, 88]. They also bear trophic, homing, and immunoregulatory abilities. Their secreted cytokines and growth factors (e.g., TGF- $\beta$  and VEGF) can further promote angiogenesis and osteogenesis [87, 89]. As a result, MSCs are efficacious in conferring pro-osteogenic properties of biomimetic scaffolds.

MSCs can be isolated from various tissues, such as bone marrow (BMSCs), umbilical cord (UCMSCs), and adipose tissue (ADMSCs). BMSCs are the most widely used stem cells in the repair of bone defects [90] and have been registered for repairing bone fracture in clinical trials [85]. However, the invasive acquisition procedure causes suffering to patients. BMSCs only comprise 0.01–0.001% of the cells in the bone marrow, which makes it difficult to obtain sufficient cells [91]. Besides, the cell number and osteogenic potential of BMSCs decline with age [92, 93]. In contrast, human UCMSCs (hUCMSCs) are atraumatically isolated from

discarded umbilical cords. Compared with BMSCs, hUCMSCs have a high cell yield and rapid proliferation property [93]. Furthermore, hUCMSCs maintain cell morphology and a high telomerase activity without showing senescence after 15 passages [94, 95]. hUCMSCs also bear lower immunogenicity and a stronger immunosuppressive capacity than BMSCs [96], which facilitate the allotransplantation of these cells when treating diseases. These characteristics make hUCMSCs promising candidates for BTE.

Various studies have shown conflicting results pertaining to the osteogenic properties of hUCMSCs. A series of *in-vitro* studies show that compared with human BMSCs (hBMSCs), hUCMSCs form less mineralized extracellular matrix, which is the final osteogenic differentiation marker, in osteogenic differentiation medium [97-99]. Sudo et al. further show that almost no mineralized extracellular matrix is formed in hUCMSCs after 28 days' induction [100]. Ciavarella et al. find that mineralized extracellular matrix is detected in osteogenically-induced hUCMSCs after 40 days' induction [101]. In contrast, when there is an osteoinductive growth factor (e.g., BMP2 and BMP7) in osteogenic differentiation medium, the osteogenic properties of hUCMSCs are significantly improved and the expression levels of osteogenic genes are comparable to those of hBMSCs [102, 103], suggesting a strong biomimetic osteogenic microenvironment is conducive to the osteogenic differentiation of hUCMSCs.

Angiogenesis is a prerequisite to the healing of bone defects, which can facilitate the transportation of nutrients and oxygen, as well as promote the migration, survival, and differentiation of MSCs to repair bone defects [104]. In BTE, a biomimetic strategy of co-culturing osteogenic and angiogenic cells is often applied to improve the osteogenic efficacy of BTE constructs [105-107]. The interactions between osteogenic and angiogenic cells remarkably promote angiogenesis and osteogenesis [105, 108]. Such a synergistic effect is directly influenced by the mixing ratio of the two cell types and the culture media [109], indicating that an optimal co-culture ratio of hUCMSC-derived osteogenic and angiogenic cells in certain culture media can yield enhanced osteogenic efficacies.

### Aims and outline of this thesis

The main aims of this thesis were to 1) develop novel biomimetic bone and periosteum constructs and 2) investigate their physicochemical properties and promoting effects on the healing of bone defects, with a final goal to provide efficacious treatment options. This thesis is subdivided into five chapters as described below.

HUCMSCs are a promising cell source for BTE. However, a series of *in-vitro* studies have shown that the osteogenic efficacy of hUCMSCs is relatively lower than that of hBMSCs. Therefore, in **Chapter 2**, we adopted a biomimetic strategy of co-culturing osteogenically- and angiogenically-committed hUCMSCs in various mixing ratios and culture media, so as to promote the osteogenic efficacy of hUCMSCs and fabricate hUCMSC-based biomimetic BTE constructs.

Furthermore, ECM hydrogels derived from intended tissues bear a tissue-specific differentiation-inducing capacity. Therefore, in **Chapter 3**, we developed an ECM hydrogel from decellularized periosteum. It was compared with a non-bone-specific ECM hydrogel — Matrigel to evaluate the pro-osteogenic function of the hydrogels in expediting the osteogenic efficacy of hUCMSCs.

Apart from the direct fabrication of biomimetic BTE constructs, BioCaP coating has long been used to confer BTE constructs an osteoconductive surface and enhanced scaffold-cell interactions in recipient sites. However, its biomedical application is limited by the low coating yield efficiency and protein-incorporation rate of the current coating procedure, which uses 1× SCPS. Therefore, in **Chapter 4**, we developed a highly concentrated 4.5× SCPS solution to harvest BioCaP coatings with enhanced coating yield efficiency and protein incorporation rate.

Additionally, pDA coating is a simple, safe, and effective method to modify scaffolds, thus covalently immobilizing growth factors and increasing surface bioactivity. Whether 3D printed TCP scaffolds functionalized by pDA-immobilized BMP2 were superior in inducing new bone formation than the superficially adsorbed one in ectopic sites was studied in **Chapter 5**.

The development of biomimetic TEP has been recognized as a promising strategy to accelerate the osseous repair of LVBDs. However, previously developed TEPs lack the periosteum-specific niches to regulate cellular activities and are hard

to realize genuine biomimetic periosteum in composition. Therefore, in **Chapter 6**, we developed a novel TEP with a decellularized periosteal ECM shell/PCL core structure by co-axial electrospinning to promote the repair of bone defects.



## REFERENCES

- [1] L. Vidal, et al., Reconstruction of Large Skeletal Defects: Current Clinical Therapeutic Strategies and Future Directions Using 3D Printing, *Front Bioeng Biotechnol* 8 (2020) 61.
- [2] A.R. Amini, et al., Bone Tissue Engineering: Recent Advances and Challenges, *Crit Rev Biomed Eng* 40(5) (2012) 363-408.
- [3] C. Mauffrey, et al., Management of Segmental Bone Defects, *J Am Acad Orthop Surg* 23(3) (2015) 143-153.
- [4] F. Mangano, et al., Maxillary Ridge Augmentation with Custom-Made CAD/CAM Scaffolds: A 1-Year Prospective Study on 10 Patients, *J Oral Implantol* 40(5) (2014) 561-569.
- [5] S. Otto, et al., Custom-Milled Individual Allogeneic Bone Grafts for Alveolar Cleft Osteoplasty — a Technical Note, *J Craniomaxillofac Surg* 45(12) (2017) 1955-1961.
- [6] D. Rohner, et al., Le Fort I Osteotomies Using Bio-Oss(R) Collagen to Promote Bony Union: A Prospective Clinical Split-Mouth Study, *Int J Oral Maxillofac Surg* 42(5) (2013) 585-591.
- [7] W. Gotz, et al., Immunohistochemical Characterization of Nanocrystalline Hydroxyapatite Silica Gel (Nanobone(R)) Osteogenesis: A Study on Biopsies from Human Jaws, *Clin Oral Implants Res* 19(10) (2008) 1016-1026.
- [8] J. Wiltfang, et al., Man as a Living Bioreactor: Prefabrication of a Custom Vascularized Bone Graft in the Gastrocolic Omentum, *Tissue Eng Part C Methods* 22(8) (2016) 740-746.
- [9] A. Ozaki, et al., Role of Fracture Hematoma and Periosteum During Fracture Healing in Rats: Interaction of Fracture Hematoma and the Periosteum in the Initial Step of the Healing Process, *J Orthop Sci* 5(1) (2000) 64-70.
- [10] M.L. Knothe Tate, et al., Testing of a New One-Stage Bone-Transport Surgical Procedure Exploiting the Periosteum for the Repair of Long-Bone Defects, *J Bone Joint Surg Am* 89(2) (2007) 307-316.
- [11] L. Zhao, et al., Repair of Long Bone Defects of Large Size Using a Tissue-Engineered Periosteum in a Rabbit Model, *J Mater Sci Mater Med* 32(9) (2021) 105.
- [12] S. Karaoglu, et al., Experimental Repair of Segmental Bone Defects in Rabbits by Demineralized Allograft Covered by Free Autogenous Periosteum, *Injury* 33(8) (2002) 679-683.
- [13] F. Luo, et al., Induced Membrane Technique Combined with Two-Stage Internal Fixation for the Treatment of Tibial Osteomyelitis Defects, *Injury* 48(7) (2017) 1623-1627.
- [14] R.J. Cuthbert, et al., Induced Periosteum a Complex Cellular Scaffold for the Treatment of Large Bone Defects, *Bone* 57(2) (2013) 484-492.
- [15] P. Raz, et al., Tensile Properties of Three Selected Collagen Membranes, *Biomed Res Int* 2019 (2019) 5163603.
- [16] R. Asmatulu, W.S. Khan, Chapter 11 — Electrospun Nanofibers for Tissue Engineering, in: R. Asmatulu, W.S. Khan (Eds.), *Synthesis and Applications of Electrospun Nanofibers*, Elsevier 2019, pp. 215-237.
- [17] F.E. Weber, Reconsidering Osteoconduction in the Era of Additive Manufacturing, *Tissue Eng Part B Rev* 25(5) (2019) 375-386.
- [18] K. Lee, et al., Growth Factor Delivery-Based Tissue Engineering: General Approaches and a Review of Recent Developments, *J R Soc Interface* 8(55) (2011) 153-170.
- [19] H. Qu, et al., Biomaterials for Bone Tissue Engineering Scaffolds: A Review, *RSC Advances* 9(45) (2019) 26252-26262.
- [20] H.D. Kim, et al., Biomimetic Materials and Fabrication Approaches for Bone Tissue Engineering, *Adv Healthc Mater* 6(23) (2017) 1700612.
- [21] J.F. Vincent, et al., Biomimetics: Its Practice and Theory, *J R Soc Interface* 3(9) (2006) 471-482.
- [22] M.K. Marei, et al., Strategy for a Biomimetic Paradigm in Dental and Craniofacial Tissue Engineering, *Biomimetics* 2013, pp. 119-162.
- [23] C.N. Kotanen, et al., Implantable Enzyme Amperometric Biosensors, *Biosens Bioelectron* 35(1) (2012) 14-26.
- [24] A. Tampieri, S. Sprio, *Bio-Inspired Regenerative Medicine: Materials, Processes, and Clinical Applications*, Jenny Stanford Publishing 2016.
- [25] M. Zhou, et al., Bioinspired Channeled, rhBMP2-Coated  $\beta$ -TCP Scaffolds with Embedded Autologous Vascular Bundles for Increased Vascularization and Osteogenesis of Prefabricated Tissue-Engineered Bone, *Mater Sci Eng C Mater Biol Appl* 118 (2021) 111389.
- [26] S. Chahal, et al., Development of Biomimetic Electrospun Polymeric Biomaterials for Bone Tissue Engineering: A Review, *J Biomater Sci Polym Ed* 30(14) (2019) 1308-1355.
- [27] C. Hu, et al., Bioinspired Surface Modification of Orthopedic Implants for Bone Tissue Engineering, *Biomaterials* 219 (2019) 119366.
- [28] E.S. Bishop, et al., 3D Bioprinting Technologies in Tissue Engineering and Regenerative Medicine: Current and Future Trends, *Genes Dis* 4(4) (2017) 185-195.
- [29] S.A.M. Tofail, et al., Additive Manufacturing: Scientific and Technological Challenges, Market Uptake and Opportunities, *Mater Today* 21(1) (2018) 22-37.
- [30] A. Abarrategi, et al., Biological Properties of Solid Free Form Designed Ceramic Scaffolds with BMP2: *In Vitro* and *In Vivo* Evaluation, *Plos One* 7(3) (2012) e34117.
- [31] B. Bisht, et al., Advances in the Fabrication of Scaffold and 3D Printing of Biomimetic Bone Graft, *Ann Biomed Eng* 49(4) (2021) 1128-1150.
- [32] N. Eliaz, N. Metoki, Calcium Phosphate Bioceramics: A Review of Their History, Structure, Properties, Coating Technologies and Biomedical Applications, *Materials (Basel)* 10(4) (2017) 334.
- [33] P. Chocholata, et al., Fabrication of Scaffolds for Bone-Tissue Regeneration, *Materials (Basel)* 12(4) (2019) 568.
- [34] S.S. Cao, et al., Prefabricated 3D Printed Tissue-Engineered Bone for Mandibular Reconstruction: A Preclinical Translational Study in Primate, *ACS Biomater Sci Eng* 7(12) (2021) 5727-5738.
- [35] S. Yadav, et al., Nanoscale Self-Assembly for Therapeutic Delivery, *Front Bioeng Biotechnol* 8 (2020) 127.
- [36] A.C. Mendes, et al., Self-Assembly in Nature: Using the Principles of Nature to

- Create Complex Nanobiomaterials, Wiley Interdiscip Rev Nanomed Nanobiotechnol 5(6) (2013) 582-612.
- [37] L.E. O'Leary, et al., Multi-Hierarchical Self-Assembly of a Collagen Mimetic Peptide from Triple Helix to Nanofibre and Hydrogel, Nat Chem 3(10) (2011) 821-828.
- [38] A.O. Brightman, et al., Time-Lapse Confocal Reflection Microscopy of Collagen Fibrillogenesis and Extracellular Matrix Assembly *in Vitro*, Biopolymers 54(3) (2000) 222-234.
- [39] B.S. Kim, et al., Decellularized Extracellular Matrix-Based Biinks for Engineering Tissue- and Organ-Specific Microenvironments, Chem Rev 120(19) (2020) 10608-10661.
- [40] Y.S. Kim, et al., Applications of Decellularized Extracellular Matrix in Bone and Cartilage Tissue Engineering, Bioeng Transl Med 4(1) (2019) 83-95.
- [41] W. Zhang, et al., Research Progress in Decellularized Extracellular Matrix-Derived Hydrogels, Regen Ther 18 (2021) 88-96.
- [42] P. Qiu, et al., Periosteal Matrix-Derived Hydrogel Promotes Bone Repair through an Early Immune Regulation Coupled with Enhanced Angio- and Osteogenesis, Biomaterials 227 (2020) 119552.
- [43] Y. Peng, et al., Decellularized Disc Hydrogels for hBMSCs Tissue-Specific Differentiation and Tissue Regeneration, Bioact Mater 6(10) (2021) 3541-3556.
- [44] J.S. Park, Electrospinning and Its Applications, Adv Nat Sci: Nanosci Nanotechnol 1(4) (2010) 043002.
- [45] T.J. Sill, H.A. von Recum, Electrospinning: Applications in Drug Delivery and Tissue Engineering, Biomaterials 29(13) (2008) 1989-2006.
- [46] F. Berton, et al., A Critical Review on the Production of Electrospun Nanofibres for Guided Bone Regeneration in Oral Surgery, Nanomaterials (Basel) 10(1) (2019) 16.
- [47] T. Wang, et al., Layer-by-Layer Nanofiber-Enabled Engineering of Biomimetic Periosteum for Bone Repair and Reconstruction, Biomaterials 182 (2018) 279-288.
- [48] M. Masoudi Rad, et al., Fabrication and Characterization of Two-Layered Nanofibrous Membrane for Guided Bone and Tissue Regeneration Application, Mater Sci Eng C Mater Biol Appl 80 (2017) 75-87.
- [49] M. Gong, et al., Icarin-Loaded Electrospun PCL/Gelatin Nanofiber Membrane as Potential Artificial Periosteum, Colloids Surf B Biointerfaces 170 (2018) 201-209.
- [50] S.J. Rapp, et al., Repairing Critical-Sized Rat Calvarial Defects with Progenitor Cell-seeded Acellular Periosteum: A Novel Biomimetic Scaffold, Surgery 152(4) (2012) 595-605.
- [51] K. Chen, et al., Decellularized Periosteum as a Potential Biologic Scaffold for Bone Tissue Engineering, Acta Biomater 19 (2015) 46-55.
- [52] J. He, et al., Preparation and Evaluation of Acellular Sheep Periosteum for Guided Bone Regeneration, J Biomed Mater Res A 108(1) (2020) 19-29.
- [53] J. Zhang, et al., Preparation and Evaluation of Tibia- and Calvarium-Derived Decellularized Periosteum Scaffolds, ACS Biomater Sci Eng 3(12) (2017) 3503-3514.
- [54] K.H. Patel, et al., Aligned Nanofibers of Decellularized Muscle ECM Support

- Myogenic Activity in Primary Satellite Cells *in Vitro*, Biomed Mater 14(3) (2019) 035010.
- [55] B. Feng, et al., Engineering Cartilage Tissue Based on Cartilage-Derived Extracellular Matrix cECM/PCL Hybrid Nanofibrous Scaffold, Mater Design 193 (2020) 108773.
- [56] J. Fernandez-Perez, et al., Characterization of Extracellular Matrix Modified Poly( $\epsilon$ -caprolactone) Electrospun Scaffolds with Differing Fiber Orientations for Corneal Stroma Regeneration, Mater Sci Eng C Mater Biol Appl 108 (2020) 110415.
- [57] B. Feng, et al., Effect of Inhomogeneity of the Electrospun Fibrous Scaffolds of Gelatin/Polycaprolactone Hybrid on Cell Proliferation, J Biomed Mater Res A 103(2) (2015) 431-438.
- [58] X. Jing, et al., Electrospinning Homogeneous Nanofibrous Poly(propylene carbonate)/Gelatin Composite Scaffolds for Tissue Engineering, Ind Eng Chem Res 53(22) (2014) 9391-9400.
- [59] J.J. Stankus, et al., Hybrid Nanofibrous Scaffolds from Electrospinning of a Synthetic Biodegradable Elastomer and Urinary Bladder Matrix, J Biomater Sci Polym Ed 19(5) (2008) 635-652.
- [60] B.N. Blackstone, et al., Tunable Engineered Skin Mechanics Via Coaxial Electrospun Fiber Core Diameter, Tissue Eng Part A 20(19-20) (2014) 2746-2755.
- [61] K. Anselme, et al., Relative Influence of Surface Topography and Surface Chemistry on Cell Response to Bone Implant Materials. Part 2: Biological Aspects, Proc Inst Mech Eng H 224(12) (2010) 1487-1507.
- [62] T. Xue, et al., Surface Modification Techniques of Titanium and Its Alloys to Functionally Optimize Their Biomedical Properties: Thematic Review, Front Bioeng Biotechnol 8 (2020) 603072.
- [63] Y. Liu, et al., The Influence of BMP2 and Its Mode of Delivery on the Osteoconductivity of Implant Surfaces During the Early Phase of Osseointegration, Biomaterials 28(16) (2007) 2677-2686.
- [64] S.J. Lee, et al., Surface Modification of 3D Printed Porous Scaffolds Via Mussel-Inspired Polydopamine and Effective Immobilization of rhBMP2 to Promote Osteogenic Differentiation for Bone Tissue Engineering, Acta Biomater 40 (2016) 182-191.
- [65] F. Barrere, et al., Biomimetic Coatings on Titanium: A Crystal Growth Study of Octacalcium Phosphate, J Mater Sci Mater Med 12(6) (2001) 529-534.
- [66] Y. Liu, et al., Biomimetic Coprecipitation of Calcium Phosphate and Bovine Serum Albumin on Titanium Alloy, J Biomed Mater Res 57(3) (2001) 327-335.
- [67] P. Sun, et al., BMP2/7 Heterodimer is a Stronger Inducer of Bone Regeneration in Peri-Implant Bone Defects Model Than BMP2 or BMP7 Homodimer, Dent Mater J 31(2) (2012) 239-248.
- [68] P. Kazimierczak, A. Przekora, Osteoconductive and Osteoinductive Surface Modifications of Biomaterials for Bone Regeneration: A Concise Review, Coatings 10(10) (2020) 971.
- [69] F. Barrère, et al., Biomimetic Calcium Phosphate Coatings on Ti6Al4V: A Crystal Growth Study of Octacalcium Phosphate and Inhibition by  $Mg^{2+}$  and  $HCO_3^-$ , Bone 25(2, Supplement 1) (1999) 107S-111S.



- [70] M. Nagano, et al., Bone Bonding Ability of an Apatite-coated Polymer Produced Using a Biomimetic Method: A Mechanical and Histological Study *in Vivo*, *J Biomed Mater Res* 31(4) (1996) 487-494.
- [71] Y. Liu, et al., Bi-Functionalization of a Calcium Phosphate-Coated Titanium Surface with Slow-Release Simvastatin and Metronidazole to Provide Antibacterial Activities and Pro-Osteodifferentiation Capabilities, *Plos One* 9(5) (2014) e97741.
- [72] T. Liu, et al., Deproteinized Bovine Bone Functionalized with the Slow Delivery of BMP2 for the Repair of Critical-Sized Bone Defects in Sheep, *Bone* 56(1) (2013) 110-118.
- [73] G. Wu, et al., The Effect of a Slow Mode of BMP2 Delivery on the Inflammatory Response Provoked by Bone-Defect-Filling Polymeric Scaffolds, *Biomaterials* 31(29) (2010) 7485-7493.
- [74] M. Godoy-Gallardo, et al., Immobilization of BMP2 and VEGF within Multilayered Polydopamine-Coated Scaffolds and the Resulting Osteogenic and Angiogenic Synergy of Co-Cultured Human Mesenchymal Stem Cells and Human Endothelial Progenitor Cells, *Int J Mol Sci* 21(17) (2020) 6418.
- [75] G.H. Lee, et al., Development of BMP2 Immobilized Polydopamine Mediated Multichannelled Biphasic Calcium Phosphate Granules for Improved Bone Regeneration, *Mater Lett* 208 (2017) 122-125.
- [76] J.S. Lee, et al., Polydopamine-Assisted BMP2 Immobilization on Titanium Surface Enhances the Osteogenic Potential of Periodontal Ligament Stem Cells Via Integrin-Mediated Cell-Matrix Adhesion, *J Cell Commun Signal* 12(4) (2018) 661-672.
- [77] S. Huang, et al., Polydopamine-Assisted Surface Modification for Bone Biosubstitutes, *Biomed Res Int* 2016 (2016) 2389895.
- [78] J. Fan, et al., Polydopamine Meets Porous Membrane: A Versatile Platform for Facile Preparation of Membrane Adsorbers, *J Chromatogr A* 1448 (2016) 121-126.
- [79] X. Zhao, et al., BMP2 Immobilized PLGA/Hydroxyapatite Fibrous Scaffold Via Polydopamine Stimulates Osteoblast Growth, *Mater Sci Eng C Mater Biol Appl* 78 (2017) 658-666.
- [80] S.H. Ku, et al., General Functionalization Route for Cell Adhesion on Non-Wetting Surfaces, *Biomaterials* 31(9) (2010) 2535-2541.
- [81] P.H. Warnke, et al., Growth and Transplantation of a Custom Vascularised Bone Graft in a Man, *Lancet* 364(9436) (2004) 766-770.
- [82] S. Vukicevic, et al., The Clinical Use of Bone Morphogenetic Proteins Revisited: A Novel Biocompatible Carrier Device Osteogrow for Bone Healing, *Int Orthop* 38(3) (2014) 635-647.
- [83] E. Gibon, et al., Inflammation, Ageing, and Bone Regeneration, *J Orthop Translat* 10 (2017) 28-35.
- [84] S. Han, et al., Programmed BMP2 Release from Biphasic Calcium Phosphates for Optimal Bone Regeneration, *Biomaterials* 272 (2021) 120785.
- [85] P. Kangari, et al., Mesenchymal Stem Cells: Amazing Remedies for Bone and Cartilage Defects, *Stem Cell Res Ther* 11(1) (2020) 492.
- [86] H. Saeed, et al., Mesenchymal Stem Cells (MSCs) as Skeletal Therapeutics — an Update, *J Biomed Sci* 23 (2016) 41.
- [87] A. Naji, et al., Biological Functions of Mesenchymal Stem Cells and Clinical Implications, *Cell Mol Life Sci* 76(17) (2019) 3323-3348.
- [88] M. Travnickova, L. Bacakova, Application of Adult Mesenchymal Stem Cells in Bone and Vascular Tissue Engineering, *Physiol Res* 67(6) (2018) 831-850.
- [89] C. Li, et al., Paracrine Effect of Inflammatory Cytokine-Activated Bone Marrow Mesenchymal Stem Cells and Its Role in Osteoblast Function, *J Biosci Bioeng* 121(2) (2016) 213-219.
- [90] X. Fu, et al., Mesenchymal Stem Cell Migration and Tissue Repair, *Cells* 8(8) (2019) 784.
- [91] M. Sabatino, et al., The Establishment of a Bank of Stored Clinical Bone Marrow Stromal Cell Products, *J Transl Med* 10 (2012) 23.
- [92] S.M. Mueller, J. Glowacki, Age-Related Decline in the Osteogenic Potential of Human Bone Marrow Cells Cultured in Three-Dimensional Collagen Sponges, *J Cell Biochem* 82(4) (2001) 583-590.
- [93] S. Kern, et al., Comparative Analysis of Mesenchymal Stem Cells from Bone Marrow, Umbilical Cord Blood, or Adipose Tissue, *Stem Cells* 24(5) (2006) 1294-1301.
- [94] G. La Rocca, et al., Isolation and Characterization of Oct-4+/HLA-G+ Mesenchymal Stem Cells from Human Umbilical Cord Matrix: Differentiation Potential and Detection of New Markers, *Histochem Cell Biol* 131(2) (2009) 267-282.
- [95] M.T. Conconi, et al., CD105(+) Cells from Wharton's Jelly Show *in Vitro* and *in Vivo* Myogenic Differentiative Potential, *Int J Mol Med* 18(6) (2006) 1089-1096.
- [96] T. Deuse, et al., Immunogenicity and Immunomodulatory Properties of Umbilical Cord Lining Mesenchymal Stem Cells, *Cell Transplant* 20(5) (2011) 655-667.
- [97] D. Kouroupis, et al., Assessment of Umbilical Cord Tissue as a Source of Mesenchymal Stem Cell/Endothelial Cell Mixtures for Bone Regeneration, *Regen Med* 8(5) (2013) 569-581.
- [98] C. Capelli, et al., Minimally Manipulated Whole Human Umbilical Cord Is a Rich Source of Clinical-Grade Human Mesenchymal Stromal Cells Expanded in Human Platelet Lysate, *Cytotherapy* 13(7) (2011) 786-801.
- [99] C. Mennan, et al., Isolation and Characterization of Mesenchymal Stem Cells from Different Regions of the Human Umbilical Cord, *Biomed Res Int* 2013 (2013) 916136.
- [100] K. Sudo, et al., Mesenchymal Progenitors Able to Differentiate into Osteogenic, Chondrogenic, and/or Adipogenic Cells *in Vitro* Are Present in Most Primary Fibroblast-Like Cell Populations, *Stem Cells* 25(7) (2007) 1610-1617.
- [101] S. Ciavarella, et al., Umbilical Cord Mesenchymal Stem Cells: Role of Regulatory Genes in Their Differentiation to Osteoblasts, *Stem Cells Dev* 18(8) (2009) 1211-1220.
- [102] T. Hou, et al., Umbilical Cord Wharton's Jelly: A New Potential Cell Source of Mesenchymal Stromal Cells for Bone Tissue Engineering, *Tissue Eng Part A* 15(9) (2009) 2325-2334.
- [103] L. E, et al., Microenvironment Influences on Human Umbilical Cord

Mesenchymal Stem Cell-Based Bone Regeneration, *Stem Cells Int* 2021 (2021) 4465022.

[104] K. Hu, B.R. Olsen, Osteoblast-Derived VEGF Regulates Osteoblast Differentiation and Bone Formation During Bone Repair, *J Clin Invest* 126(2) (2016) 509-526.

[105] J. Chen, et al., Angiogenic and Osteogenic Synergy of Human Mesenchymal Stem Cells and Human Umbilical Vein Endothelial Cells Co-Cultured on a Nanomatrix, *Sci Rep* 8(1) (2018) 15749.

[106] W.L. Dissanayaka, et al., Co-Culture of Dental Pulp Stem Cells with Endothelial Cells Enhances Osteo-/Odontogenic and Angiogenic Potential *in Vitro*, *J Endod* 38(4) (2012) 454-463.

[107] S. Shanbhag, et al., Cell Cotransplantation Strategies for Vascularized Craniofacial Bone Tissue Engineering: A Systematic Review and Meta-Analysis of Preclinical *in Vivo* Studies, *Tissue Eng Part B Rev* 23(2) (2017) 101-117.

[108] L. Li, et al., Enhanced Bone Tissue Regeneration of a Biomimetic Cellular Scaffold with Co-Cultured MSCs-Derived Osteogenic and Angiogenic Cells, *Cell Prolif* 52(5) (2019) e12658.

[109] J. Ma, et al., Co-Culture of Osteoblasts and Endothelial Cells: Optimization of Culture Medium and Cell Ratio, *Tissue Eng Part C Methods* 17(3) (2011) 349-357.

## CHAPTER 2

A novel method to improve the osteogenesis capacity of hUCMSCs  
with dual-directional pre-induction under screened co-culture  
conditions

Qiong Rong<sup>#</sup>, Shuyi Li<sup>#</sup>, Yang Zhou, Yuanming Geng, Shangbin Liu, Wanqiu  
Wu, Tim Forouzanfar, Gang Wu, Zhiyong Zhang, Miao Zhou

Cell proliferation, 2020, 53:e12740.

**ABSTRACT**

**Objectives:** Mesenchymal stem cell (MSC)-based therapy is a promising method to promote bone regeneration. However, the usage of human bone marrow mesenchymal stem cells (hBMSCs) is restricted by an invasive harvesting process and slow proliferation rate. As an alternative cell source to hBMSCs, human umbilical cord mesenchymal stem cells (hUCMSCs) bear a non-invasive harvesting process, fast proliferation ability, and low immunogenicity. However, multiple studies have shown that the osteogenic efficacy of hUCMSCs is lower than that of hBMSCs. To approach this problem, a co-culture strategy of hUCMSC-derived osteogenic and angiogenic cells was proposed, as osteogenesis and angiogenesis are highly coupled during bone formation.

**Materials and methods:** Herein, hUCMSCs were pre-treated in the respective induction media to produce osteogenic and angiogenic cells. We further screened the optimal mixing ratios of both cell types and culture media by assessing their *in-vitro* osteogenic differentiation efficacies. Furthermore, after such a pre-treatment for 3 days, the osteogenic and angiogenic cells were loaded onto customized tricalcium phosphate (TCP) scaffolds to repair bone defects.

**Results:** Osteogenic and angiogenic cells that were mixed at a ratio of 3:1 and co-cultured in the screened medium (osteogenic medium/endothelial cell induction medium = 3:1) showed more mineralization nodules than the other groups. Similarly, the expression levels of osteogenesis/angiogenesis-related genes (ALP, RUNX2, ANG, and CD146) were relatively higher than those of the corresponding mono-cultured cells. Further evidence from micro-CT and histological examinations of the repair of bone defects showed that the 3:1 group bore the best restoration outcome.

**Conclusions:** Our work demonstrated a feasible approach to improve osteogenesis using the co-culture strategy of dual-directionally differentiated hUCMSCs. This may establish a novel method to fabricate tissue-engineered bone grafts with 3D printed TCP and hUCMSCs.

**Keywords:** hUCMSCs; Dual-directional differentiation; Osteogenesis; Co-culture; Bone defects.

**1. INTRODUCTION**

Large bone defects resulting from trauma, infection, tumor resection, or congenital deformities severely affect the original contours and functions of bones. Autologous bone grafts, which are considered the “gold standard” for bone transplantation, require a second surgical site, inevitably causing further tissue damage and bringing serious physical, psychological, and economic burdens to patients [1]. To attain a non-invasive, safe, and customized rehabilitation of bone defects, mesenchymal stem cells (MSCs) have been used to facilitate the fabrication of customized, bioactive tissue-engineered bone grafts based on three-dimensional (3D) printed scaffolds [2, 3]. This may provide a promising therapeutic strategy for clinical settings. To date, MSCs have been extensively used to promote bone regeneration, especially MSCs isolated from bone marrow, which are characterized by a favorable osteogenic differentiation capacity and thereby frequently used in bone tissue engineering (BTE) [4]. However, the limited acquisition number of human bone marrow mesenchymal stem cells (hBMSCs) cannot meet the huge demands of bone repair. Besides, their cellular activities are largely influenced by the age and health status of the donor [5]. In contrast, MSCs from the Wharton's jelly of the neonatal umbilical cord, which are referred to as human umbilical cord mesenchymal stem cells (hUCMSCs), possess a high cell yield and rapid proliferation capacity. They secrete abundant cytokines related to cell migration, inflammation, immune regulation, angiogenesis (e.g., vascular endothelial growth factor (VEGF), insulin-like growth factor-1 (IGF-1), transforming growth factor, and platelet-derived growth factor (PDGF)), neurogenic and wound healing processes [6-8]. Furthermore, hUCMSCs do not express the major histocompatibility complex II (MHC II) and costimulatory molecules (CD80 and CD86), which are responsible for the alloimmune responses [9]. Therefore, the usage of hUCMSCs may be a promising choice to enhance the bioactivity of tissue-engineered bone grafts [10]. Studies have shown that hUCMSCs promote osteogenesis when seeded on the scaffolds and are suitable seed cells for BTE [11]. However, some studies have found that the osteogenic efficacy of hUCMSCs is weaker than that of hBMSCs. It is therefore necessary to enhance their osteogenic efficacy [12].

Due to the lack of nutrition and oxygen supply, the closer MSCs are to the

center of the scaffolds, the harder it is for them to survive. Studies have demonstrated that being within a 200- $\mu\text{m}$  distance from a blood vessel is critical for the survival and retention of viable cells [13, 14]. VEGF derived from osteoblasts, BMSCs, hUCMSCs, or human adipose mesenchymal stem cells (hADMSCs) is important in view of the fact that VEGF plays a vital role in facilitating angiogenesis and osteogenesis [8, 15-18]. Because a high or low concentration of VEGF could compromise bone formation, an optimal concentration of VEGF is required for angiogenesis and osteogenesis coupling in intramembranous ossification [17]. Given these phenomena, a co-culture system of osteogenic cells (e.g., BMSCs and osteoblasts) and angiogenic cells (e.g., endothelial progenitor cells and endothelial cells) is developed, which shows a synergistic effect in promoting osteogenesis and angiogenesis. This favors the survival and proliferation of osteoblasts in the scaffolds, thus ensuring successful ossification of tissue-engineered bone grafts [19, 20]. Nevertheless, it is difficult to culture endothelial progenitor cells and endothelial cells *in vitro*, and the number of isolated cells and proliferation ability are limited [21]. The widely used cells for co-culture, such as BMSCs and endothelial progenitor cells, further involve an invasive harvesting process, which brings pain to patients and increases the risks of infection. To avoid these problems, the usage of a single type of MSCs with abundant sources, noninvasive harvest, rapid proliferation, and multilineage differentiation would be a feasible solution. To date, however, studies on the dual-directional differentiation of a single type of stem cells have been scarce.

The outcome of osteogenesis is directly influenced by the mixing ratio of the two cell types and the co-culture media [22]. Due to the variety of cell types and treatment methods used by researchers, no co-culture standard has been established so far. Most researchers prefer to mix the two types of cells at a ratio of 1:1 and culture them in the osteogenic medium or the mixture of media (50% osteogenic medium and 50% endothelial growth medium) [20, 23, 24]. To date, however, no report has elaborated on the culture conditions concerning the bi-directional differentiation of hUCMSCs.

In this study, hUCMSCs were pre-induced to differentiate into osteogenic and angiogenic cells separately. They were then co-cultured at different ratios in the

screened culture media. A series of examinations were conducted to explore and analyze the osteogenic outcomes of the co-cultured cells. With a view to identifying a state-of-the-art method for applying hUCMSCs in BTE, tissue-engineered bone grafts of 3D printed tricalcium phosphate (TCP) scaffolds incorporated with different ratios of the induced cells were used to repair critical-sized calvarial bone defects in rats. This novel strategy would expand the applications of hUCMSCs in BTE.

## 2. MATERIALS AND METHODS

### 2.1 Isolation, culture, and identification of hUCMSCs

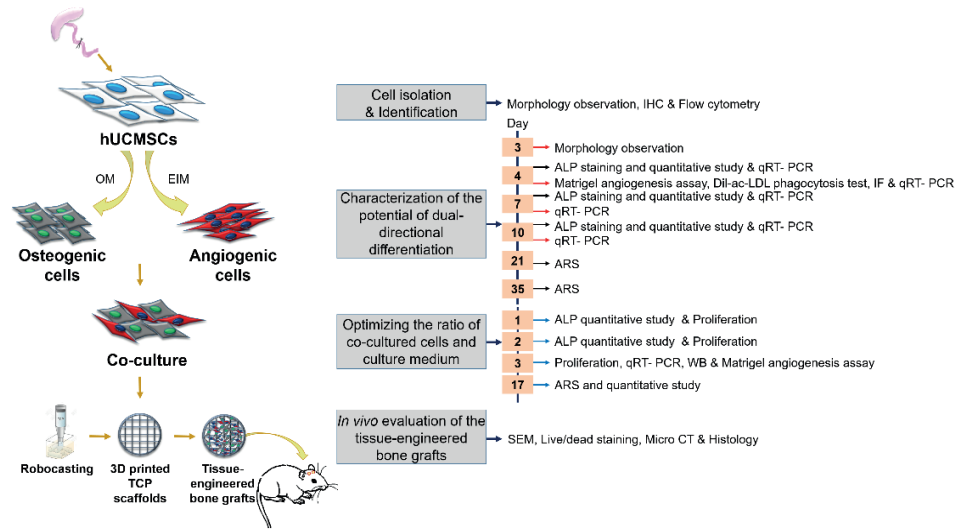
The experimental design of this study was briefly illustrated in Figure S1. The umbilical cord tissues were provided by the Human Stem Cell Bank of The Third Affiliated Hospital of Guangzhou Medical University. The umbilical cord tissues were used for cell isolation and histological observation. After being sterilized and thoroughly washed, the umbilical vein, arteries, and umbilical cord envelope were removed, and the Wharton's jelly was obtained. After the Wharton's jelly had been cut into pieces, 0.1% type II collagenase (Sigma-Aldrich, USA) was used for digestion at 4 °C overnight. The tissue suspension was then screened, plated in MSC medium (SM, Table 1), and incubated in 5% CO<sub>2</sub> at 37 °C. After 3 days, the growth of adherent hUCMSCs was observed. Passage 4–8 was chosen for subsequent experiments.

For identification,  $6 \times 10^5$  hUCMSCs in 10% PBS were incubated with FITC-labeled mouse anti-human IgG1 kappa isotype (eBioscience, USA), mouse anti-human CD73 (eBioscience, USA) and CD90 (eBioscience, USA), PE-labeled mouse anti-human IgG1 kappa Isotype (Santa Cruz, USA), mouse anti-human CD34 (Santa Cruz, USA) and CD45 (Santa Cruz, USA) on ice for 30 min. Flow cytometry (BD, USA) was applied for detection and analysis.

### 2.2 Co-culture of dual-directional induction of hUCMSCs

A series of culture media were applied in the study (Table 1). When the cells reached 70–80% confluence, the culture medium was changed from the proliferation medium (PM) to the osteogenic medium (OM) to test osteogenic differentiation of hUCMSCs. Endothelial cell induction medium (EIM) was used to test angiogenic differentiation of hUCMSCs. After being induced in the respective

media for 3 days, the osteogenically-induced hUCMSCs (os-hUCMSCs) and angiogenically-induced hUCMSCs (an-hUCMSCs) were co-cultured in varied ratios with different culture media for another 3 days before being studied *in vitro* and *in vivo* (Table 2).



**Supplementary figure 1.** Schematic illustration of the study indicating the isolation of hUCMSCs, dual-directional induction and differentiation, screened co-culture conditions, and the final repair of calvarial bone defects of rats with 3D printed TCP scaffolds. In the timeline (right), the black, red, and blue arrows represent the examinations of osteogenesis and angiogenesis of the induced hUCMSCs and osteogenesis of the co-cultured cells.

**Table 1.** Culture media.

Abbreviated name	Full name	Components	Brand/Country
SM	Mesenchymal stem cells medium	MGro-500 chemically defined medium (MesenGro basal medium, 450 mL; MesenGro supplement, 50 mL)	StemRD/USA
PM	Proliferation medium	High-glucose Dulbecco's modified Eagle's medium 10% fetal bovine serum (FBS) 1% penicillin-streptomycin (PS)	Gibco/USA

OM	Osteogenic medium	PM	
		100 nM dexamethasone	Solarbio/China
		10 mM $\beta$ -glycerophosphate	Sigma/Germany
		50 $\mu$ g/mL L-ascorbic acid	Sigma/China
EGM	Endothelial cell growth medium-2	Endothelial cell basal medium-2 EGM-2 BulletKit (10 mL FBS, 0.2 mL hydrocortisone, 2.0 mL hFGF-B, 0.5 mL VEGF, 0.5 mL ascorbic acid, 0.5 mL hEGF, 0.5 mL GA-1000, 0.5 mL heparin)	Lonza/USA
EIM	Endothelial cell induction medium	EGM 25 ng/mL human VEGF 10 ng/mL human bFGF	PeproTech/USA
EMM	Equivalent mixed medium	1:1 mixture of OM and EIM	/
PMM	Proportional mixed medium	OM:EIM = os-hUCMSCs : an-hUCMSCs	/

**Table 2.** Cell ratios and culture media used for the co-culture experiments.

No.	Cell types	Cell ratios	Culture medium			
			1	2	3	4
1	os-hUCMSCs: an-hUCMSCs	4:0	OM			
2	os-hUCMSCs: an-hUCMSCs	3:1	PM	OM	EMM (2:2)	PMM (3:1)
3	os-hUCMSCs: an-hUCMSCs	2:2			EMM (2:2)/	PMM (2:2)
4	os-hUCMSCs: an-hUCMSCs	1:3			EMM (2:2)	PMM (1:3)
5	os-hUCMSCs: an-hUCMSCs	0:4	EIM			



## 2.3 Characterization of the osteogenic and angiogenic capacities of hUCMSCs

### 2.3.1 Proliferation study

During the observation period of 1 to 7 days, the cultured cells were incubated with the culture medium and Alamarblue (Invitrogen, USA) (v/v = 10:1) for 3 h on each day before the test. The optical density (OD) values were then examined at 570 nm and 600 nm. The percentage of proliferation was calculated using the following formula:

$$(\%) = [117216 \times A_{570} - 80586 \times A_{600} (\text{sample})] / [117216 \times A_{570} - 80586 \times A_{600} (\text{control})] \times 100\%$$

### 2.3.2 Alkaline phosphatase (ALP) activity

ALP quantitative and qualitative studies were carried out. According to the manufacturer's instructions for the ALP quantitative kit (Nanjing Jiancheng Bioengineering Institute, China), cell lysis and centrifugation were performed. Thereafter, 30  $\mu\text{L}$  of supernatant from each sample was incubated with 50  $\mu\text{L}$  of buffer solution and 50  $\mu\text{L}$  of matrix solution at 37  $^{\circ}\text{C}$  for 15 min. Subsequently, 150  $\mu\text{L}$  of color developer was added, and the OD values were analyzed at 520 nm. The protein concentration of each sample was determined using the BCA protein quantitative kit (Best Bio, China) for normalization. The ALP activity was expressed as King unit per gram of protein. For the ALP staining, the diethyl 2, 5-di (thiophen-2-yl) terephthalate, 5-bromo-4-chloro-3-indolyl phosphate (BCIP), and nitro-blue-tetrazolium (NBT) were mixed at a ratio of 300:1:2 to produce the BCIP/NBT staining working reagent (Beyotime, China). All the samples were fixed in 4% paraformaldehyde (PFA) for 15 min before being incubated with the staining working reagent for 20 min.

### 2.3.3 Alizarin red S staining (ARS)

After the samples had been fixed, ARS solution (0.2%, pH 8.3) was added and incubated for 10 min. The wells were then rinsed with distilled water to remove the nonspecific staining. Images were taken using a stereomicroscope to visualize the mineralized matrix. For the quantitative analysis, 10% hexadecyl pyridinium chloride monohydrate (CPC) was used to dissolve the mineralized nodules. The colorimetric absorbance was then measured at 562 nm.

### 2.3.4 Matrigel angiogenesis assay

Angiogenic capacity was measured using the Matrigel angiogenesis assay. Briefly, 10  $\mu\text{L}$  of ice-cold Matrigel (354230, BD Biosciences) was added into the angiogenesis slides (Ibidi, Germany) and incubated at 37  $^{\circ}\text{C}$  for 30 min. Thereafter, 50  $\mu\text{L}$  of cell suspension ( $2 \times 10^4$  cells) were placed into each well and imaged after being incubated for 2.5 h to observe the tube formation.

### 2.3.5 Acetylated low-density lipoprotein labeled with Dil (Dil-ac-LDL) phagocytosis test

Before testing, the culture medium was changed to EIM containing 10  $\mu\text{g}/\text{mL}$  Dil-ac-LDL (Invitrogen, USA). After the samples had been incubated at 37  $^{\circ}\text{C}$  for 4 h and washed with PBS several times, nuclei staining was carried out using 5  $\mu\text{g}/\text{mL}$  Hoechst (Sigma-Aldrich, USA). A confocal laser scanning microscope (CLSM, Leica, Germany) was used for observation.

### 2.3.6 Immunofluorescent staining

After angiogenic induction, the cells were fixed before being penetrated by the frozen methanol at 20  $^{\circ}\text{C}$  for 10 min. Blocking buffer (Beyotime, China) was used to block the endogenous peroxidase at room temperature for 1 h. Monoclonal antibodies, including EphrinB2 (1:100, Abcam, UK) and EphB4 (1:800, CST, USA), were incubated with the cells at 4  $^{\circ}\text{C}$  overnight, followed by incubation with the secondary antibody (1:750, Biotium, USA) for 1 h. Thereafter, 5  $\mu\text{g}/\text{mL}$  Hoechst (Sigma-Aldrich, USA) was used for nuclei staining for 15 min. The samples were photographed by the CLSM.

### 2.3.7 Quantitative reverse transcription-polymerase chain reaction (qRT-PCR)

Total RNA was extracted from the target cells using the TRIzol reagent (Invitrogen, USA) and quantified using a NanoDrop 2000 Spectrophotometer (Thermo Fisher Scientific, USA). Thereafter, 500 ng of total RNA from each sample was used to synthesize complementary DNA (cDNA) via PrimeScript<sup>TM</sup> RT Master Mix (Takara, China). Finally, 10 ng of cDNA from each sample was used for qPCR with TB Green Premix Ex Taq II (Takara, China) and synthesized primers (Generay, China) in real-time fluorescent quantitative PCR (Bio-Rad, USA). The relative gene expression was calculated using  $2^{-\Delta\Delta\text{Ct}}$  and GAPDH as the housekeeping gene. The primer sequences were listed in Table 3. The examined genes were ALP, runt-

related transcription factor 2 (RUNX2), collagen type I (COL I), osteopontin (OPN), EFNB2, EPHB4, VEGF, basic fibroblast growth factor (bFGF), SERPINF1, ANGPTL1, SPROUTY1, angiogenin (ANG), CD146, and PDGFB.

### 2.3.8 Western blotting

For cell lysis, RIPA buffer containing 1% proteinase inhibitor, cocktail (ComWin Biotech, China) was added, followed by centrifugation. The supernatant was harvested and quantified using the BCA kit before being subjected to western blot analysis. The protein (20 µg) was separated using 10% sodium dodecyl sulfate-polyacrylamide gel electrophoresis. The targeted protein was then transferred to a polyvinylidene difluoride membrane and blocked with 1% PBST containing 3% FBS for 1 h. The primary antibodies rabbit anti-human RUNX2 (1:1000, CST, USA), mouse anti-human CD146 (1:1000, CST, USA), and rabbit anti-human β-actin (1:1000, CST, USA) were incubated with the cells at 4 °C overnight. The secondary antibodies goat anti-rabbit (1:2000, CST, USA) and rabbit anti-mouse (1:2000, CST, USA) were then incubated for 1 h. Finally, chemiluminescence detection reagents (ECL, Amersham) were mixed and added onto the membrane and exposed to an X-ray film. A gel imaging system (Bio-Rad, USA) was used for capturing images, and the final results were analyzed using Image J.

**Table 3.** Primers sequences used for the qRT-PCR analysis.

No.	Primer name	Sequence
1	ALP	sense: GGCTGTAAGGACATCGCCTA antisense: GGGTCAAGGGTCAGGAGTTC
2	RUNX2	sense: TACTATGGCACTTCGTCAGGA antisense: GATTCATCCATTCTGCCACTA
3	COL I	sense: CGATGGATTCCAGTTCGATGTGGT antisense: TGTTCTTGCAAGTGGTAGGTGATG
4	OPN	sense: GCTAAACCCTGACCCATC antisense: CTTTCGTTGGACTTACTTGG
5	EFNB2	sense: CTCCTCAACTGTGCCAAACCA antisense: GGTATCCAGGCCCTCCAAA

6	EPHB4	sense: GATGCCTGGAGTTACGGGATTG antisense: TCCAGCATGAGCTGGTGGAG
7	VEGF	sense: GGAGGCAGAGAAAAGAGAAAGTGT antisense: TAAGAGAGCAAGAGAGAGCAAAAAGA
8	bFGF	sense: AGTCTTCGCCAGGTCATTGAGATC antisense: CGTCCTGAGTATTCGGCAACAG
9	SERPINF1	sense: ATAGTCCAGCGGGAAGGT antisense: TAGCAAGATCACAGGCAAAC
10	ANGPTL1	sense: TACCTCCCAGCAGACCAG antisense: TTTTCCCGACAAGACACC
11	SPROUTY1	sense: ATTGCCCTTTCAGACCTA antisense: AATAATAACTACGAGCACAGAC
12	ANG	sense: TGGTGACCTGGAAAGAAG antisense: GCACTATGATGCCAAACC
13	CD146	sense: GAGACAGGTGTTGAATGCACG antisense: TGTTGGCTCTGGTATGAGGAC
14	PDGFB	sense: ATGGAGTTTGCTGTTGAGGTGG antisense: GCAGGGTGGAGGTAGAGAGATG
15	GAPDH	sense: GCACCGTCAAGGCTGAGAAC antisense: TGGTGAAGACGCCAGTGGAA

## 2.4 Construction and characterization of tissue-engineered bone grafts

### 2.4.1 Fabrication of 3D printed TCP scaffolds

Briefly, β-TCP (Kunshan Chinese Technology New Materials Co., Ltd., China) ink was prepared by dispersing the TCP powder in a dispersant with distilled water, hydroxypropyl methylcellulose, and polyethylenimine (PEI). A 3D bioprinter (Regenovo, China) was used to design and print the scaffolds. To obtain final scaffolds with a diameter of 5 mm and thickness of 1 mm, the printing parameters were set as 700 µm in distance and 200 µm in height. After being printed, the scaffolds were air-dried for 24 h and sintered at 1100 °C for 3 h.

### 2.4.2 Constructing a tissue-engineered bone graft

The sterile 3D TCP scaffolds were soaked in the culture medium overnight and air-dried. Afterwards, 15 µL cell suspension ( $6.67 \times 10^6$ /mL) of the 3:1 or 4:0 group

was seeded onto the scaffolds. After adhesion of 3 h, the culture medium was refilled.

#### **2.4.3 Scanning electron microscopy (SEM)**

The morphology of the scaffolds and attached cells was observed by SEM (S3400N, Hitachi, Japan). Before the test, 2.5% glutaraldehyde (Leagene, China) was added to the samples for fixation. The samples were then dehydrated using gradient concentrations of alcohol, followed by air-drying. The samples were sputter-coated with Au–Pd plasma and then mounted on the SEM for observation.

#### **2.4.4 Live/dead staining**

Three days post-cell seeding, a live/dead staining kit (BestBio, China) was used for characterization according to the manufacturer's instructions. The samples were observed under the CLSM.

### **2.5 In-vivo study and analysis**

With the approval of the Ethics Committee of Guangzhou Medical University (GY2019-031), 12 male Sprague-Dawley rats (12 weeks, weights of 250–300 g) were chosen for the bone repair study. The rats were divided into the following four groups: blank, scaffold, 4:0 and 3:1. The 4:0 and 3:1 groups were chosen on the basis of the results of the aforementioned studies ( $n = 6$ ). Two critical-sized calvarial bone defects were created per rat. Sodium pentobarbital (30 mg/kg) was used to induce general anesthesia by intraperitoneal injection. After being shaved and sterilized, the soft tissue was cut along the middle line of the skulls of rats. The muscles and periosteum were separated bluntly to thoroughly expose the operation area. A full-thickness bone defect with a diameter of 5 mm was created with a trephine under continuous saline irrigation. The bone grafts were implanted, and the wounds were closed with strict sutures. Penicillin 400,000 U was injected intramuscularly for 3 days after the operation. Four weeks later, the rats received euthanasia with inhalation anesthesia using isoflurane (Yipin, China). The specimens were harvested and fixed in 4% PFA for further studies.

#### **2.5.1 Micro-CT analysis**

Micro-CT (SkyScan 1172, Bruker, Belgium) was used for the radiographic analysis. The scanning parameters included 1-mm thickness of aluminum filter, resolution of  $2000 \times 1332$ , 9- $\mu\text{m}$  pixel size, voltage of 80 kV, and current of 100  $\mu\text{A}$ .

NRecon 1.0 software was then used to rebuild, Dataviewer for ROI selection, and CTAn1.13 software for new bone volume, trabecular number, and thickness analyses. As no bone formation was detected in the center of the defect in the blank group, the new bone volume, trabecular number, and thickness were set as zero.

#### **2.5.2 Histological study**

The harvested calvarial specimens were decalcified using 10% EDTA for 4 weeks. Thereafter, they were washed overnight, dehydrated, embedded in paraffin, and sliced into 4- $\mu\text{m}$ -thick sections. To detect the tissue structures, the harvested umbilical cord was prepared and sliced following the aforementioned method. For the immunohistochemical staining analysis, the umbilical cord tissue was subjected to CD31 and CD34 staining. After pretreatment, the samples were incubated with mouse anti-human CD31 (1:1600, CST, USA) and rabbit anti-human CD34 (1:200, Abcam, USA) at 4 °C overnight. After rewarming and 10% PBS washing of the samples, the secondary antibodies rabbit anti-mouse (1:200, CST, USA) and goat anti-rabbit (1:200, CST, USA) were added and incubated at 37 °C for 1 h. Afterwards, 10% DAB was used for staining followed by hematoxylin to stain the nuclei.

Hematoxylin & eosin (H&E) staining was performed using an automatic dyeing machine (Sakura, Japan). According to the manufacturer's instructions, a Masson trichrome staining kit (Servicebio) was used. After dewaxing, the following series of staining tests were performed: hematoxylin dyeing for 3 min, acid fuchsin dyeing for 5–10 min, molybdenum phosphate acid dipping for 1–3 min, and aniline blue dyeing for 3–6 min. For the quantitative analysis, the percentage of the new bone volume was calculated using the following formula:  $\text{new bone area}/\text{total area} \times 100\%$ .

### **2.6 Statistical analysis**

All data were expressed as the mean  $\pm$  standard deviation (SD) from at least three independent tests. GraphPad Prism 6.0e was used for the statistical analyses. The differences among the groups were analyzed using one-way analysis of variance (ANOVA), followed by the *post-hoc* test of Tukey. A two-way ANOVA was used to assess the differences among the groups at multiple time points, followed by Sidak's *post-hoc* test. The significance level was set at  $P < 0.05$ .



### 3. RESULTS

#### 3.1 Characteristics of the umbilical cord and hUCMSCs from the Wharton's jelly

The structures of the umbilical cord tissue were demonstrated by H&E staining. Two darkly-stained round arteries coupled with one oval-shaped vein were observed in the central part of the pink-stained Wharton's jelly, which was surrounded by a thin layer of epithelium. At a high magnification, the Wharton's jelly was loose with scattered eosinophilic-stained mononuclear cells (Figure 1A). The immunohistochemical staining showed that the Wharton's jelly did not contain CD31- or CD34-positive hematopoietic cells. These brown-stained cells could be observed in the arteries and the vein (Figure 1B). The isolated P1 cells from the Wharton's jelly were homogeneous, bipolar spindle-shaped and arranged in a whirlpool (Figure 1C). The flow cytometric analysis showed that more than 99% of the cells expressed the surface markers of CD73 and CD90 of MSCs, but did not express the hematopoietic cells' markers of CD34 and CD45 (Figure 1D).

#### 3.2 Osteogenic differentiation of hUCMSCs

To evaluate the osteogenic differentiation capacity of hUCMSCs, the ALP activity in the quantitative and qualitative analyses, osteogenesis-related genes expression, and mineralized nodules formation were studied. After 4, 7, and 10 days of osteogenic induction, the ALP staining of the hUCMSCs in OM became purple and darker than that in PM, and the darkest color was observed on the 4<sup>th</sup> day (Figure 2A). These results were consistent with the quantitative examination of ALP activity (Figure 2B). It's showed that the ALP activity increased significantly during the observed period in OM compared with that in PM and reached the highest level on the 4<sup>th</sup> day, which was twice and three times higher than that on the 7<sup>th</sup> and 10<sup>th</sup> days. The mRNA expression levels of ALP and OPN increased significantly after osteogenic induction at all detected time points, while the mRNA expression levels of RUNX2 and COL I increased significantly only on the 4<sup>th</sup> day (Figure 2C). ARS showed scattered calcium nodules in week 3 post-induction, which increased remarkably after 5 weeks. No calcium nodules were found in the PM group (Figure 2D).

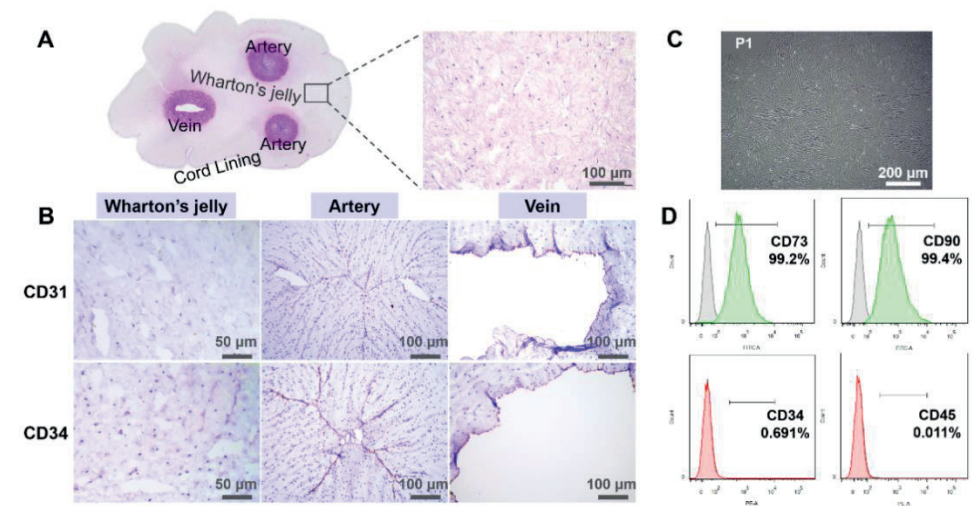


**Figure 1.** Characteristics of the umbilical cord and hUCMSCs from the Wharton's jelly. A: H&E staining of the umbilical cord tissue. Light pink represents the Wharton's jelly, and dark pink refers to the arteries and vein. At a high magnification, loose and irregular jelly-like tissue was observed with nuclei stained dark blue. B: Immunohistochemical staining of the Wharton's jelly, arteries, and vein with CD31 and CD34. Positive brown-stained cells could only be detected in the arteries and vein. C: Wharton's jelly-derived P1 cells with homogeneous bipolar spindle-like shape, aligning in a whirlpool. D: Surface markers of P5 cells.

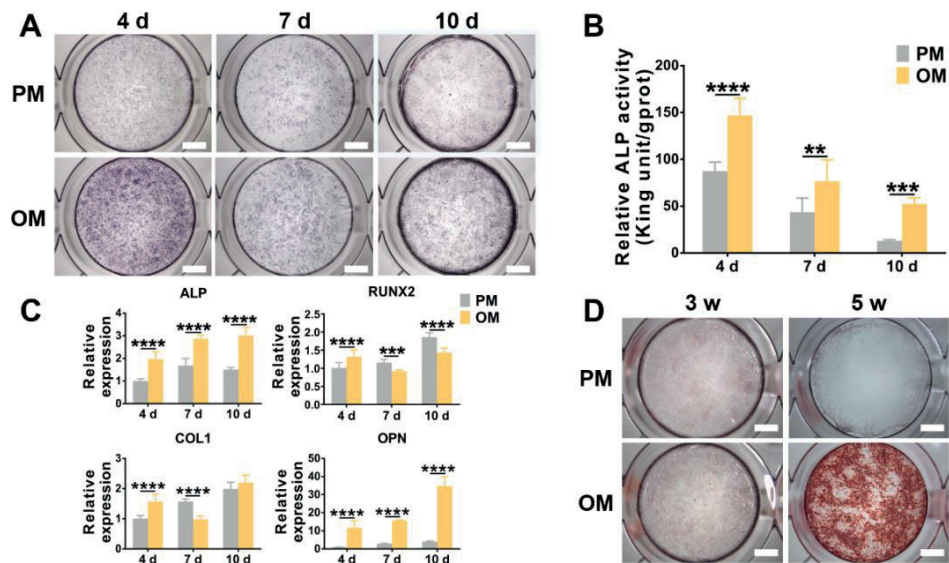


**Figure 2.** Osteogenic differentiation of hUCMSCs. A & B: ALP staining and quantitative analysis of non- and osteogenically-induced hUCMSCs on days 4, 7 and 10. C: The expression levels of osteogenesis-related genes ALP, RUNX2, COL I, and OPN on days 4, 7 and 10. D: ARS of non- and osteogenically-induced hUCMSCs in weeks 3 and 5. More red-stained calcium depositions were observed in OM than in PM in week 5. Scale bar = 200  $\mu$ m. \*\*  $p < 0.01$ ; \*\*\*  $p < 0.001$ ; \*\*\*\*  $p < 0.0001$ .

### 3.3 Angiogenic differentiation of hUCMSCs

Three days post-EIM induction, the induced hUCMSCs became elongated and polygonal with a large number of vascular-like structures (Figure 3A). As tube formation on the Matrigel and ac-LDL phagocytosis are the two representative experiments for determining whether the induced MSCs bear endothelial cells' functions, we performed the two tests to examine the morphological and functional changes of hUCMSCs. The analyses showed that the an-hUCMSCs incubated on the Matrigel for 2.5 h were able to form a reticular structure resembling vessels, while the non-induced hUCMSCs were distributed in clusters (Figure 3B). Similarly, the an-hUCMSCs engulfed Dil-ac-LDL with red fluorescent-labeled ac-LDL around the blue nuclei, while the non-induced MSCs did not possess the same function (Figure 3C). The immunofluorescence staining showed that after the angiogenic

induction, the cells connected in a circular pattern and expressed both the arterial endothelial cell marker EphrinB2 and the venous endothelial cell marker EphB4 (Figure 3D). QRT-PCR examination detected the expression levels of pro-angiogenic genes EFNB2, EPHB4, VEGF, and bFGF on the 4<sup>th</sup>, 7<sup>th</sup>, and 10<sup>th</sup> day after induction. The expression of EFNB2, VEGF, and bFGF significantly enhanced on the 4<sup>th</sup> day. The expression levels of all the tested genes declined significantly on the 7<sup>th</sup> and 10<sup>th</sup> days (Figure 3E). In contrast, the expression levels of anti-angiogenic genes SERPINF1 and ANGPTL1 increased over the whole period. The trend was opposite to that of the anti-angiogenic gene SPROUTY1 and pro-angiogenic genes (Figure 3F).

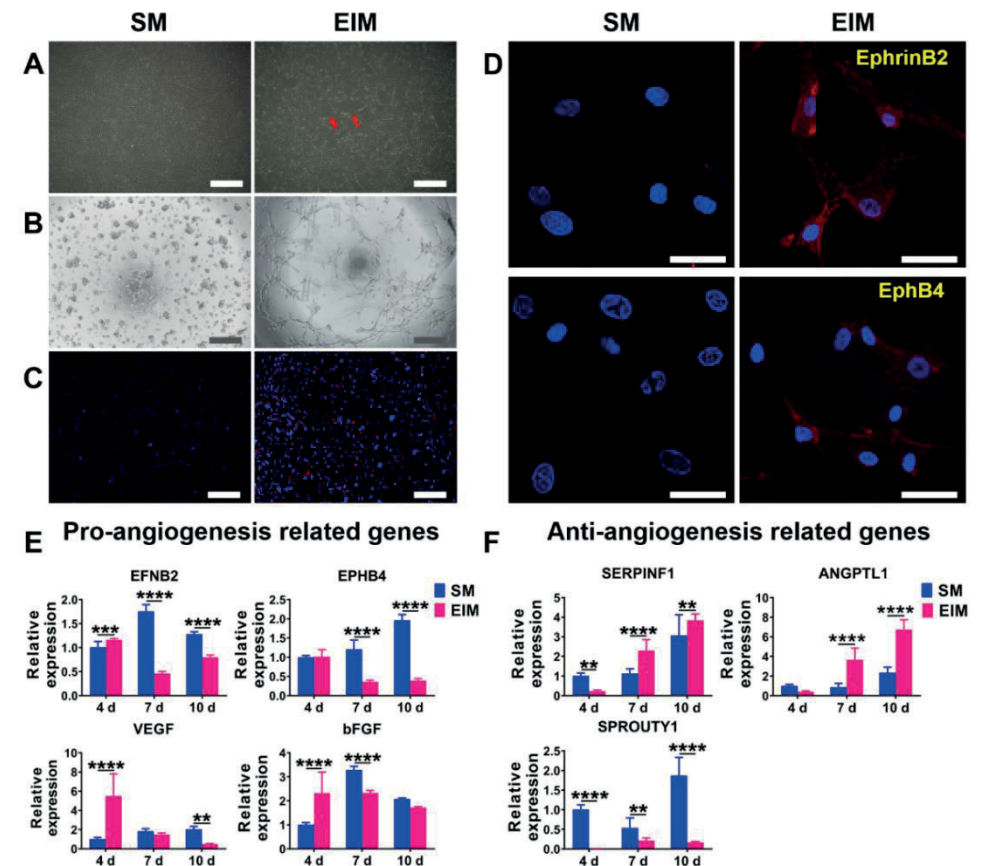


**Figure 3.** Angiogenic differentiation of hUCMSCs. After the angiogenic induction, the morphology of hUCMSCs changed to vascular-like structures, indicated by the red arrows in

phase-contrast microscopy images (A). The an-hUCMSCs bore angiogenic ability in Matrigel (B) and Dil-ac-LDL phagocytosis test (C), which showed blue-stained nuclei and red-stained Dil-labeled ac-LDL in the cells. D: The immunofluorescence assay validated the expression of the EphrinB2 and EphB4 proteins. E: The mRNA expression of the pro-angiogenesis-related genes EFNB2, EPHB4, VEGF, and bFGF, as well as (F) anti-angiogenesis-related genes SERPINF1, ANGPTL1, and SPROUTY1 after induction on days 4, 7 and 10. A–C, scale bar = 200  $\mu\text{m}$ ; D, scale bar = 50  $\mu\text{m}$ . \*\*  $p < 0.01$ ; \*\*\*  $p < 0.001$ ; \*\*\*\*  $p < 0.0001$ .

### 3.4 Screening the co-culture media

When the os-hUCMSCs and an-hUCMSCs were co-cultured for 17 days, ARS showed that the cells co-cultured in PM at ratios of 3:1, 2:2, and 1:3 also had an osteogenic differentiation ability with calcium nodules formation (Figure 4A), which did not differ statistically from that of the positive control group (Figure 4B). Similarly, there was no significant difference between PM, OM, EMM and PMM of 1:3 groups and the positive control group. Only in PMM (3:1) culture medium did a large number of scattered calcium nodules form in 3:1 group (Figure 4A), which were dramatically increased compared with those of the other groups. The 3:1 group exhibited an OD value of about 5.1 times higher than that of the control group (Figure 4B). PMM was therefore selected as the co-culture medium.

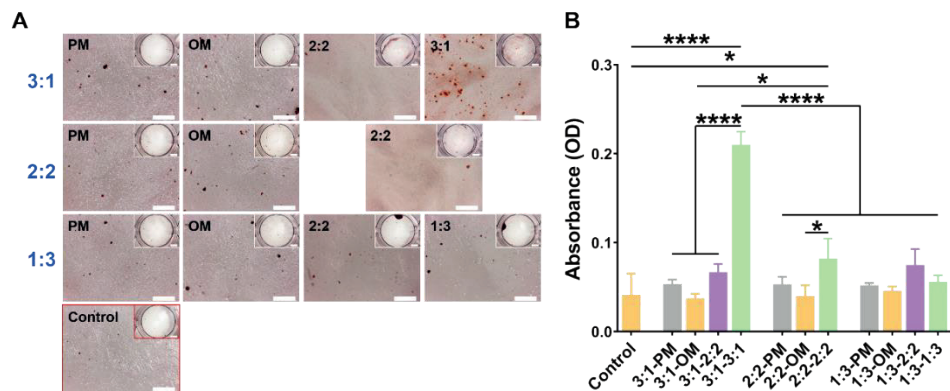


**Figure 4.** Screening the co-culture media for the dual-directional induction of hUCMSCs. A: ARS results of os-hUCMSCs and an-hUCMSCs co-cultured at varied ratios in different media for 17 days. Scale bar = 100  $\mu\text{m}$ ; Inset image, scale bar = 200  $\mu\text{m}$ . Osteogenically-induced hUCMSCs in OM were set as the positive control group. B: Quantitative assay of calcium nodules. \*  $p < 0.05$ ; \*\*\*\*  $p < 0.0001$ .

### 3.5 Effects of co-culture on the osteogenesis and angiogenesis of hUCMSCs

After co-culture, the cell proliferation rate and ALP activity of the 3:1 group were similar to those of the 4:0 group in OM, which was the positive control (Figure 5A & B). The expression levels of osteogenesis-related genes RUNX2 and ALP, and RUNX2 protein in group 3:1 were significantly higher than that of the 4:0 group (Figure 5C & D). The proliferation rates in the 2:2 and 1:3 groups maintained at a high level during the overall observation period (Figure 5A). The 2:2 group bore the highest expression levels of ALP, RUNX2, and the RUNX2 protein (Figure 5C & D). In contrast, the ALP activities of the 1:3 group on the 1<sup>st</sup> and 2<sup>nd</sup> days were the highest compared with those of the others (Figure 5B), while the gene expression of ALP decreased after 3 days' co-culture. The expression levels of gene and protein of RUNX2 were still higher than those of the 4:0 group (Figure 5C & D). Angiogenic analysis showed that ANG mRNA expression on the 3<sup>rd</sup> day was higher in the 3:1 group than that of the 0:4 group, as were PDGFB mRNA expression in the 2:2 group and VEGF mRNA expression in the 1:3 group (Figure 5C). These differences were statistically significant. The gene and protein expression of CD146, which is a marker of pericytes related to vascular stability, were higher in the 3:1 group than in the 0:4 group (Figure 5C–E).

To further illustrate the angiogenic capacity of the co-culture system, the Matrigel tube formation assay was performed. After 3 days of pre-induction (which was labeled as 0 day), the number of vascular tubules that formed on the Matrigel was positively correlated with the percentage of mixed an-hUCMSCs; the shapes of the vascular tubules were more completely and continuously circular (Figure 6). After 3 days of co-culture, the 0:4 group still possessed good angiogenic ability, while the tube formation of the other groups weakened with only a small number of branching structures (Figure 6).



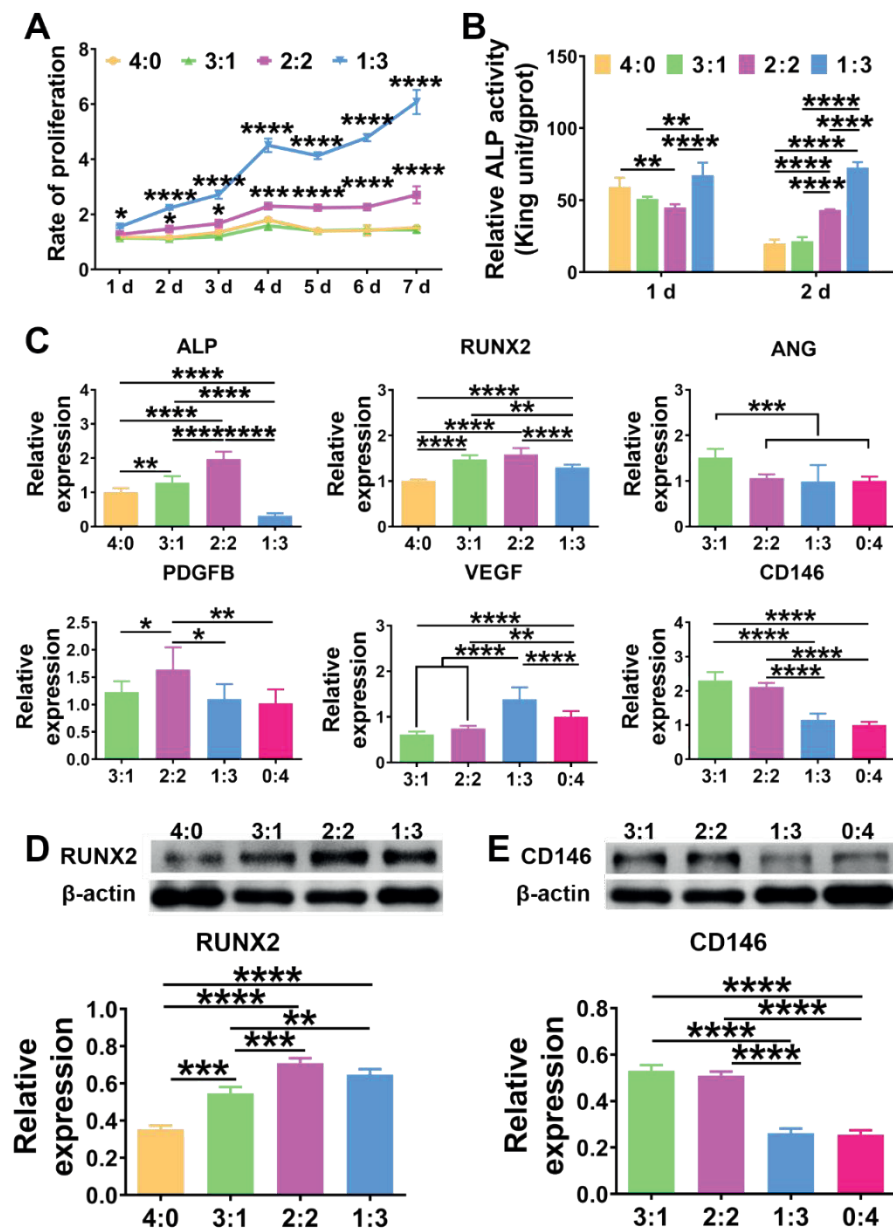


**Figure 5.** The co-culture of hUCMSC-derived osteogenic and angiogenic cells. A: Cell proliferation curves. B: Quantification of ALP activity. C: Expression levels of osteogenesis- and angiogenesis-related genes after co-culture for 3 days. D–E: RUNX2 and CD146 protein expression after co-culture for 3 days. \*  $p < 0.05$ ; \*\*  $p < 0.01$ ; \*\*\*  $p < 0.001$ ; \*\*\*\*  $p < 0.0001$ .

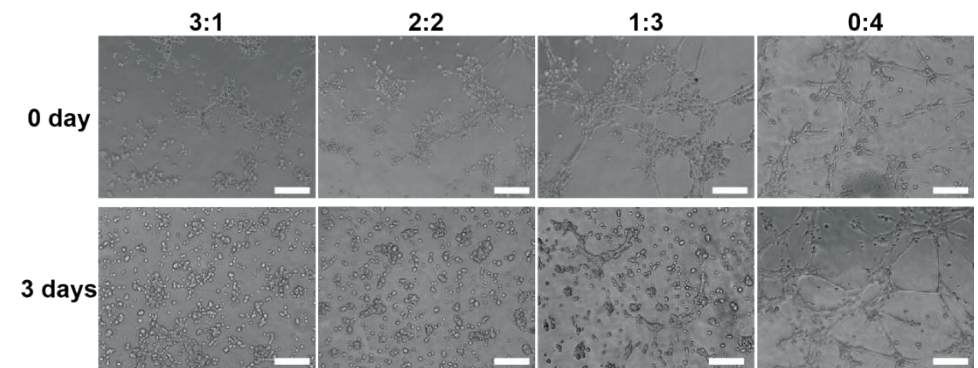


**Figure 6.** Tube formation capacity of the co-cultured cells. The percentage of mixed an-hUCMSCs was positively correlated with the number of vascular tubules formed on the Matrigel. Only a few branches were observed in the 3:1 and 2:2 groups. Scale bar = 200  $\mu\text{m}$ .

### 3.6 Characterization of the tissue-engineered constructs with co-cultured dual-directionally differentiated hUCMSCs

SEM showed that the struts of the 3D printed TCP scaffolds were delicate and uniform with a pore size ranging from 350 to 400  $\mu\text{m}$  (Figure 7A). At 3500 $\times$  magnification, microporous and nanoporous structures could be observed (Figure 7B). Live/dead staining results showed that green-stained live cells attached to the scaffold with barely visible red-stained dead cells (Figure 7C). Similarly, the hierarchically porous structure was beneficial to the growth and migration of MSCs, suggesting that the 3D scaffolds possessed excellent cytocompatibility and this combination was feasible for the fabrication of bone grafts (Figure 7D).

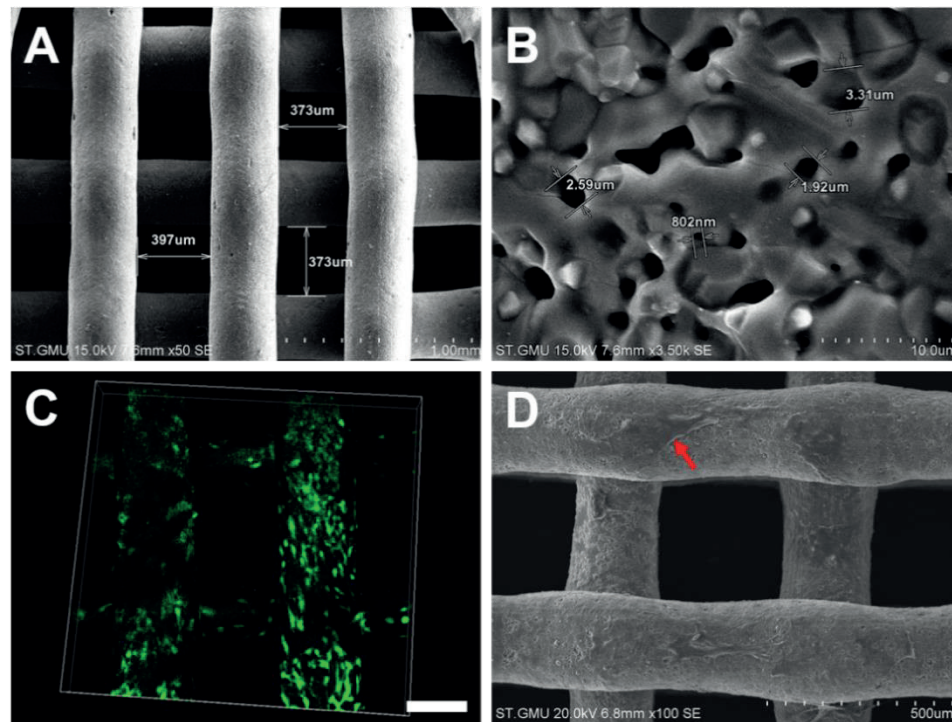


**Figure 7.** Characterization of the tissue-engineered constructs with co-cultured dual-directionally differentiated hUCMSCs. A: Surface architecture and (B) microstructure of the scaffolds under SEM. C: Live/dead staining results showed green-stained living cells attached to the scaffold. D: Dual-directionally differentiated hUCMSCs spread well on the scaffolds showed by SEM. The red arrow refers to dual-directionally differentiated hUCMSCs. Scale bar = 200  $\mu$ m.

### 3.7 Rehabilitation of the critical-sized bone defects

After the operation, all rats recovered well. Four weeks later, micro-CT showed that only a small amount of new bone grew from the host bone in the periphery of the defects in the blank group. There was still little bone formed around the implanted scaffolds. After the incorporation of the os-hUCMSCs, much new bone grew evenly along the scaffolds. Moreover, the 3:1 ratio of os-hUCMSCs/an-hUCMSCs significantly enhanced the new bone volume, trabecular number, and thickness (Figure 8A & B).

To further ensure the outcome pertaining to bone formation, H&E and Masson

trichrome staining were both performed. From the gross view of the newly regenerated tissues in the defect area, there were prominent amounts of pink-stained connective tissues with slightly new bone regenerated along the host bone in the blank group. With implanted scaffolds, osteoid and a few capillaries were observed in the central area of the defects. After implanting the os-hUCMSCs coated scaffolds, red-stained mature bone regenerated in the central area with dense, regular connective tissues along the porous structures of the decalcified TCP scaffolds. In the 3:1 group, abundant mature bone scattered with dark pink-stained bone lacuna surrounded by connective tissues (Figure 8A). The Masson trichrome staining revealed dark red-stained mature bone and light blue-stained collagen in the 3:1 group. Relatively small amounts of mature bone formed in the 4:0 group, and no bone regenerated in the groups with or without the scaffolds. The quantitative analysis validated that the 3:1 group bore the greatest bone formation than the other groups (Figure 8C).

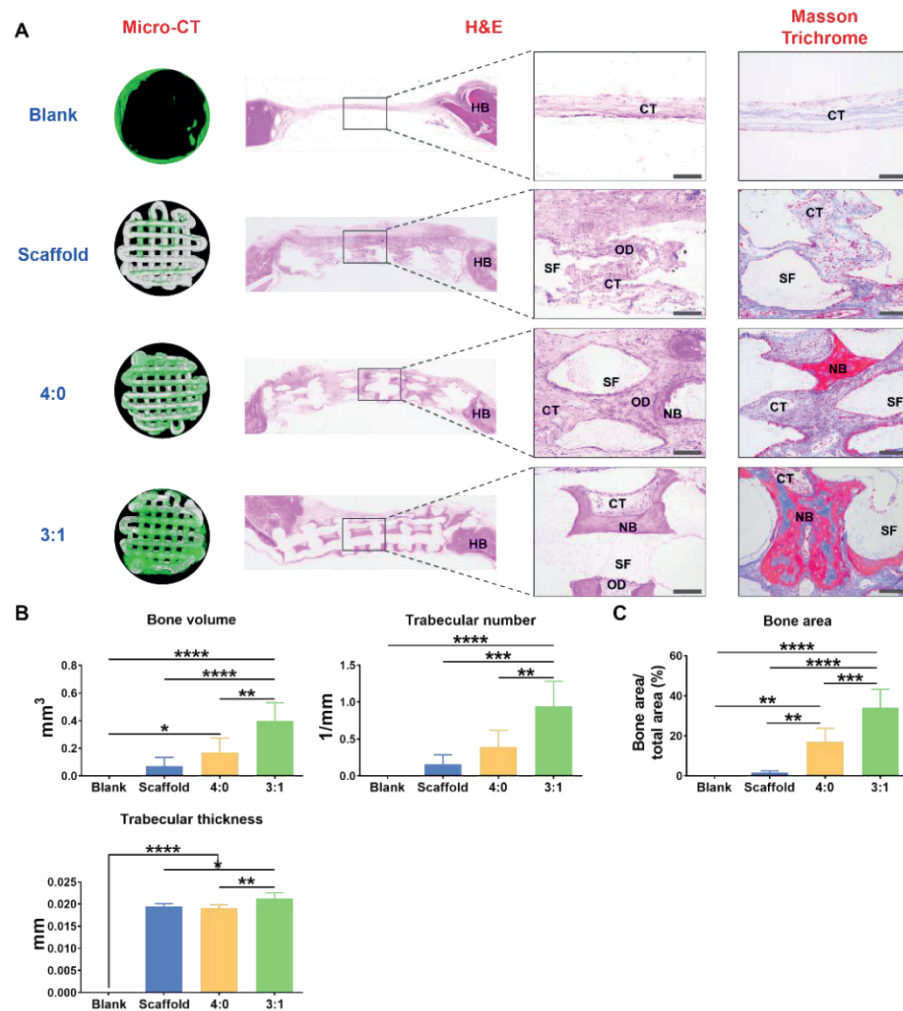


**Figure 8.** *In-vivo* rehabilitation outcomes of the calvarial bone defects in rats. A: Micro-CT and histological results validating the reconstruction outcomes. In the micro-CT results, green-stained tissue refers to the newly formed bone, while the grey stands for the 3D scaffold. The histological analysis showed that pink-stained homogeneous osteoid and new bone structures from H&E staining and dark red-stained mature bone and light blue-stained collagen tissues from Masson trichrome staining could be detected in the 3:1 group. CT: connective tissue; SF: scaffold; OD: osteoid; NB: new bone; HB: host bone. B: Quantitative comparisons of new bone volume, trabecular number, and thickness among the studied groups. C: Percentage of new bone calculated by the histological study. Scale bar = 100  $\mu$ m. \*  $p < 0.05$ ; \*\*  $p < 0.01$ ; \*\*\*  $p < 0.001$ ; \*\*\*\*  $p < 0.0001$ .

## 4. DISCUSSION

With the increasing demands of bioactive bone grafts in clinical settings, MSCs have been regarded as an ideal approach to enhance the osteogenic, angiogenic, and immunoregulatory capacities of bio-scaffolds. The larger bone scaffolds are, the harder it is for seeded cells to live inside them due to the limited perfusion and migration of capillaries. In this study, the dual-directional differentiations of hUCMSCs were conducted, which were then co-cultured under screened conditions to enhance osteogenic capacity, thus facilitating the fabrication of bioactive tissue-engineered bone grafts to repair critical-sized bone defects.

After culturing hUCMSCs in OM, we found that the ALP activity and osteogenic genes (ALP, RUNX2, COL 1, and OPN) expression levels in hUCMSCs were significantly higher than those in non-induced hUCMSCs. The ARS results showed that only dispersed punctiform calcium nodules appeared in week 3, which was consistent with previous studies [25-27]. Flaky calcification did not occur until week 5, suggesting that hUCMSCs achieved a similar osteogenic outcome to that of hBMSCs when being induced for a longer time. This outcome may result from the different origins of the two cell types: hBMSCs are more likely to express the same genes as osteoblasts, while hUCMSCs tend to express the same genes as embryonic stem cells [25]. Batsali et al. find that the expression levels of the genes related to WNT signaling pathway are significantly lower in hUCMSCs during osteogenic differentiation than in hBMSCs, while WNT-1 inducible-signaling pathway protein-1 (WISP1) can induce significantly increased expression of osteogenesis-related genes [27]. Thus, the inadequate activation of the WNT signaling pathway in hUCMSCs may lead to a relatively low osteogenic ability.

Previously reported methods of angiogenic induction include cytokine induction [28], hypoxia induction [29, 30], co-culture induction [31, 32] and gene transfection induction [33]. The angiogenesis-related cytokine-induced differentiation of MSCs into angiogenic cells is the most commonly used approach. Herein, EIM was prepared by adding VEGF and bFGF to EGM. After a 4-day induction, tube formation and ac-LDL phagocytosis were found in an-hUCMSCs, which were consistent with other reports [34, 35]. The expression levels of the artery- and vein-specific proteins (EphrinB2 and EphB4) increased [28, 36]. The



angiogenic genes expression levels of EFNB2, EPHB4, VEGF, and bFGF were higher than those in the non-induced group on the 4<sup>th</sup> day, while they were lower on the 7<sup>th</sup> and 10<sup>th</sup> days. In contrast, anti-angiogenic genes expression levels of SERPINF1 and ANGPTL1 showed the opposite outcome. Only the expression of SPROUTY1 was lower than that of the non-induced group. Similarly, Konig et al. show that angiogenically-induced human amniotic stromal cells (hAMSCs) bear a significant down-regulation of the pro-angiogenic genes expression (e.g., VEGF and fibroblast growth factor-2) and up-regulation of the anti-angiogenic genes expression (e.g., SERPINF1 and SPROUTY1) [37]. It can be speculated that after angiogenic induction, hUCMSCs prevent themselves from differentiating into mature endothelial cells by up-regulating the expression levels of anti-angiogenic genes. Compared with the results of other studies that focus on inducing MSCs to differentiate into angiogenic cells, in which the expression levels of angiogenic genes increase significantly [35, 38], our results were different. This may be attributed to the following reasons. First, the purity and angiogenic differentiation ability of MSCs are directly determined by cell types and sources. For example, bone marrow and fat are highly vascularized tissues. It is difficult to ensure that no endothelial cells or endothelial progenitor cells are included in isolated hBMSCs and hADMSCs [37]. In contrast, no capillaries exist in the Wharton's jelly. Furthermore, hADMSCs secrete more angiogenesis-related proteins than hBMSCs and hUCMSCs [26], which can also influence their angiogenic differentiation. Second, the compositions of the induction media are also different. The concentration of VEGF directly affects the results of the study because VEGF is crucial to trigger vascular development and the formation of blood vessels [37, 39]. Chen et al. [35] and Xu et al. [34] prove that the VEGF concentration of 50 or 100 ng/mL is more likely to cause changes in the expression levels of angiogenesis-related genes and proteins as well as final functions, while a low concentration of VEGF may not be enough to achieve these effects. In contrast, Konig et al. just utilize EGM-2 for the induction of hADMSCs [37]. In our study, 25 ng/mL of VEGF and 10 ng/mL of bFGF were added to EGM-2 to induce the hUCMSCs, which showed that there were only consistent changes in the expression levels of angiogenesis-related genes and proteins as well as their functions in a short

induction time. Third, the induction duration is also different between our study and previous studies, which report 5- [37], 7- [40], 9- [34], 12- [35], or 14-day [38, 41] induction periods or a much longer period of time.

Multiple studies have shown that compared with being cultured alone, osteogenic cells co-cultured with angiogenic cells resemble the physiological conditions *in vivo*, which shows synergistic effects on the processes of osteogenesis and angiogenesis [20, 42, 43]. Yang et al. attempt to induce the dual-directional differentiation of hADMSCs into osteogenic and angiogenic cells. The expression levels of osteogenesis- and angiogenesis-related genes and proteins increase significantly with a 1:1 co-culture ratio compared with 2:1 and 1:2 ratios [40]. To further study the osteogenesis of the co-cultured cells, we extended the mixing ratios and related culture media. ARS was selected to screen the optimal co-culture strategy. The 3:1 ratio of osteogenic cells/angiogenic cells cultured in the same ratio of OM/EIM bore the highest amount of calcium nodules formation than the other groups. As to the 3:1 group, the cell proliferation rate was consistent with that of the 4:0 group, but much slower than that of the 2:2 and 1:3 groups. This might be attributed to that the culture media of the 2:2 and 1:3 groups bore higher amounts of growth factors than those of the 4:0 and 3:1 groups. Compared with the cells in 4:0 group, cells in the 3:1 group bore a significantly increased expression of the early osteogenic genes (ALP and RUNX2), pro-angiogenesis-related gene ANG [44], and the pericyte-associated surface marker CD146 [45, 46]. These results suggested that the 3:1 co-culture system could effectively promote physiological processes related to osteogenesis and angiogenesis, thereby accelerating the osteogenic differentiation of hUCMSCs.

Biocompatible 3D printed  $\beta$ -TCP scaffolds [47, 48] were used as carriers of hUCMSC-derived osteogenic cells and angiogenic cells, so as to fabricate bioactive tissue-engineered bone grafts to repair the critical-sized calvarial bone defects of rats. The results further validated that the 3:1 group bore an optimal rehabilitation outcome compared with the other groups. Similarly, Zhou et al. find that the bone constructs of co-cultured BMSCs and BMSC-derived angiogenic cells on TCP scaffolds display a favorable repair outcome compared with constructs of mono-cultured BMSCs [49].

Though the co-culture system of dual-directionally pre-induced hUCMSCs could effectively promote osteogenesis, better than the mono-cultured hUCMSCs, the optimal pre-induction time and co-culture conditions need to be further studied. At present, many *in-vitro* studies have shown that there are several communication modes between osteogenic and angiogenic cells. First, soluble paracrine cytokines from endothelial cells, such as BMP2, VEGF, and IGF-1, promote the osteogenesis of BMSCs [50]. Second, the extracellular matrix plays a pivotal role in the communication between the two cell types [51-53]. Third, multiple scholars believe that the direct contact between cells allows angiogenic cells to promote the functions of BMSCs, and gap junctions are of paramount importance during this process [54]. Finally, *in-vivo* studies of long bone have shown that H-type blood vessels are important structures for the coupling effects of osteogenesis and angiogenesis [55], which are mediated by Notch signaling pathway of endothelial cells [56]. It is therefore important to further study whether there are similar communication modes between co-cultured hUCMSC-derived osteogenic and angiogenic cells.

Despite the promising results, there are several limitations in this study. First, dual-directionally pre-induced hUCMSCs should be labeled to identify the phenotypic changes after pre-induction and co-culture using flow cytometry as well as cell transformation after implantation. Second, cells from human were directly used in non-immunodeficient SD rats, and no immunosuppressive agents were injected after the operation. Although the literature has shown that the immunogenicity of hUCMSCs is low, the immune response is activated inevitably. Third, the genomes and proteomes of the dual-directionally differentiated hUCMSCs should be analyzed to clarify the induction efficacy and interactions between the cells. These limitations will be gradually addressed in follow-up experiments.

## 5. CONCLUSION

Our study validated that hUCMSCs bore a slightly low osteogenic efficacy and could be induced and differentiated into angiogenic cells with endothelial functions. The osteogenic capacity of dual-directionally differentiated hUCMSCs co-cultured

in PM was dramatically enhanced. Besides, the 3:1 group showed an optimal osteogenic capacity both *in vitro* and *in vivo* when being cultured in the same proportion of mixed media. This co-culture strategy of dual-directional pre-induction of hUCMSCs provides a novel approach for the construction of bioactive tissue-engineered bone grafts with enhanced osteogenesis for clinical transplantation.



## REFERENCES

- [1] R.J. O'Keefe, J. Mao, Bone Tissue Engineering and Regeneration: From Discovery to the Clinic — an Overview, *Tissue Eng Part B Rev* 17(6) (2011) 389-392.
- [2] A.M. Yousefi, et al., Prospect of Stem Cells in Bone Tissue Engineering: A Review, *Stem Cells Int* 2016 (2016) 6180487.
- [3] J.R. Perez, et al., Tissue Engineering and Cell-Based Therapies for Fractures and Bone Defects, *Front Bioeng Biotechnol* 6 (2018) 105.
- [4] G. Wang, et al., Enhanced Adhesion and Proliferation of Bone Marrow Mesenchymal Stem Cells on  $\beta$ -Tricalcium Phosphate Modified by an Affinity Peptide, *Mol Med Rep* 19(1) (2019) 375-381.
- [5] S.M. Mueller, J. Glowacki, Age-Related Decline in the Osteogenic Potential of Human Bone Marrow Cells Cultured in Three-Dimensional Collagen Sponges, *J Cell Biochem* 82(4) (2001) 583-590.
- [6] P. Kuchroo, et al., Paracrine Factors Secreted by Umbilical Cord-Derived Mesenchymal Stem Cells Induce Angiogenesis *in Vitro* by a VEGF-Independent Pathway, *Stem Cells Dev* 24(4) (2015) 437-450.
- [7] J. Li, et al., Human Umbilical Cord Mesenchymal Stem Cells Improve the Reserve Function of Perimenopausal Ovary Via a Paracrine Mechanism, *Stem Cell Res Ther* 8(1) (2017) 55.
- [8] L. Bai, et al., Bioactive Molecules Derived from Umbilical Cord Mesenchymal Stem Cells, *Acta Histochem* 118(8) (2016) 761-769.
- [9] S. Liu, et al., Immune Characterization of Mesenchymal Stem Cells in Human Umbilical Cord Wharton's Jelly and Derived Cartilage Cells, *Cell Immunol* 278(1-2) (2012) 35-44.
- [10] M.E. Klontzas, et al., Bone and Cartilage Regeneration with the Use of Umbilical Cord Mesenchymal Stem Cells, *Expert Opin Biol Ther* 15(11) (2015) 1541-1552.
- [11] B. Ye, et al., Rapid Biomimetic Mineralization of Collagen Fibrils and Combining with Human Umbilical Cord Mesenchymal Stem Cells for Bone Defects Healing, *Mater Sci Eng C Mater Biol Appl* 68 (2016) 43-51.
- [12] P. Cassar, R. Blundell, The Use of Umbilical Stem Cells, *Open J Pathol* 06(01) (2016) 41-56.
- [13] J. Rouwkema, A. Khademhosseini, Vascularization and Angiogenesis in Tissue Engineering: Beyond Creating Static Networks, *Trends Biotechnol* 34(9) (2016) 733-745.
- [14] Z. Wang, et al., Nanomaterial Scaffolds to Regenerate Musculoskeletal Tissue: Signals from within for Neovessel Formation, *Drug Discov Today* 22(9) (2017) 1385-1391.
- [15] H. Lu, et al., Human Adipose Mesenchymal Stem Cells Show More Efficient Angiogenesis Promotion on Endothelial Colony-Forming Cells Than Umbilical Cord and Endometrium, *Stem Cells Int* 2018 (2018) 7537589.
- [16] M. Nasser, et al., Engineering Microenvironments Towards Harnessing Pro-Angiogenic Potential of Mesenchymal Stem Cells, *Mater Sci Eng C Mater Biol Appl* 102 (2019) 75-84.
- [17] K. Hu, B.R. Olsen, Osteoblast-Derived VEGF Regulates Osteoblast Differentiation and Bone Formation During Bone Repair, *J Clin Invest* 126(2) (2016) 509-526.
- [18] E. Schipani, et al., Regulation of Osteogenesis-Angiogenesis Coupling by HIFs and VEGF, *J Bone Miner Res* 24(8) (2009) 1347-1353.
- [19] Y. Deng, et al., 3D Printed Scaffolds of Calcium Silicate-Doped  $\beta$ -TCP Synergize with Co-Cultured Endothelial and Stromal Cells to Promote Vascularization and Bone Formation, *Sci Rep* 7(1) (2017) 5588.
- [20] J. Chen, et al., Angiogenic and Osteogenic Synergy of Human Mesenchymal Stem Cells and Human Umbilical Vein Endothelial Cells Co-Cultured on a Nanomatrix, *Sci Rep* 8(1) (2018) 15749.
- [21] P. Simara, et al., Reprogramming of Adult Peripheral Blood Cells into Human Induced Pluripotent Stem Cells as a Safe and Accessible Source of Endothelial Cells, *Stem Cells Dev* 27(1) (2018) 10-22.
- [22] J. Ma, et al., Co-Culture of Osteoblasts and Endothelial Cells: Optimization of Culture Medium and Cell Ratio, *Tissue Eng Part C Methods* 17(3) (2011) 349-357.
- [23] Y. Zhang, et al., Efficiency of Co-Culture with Angiogenic Cells or Physiological BMP2 Administration on Improving Osteogenic Differentiation and Bone Formation of MSCs, *J Biomed Mater Res A* 107(3) (2019) 643-653.
- [24] F. Simunovic, et al., Increased Extracellular Matrix and Proangiogenic Factor Transcription in Endothelial Cells after Cocultivation with Primary Human Osteoblasts, *J Cell Biochem* 114(7) (2013) 1584-1594.
- [25] J.Y. Hsieh, et al., Functional Module Analysis Reveals Differential Osteogenic and Stemness Potentials in Human Mesenchymal Stem Cells from Bone Marrow and Wharton's Jelly of Umbilical Cord, *Stem Cells Dev* 19(12) (2010) 1895-1910.
- [26] P.R. Amable, et al., Protein Synthesis and Secretion in Human Mesenchymal Cells Derived from Bone Marrow, Adipose Tissue and Wharton's Jelly, *Stem Cell Res Ther* 5(2) (2014) 53.
- [27] A.K. Batsali, et al., Differential Expression of Cell Cycle and Wnt Pathway-Related Genes Accounts for Differences in the Growth and Differentiation Potential of Wharton's Jelly and Bone Marrow-Derived Mesenchymal Stem Cells, *Stem Cell Res Ther* 8(1) (2017) 102.
- [28] X.L. Aranguren, et al., *In Vitro* and *in Vivo* Arterial Differentiation of Human Multipotent Adult Progenitor Cells, *Blood* 109(6) (2007) 2634-2642.
- [29] K.H. Han, et al., Enhancement of Angiogenic Effects by Hypoxia-Preconditioned Human Umbilical Cord-Derived Mesenchymal Stem Cells in a Mouse Model of Hindlimb Ischemia, *Cell Biol Int* 40(1) (2016) 27-35.
- [30] S. Kusuma, et al., Low Oxygen Tension Enhances Endothelial Fate of Human Pluripotent Stem Cells, *Arterioscler Thromb Vasc Biol* 34(4) (2014) 913-920.
- [31] B. Joddar, et al., A Contact-Based Method for Differentiation of Human Mesenchymal Stem Cells into an Endothelial Cell-Phenotype, *Cell Biochem Biophys* 76(1-2) (2018) 187-195.
- [32] D. Li, et al., Vascularization Converts the Lineage Fate of Bone Mesenchymal Stem Cells to Endothelial Cells in Tissue-Engineered Bone Grafts by Modulating FGF2-Rhoa/Rock Signaling, *Cell Death Dis* 9(10) (2018) 959.

- [33] A. Cochrane, et al., Quaking Is a Key Regulator of Endothelial Cell Differentiation, Neovascularization, and Angiogenesis, *Stem Cells* 35(4) (2017) 952-966.
- [34] Y. Xu, et al., Umbilical Cord-Derived Mesenchymal Stem Cells Isolated by a Novel Explantation Technique Can Differentiate into Functional Endothelial Cells and Promote Revascularization, *Stem Cells Dev* 19(10) (2010) 1511-1522.
- [35] M.Y. Chen, et al., Endothelial Differentiation of Wharton's Jelly-Derived Mesenchymal Stem Cells in Comparison with Bone Marrow-Derived Mesenchymal Stem Cells, *Exp Hematol* 37(5) (2009) 629-640.
- [36] G. Zhang, et al., Arterial-Venous Endothelial Cell Fate Is Related to Vascular Endothelial Growth Factor and Notch Status During Human Bone Mesenchymal Stem Cell Differentiation, *FEBS Lett* 582(19) (2008) 2957-2964.
- [37] J. Konig, et al., Amnion-Derived Mesenchymal Stromal Cells Show Angiogenic Properties but Resist Differentiation into Mature Endothelial Cells, *Stem Cells Dev* 21(8) (2012) 1309-1320.
- [38] H. Orbay, et al., The Effects of Adipose-Derived Stem Cells Differentiated into Endothelial Cells and Osteoblasts on Healing of Critical Size Calvarial Defects, *J Craniofac Surg* 28(7) (2017) 1874-1879.
- [39] A.K. Olsson, et al., VEGF Receptor Signalling — in Control of Vascular Function, *Nat Rev Mol Cell Biol* 7(5) (2006) 359-371.
- [40] H. Yang, et al., Differentiated Adipose-Derived Stem Cell Co-Cultures for Bone Regeneration in Rada16-1 *in Vitro*, *J Cell Physiol* 233(12) (2018) 9458-9472.
- [41] C.C. Doan, et al., Differentiation of Umbilical Cord Lining Membrane-Derived Mesenchymal Stem Cells into Endothelial-Like Cells, *Iran Biomed J* 18(2) (2014) 67-75.
- [42] W.L. Dissanayaka, et al., Co-Culture of Dental Pulp Stem Cells with Endothelial Cells Enhances Osteo-/Odontogenic and Angiogenic Potential *in Vitro*, *J Endod* 38(4) (2012) 454-463.
- [43] S. Shanbhag, et al., Cell Cotransplantation Strategies for Vascularized Craniofacial Bone Tissue Engineering: A Systematic Review and Meta-Analysis of Preclinical *in Vivo* Studies, *Tissue Eng Part B Rev* 23(2) (2017) 101-117.
- [44] B.S. Kim, et al., Angiogenin-Loaded Fibrin/Bone Powder Composite Scaffold for Vascularized Bone Regeneration, *Biomater Res* 19 (2015) 18.
- [45] A.W. James, et al., Pericytes for the Treatment of Orthopedic Conditions, *Pharmacol Ther* 171 (2017) 93-103.
- [46] Y. Wang, et al., Relative Contributions of Adipose-Resident CD146(+) Pericytes and CD34(+) Adventitial Progenitor Cells in Bone Tissue Engineering, *NPJ Regen Med* 4 (2019) 1.
- [47] P. Miranda, et al., Sintering and Robocasting of  $\beta$ -Tricalcium Phosphate Scaffolds for Orthopaedic Applications, *Acta Biomater* 2(4) (2006) 457-466.
- [48] C.F. Marques, et al., Biphasic Calcium Phosphate Scaffolds Fabricated by Direct Write Assembly: Mechanical, Anti-Microbial and Osteoblastic Properties, *J Eur Ceram Soc* 37(1) (2017) 359-368.
- [49] J. Zhou, et al., The Repair of Large Segmental Bone Defects in the Rabbit with Vascularized Tissue Engineered Bone, *Biomaterials* 31(6) (2010) 1171-1179.
- [50] Y.N. Jiang, et al., Tension-Loaded Bone Marrow Stromal Cells Potentiate the Paracrine Osteogenic Signaling of Co-Cultured Vascular Endothelial Cells, *Biol Open* 7(6) (2018) bio032482.
- [51] Y. Schmidt, et al., Osteoblastic Alkaline Phosphatase mRNA Is Stabilized by Binding to Vimentin Intermediary Filaments, *Biol Chem* 396(3) (2015) 253-260.
- [52] F.M. Lampert, et al., Transcriptomic Changes in Osteoblasts Following Endothelial Cell-Cocultivation Suggest a Role of Extracellular Matrix in Cellular Interaction, *J Cell Biochem* 117(8) (2016) 1869-1879.
- [53] F. Simunovic, et al., Increased Differentiation and Production of Extracellular Matrix Components of Primary Human Osteoblasts after Cocultivation with Endothelial Cells: A Quantitative Proteomics Approach, *J Cell Biochem* 120(1) (2019) 396-404.
- [54] F. Villars, et al., Effect of HUVEC on Human Osteoprogenitor Cell Differentiation Needs Heterotypic Gap Junction Communication, *Am J Physiol Cell Physiol* 282(4) (2002) C775-785.
- [55] A.P. Kusumbe, et al., Coupling of Angiogenesis and Osteogenesis by a Specific Vessel Subtype in Bone, *Nature* 507(7492) (2014) 323-328.
- [56] S.K. Ramasamy, et al., Endothelial Notch Activity Promotes Angiogenesis and Osteogenesis in Bone, *Nature* 507(7492) (2014) 376-380.

Decellularized periosteum-derived hydrogels promote the proliferation, migration, and osteogenic differentiation of human umbilical cord mesenchymal stem cells

Shuyi Li<sup>#</sup>, Rongli Deng<sup>#</sup>, Tim Forouzanfar, Gang Wu, Daping Quan,  
Miao Zhou

Gels, 2022, 8(5):294.

## ABSTRACT

Human umbilical cord mesenchymal stem cells (hUCMSCs) are promising stem cells for bone tissue engineering, which have a non-invasive harvesting process, high cell yield, favorable proliferation capacity, and low immunogenicity. However, the osteogenic efficacy of hUCMSCs is relatively lower than that of human bone marrow mesenchymal stem cells (hBMSCs). Hydrogels from decellularized extracellular matrix (dECM) preserve the biological compositions and functions of natural ECM, which can provide tissue-specific cues to regulate phenotypic expression and cell fate. It is unknown, however, whether hydrogels from periosteum can serve as pro-osteogenic carriers of hUCMSCs. Herein, a decellularized periosteum-derived hydrogel (dPH) was fabricated to reveal the effects of periosteum-specific cues on the bioactivities of hUCMSCs. A widely used non-bone/periosteum-derived ECM hydrogel product — Matrigel, was used as the control group. After decellularization, the absence of nuclei in the histological analysis indicated the successful removal of cellular components, which was also confirmed by DNA content quantification. The storage modulus of dPH increased (from  $164.49 \pm 29.92$  Pa to  $855.20 \pm 20.67$  Pa) with the increasing concentration (from 0.5% to 1%). With a highly porous, fibrous microstructure, dPH had a more hydrophilic surface than Matrigel, of which the water contact angle reduced by  $62.62 \pm 0.04\%$ . Furthermore, dPH prominently promoted the initial cellular spreading with a significantly higher cell surface area (1.47-fold), cell spreading length (1.45-fold) and proliferation (about 1.05–1.13-fold) of hUCMSCs than those of Matrigel. Additionally, dPH was conducive to cell migration, whereas no cells migrated to Matrigel in the Transwell model. Compared with those of the Matrigel group, the osteogenesis-related genes expression levels (RUNX2, ALP, OPN, and OCN) and mineralized matrix formation (9.74-fold) of the hUCMSCs significantly increased in the dPH group. Our study indicated that dPH could provide a pro-osteogenic microenvironment for hUCMSCs, thereby revealing a promising application potential to repair bone defects.

**Keywords:** Periosteum; Decellularized extracellular matrix-derived hydrogels; Matrigel; hUCMSCs; Osteogenic differentiation.

## 1. INTRODUCTION

Mesenchymal stem cell (MSC)-based constructs have been considered promising alternatives to autologous bone grafts in repairing bone defects [1, 2]. MSCs are multipotent stem cells and can differentiate into diverse cell types, such as osteoblasts, chondrocytes, and adipocytes under specific stimuli from culture media or biomaterials [3, 4]. MSCs can be isolated from various tissues, such as bone marrow, umbilical cord, and adipose tissue. Human bone marrow mesenchymal stem cells (hBMSCs) are the most widely used stem cells for promoting bone regeneration [5]. However, the invasive harvesting process, low yield, and slow proliferation rate of hBMSCs restrict their clinical applications [6, 7]. In contrast, human umbilical cord mesenchymal stem cells (hUCMSCs) are primitive and possess a non-invasive harvesting procedure, an abundant source, and a high cell yield [8], which ensure a sufficient number of cells for bone tissue engineering (BTE). hUCMSCs also have a significantly higher proliferation capacity than hBMSCs and maintain high activity after multiple passages [9, 10]. Moreover, hUCMSCs show lower expression levels of human leukocyte antigen (HLA) I/II and a higher production of tolerogenic IL-10, transforming growth factor- $\beta$  (TGF- $\beta$ ), and HLA-G than hBMSCs. These indicate low immunogenicity and a strong immunosuppressive capacity of hUCMSCs and thereby support the application of allogenic hUCMSCs [11, 12]. These characteristics make hUCMSCs promising MSCs for BTE. However, a series of *in-vitro* studies have shown that hUCMSCs form less mineralized extracellular matrix — the final osteogenic differentiation marker — than that of hBMSCs in osteogenic differentiation medium [10, 13, 14]. This suggests a relatively lower osteogenic capacity of hUCMSCs. Sudo et al. show that almost no mineralized extracellular matrix is formed in hUCMSCs when being cultured on collagen type I-coated plastic dishes in osteogenic medium (OM) for 28 days [15]. Ciavarella et al. find mineralized extracellular matrix is detected in osteogenically-committed hUCMSCs after 40 days [16]. The microenvironment where hUCMSCs reside serves as an important regulatory role in the process of proliferation and osteogenic differentiation [17]. When OM contains osteoinductive growth factors, such as bone morphogenetic protein-2 (BMP2) and BMP7, the osteogenic property of hUCMSCs is significantly improved, and the expression

levels of osteogenic genes are comparable to those in hBMSCs [17, 18]. Our group adopted a biomimetic strategy of co-culturing osteogenically- and angiogenically-committed hUCMSCs in certain ratios and screened culture media to enhance their osteogenic efficacy [19]. These studies indicate that a strong osteogenic microenvironment is conducive to the osteogenic differentiation of hUCMSCs.

Natural extracellular matrix (ECM) has garnered extensive attention because it provides essential physical support for cells and initiates crucial biological signals which are necessary for tissue morphogenesis, differentiation, and homeostasis [20]. ECM is mainly composed of fibrous proteins (e.g., collagen type I, II, III, IV, VI, X, and elastin) and glycoproteins (e.g., proteoglycans, fibronectin, and laminin) [21]. It possesses abundant cell-recognition sites and various protein-adhesive domains to localize and deliver growth factors (e.g., BMP2, vascular endothelial growth factor (VEGF), and TGF- $\beta$ ), which can regulate cellular activities and phenotypic expression [21, 22]. Given their structural similarity to natural ECM, tunable physicochemical properties, and high operability, hydrogels that are derived from ECM components, such as collagen and complex mixtures of ECM proteins (e.g., Matrigel), are widely used in tissue engineering and regenerative medicine [23, 24]. Matrigel is derived from the basement membrane of murine Engelbreth-Holm-Swarm (EHS) tumors and contains a mixture of ECM proteins, such as laminin, collagen type IV, perlecan, entactin, and growth factors [25]. It has been extensively applied to culture cells in 2D/3D ways and promotes cell growth and differentiation [26]. As a non-bone-specific hydrogel, Matrigel primarily functions to provide a 2D/3D culture platform for adipose tissue-derived MSCs. Matrigel-coated culture plates show significantly enhanced extracellular matrix mineralization compared to that of polystyrene culture plates [27]. However, due to its origin from mouse tumors, the safety of Matrigel is a major concern. Furthermore, Matrigel may not contain all the necessary biological cues for osteogenesis. Therefore, an ECM-derived hydrogel specific for osteogenesis with a safe origin is in high demand, which can not only deliver cells to defect areas, but also provide a pro-osteogenic microenvironment to support and regulate cellular activities.

ECM hydrogels derived from decellularized tissues have been widely applied to repair tissue injuries or defects, such as intervertebral discs [28], peripheral

nerves [29], and bones [30]. It has already been established that the ECM hydrogel bears a tissue-specific induction property. For example, ECM hydrogels from decellularized nucleus pulposus (NP) induce hBMSCs to differentiate into NP-like cells, while the hydrogels from decellularized annulus fibrosus (AF) induce the formation of AF-like cells [28]. Similarly, ECM hydrogels from the peripheral nerve matrix are more effective in supporting myelination, whereas hydrogels from the spinal cord promote synapse formation [31]. As a connective tissue membrane covering the outer surface of bone, periosteum is essential to regulate bone development and regeneration [32]. Periosteum contains cells related to bone formation (e.g., osteoprogenitor cells and osteoblasts), growth factors (e.g., BMPs and VEGF), and a specific 3D ECM microenvironment [33]. It can facilitate bone regeneration in acute bone fractures and critical-sized bone defects [34, 35]. ECM from decellularized periosteum preserves the functional components (e.g., collagen and glycosaminoglycans (GAGs)) and has superior osteogenic activities both *in vitro* and *in vivo* [36]. Therefore, ECM hydrogels from decellularized periosteum resemble the functions of periosteum, which significantly promote osteogenic differentiation of mouse BMSCs compared with pure collagen hydrogels [30]. It remains unknown whether ECM hydrogels from periosteum can serve as pro-osteogenic carriers for hUCMSCs.

We hypothesized that the decellularized periosteum-derived hydrogel (dPH) could be used as a favorable carrier of hUCMSCs and provide a periosteum-specific pro-osteogenic microenvironment to promote their osteogenic differentiation. In this study, dPH was made from decellularized periosteum (DP). The physicochemical properties of dPH, such as microstructure, gelation kinetics, rheological property and hydrophilicity were evaluated. Furthermore, hUCMSCs were seeded onto dPH and Matrigel-coated coverslips to assess cellular activities and osteogenic differentiation. These studies would provide fundamental results for the application of dPH-carried hUCMSCs to promote the repair of bone defects.

## 2. MATERIALS AND METHODS

### 2.1 Fabrication of the decellularized periosteum-derived hydrogel

Periosteum were harvested from fresh porcine femoral bones in a slaughterhouse.



Under sterilized conditions, the periosteal tissues were washed with deionized water and subjected to freeze-thaw cycles (-80 °C–37 °C) for three times. Thereafter, the periosteal tissues were decellularized by 1% Triton X-100, 1% sodium dodecyl sulfate (Sigma-Aldrich, USA), and 50 U/mL DNase (Sigma-Aldrich, USA) successively. The resultant tissues were washed thoroughly and sterilized in 75% medical-grade ethanol before being lyophilized. The lyophilized decellularized tissues were milled into powder and digested in 1 mg/mL pepsin solution (dissolved in 0.01 M HCl, Sigma-Aldrich, USA) for 7 h under constant stirring. The pre-gel solution was centrifuged (3000 rpm, 4 °C for 10 min) to precipitate and remove the undigested particulate residues. To construct dPH, the fresh pre-gel solution was neutralized using pre-cooled 1M NaOH and HCl solutions to a pH of 7.4. Subsequently, 10× phosphate buffer saline (PBS, 1/9 of the final volume) was used to equilibrate its salinity. The neutralized dPH solution was incubated at 37 °C for 15–30 min to induce gelation. Commercially available growth factor reduced Matrigel® basement membrane matrix (7.6 mg/mL in protein concentration; 356231, Corning) was used as the control group to evaluate cellular responses.

## 2.2 Characterization of DP

ECM structure of DP and the presence of nuclei were assessed by hematoxylin and eosin (H&E) staining, picosirius red staining, and DNA content quantification. As to H&E staining and picosirius red staining, native periosteum and DP were fixed in 10% neutral buffered formalin solution, dehydrated, embedded in paraffin, and sectioned into 5-µm slices. The slices were stained with the H&E solution and picosirius red.

The DNA concentration was examined using the Quant-iT™ PicoGreen™ dsDNA Reagent (Invitrogen, USA). In brief, the lyophilized DP and native periosteum were digested with Proteinase K, purified with the TIANamp Genomic DNA kit (Tiangen, China), and then incubated with Picogreen according to the manufacturer's instructions. Total DNA content was tested by a microplate reader (Synergy™ HTX, Biotek, USA) (excitation wavelength: 485 nm; emission wavelength: 528 nm).

## 2.3 Turbidimetric gelation kinetics

The turbidimetric gelation kinetics were determined spectrophotometrically as

previously described [37, 38]. Pre-gel dPH solutions with concentrations of 1% and 0.5% were transferred to a pre-cooled 96-well plate at 100 µL per well in triplicates. The plates were placed in an incubator with a constant temperature of 37 °C. The turbidity value of each well was measured at 405 nm every 5 min for 1 h using the microplate reader. The absorbance values were recorded and normalized according to the following equation: normalized absorbance =  $(A - A_0)/(A_{max} - A_0)$ , where A is the absorbance at a pre-determined time,  $A_0$  is the initial absorbance, and  $A_{max}$  is the maximum absorbance. The lag phase was calculated as the intercept of the linear portion of the curve with an absorbance of 0.  $T_{1/2}$  referred to the time needed to reach 50% of the maximum absorbance value. The gelation speed represented the slope of the linear portion of the gelation curve.

## 2.4 Rheological properties of dPH

The rheological properties of dPH at different concentrations (1% and 0.5%) were assessed with a strain-controlled rheometer (HAAKE MARS III, Thermo Scientific, Germany) using an oscillatory time sweep. Briefly, pre-cooled pH- and ion-balanced dPH solution (350 µL) was transferred to the plate of the rheometer with a homogeneous distribution. The gap distance was 0.9 mm. The frequency was set to 1 Hz with a strain of 1%. The temperature increased from 20 °C to 40 °C at 210 °C/min. The storage modulus ( $G'$ ) and loss modulus ( $G''$ ) were recorded.

## 2.5 Morphologies of dPH and Matrigel

The microstructures of dPH and Matrigel were observed using scanning electron microscopy (SEM, S3400N, Hitachi, Japan). Before the test, the two hydrogels were fixed in 2.5% glutaraldehyde for 1 h and subjected to thorough washing in deionized water. The samples were dehydrated in gradient concentrations of ethanol (30%, 50%, 80%, and 100% for 15 min each). After that, the samples were immersed in deionized water and freeze-dried. The lyophilized samples were torn to generate a fracture surface, sputter-coated with Au–Pd, and observed using SEM.

## 2.6 Hydrophilic properties

A water contact angle (WCA) test was used to measure the hydrophilicity of dPH and Matrigel with a precise goniometer (DSA 100, KRÜSS GmbH Co., Germany). A 3.5 µL drop of water was added on dPH or Matrigel pre-coated

coverslips ( $\phi = 14$  mm). All the tests were repeated six times.

## 2.7 Evaluations of cellular activities

### 2.7.1 Cell culture

Commercially available hUCMSCs (OriCell®, Cyagen, China) were used to evaluate the cellular activities on the hydrogels. HUCMSCs were cultured in a specialized hMSC medium (P4–P6, Nuwacell Ltd., China) and incubated in a humidified atmosphere with 5% CO<sub>2</sub> at 37 °C. The medium was changed every 3–4 days. When the cells reached 70–80% confluence, the hUCMSCs were detached, counted, and used for subsequent tests.

### 2.7.2 Cellular morphologies on the hydrogels

Before seeding the cells, dPH (7.6 mg/mL) and Matrigel were coated onto coverslips ( $\phi = 14$  mm; 150  $\mu$ L) and incubated at 37 °C for 30 min to allow thorough gelation. HUCMSCs ( $2 \times 10^4$ /mL) were seeded onto the coated coverslips and cultured in the hMSC medium. The cellular morphologies were recorded 24 h later using phase-contrast microscopy (PCM, Leica, Germany) with three different regions of interest. The cell spreading surface area and cell length were measured using ImageJ 1.46r software (National Institute of Health, USA). The cells were fixed in 4% paraformaldehyde solution 48 h later and observed using SEM and confocal laser scanning microscopy (CLSM, Leica, Germany). Before being observed under SEM, the cells were dehydrated in gradient concentrations of ethanol and sputter-coated with Au–Pd. As to immunofluorescent staining of the cytoskeleton, the cells were permeabilized with 0.1% Triton X-100 solution for 5 min. After thorough washing, rhodamine phalloidin-labeled FITC solution (Cytoskeleton, USA) was added and incubated for 30 min to visualize F-actin in the cells (30 min), and DAPI solution was applied to stain the nuclei (5 min).

### 2.7.3 Cell proliferation

For the cell proliferation analysis, 100  $\mu$ L of hUCMSCs ( $5 \times 10^4$ /mL) were seeded onto dPH and Matrigel-coated 96-well plate (15  $\mu$ L/well). They were cultured in hMSC medium continuously for 5 days. The Alamarblue assay was used to assess metabolic activity. Each day before the assay, 100  $\mu$ L of new culture medium with 10  $\mu$ L Alamarblue reagent (Invitrogen™, USA) was added to each well. After the samples had been incubated at 37 °C for 3 h, the optical density (OD)

values were recorded at 570 nm and 600 nm using a microplate reader. The rate of cell proliferation was calculated according to the manufacturer's protocol.

### 2.7.4 Transwell chemotaxis assay

To assess the migration of hUCMSCs to dPH and Matrigel, a Transwell-24 plate with a pore size of 8  $\mu$ m (Costar, Corning) was used. DPH and Matrigel (80  $\mu$ L/well) were pre-coated in the lower chambers. Thereafter, 100  $\mu$ L of  $2 \times 10^5$ /mL hUCMSCs was seeded into the upper chambers and cultured in high glucose Dulbecco's modified Eagle's medium (DMEM) containing 1% fetal bovine serum (FBS) and 1% penicillin-streptomycin (PS). 600  $\mu$ L of standard DMEM solution was added to the lower chamber. After incubation for 12 h, the non-migrating cells in the upper chamber were scraped away. The migrated cells at the bottom of the upper chamber membrane were then fixed in 4% paraformaldehyde solution. 0.1% crystal violet (Beyotime Biotechnology, China) was applied to stain the cells for 20 min. The migrated cells were captured and counted.

### 2.7.5 Osteogenic activity

To evaluate the osteogenic responses of hUCMSCs on dPH (7.6 mg/mL) and Matrigel, hUCMSCs ( $2 \times 10^5$ /well) were seeded onto dPH and Matrigel-coated 6-well plates. They were cultured in the osteogenic medium, which contained DMEM, 10% FBS, 1% PS, 100 nmol/L dexamethasone, 10 mmol/L  $\beta$ -glycerophosphate, and 50  $\mu$ g/mL L-ascorbic acid. The medium was changed every 3 days.

After being cultured in the osteogenic medium for 14 days, hUCMSCs were harvested to test the genes expression profiles by quantitative reverse transcription-polymerase chain reaction (qRT-PCR) assay. Briefly, TRIzol® (Invitrogen, USA) was used to extract total RNA. The quality and concentration of isolated RNA were evaluated using NanoDrop 2000 spectrophotometer (Thermo Fisher Scientific, USA) at 260/280 nm. Subsequently, RNA was reverse-transcribed into cDNA via PrimeScript™ RT Master Mix (TaKaRa, China). QPCR analysis was conducted using TB Green™ Premix Ex Taq™ II (TaKaRa, China) and synthesized primers (Generay, China) in a Real-Time fluorescent qPCR system (Bio-Rad, USA). The expression levels of runt-related transcription factor 2 (RUNX2), alkaline phosphatase (ALP), osteopontin (OPN), and osteocalcin (OCN) were normalized to housekeeping gene glyceraldehyde 3-phosphate dehydrogenase (GAPDH). The

primer sequences were listed in table 1.

**Table 1.** The sequences of primers used for qRT-PCR analysis.

No.	Primer name	Sequences
1	RUNX2	sense: TACTATGGCACTTCGTCAGGA antisense: GATTCATCCATTCTGCCACTA
2	ALP	sense: GGCTGTAAGGACATCGCCTA antisense: GGGTCAAGGGTCAGGAGTTC
3	OPN	sense: GCTAAACCCTGACCCATC antisense: CTTTCGTTGGACTTACTTGG
4	OCN	sense: AGGGCAGCGAGGTAGTGAAG antisense: CTCCTGAAAGCCGATGTGGT
5	GAPDH	sense: GCACCGTCAAGGCTGAGAAC antisense: TGGTGAAGACGCCAGTGGA

Alizarin red S staining (ARS) was used to evaluate osteogenic mineralization. After thorough washing, hUCMSCs were fixed in 4% paraformaldehyde solution for 30 min. ARS reagent (0.2%, pH 8.3) was added and co-cultured for 10 min. Non-specific staining was removed by repeated washing. The mineralization nodules were recorded using phase-contrast microscopy. For the quantitative evaluation, 10% hexadecyl pyridinium chloride monohydrate (CPC) was added to dissolve the mineralized nodules. The colorimetric absorbance was measured at 562 nm using the microplate reader.

### 2.8 Statistical analysis

The data were expressed as the mean  $\pm$  standard deviation (SD). Statistical analyses were performed using SPSS 20.0 software (SPSS, Chicago, IL, USA). The differences between the two studied groups were assessed by the Student's *t*-test.  $P < 0.05$  was considered to be statistically significant.

## 3. RESULTS

### 3.1 Characterization of DP

H&E staining showed that native periosteum had a bilayer ECM structure with dark-blue stained nuclei. In contrast, the ECM structure of DP was loosely disposed and

no dark-blue stained nuclei were detected (Figure 1A), suggesting an efficient removal of cellular components. Besides, DNA quantitative analysis showed that DP had a significantly lower DNA content ( $10.75 \pm 1.4$  ng/mg) than the native periosteum ( $749.67 \pm 32.50$  ng/mg) ( $p < 0.001$ ). The DNA content in the DP was lower than the internationally required criterion of 50 ng/mg (Figure 1B) [39]. Under a polarized microscope, the picosirius red-stained native periosteum displayed closely-packed, red-stained collagen type I and green-stained collagen type III fibers [40]. A similar phenomenon was observed in the DP although its fibrous layer was not intensely stained with red dye.

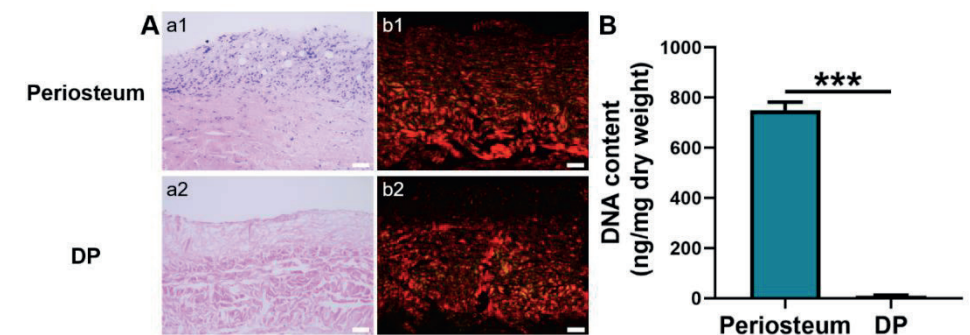


**Figure 1.** Characterization of periosteum and DP. A: Histological analysis. a1–a2: H&E staining. b1–b2: Picosirius red staining. B: DNA content quantification. Scale bar = 50  $\mu$ m. \*\*\*  $p < 0.001$ .

### 3.2 Turbidimetric gelation kinetics

As illustrated in Figure 2A, the DP was milled into powder and underwent the digestion process. After gelation, dPH was semi-transparent and self-supportive (inset image) (Figure 2A). The turbidimetric gelation kinetics of 1% dPH was a sigmoidal shape whereas the curve of 0.5% dPH was an exponential shape (Figure 2B). 1% dPH had an average lag phase of  $18.32 \pm 0.40$  min.  $T_{1/2}$  of 0.5% dPH and 1% dPH were  $6.35 \pm 0.70$  min and  $24.66 \pm 0.99$  min, respectively ( $p < 0.001$ ) (Figure 2C). Additionally, 0.5% dPH shared a similar gelation speed with 1% dPH ( $0.044 \pm 0.007$ /min and  $0.056 \pm 0.01$ /min, respectively) (Figure 2D). The maximum turbidity value of 1% dPH was higher than that of 0.5% dPH.



### 3.3 Rheological properties of dPH

Different rheological properties of 1% and 0.5% dPH could be observed in Figure 2E–G.  $G'$  and  $G''$  of both 1% and 0.5% dPH increased as the temperature rose to 40 °C. Furthermore, 1% dPH had a longer lag period than did 0.5% dPH. The sol-gel transition period of 1% dPH lasted  $7.55 \pm 0.40$  min, and the  $G'$  was  $855.20 \pm 20.67$  Pa. In comparison, the sol-gel transition time of 0.5% dPH was  $6.26 \pm 0.60$  min ( $p < 0.05$ ) (Figure 2F & G) and the  $G'$  was  $164.49 \pm 29.92$  Pa ( $p < 0.001$ ). In each concentration of dPH,  $G'$  was higher than  $G''$ .

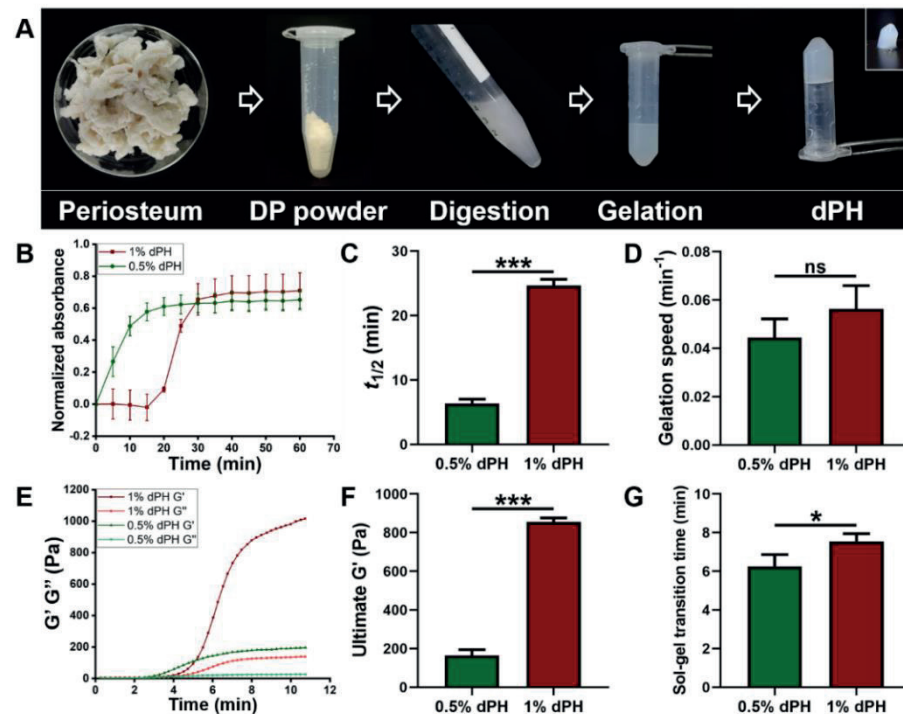


**Figure 2.** The fabrication process of dPH, its turbidimetric gelation kinetics, and rheological properties. A: Fabrication process of dPH. B: Representative normalized absorbance curve of 0.5% and 1% dPH. C: Time to reach 50% complete gelation of 0.5% and 1% dPH. D: Gelation speed of 0.5% and 1% dPH. E: Representative rheological property curve of dPH.  $G'$  represents the storage modulus, and  $G''$  represents the loss modulus. F: Ultimate storage modulus of 0.5% and 1% dPH. G: Sol-gel transition time of 0.5% and 1% dPH. ns, no significant difference, \*  $p < 0.05$ , \*\*\*  $p < 0.001$ .

### 3.4 Characterization of dPH and Matrigel

SEM revealed that Matrigel had a dense microstructure while dPH was porous with an interwoven network. Furthermore, dPH had an average pore size of  $2.07 \pm 0.63 \mu\text{m}$  (Figure 3A). In the hydrophilic study, Matrigel had a hydrophobic surface with a WCA of  $130.45 \pm 7.17^\circ$ . In contrast, dPH was hydrophilic with a WCA of  $48.63 \pm 4.26^\circ$ , which was significantly lower than that of Matrigel ( $p < 0.001$ ) (Figure 3B & C).

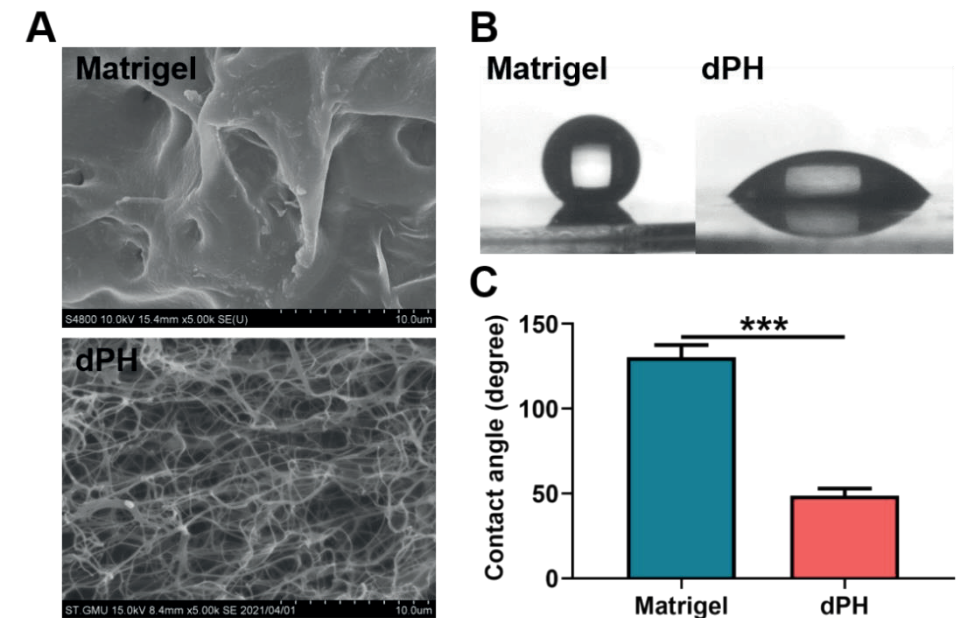


**Figure 3.** Morphological observations and hydrophilic study of Matrigel and dPH. A: Representative images of Matrigel and dPH observed using SEM. B: Representative optical images of the hydrophilic study. C: Quantitative analysis of WCA. \*\*\*  $p < 0.001$ .

### 3.5 Cellular activities

The initial cellular activities were recorded by observing the morphologies of hUCMSCs on the two hydrogels. After seeding the cells for 24 h, most of the hUCMSCs on Matrigel had not spread and displayed a round appearance (Figure 4A). In contrast, most of the hUCMSCs on dPH had pseudopodia and interacted with the surrounding dPH fibers. hUCMSCs on dPH possessed a significantly

higher cell spreading surface area and cell length than those on Matrigel ( $p < 0.05$ ) (Figure 4B & C). The morphologies of hUCMSCs were observed 48 h later using CLSM and SEM. Immunofluorescent staining showed that the cells on dPH stretched to form a spindle-shaped structure. SEM displayed that the hUCMSCs surrounded by dPH fibers elongated and became slender. In contrast, the cells on Matrigel began to spread into a polygonal shape. Some of the cells had pseudopodia and attached to the surrounding Matrigel (Figure 4A). In the cell proliferation test, the hUCMSCs grew more rapidly on dPH than those on Matrigel at all observed time points ( $p < 0.05$ ) (Figure 4D).

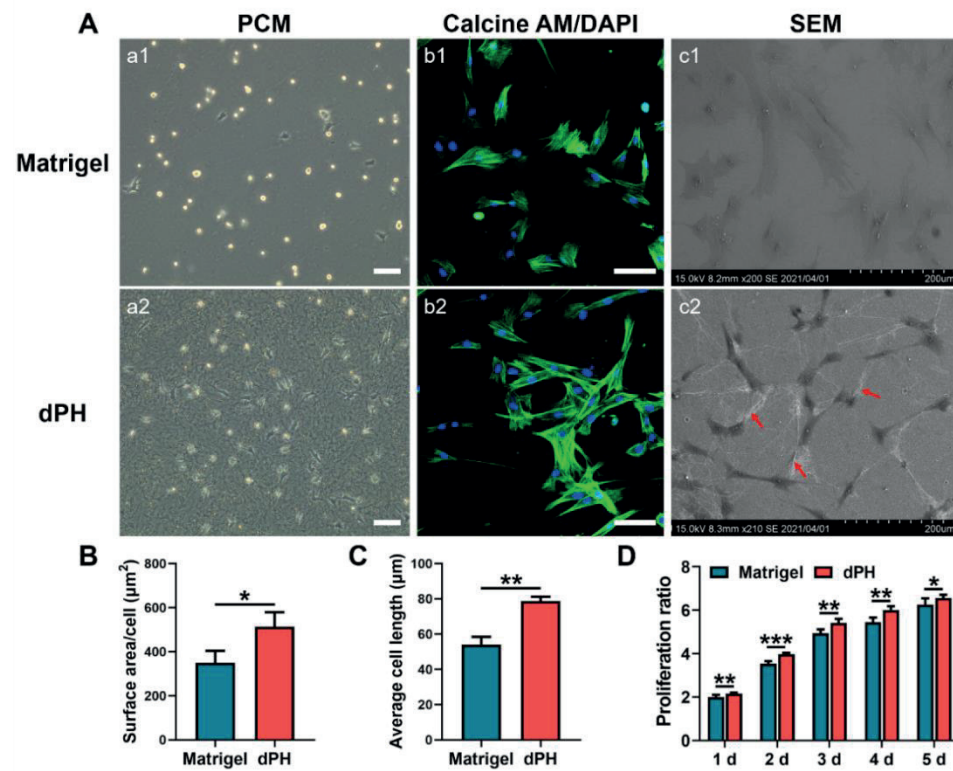


**Figure 4.** Morphological analysis and proliferation rate of hUCMSCs cultured on Matrigel and dPH. A: Representative images of hUCMSCs cultured on Matrigel and dPH. a1–a2: Phase-contrast micrographs of hUCMSCs cultured on Matrigel and dPH for 24 h. b1–b2: Cytoskeletal staining of hUCMSCs cultured on Matrigel and dPH for 48 h. c1–c2: SEM images of hUCMSCs cultured on Matrigel and dPH for 48 h. The red arrows indicate the nanofibers of dPH. B & C: Cell surface area and length of hUCMSCs when being cultured

on Matrigel and dPH for 24 h. D: The proliferation rate of hUCMSCs when being cultured on Matrigel and dPH. Scale bar = 100  $\mu\text{m}$ . \*  $p < 0.05$ , \*\*  $p < 0.01$ , \*\*\*  $p < 0.001$ .

### 3.6 Transwell chemotaxis assay

The chemotaxis of the hUCMSCs was evaluated, which were not in direct contact with dPH or Matrigel (Figure 5). In the Matrigel-coated wells, no hUCMSCs migrated to the lower chamber. In contrast, a significantly higher number of migrated cells were observed in the dPH group ( $p < 0.01$ ), indicating that dPH exhibited a strong chemotactic effect.

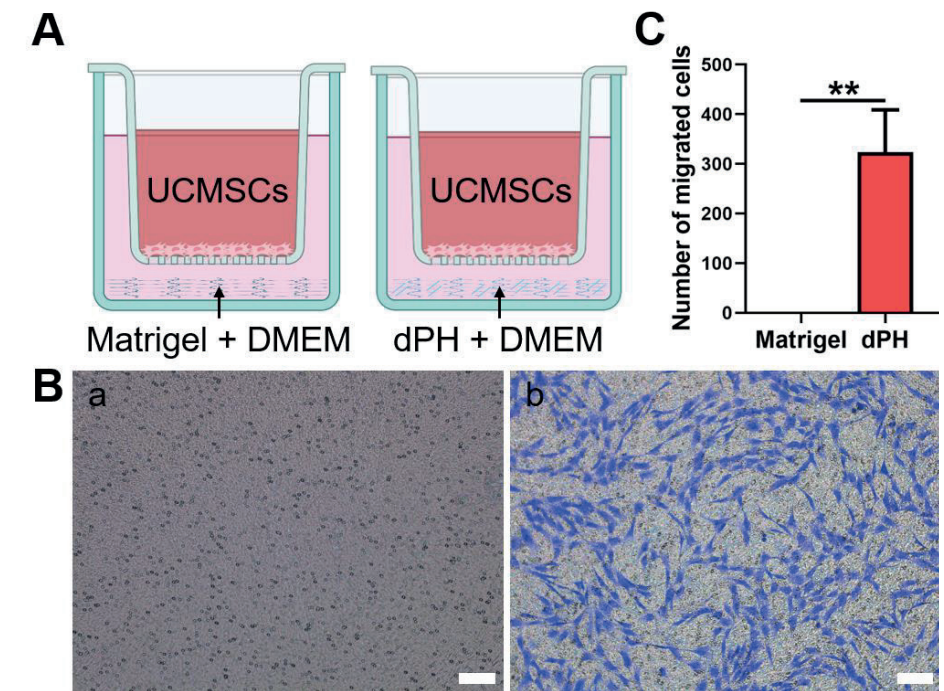


**Figure 5.** The chemotactic assay of Matrigel and dPH. A: Schematic illustration of the assay. B: HUCMSCs migrated through the upper chamber membranes of Transwell to Matrigel (A) and dPH (B) after 12 h. C: Number of migrated cells in dPH and Matrigel. Scale bar = 100  $\mu\text{m}$ . \*\*  $p < 0.01$ .

### 3.7 Osteogenic activities

On day 14, qPCR results showed that the hUCMSCs cultured on dPH had



significantly higher expression levels of RUNX2, ALP, OPN, and OCN than those on Matrigel (Figure 6A). As to matrix mineralization assay, a consistently higher mineralized matrix was observed in the dPH group than that in the Matrigel group, which was also confirmed by the quantitative analysis (Figure 6B & C). The aforementioned results indicated that the hUCMSCs cultured on dPH were more inclined towards osteogenic differentiation.

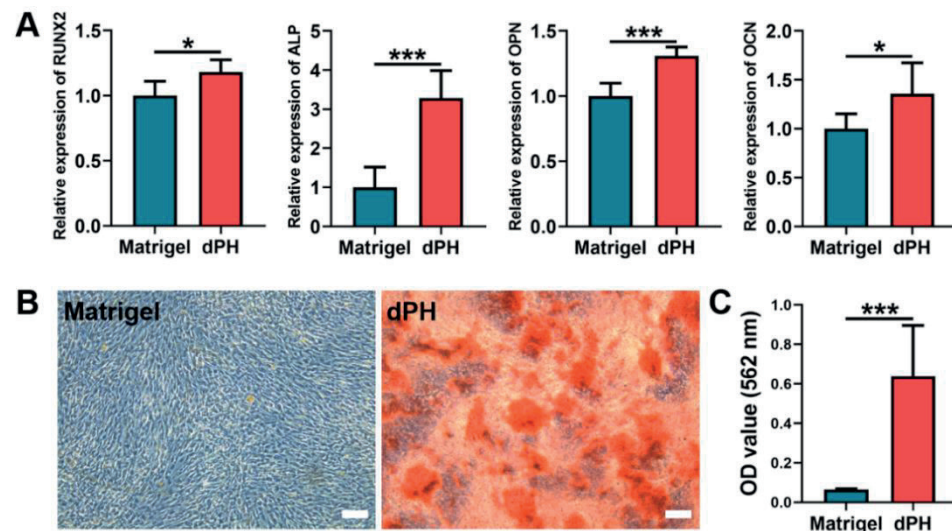


**Figure 6.** *In vitro* osteogenic differentiation of hUCMSCs after being cultured on Matrigel and dPH for 14 days. A: Expression levels of osteogenesis-related genes (RUNX2, ALP, OPN, and OCN). B: ARS staining of the mineralized matrix formation of hUCMSCs cultured on Matrigel and dPH. C: Quantitative analysis of ARS. Scale bar = 100  $\mu$ m. \*  $p < 0.05$ , \*\*\*  $p < 0.001$ .

#### 4. DISCUSSION

The major concern of MSC-based therapy in BTE is the survival and bioactivity of seed cells. A tissue-specific ECM microenvironment is of paramount importance for regulating cellular activities. We fabricated a novel decellularized periosteum-derived hydrogel (dPH), aiming to provide a pro-osteogenic microenvironment for hUCMSCs to improve the osteogenic efficacy. DPH had a fibrous microstructure with a significantly higher hydrophilic surface than that of the basement membrane-derived Matrigel. Furthermore, dPH exhibited a prominent effect on cellular spreading, migration, and proliferation. Moreover, enhanced osteogenesis-related genes expression levels and mineralized matrix formation were observed in hUCMSCs when being cultured on dPH. These results showed that dPH could provide a favorable osteogenic microenvironment for hUCMSCs, indicating a promising application potential for the repair of bone defects.

The microenvironment surrounding cells provides both biophysical and biochemical signals which affect cellular bioactivities. Viscoelastic properties (e.g., gelation kinetics and gel stiffness) are crucial to the application of ECM hydrogels [23]. Turbidimetric gelation kinetics indicate the process of hydrogel formation: collagen monomeric components self-assemble into fibrils and then into collagen fibers, which can further interweave with themselves and other ECM molecules, thus forming a fibrous network [41]. This self-assembly process of collagen type I can be altered by collagen type V, GAGs, and proteoglycans (PGs) [42, 43]. Decellularized brain-derived ECM hydrogels have an exponential curve shape of gelation kinetics with an approximate 3-min lag in fibrillogenesis [41]. This gelation kinetics curve is consistent with that of the 0.5% dPH. However, no lag phase was observed in the 0.5% dPH, which might be attributed to a longer time interval between tests. The gelation kinetics curves of most other ECM-derived hydrogels present a sigmoid shape. In these hydrogels, decellularized cartilage-derived ECM hydrogels have a short lag phase of 8 min, while the lag phases of hydrogels from the dermis and urinary bladder range from 15 to 25 min, which is consistent with that of 1% dPH [37, 44, 45]. Rheology is extensively used to determine the stiffness and gelation time of hydrogels [23].  $G'$  represents the stiffness, and  $G''$  refers to the viscosity of a specific hydrogel [46]. After complete gelation,  $G'$  was higher than  $G''$ ,

indicating that dPH formed a solid structure. The stiffness increased from  $164.49 \pm 29.92$  Pa to  $855.20 \pm 20.67$  Pa following a rising concentration in dPH. The value of this mechanical property was lower than that of the range in which osteogenesis usually occurs ( $G'$  of 3.7–10.7 kPa) [47]. However, gelatin-based hydrogels with a lower stiffness ( $G'$  of  $538 \pm 91$  Pa) support better osteogenesis with a more intense mineralized matrix formation than stiff hydrogels ( $G'$  of  $7263 \pm 287$  Pa) [47]. The gelation kinetics and  $G'$  of dPH could be adjusted by its concentration, which indicated that the lag time and mechanical stiffness of dPH might be tailored for specific applications in repairing bone defects.

Apart from the mechanical properties, the biochemical characteristics also support the bioactivities of dPH. Picosirius red staining qualitatively showed that collagen was well preserved in the DP. The effective preservation of fibronectin and GAGs in the DP was observed in our previous study [48]. Preserved collagen and fibronectin can provide binding sites to facilitate cell adhesion, spreading, migration, and proliferation [49, 50]. When dPH and Matrigel were co-cultured with hUCMSCs, a significantly higher initial cell spreading surface area (1.47-fold), cell spreading length (1.45-fold), and growth (1.05–1.13-fold) were observed in dPH than in Matrigel. This may be attributed to the following mechanisms: first, we showed that dPH was more hydrophilic than Matrigel, which might have exerted a positive effect on initial cell spreading on dPH; second, periosteal ECM hydrogels contain various cell adhesion-related proteins, such as fibronectin, fibrillin-1, vitronectin, and thrombospondin 4 [30], while Matrigel lacks these proteins [25, 51]. Some other studies have also reported a higher cell proliferation in ECM hydrogels than in Matrigel. For example, Miao et al. show that the proliferation of chondrocytes is significantly higher in collagen than in Matrigel [52]. Similarly, a decellularized brain matrix markedly supports and promotes dendritic formation of neurons as opposed to Matrigel [53].

As a promising alternative cell source to BMSCs in BTE, hUCMSCs have been studied in different scenarios with conflicting osteogenic outcomes. Chen et al. find that hUCMSC-based macro-porous calcium phosphate cement (CPC) constructs have similar bone regeneration properties to those of hBMSC-based CPC constructs *in vivo* [54]. Kouroupis et al. directly compare the osteogenic

properties of hBMSCs and hUCMSCs and find that the mineralized matrix formation is significantly lower in hUCMSCs than that in hBMSCs [13], indicating a relatively lower osteogenic ability of hUCMSCs. hUCMSCs tend to express more angiogenesis- and growth-related genes, while hBMSCs express more osteogenic genes. Furthermore, hUCMSCs are more primitive than BMSCs and are not so sensitive to environmental stimulations [55]. Therefore, when hUCMSCs were cultured on Matrigel in OM, no mineralized nodules formed after 14 days. On the contrary, distinctly elevated mineralized matrix formation (9.74-fold) and genes expression levels were found when hUCMSCs were cultured with dPH, which might be due to the soluble bioactive agents in dPH. For example, periostin can significantly promote the migration and mineralized matrix formation of MSCs [56]. ECM hydrogels also serve as pools of various growth factors, such as VEGF and TGF- $\beta$  [57, 58]. Whether dPH contains all of these bioactive factors will be analyzed in our future study.

Recruiting cells from local sites is one of the main methods to gather sufficient cells to promote tissue repair. Fibronectin, vitronectin, and collagen type I can induce the dose-dependent chemotaxis of hMSCs, and fibronectin has the strongest chemotactic response [59]. ECM scaffolds derived from small intestinal submucosa are able to recruit cells to defect sites [60]. The degradation products of ECM can also regulate the migration of progenitor cells [61]. Compared with Matrigel, dPH induced a markedly migration of hUCMSCs in the Transwell model. This indicated that there were soluble ECM proteins in dPH that might guide cells towards defects when being implanted *in vivo*. The secreted protein acidic and rich in cysteine (SPARC) and insulin-like growth factor-binding 5 in periosteal ECM hydrogels have shown positive effects on cell migration [30]. To date, it remains unclear how the ECM regulates cellular activities. Our future studies will therefore focus on the extraction of dPH proteins and the characterization of their functions and related mechanisms.

## 5. CONCLUSION

The decellularized periosteum-derived hydrogel had a fibrous morphology and hydrophilic surface. It provided both unique biophysical and biochemical signals to

regulate the bioactivities of hUCMSCs. Furthermore, dPH exhibited a prominent effect on promoting the initial cellular spreading, migration, and proliferation of hUCMSCs. With an improved simulation of the periosteal microenvironment, dPH was associated with enhanced osteogenesis-related genes expression and mineralized matrix formation of hUCMSCs than those of Matrigel. These results suggested that dPH might potentially be used as a favorable carrier for hUCMSCs to promote bone regeneration.

## REFERENCES

- [1] P. Rosset, et al., Cell Therapy for Bone Repair, *Orthop Traumatol Surg Res* 100(1 Suppl) (2014) S107-112.
- [2] Y. Zhuang, et al., A Novel Cytotherapy Device for Rapid Screening, Enriching and Combining Mesenchymal Stem Cells into a Biomaterial for Promoting Bone Regeneration, *Sci Rep* 7(1) (2017) 15463.
- [3] A. Najji, et al., Biological Functions of Mesenchymal Stem Cells and Clinical Implications, *Cell Mol Life Sci* 76(17) (2019) 3323-3348.
- [4] M. Travnickova, L. Bacakova, Application of Adult Mesenchymal Stem Cells in Bone and Vascular Tissue Engineering, *Physiol Res* 67(6) (2018) 831-850.
- [5] X. Fu, et al., Mesenchymal Stem Cell Migration and Tissue Repair, *Cells* 8(8) (2019) 784.
- [6] M.E. Klontzas, et al., Bone and Cartilage Regeneration with the Use of Umbilical Cord Mesenchymal Stem Cells, *Expert Opin Biol Ther* 15(11) (2015) 1541-1552.
- [7] A. Oryan, et al., Role of Mesenchymal Stem Cells in Bone Regenerative Medicine: What Is the Evidence?, *Cells Tissues Organs* 204(2) (2017) 59-83.
- [8] H. Zhang, et al., Isolation and Characterization of Mesenchymal Stem Cells from Whole Human Umbilical Cord Applying a Single Enzyme Approach, *Cell Biochem Funct* 30(8) (2012) 643-649.
- [9] G. La Rocca, et al., Isolation and Characterization of Oct-4+/HLA-G+ Mesenchymal Stem Cells from Human Umbilical Cord Matrix: Differentiation Potential and Detection of New Markers, *Histochem Cell Biol* 131(2) (2009) 267-282.
- [10] C. Capelli, et al., Minimally Manipulated Whole Human Umbilical Cord Is a Rich Source of Clinical-Grade Human Mesenchymal Stromal Cells Expanded in Human Platelet Lysate, *Cytotherapy* 13(7) (2011) 786-801.
- [11] T. Deuse, et al., Immunogenicity and Immunomodulatory Properties of Umbilical Cord Lining Mesenchymal Stem Cells, *Cell Transplant* 20(5) (2011) 655-667.
- [12] M.L. Weiss, et al. Immune Properties of Human Umbilical Cord Wharton's Jelly-Derived Cells, *Stem Cells*, 26(11) (2008) 2865-2874.
- [13] D. Kouroupis, et al., Assessment of Umbilical Cord Tissue as a Source of Mesenchymal Stem Cell/Endothelial Cell Mixtures for Bone Regeneration, *Regen Med* 8(5) (2013) 569-581.
- [14] C. Mennan, et al., Isolation and Characterisation of Mesenchymal Stem Cells from Different Regions of the Human Umbilical Cord, *Biomed Res Int* 2013 (2013) 916136.
- [15] K. Sudo, et al., Mesenchymal Progenitors Able to Differentiate into Osteogenic, Chondrogenic, and/or Adipogenic Cells *in Vitro* Are Present in Most Primary Fibroblast-Like Cell Populations, *Stem Cells* 25(7) (2007) 1610-1617.
- [16] S. Ciavarella, et al., Umbilical Cord Mesenchymal Stem Cells: Role of Regulatory Genes in Their Differentiation to Osteoblasts, *Stem Cells Dev* 18(8) (2009) 1211-1220.
- [17] L. E, et al., Microenvironment Influences on Human Umbilical Cord Mesenchymal Stem Cell-Based Bone Regeneration, *Stem Cells Int* 2021 (2021)



4465022.

- [18] T. Hou, et al., Umbilical Cord Wharton's Jelly: A New Potential Cell Source of Mesenchymal Stromal Cells for Bone Tissue Engineering, *Tissue Eng Part A* 15(9) (2009) 2325-2334.
- [19] Q. Rong, et al., A Novel Method to Improve the Osteogenesis Capacity of hUCMSCs with Dual-Directional Pre-Induction under Screened Co-Culture Conditions, *Cell Prolif* 53(2) (2020) e12740.
- [20] C. Frantz, et al., The Extracellular Matrix at a Glance, *J Cell Sci* 123(24) (2010) 4195-4200.
- [21] B.S. Kim, et al., Decellularized Extracellular Matrix-Based Biinks for Engineering Tissue- and Organ-Specific Microenvironments, *Chem Rev* 120(19) (2020) 10608-10661.
- [22] Y.S. Kim, et al., Applications of Decellularized Extracellular Matrix in Bone and Cartilage Tissue Engineering, *Bioeng Transl Med* 4(1) (2019) 83-95.
- [23] L.T. Saldin, et al., Extracellular Matrix Hydrogels from Decellularized Tissues: Structure and Function, *Acta Biomater* 49 (2017) 1-15.
- [24] W. Zhang, et al., Research Progress in Decellularized Extracellular Matrix-Derived Hydrogels, *Regen Ther* 18 (2021) 88-96.
- [25] E.A. Aisenbrey, W.L. Murphy, Synthetic Alternatives to Matrigel, *Nat Rev Mater* 5(7) (2020) 539-551.
- [26] H.K. Kleinman, G.R. Martin, Matrigel: Basement Membrane Matrix with Biological Activity, *Semin Cancer Biol* 15(5) (2005) 378-386.
- [27] B.J. Kang, et al., Effect of Matrigel on the Osteogenic Potential of Canine Adipose Tissue-Derived Mesenchymal Stem Cells, *J Vet Med Sci* 74(7) (2012) 827-836.
- [28] Y. Peng, et al., Decellularized Disc Hydrogels for hBMSCs Tissue-Specific Differentiation and Tissue Regeneration, *Bioact Mater* 6(10) (2021) 3541-3556.
- [29] T. Lin, et al., Hydrogel Derived from Porcine Decellularized Nerve Tissue as a Promising Biomaterial for Repairing Peripheral Nerve Defects, *Acta Biomater* 73 (2018) 326-338.
- [30] P. Qiu, et al., Periosteal Matrix-Derived Hydrogel Promotes Bone Repair through an Early Immune Regulation Coupled with Enhanced Angio- and Osteogenesis, *Biomaterials* 227 (2020) 119552.
- [31] J.L. Zou, et al., Peripheral Nerve-Derived Matrix Hydrogel Promotes Remyelination and Inhibits Synapse Formation, *Adv Funct Mater* 28(13) (2018) 1705739.
- [32] Y. Lou, et al., Periosteal Tissue Engineering: Current Developments and Perspectives, *Adv Healthc Mater* 10(12) (2021) e2100215.
- [33] W. Zhang, et al., Periosteum and Development of the Tissue-Engineered Periosteum for Guided Bone Regeneration, *J Orthop Translat* 33 (2022) 41-54.
- [34] A. Ozaki, et al., Role of Fracture Hematoma and Periosteum During Fracture Healing in Rats: Interaction of Fracture Hematoma and the Periosteum in the Initial Step of the Healing Process, *J Orthop Sci* 5(1) (2000) 64-70.
- [35] M.L. Knothe Tate, et al., Surgical Membranes as Directional Delivery Devices to Generate Tissue: Testing in an Ovine Critical Sized Defect Model, *Plos One* 6(12)

(2011) e28702.

- [36] J. Zhang, et al., Preparation and Evaluation of Tibia- and Calvarium-Derived Decellularized Periosteum Scaffolds, *ACS Biomater Sci Eng* 3(12) (2017) 3503-3514.
- [37] D.O. Freytes, et al., Preparation and Rheological Characterization of a Gel Form of the Porcine Urinary Bladder Matrix, *Biomaterials* 29(11) (2008) 1630-1637.
- [38] M.J. Sawkins, et al., Hydrogels Derived from Demineralized and Decellularized Bone Extracellular Matrix, *Acta Biomater* 9(8) (2013) 7865-7873.
- [39] P.M. Crapo, et al., An Overview of Tissue and Whole Organ Decellularization Processes, *Biomaterials* 32(12) (2011) 3233-3243.
- [40] G.S. Montes, Structural Biology of the Fibres of the Collagenous and Elastic Systems, *Cell Biol Int* 20(1) (1996) 15-27.
- [41] C.J. Medberry, et al., Hydrogels Derived from Central Nervous System Extracellular Matrix, *Biomaterials* 34(4) (2013) 1033-1040.
- [42] A.O. Brightman, et al., Time-Lapse Confocal Reflection Microscopy of Collagen Fibrillogenesis and Extracellular Matrix Assembly *in Vitro*, *Biopolymers* 54(3) (2000) 222-234.
- [43] D.E. Birk, et al., Collagen Fibrillogenesis *in Vitro*: Interaction of Types I and V Collagen Regulates Fibril Diameter, *J Cell Sci* 95 ( Pt 4) (1990) 649-657.
- [44] D. Gong, et al., *Ex Vivo* and *in Vivo* Properties of an Injectable Hydrogel Derived from Acellular Ear Cartilage Extracellular Matrix, *Front Bioeng Biotechnol* 9 (2021) 740635.
- [45] M.T. Wolf, et al., A Hydrogel Derived from Decellularized Dermal Extracellular Matrix, *Biomaterials* 33(29) (2012) 7028-7038.
- [46] M. Yu, et al., Buckwheat Self-Assembling Peptide-Based Hydrogel: Preparation, Characteristics and Forming Mechanism, *Food Hydrocoll* (2021) 107378.
- [47] S. Zigon-Branc, et al., Impact of Hydrogel Stiffness on Differentiation of Human Adipose-Derived Stem Cell Microspheroids, *Tissue Eng Part A* 25(19-20) (2019) 1369-1380.
- [48] S. Li, et al., Development and Fabrication of Co-Axially Electrospun Biomimetic Periosteum with a Decellularized Periosteal ECM Shell/PCL Core Structure to Promote the Repair of Critical-Sized Bone Defects, *Composites Part B: Engineering* 234 (2022) 109620.
- [49] M. Zhang, et al., Influencing Factors and Strategies of Enhancing Nanoparticles into Tumors *in Vivo*, *Acta Pharm Sin B* 11(8) (2021) 2265-2285.
- [50] C. Somaiah, et al., Collagen Promotes Higher Adhesion, Survival and Proliferation of Mesenchymal Stem Cells, *Plos One* 10(12) (2015) e0145068.
- [51] T.L. Sellaro, et al., Maintenance of Human Hepatocyte Function *in Vitro* by Liver-Derived Extracellular Matrix Gels, *Tissue Eng Part A* 16(3) (2010) 1075-1082.
- [52] Z. Miao, et al., Collagen, Agarose, Alginate, and Matrigel Hydrogels as Cell Substrates for Culture of Chondrocytes *in Vitro*: A Comparative Study, *J Cell Biochem* 119(10) (2018) 7924-7933.
- [53] J.A. DeQuach, et al., Decellularized Porcine Brain Matrix for Cell Culture and Tissue Engineering Scaffolds, *Tissue Eng Part A* 17(21-22) (2011) 2583-2592.

- [54] W. Chen, et al., Umbilical Cord and Bone Marrow Mesenchymal Stem Cell Seeding on Macroporous Calcium Phosphate for Bone Regeneration in Rat Cranial Defects, *Biomaterials* 34(38) (2013) 9917-9925.
- [55] J.Y. Hsieh, et al., Functional Module Analysis Reveals Differential Osteogenic and Stemness Potentials in Human Mesenchymal Stem Cells from Bone Marrow and Wharton's Jelly of Umbilical Cord, *Stem Cells Dev* 19(12) (2010) 1895-1910.
- [56] Y. Tang, et al., Periostin Promotes Migration and Osteogenic Differentiation of Human Periodontal Ligament Mesenchymal Stem Cells Via the Jun Amino-Terminal Kinases (Jnk) Pathway under Inflammatory Conditions, *Cell Prolif* 50(6) (2017).
- [57] T. Davidov, et al., Extracellular Matrix Hydrogels Originated from Different Organs Mediate Tissue-Specific Properties and Function, *Int J Mol Sci* 22(21) (2021).
- [58] R. Liang, et al., Positive Effects of an Extracellular Matrix Hydrogel on Rat Anterior Cruciate Ligament Fibroblast Proliferation and Collagen mRNA Expression, *J Orthop Translat* 3(3) (2015) 114-122.
- [59] M.M. Thibault, et al., Fibronectin, Vitronectin, and Collagen I Induce Chemotaxis and Haptotaxis of Human and Rabbit Mesenchymal Stem Cells in a Standardized Transmembrane Assay, *Stem Cells Dev* 16(3) (2007) 489-502.
- [60] T. Zantop, et al., Extracellular Matrix Scaffolds Are Repopulated by Bone Marrow-Derived Cells in a Mouse Model of Achilles Tendon Reconstruction, *J Orthop Res* 24(6) (2006) 1299-1309.
- [61] V. Agrawal, et al., Recruitment of Progenitor Cells by an Extracellular Matrix Cryptic Peptide in a Mouse Model of Digit Amputation, *Tissue Eng Part A* 17(19-20) (2011) 2435-2443.

**CHAPTER 4**

Highly efficient biphasic calcium-phosphate coating procedure with  
an enhanced coating yield and protein incorporation rate

Ping Sun<sup>#</sup>, Shuyi Li<sup>#</sup>, Jianhua Niu, Min Yi, Weixing Xu, Liyong Wu,  
Gang Wu

*Materials express*, 2021, 11(8):1428-1437.

## ABSTRACT

A biomimetic biphasic calcium-phosphate (CaP)-coating is a promising surface modification for functionalizing various endosseous biomaterials. However, its biomedical application is limited by the low coating yield efficiency and protein-incorporation rate of the current coating procedure using 1× supersaturated CaP solution (SCPS). In this study, we developed a highly concentrated (4.5×) SCPS and compared the physicochemical properties of thereby-produced new coating with the one formed using 1× SCPS. Two milliliters of 4.5× SCPS formed a much thicker (110 μm) coating on a titanium disc (4 × 4 × 1 mm) than that (29 μm) of 1× SCPS. On X-ray diffraction analysis, the new coating formed in 4.5× SCPS had characteristic dicalcium-phosphate dehydrate and apatite peaks, in contrast to the apatite-only peak of the 1× SCPS-coating. Under acidic condition (pH 4.5), the 4.5× SCPS-coating released significantly less Ca<sup>2+</sup> than the 1× SCPS-coating. FITC-bovine serum albumin incorporation in the 4.5× SCPS-coating (81.20 ± 6.42%) was significantly higher than in the 1× SCPS-coating (21.86 ± 1.90%). Thus, this modified coating procedure holds promise for biomedical applications.

**Keywords:** Biomimetic; Calcium-phosphate; Surface modification; Supersaturated calcium-phosphate solution; Coating.

## 1. INTRODUCTION

Because of their bone-like composition, good biocompatibility, and capacity to regulate various osteogenic events, calcium-phosphate (CaP) coatings are among the most widely employed surface modifications for promoting osseointegration and osteoconductivity of endosseous implants and bone-defect-filling materials [1, 2]. Currently, there are two major methods for preparing CaP-based coatings: 1) physical deposition techniques and 2) wet-chemical techniques [3]. Physical deposition techniques consist of various thermal processes, such as vacuum plasma spraying [4] and suspension plasma spraying [5]. The major limitation of the physical deposition technique is that the unphysiological coating condition (> 1000 °C) makes it impossible to incorporate bioactive agents that can promote osteogenic activities [3]. Therefore, a recent trend in the field of biomaterial research involves the development of novel wet-chemical deposition techniques to prepare bioactive CaP coatings [6, 7].

The biomimetic coating procedure was first proposed in the 1990s [8, 9]. The biomimetic process enables the formation of a dense, uniform, and typically low-crystalline apatite [6] by immersing biomaterials in simulated body fluid (SBF) with ion concentrations, pH, and temperature approximating those of human blood plasma [10, 11]. Such physiological conditions enable the co-precipitation of a large variety of bioactive agents with biomimetic coatings and retain their bioactivities [3]. However, implementation of the original biomimetic coating procedure is limited by its time-consuming nature (typically 14 days) and the dependence on functional groups of biomaterials for nucleation [12, 13]. Taset et al. manage to accelerate the coating process significantly, to several hours, by increasing the SBF concentration 10 times (10× SBF) [14]. However, the intrinsic dependence of SBF on the functional groups of biomaterials remains unsolved.

In 2000, Prof. Dr. Klaas de Groot and his colleagues developed a biphasic biomimetic coating protocol: an amorphous CaP seeding layer is formed through incubation in a 5× SBF solution, and a subsequent CaP crystalline layer is formed through incubation in a supersaturated calcium-phosphate solution (SCPS) [15, 16]. This biphasic biomimetic method enables the formation of a crystalline CaP-coating within 3 days. Furthermore, this coating can be applied to various biomaterials with

diverse three-dimensional geometries, topographies, and surface chemistries, such as metallic (titanium alloy [17-21]), inorganic (TCP and Bio-Oss® [22, 23]), and polymeric (naturally derived collagen and synthetic poly(lactic-co-glycolic acid) [24, 25]) materials. The broad applicability of this biomimetic coating is largely attributed to the amorphous CaP seeding layer, which forms a mechanism of mechanical gompnosis rather than a chemical reaction with active chemical groups [24]. Furthermore, the amorphous CaP layer is indispensable for the growth of the subsequent crystalline CaP layer. The subsequent crystalline phase can be used to co-precipitate, incorporate, and slowly release various bioactive agents [26], particularly bone morphogenetic protein-2 (BMP2), an osteoinductive growth factor [17-25]. The coating-incorporated BMP2 shows significantly higher osteoinductive efficiency than the superficially adsorbed BMP2, which can be attributed to the slow delivery property of the coating [17, 23, 25]. However, due to the low ion concentration of SCPS, the coating efficiency and incorporation rate of expensive bioactive agents are relatively low (around 21%) [22], hindering its application in biomedical fields. Yu et al. attempt to improve the incorporation rate to 90% by adjusting the ratio of the substrate surface area to the modified SBF (mSBF) volume, applying only 1 mL mSBF [27]. However, they did not report the final coating thickness, and a certain coating thickness is necessary to restore a sufficient amount of bioactive agents and ensure an adequate length of time for drug delivery to support bone formation [19].

In this study, we modified the original 1× SCPS and developed a new SCPS containing 4.5 times concentrations of major ions ( $\text{Ca}^{2+}$  and  $\text{PO}_4^{3-}$ ) so as to decrease the solution volume per unit substrate surface area with a view to shortening the coating duration, increasing the coating yield efficiency, and enhancing the incorporation efficiency of bioactive agents. This new coating showed significantly higher coating yield efficiency and protein-incorporation rate, thus bearing a promising application potential in biomedical fields.

## 2. MATERIALS AND METHODS

### 2.1 Experimental design

We here developed a new 4.5× SCPS and assessed its volume-dependent

changes in coating thickness and morphology, as compared to 1× SCPS. We further monitored the time-dependent changes in the pH and calcium ion ( $\text{Ca}^{2+}$ ) concentration of SCPS during the coating procedure. Thereafter, we characterized the composition of the coating using energy dispersive X-ray spectroscopy (EDS), attenuated total reflection-Fourier transform infrared spectroscopy (ATR-FTIR), and X-ray diffraction (XRD). Fluorescein isothiocyanate-labeled bovine serum albumin (FITC-BSA) was used as a model protein to evaluate the incorporation rate.

### 2.2 BioCaP-coating procedure

The coatings were prepared according to a well-established biphasic biomimetic coating protocol [16, 19]. Briefly, titanium discs (4 mm in length and width, 1 mm in thickness) were first immersed into 5× SBF at 37 °C for 24 h, to prepare a very thin amorphous CaP (ACP) seeding layer. After drying, ACP-coated titanium discs were immersed into 1× SCPS at 37 °C or 4.5× SCPS at room temperature, with volumes of 0.1, 0.3, 1, 2, 4, and 6 mL per disc. The concentrations of the ions in 5× SBF, 1×, and 4.5× SCPS were listed in Table 1.

**Table 1.** Inorganic ions composition of 5× simulated body fluid (SBF), 1× supersaturated calcium-phosphate solution (SCPS), and 4.5× SCPS.

(mM)	$\text{Na}^+$	$\text{Ca}^{2+}$	$\text{Mg}^{2+}$	$\text{Cl}^-$	$\text{HPO}_4^{2-}$	$\text{HCO}_3^-$	pH	Temperature
5× SBF	715.0	12.5	7.5	724.0	5.0	21.0	6.0	37 °C
1× SCPS	140.0	4.0	/	184.0	2.0	/	7.4	37 °C
4.5× SCPS	630.0	18.0	/	828.0	9.0	/	6.2	Room temperature

### 2.3 Coating thickness

Titanium discs were embedded in methylmethacrylate (MMA). Two-hundred-micrometer-thick cross-sections were prepared perpendicular to the surface of the titanium discs from the embedded material. The sections were then affixed to Plexiglass holders and ground to a thickness of about 80 μm. The sections were stained with 0.1% basic fuchsin to visualize the coating layer. The cross-sections were then examined and photographed in color using a stereomicroscope (Stemi

SV6, Carl Zeiss, Jena, Germany) with a cold light source (KL 2500 LCD, Carl Zeiss). A point-counting method [28] was adopted to measure the surface area of the coating layer. The average thickness of the coating was calculated by dividing the surface area of the coating layer by the length of the coated titanium surface.

#### 2.4 Characterization of the BioCaP-coatings

The morphology of the BioCaP-coating was observed using field emission scanning electron microscopy (FESEM, Phillips/FEI XL-30). EDS analysis was also performed to reveal the relative densities of calcium and phosphorus on the coatings, from which the calcium-to-phosphorus ratios were calculated. In addition, the biomimetic coatings were further characterized using XRD (X'Pert PRO, PANalytical, Malvern, UK) for phase composition and ATR-FTIR for chemical groups. Briefly, XRD analysis was performed with a scanning range of 2.00–80.00°, a speed of 2°/min, and a scanning interval of 0.02°. ATR-FTIR was tested using FTIR (Avatar 360 Nicolet spectrometer, Thermo Fisher Scientific, Waltham, MA, USA) transmittance spectra from 4000 to 400 cm<sup>-1</sup> wavenumber.

#### 2.5 Ca<sup>2+</sup>-release profile from the coatings under different pH conditions

To detect Ca<sup>2+</sup>-release kinetics from the coatings, a coated titanium disc was immersed in 0.5 mL of the following buffers: 0.05 M Tris-HCl at pH 7.4 [24] or 0.1 M acetate buffer at pH 6.0 or 4.5 [29]. The test was performed at 37 °C on a shaker with a speed of 60 rpm. At predetermined time points of 4, 5, 9 h, 1, 2, 3, 5, 8, 11, 14, 17, 21, 27, and 35 days, the supernatants were harvested with the same volume of the new medium. Finally, after dilution of the samples in lanthanum reagent [0.5 wt% La(NO<sub>3</sub>)<sub>3</sub>·6H<sub>2</sub>O (Merck, Darmstadt, Germany)] in 0.05 M HCl, the Ca<sup>2+</sup> content in the solution was measured using atomic absorption spectroscopy (AAnalyst 100, PerkinElmer, Foster City, CA, USA) in triplicate, and the cumulative release profiles were analyzed.

#### 2.6 Rate of incorporation of a model protein — FITC-BSA

Using the volume-dependent coating thickness data, we found that 0.45 mL 4.5× SCPS produced a similar coating thickness (about 71 μm) as 6 mL of 1× SCPS on a single titanium disc (4 mm in length and width, 1 mm in thickness). To investigate the rate of incorporation of FITC-BSA with a similar coating thickness, we adopted this setting. FITC-BSA (5 μg/mL) was used as a model protein in this

study, as in a previous study [24]. After the coating procedure, the coating was dissolved in 0.5 mL 0.5 M EDTA (pH 8.0) and vortexed twice for 5 min to retrieve the incorporated FITC-BSA. The fluorescence density of the solution or its dilution was measured using a spectrophotometer (excitation wavelength: 485 nm; emission wavelength: 519 nm). The amount of FITC-BSA was estimated by creating a standard curve of FITC-BSA in 0.5 M EDTA. The incorporation rate was calculated by dividing the total incorporated FITC-BSA by the total FITC-BSA added to the SCPS. Five samples were used in each group.

#### 2.7 Statistical analysis

The quantitative data in Figure 1, 3, 4, 7, and 8 were derived from 3 independent experiments with quadruplicate samples and were presented as mean ± standard deviation (SD). Data pertaining to the changes in pH and Ca<sup>2+</sup> levels were compared using the one-way analysis of variance. *Post-hoc* comparisons were performed using Bonferroni corrections. Data pertaining to the total amount of released Ca<sup>2+</sup> in the same buffer, as well as the incorporation rate of FITC-BSA, were compared using an unpaired *t*-test. The level of significance was set at *P* < 0.05.

### 3. RESULTS AND DISCUSSION

#### 3.1 Development of highly concentrated (4.5×) SCPS for the crystalline CaP coating layer

In this study, we hypothesized that significantly enhanced concentrations of major ions such as Ca<sup>2+</sup> and PO<sub>4</sub><sup>3-</sup> would enhance the coating yield efficiency and lower down needed coating solution volume so as to enhance protein-incorporation rate. In our preliminary experiment, we first attempted to prepare 1×, 2×, 3×, 4×, and 5× SCPS by proportionally increasing the amount of chemicals and acids accordingly. We found that the pH values in SCPS had to be lowered with the increase in the concentration of SCPS to maintain a stable saturation status without an immediate precipitation within the solutions. For the 5× SCPS, the initial pH value needed to be lowered down to about 5.9 to maintain this status. However, a crystalline coating layer could be obtained in the 1×, 2×, 3×, 4× SCPS but not in 5× SCPS at 37 °C. Instead, an immediate precipitation with large crystals within the 5× SCPS solution



was detected and no visible crystalline coating formed on the titanium discs. We further tried to use 5× SCPS at room temperature to test whether a crystalline layer of coating could form. In such a condition, although the immediate precipitation with large crystals within the solution was not detected, there was still no crystalline coating layer formed on the titanium discs. The amorphous CaP-coating procedure in 5× SBF started at a pH value of about 6 and ended when the pH value increased above 8.2, due to the release of CO<sub>2</sub> from the 5× SBF solution [15, 16]. Therefore, the pH value for the formation of amorphous CaP coating was much higher than pH 5.9 — the pH value for 5× SCPS. Consequently, the failure to form a crystalline coating layer using 5× SCPS was most probably caused by the rapid dissolution of the amorphous CaP seeding layer in the 5× SCPS solution due to its acidic property. Thereafter, to achieve maximal ion concentrations, we tried 4.5× SCPS at room temperature and found that a visible crystalline coating could be reproducibly prepared on amorphous CaP-coated titanium discs. These results indicated that 4.5× SCPS was the most concentrated SCPS to form a crystalline coating on amorphous CaP-coated titanium discs. Consequently, we decided to adopt 4.5× SCPS and characterized the newly produced coating formed at room temperature using the originally produced coating formed in 1× SCPS at 37 °C as a control.

### **3.2 The coating yield efficiency of 4.5× SCPS was significantly higher than that of 1× SCPS**

We first compared the volume-dependent efficiency of 4.5× SCPS in forming a crystalline CaP coating on a titanium disc (4 mm in length and width, 1 mm in thickness) with that of 1× SCPS. The coated titanium discs were embedded in MMA. The samples were then cross-sectioned using a microtome and stained using basic fuchsin to show the coatings. Thereafter, we adopted a stereomicroscope to take images and used a point-counting method [28] to calculate the average coating thickness on the cross-sections of the coated titanium discs. The stereomicroscopic images (Figure 1A) were not in the same resolution as the light microscopic images as in our previous publication [19]. Albeit so, in comparison with light microscopic images, these stereomicroscopic images were more optimal to show the distribution and homogeneity of the coatings along the surface of the titanium discs, which enabled us to do a maximal sampling of the coatings to ensure the accuracy

of the measurements. Consequently, the stereomicroscopic images were more suitable for the main purpose of this research.

For both 1× SCPS and 4.5× SCPS, a higher volume of SCPS was associated with a higher coating thickness (Figure 1A). We found that 0.3 mL of 4.5× SCPS led to a continuous coating layer, while 0.3 mL of 1× SCPS formed a thin and discontinuous coating layer (Figure 1A). Moreover, 2 mL of 4.5× SCPS was already capable of forming a very thick (about 110- $\mu$ m-thick) coating, while 2 mL of 1× SCPS only formed a continuous thin (29- $\mu$ m-thick) coating layer. Quantitative data showed a positive linear correlation between the coating thickness and the solution volume of 1× SCPS, with a coefficient of determination of about 0.99. These data indicated that the coating thickness could be increased proportionally by increasing the volume of the 1× SCPS solution. In contrast, a biphasic pattern was found in the relationship between the volume of 4.5× SCPS and the thickness of the produced coating. The initial rapid increase in coating thickness was detected when the volume of 4.5× SCPS ranged from 0.1 to 1 mL, which was followed by a relatively slower increase pattern at higher solution volumes (2–6 mL) (Figure 1B). We established a positive logarithmic correlation between the volume of 4.5× SCPS and the coating thickness with a coefficient of determination of about 0.99 (Figure 1B). The coating thickness formed in 6 mL of 4.5 × SCPS reached  $136 \pm 6 \mu\text{m}$ , which was 1.9 times than that of 6 mL 1× SCPS ( $71 \pm 8 \mu\text{m}$ ).

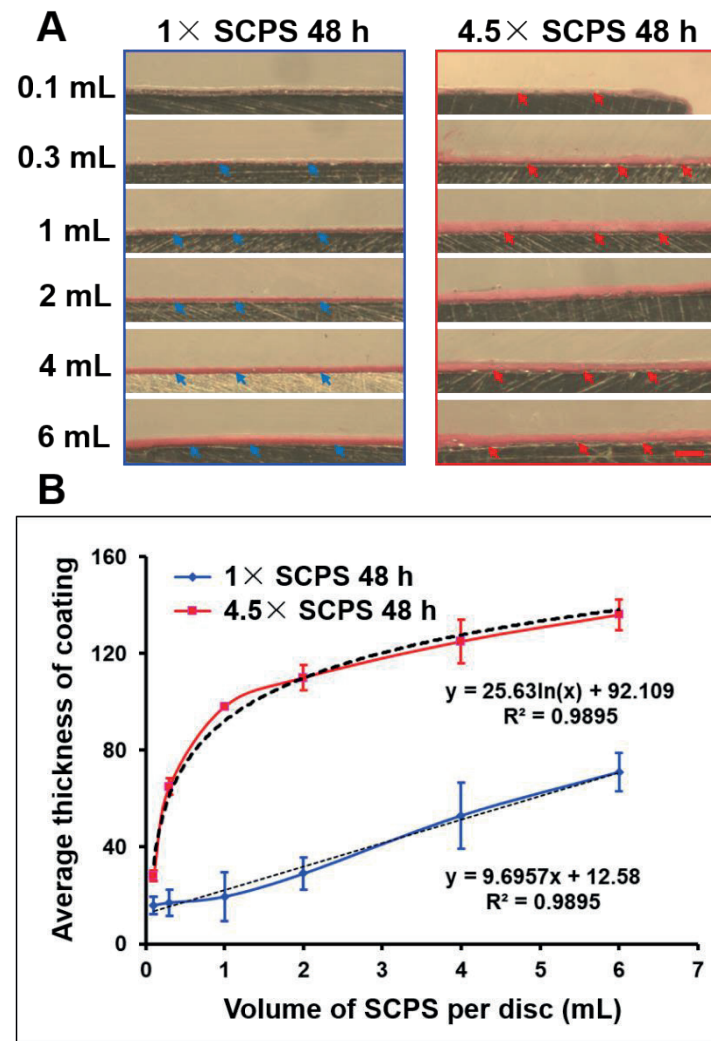


**Figure 1.** A: Stereomicroscopic images of the cross-sections of titanium discs (4 mm in length and width, 1 mm in thickness) with crystalline CaP coatings obtained through incubation in 0.1, 0.3, 1, 2, 4, and 6 mL of 1× SCPS and 4.5× SCPS for 48 h. The cross-sections were stained with basic fuchsin. B: Quantitative analysis of the relationship between the solution volume of SCPS and the average coating thickness, gauged using a point-counting method. Scale bars = 200 μm.

Using FESEM, we characterized the morphology of the coating formed by both SCPSs. For 0.1 mL of 1× SCPS, the FESEM image at a magnification of 1000× still

showed a spherical or semi-spherical morphology, which is typical of amorphous CaP [24] and indicated that the crystalline CaP layer was very thin (Figure 2). The FESEM image at a magnification of 5000× showed a mesh-like morphology, which was similar to the biomimetic coating obtained at a low solution volume-to-surface area ratio [30]. Such a topographic pattern of amorphous CaP was still visible when the coating solution volume was increased to 2 mL. For 1 mL, 1× SCPS formed a typical plate-like crystalline layer [24] and the plate increased in size with the increase of the solution volume. In contrast, the morphology of amorphous CaP was not visible even after incubation in 0.1 mL of 4.5× SCPS. Instead, a crystalline structure was observed (Figure 2). After incubation in 1 mL of 4.5× SCPS, the plates became markedly larger and clustered in a rose-like morphology. No further changes were found in the coating morphology, even when the volume of 4.5× SCPS was increased to 6 mL (Figure 2).

### 3.3 Time-dependent changes in pH values and Ca<sup>2+</sup> concentration during the coating procedure

The time-dependent changes in the pH and Ca<sup>2+</sup> concentration were monitored during the coating procedure. In contrast to 1× SCPS, the initial pH value of the 4.5× SCPS was about 6.2. Using a pH meter, we found that the pH values of both SCPSs decreased over time during the coating procedure. For 1× SCPS, the pH value decreased significantly from 7.4 to about 7.0 within the first 5 h ( $p < 0.05$ ) and was maintained at this level for the remainder of the coating procedure (Figure 3A). In contrast, significant decreases in the pH value of 4.5× SCPS were detected at all time points (5, 24, and 48 h) ( $p < 0.05$ ), eventually reaching a decrease of 5.75 (Figure 3A). Similar to the patterns of pH changes, the concentration of Ca<sup>2+</sup> significantly decreased from 4.0 mM to 3.2 mM within 5 h ( $p < 0.05$ ) and gradually decreased to 2.6 mM, with about 35% of Ca<sup>2+</sup> depleted by the end of the coating procedure (Figure 3B). For 4.5× SCPS, significant Ca<sup>2+</sup> concentration decreases were found at 5 h ( $p < 0.05$ ) and at 24 h post-incubation, and was maintained at about 13 mM, constituting about 30% Ca<sup>2+</sup> depletion by the end of the coating procedure.

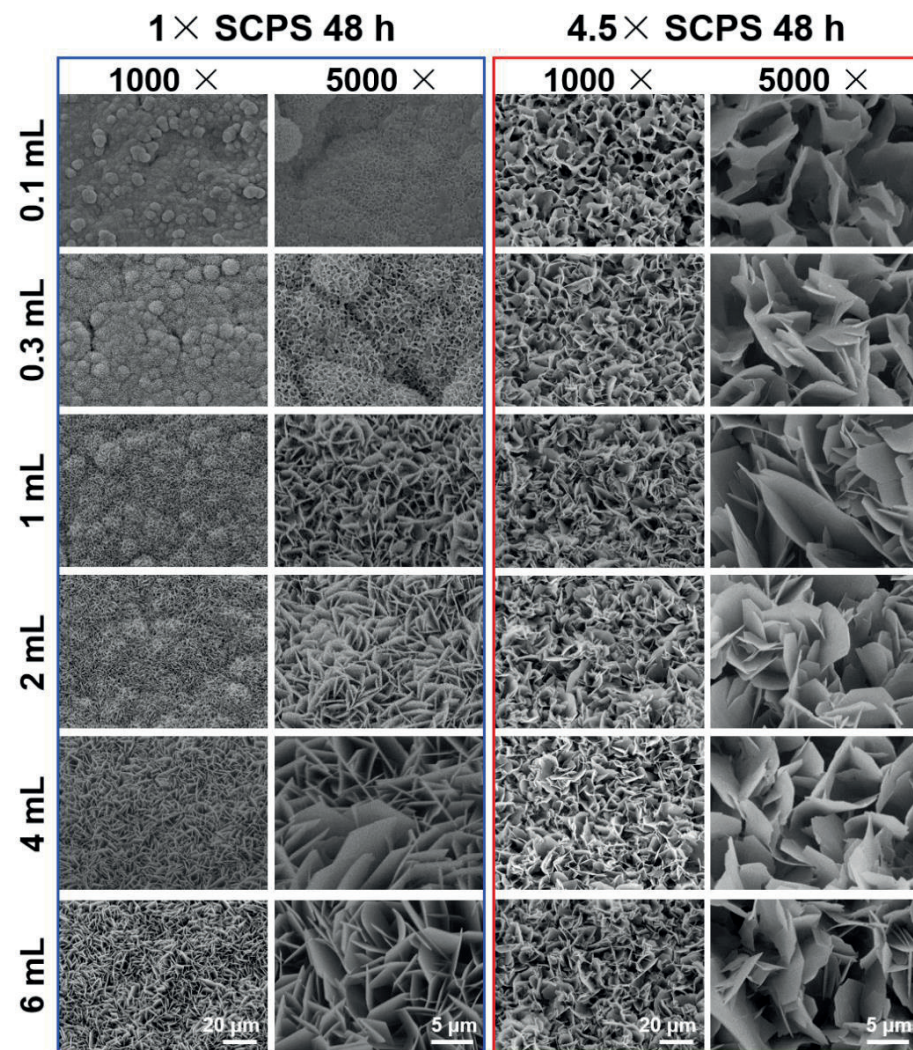


**Figure 2.** FESEM images showing the morphologies of CaP coatings obtained by incubating amorphous CaP-coated titanium discs (4 mm in length and width, 1 mm in thickness) in 0.1, 0.3, 1, 2, 4, and 6 mL of 1× SCPS and 4.5× SCPS for 48 h with a low magnification (1000×) and high magnification (5000×).

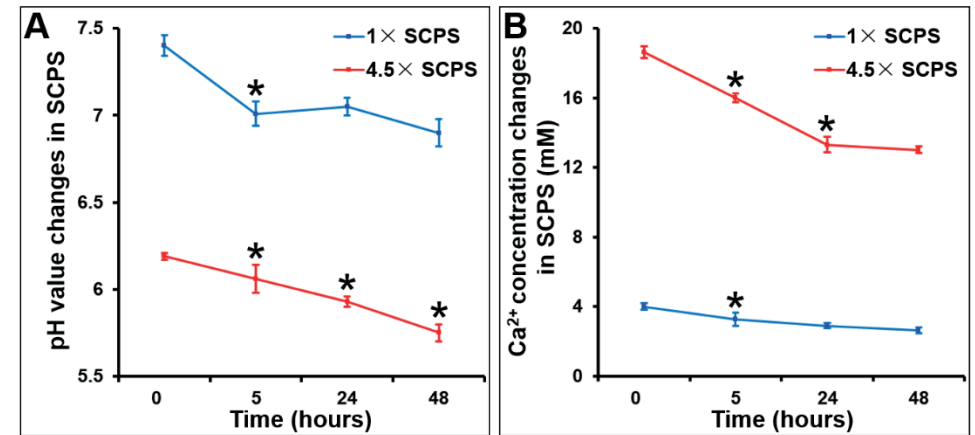


**Figure 3.** The time-dependent changes of (A) pH values and (B) calcium ions ( $\text{Ca}^{2+}$ ) of 1× SCPS and 4.5× SCPS solutions during the coating procedure. \* compared with the former time point,  $p < 0.05$ .

### 3.4 Characterization of the coating formed in 4.5× SCPS

EDS analysis showed that the coatings formed in both 1× SCPS and 4.5× SCPS mainly consisted of calcium, phosphorus, and oxygen elements (Figure 4A) after 48 h of incubation. The Ca/P ratio of the coatings showed a similar change pattern: an initial decrease within 5 h, followed by an increase. The final Ca/P ratios were 1.35 and 1.26 for 1× SCPS and 4.5× SCPS, respectively (Figure 4B).

In addition, the ATR-FTIR spectra of the 1× SCPS and 4.5× SCPS groups were characterized by peaks of  $\text{PO}_4^{3-}$  at wavelengths of  $1018\text{--}1021\text{ cm}^{-1}$  ( $\nu_3$ ) and  $560\text{ cm}^{-1}$  ( $\nu_4$ ) [31, 32], indicating that the BioCaP-coatings were successfully deposited onto the titanium discs (Figure 5). After 5 h of incubation in 1× SCPS, the peaks at  $1018\text{--}1021\text{ cm}^{-1}$  ( $\nu_3$ ) and  $560\text{ cm}^{-1}$  ( $\nu_4$ ) became slightly more visible and continued to become more pronounced with the time during the coating process (Figure 5A). In contrast, the peaks were markedly more significant after 5 h of incubation in 4.5× SCPS than they were in 1× SCPS (Figure 5B). The peaks became only slightly more significant with time, which indicated that 5 h of incubation enabled the formation of a pronounced crystalline coating.



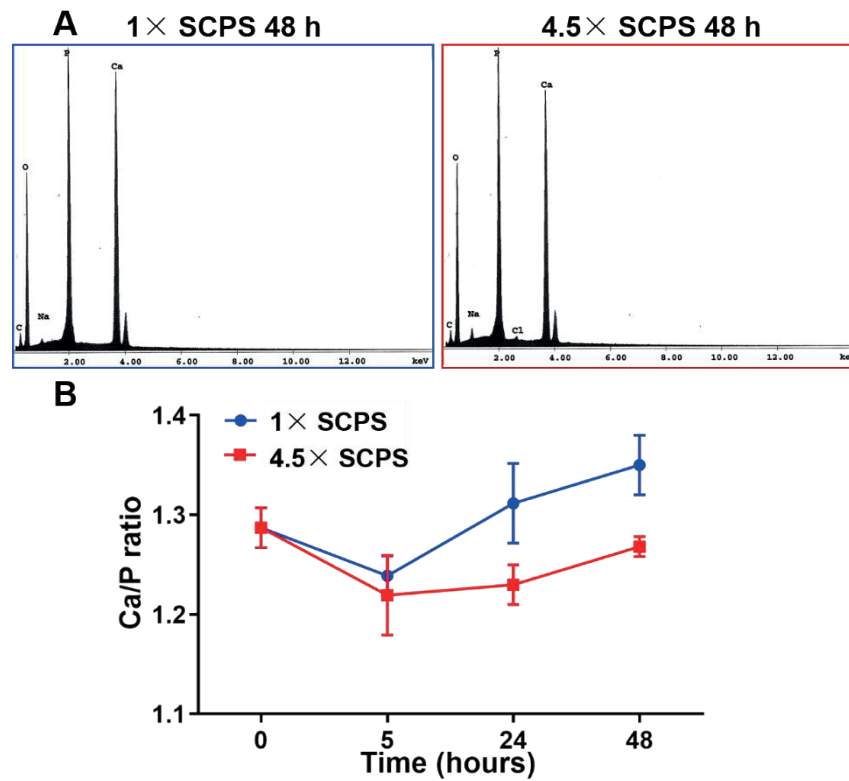


**Figure 4.** A: EDS analysis of CaP coatings obtained by incubating amorphous CaP-coated titanium discs in 1× SCPS or 4.5× SCPS for 48 h. B: Calculation of the ratio of calcium to phosphorus using the data of EDS analysis.

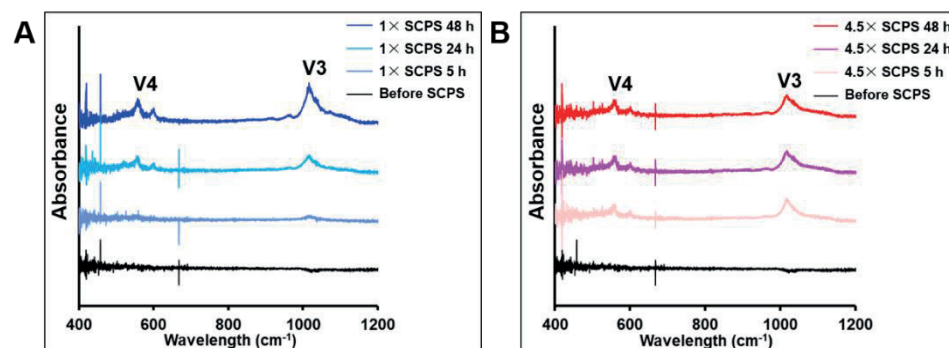


**Figure 5.** ATR-FTIR analysis of chemical groups of the CaP coatings obtained by incubating amorphous CaP-coated titanium discs in 1× SCPS (A) or 4.5× SCPS (B) for 5, 24, and 48 h.

The XRD patterns of the titanium discs before coating, in the 1× SCPS, and the 4.5× SCPS are presented in Figure 6. The characteristic diffraction peaks at  $2\theta = 35.5^\circ, 38.4^\circ, 40.3^\circ, 53.4^\circ, 63.1^\circ,$  and  $71.4^\circ$  corresponded to the (1000), (0002), (1011), (1012), (1120), and (1013) planes of titanium (Figure 6) [33]. The coating formed by incubation in 1× SCPS bore two characteristic peaks at  $2\theta = 26.1^\circ$  and  $31.5^\circ$ , corresponding to the (002) and (211) planes of hydroxyapatite (JCPDS no. 09–0432) (Figure 6A) [34]. These peaks became visible after 5 h of incubation in 1× SCPS and became more significant with the progress of the coating procedure. Similarly, the coatings formed by incubation in 4.5× SCPS also bore the two characteristic peaks of hydroxyapatite. Furthermore, this new coating also contained a very sharp, high peak at  $2\theta = 11.7^\circ$ , which corresponded to dicalcium-phosphate dihydrate (DCPD) (JCPDS no. 9–77) (Figure 6B) [34]. These findings suggested that the coating was a complex of DCPD and apatite. DCPD is biocompatible, biodegradable, and osteoconductive, and can be converted into dicalcium-phosphate anhydrous (DCPA) ( $\text{pH} < 6$ ), octacalcium-phosphate (OCP) ( $\text{pH} = 6\text{--}7$ ), or precipitated hydroxyapatite (pHAp) ( $\text{pH} > 7$ ) [1]. In medicine, DCPD is used in the production of CaP cement [35]. It has been observed that DCPD can either be converted into hydroxyapatite [36] or be degraded and replaced by bone *in vivo*. The *in-vivo* biocompatibility of the novel coating should be further tested.

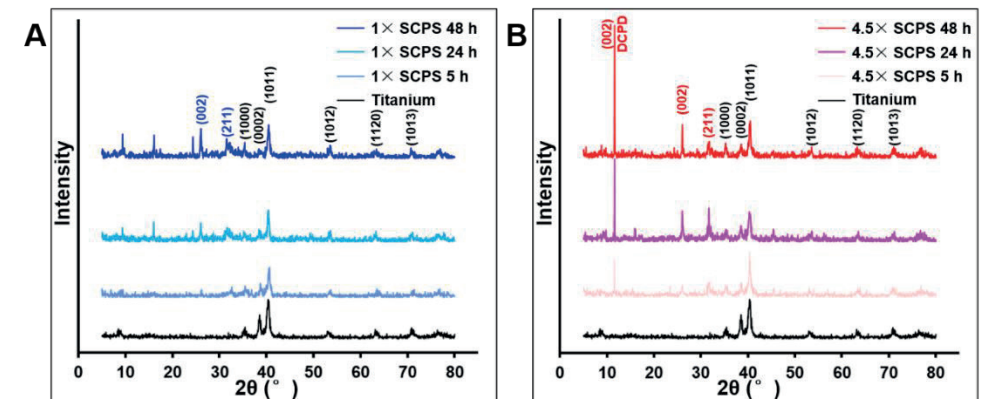


**Figure 6.** XRD analysis of the CaP coatings obtained by incubating amorphous CaP-coated titanium discs in 1× SCPS (A) or 4.5× SCPS (B) for 5, 24, and 48 h.

### 3.5 Ca<sup>2+</sup>-release profile from coatings

An acidic solution was selected to imitate a surgical site (where the initial environment could be acidic) as well as the effect of osteoclasts (which degrade bone by acid secretion) [37]. Under physiological conditions, at pH 7.4, Ca<sup>2+</sup> ions were released at a low level (Figure 7). The release profiles for both SCPSs were identical, with an average amount of about 0.17 µg per day released from both coatings. In the release buffer with pH 6.0, the release profiles for both SCPSs were still largely similar, with an average amount of about 0.78 µg per day released from both coatings. This phenomenon was in accordance with zinc ion dissolution from the zinc hydroxyapatite membrane, which also displayed higher release kinetics in acetate buffer (pH 4.5) and lower release in phosphate-buffered saline [37]. Under strong acidic conditions (pH 4.5), the total amount of Ca<sup>2+</sup> ion released from the 1× SCPS group (59.95 ± 1.39 µg) was significantly higher than that from the 4.5× SCPS group (32.67 ± 0.03 µg) ( $p < 0.001$ ). The profile of Ca<sup>2+</sup> release from the coating obtained in 4.5× SCPS did not change markedly, even in a strongly acidic microenvironment, which could be explained by the solid architecture and higher amounts of BioCaP deposited onto the discs. The faster dissolution rate of the 1× SCPS group was due to the free H<sup>+</sup>, which affected the nucleation of apatite with a loose structure. This finding suggested that BioCaP-coatings fabricated in 4.5× SCPS demonstrated acid-resistant properties against osteoclastic resorption, which may indicate slow degradation *in vivo*.

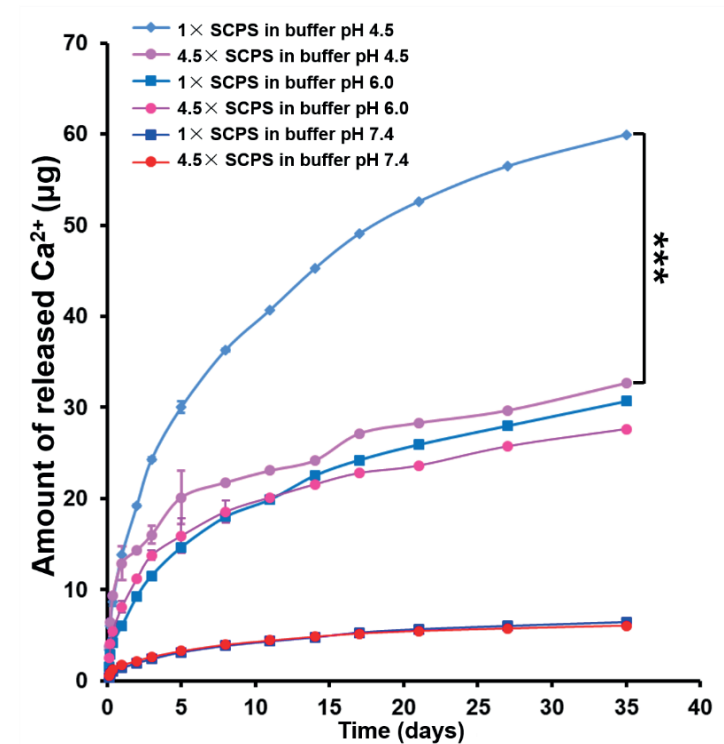


**Figure 7.** The release profiles of Ca<sup>2+</sup> from the CaP coatings obtained by incubating amorphous CaP-coated titanium discs from 1× SCPS or 4.5× SCPS of 48 h in buffers with neutral (pH = 7.4), and acid conditions (pH = 6.0 and 4.5). \*\*\*  $p < 0.001$ .

### 3.6 Rate of incorporation of the model protein FITC-BSA

The rate of incorporation of FITC-BSA in the 4.5× SCPS coating was 81.20 ± 6.42%, which was significantly higher than that of 21.86 ± 1.90% of the 1× SCPS coating ( $p < 0.001$ ). Such a higher incorporation rate of FITC-BSA was largely due to the reduced solution volume and enhanced coating yield (Figure 8).



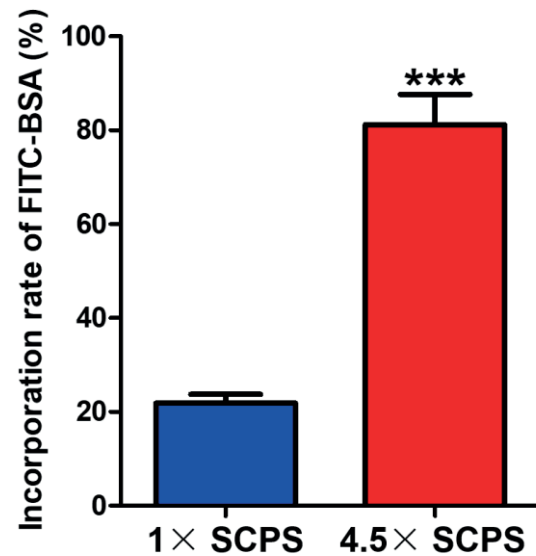


**Figure 8.** The rate of incorporation of a model protein — FITC-BSA, in the coatings obtained with 1× SCPS or 4.5× SCPS. \*\*\*  $p < 0.001$ .

#### 4. CONCLUSION

We have developed a new biphasic biomimetic coating procedure (4.5× SCPS) and the thereby produced coating has shown a series of advantages over the original coating using the current protocol, such as significantly higher coating yield efficiency and protein-incorporating rate. Furthermore, the new coating was identified as DCPD/apatite crystalline and showed a strong acid-resistant property, which enabled a slow coating dissolution and thus a slow delivery of bioactive agents in acidic environments, such as inflammation. These properties conferred the new coating a promising potential in the functionalization of titanium implants for biomedical applications. On the other hand, the biological properties of the new coating might be altered due to the changes in its physicochemical properties. Therefore, further *in-vitro* and *in-vivo* experiments are highly needed to be performed to further evaluate the biological properties of this coating. Furthermore, it remains to be elucidated how the high ion concentration in the new coating solution influences the bioactivity of various types of bioactive agents.

#### REFERENCES

- [1] N. Eliaz, N. Metoki, Calcium Phosphate Bioceramics: A Review of Their History, Structure, Properties, Coating Technologies and Biomedical Applications, *Materials (Basel)* 10(4) (2017) 334.
- [2] P. Sun, et al., BMP2/7 Heterodimer Is a Stronger Inducer of Bone Regeneration in Peri-Implant Bone Defects Model Than BMP2 or BMP7 Homodimer, *Dent Mater J* 31(2) (2012) 239-248.
- [3] R.A. Surmenev, et al., Significance of Calcium Phosphate Coatings for the Enhancement of New Bone Osteogenesis — a Review, *Acta Biomater* 10(2) (2014) 557-579.
- [4] H.C. Gledhill, et al., Direct Morphological Comparison of Vacuum Plasma Sprayed and Detonation Gun Sprayed Hydroxyapatite Coatings for Orthopaedic Applications, *Biomaterials* 20(4) (1999) 315-322.
- [5] Y. Huang, et al., Hydroxyapatite Coatings Deposited by Liquid Precursor Plasma Spraying: Controlled Dense and Porous Microstructures and Osteoblastic Cell Responses, *Biofabrication* 2(4) (2010) 045003.
- [6] A. Oyane, et al., Calcium Phosphate Composite Layers for Surface-Mediated Gene Transfer, *Acta Biomater* 8(6) (2012) 2034-2046.
- [7] A.W. Nijhuis, et al., Wet-Chemical Deposition of Functional Coatings for Bone Implantology, *Macromol Biosci* 10(11) (2010) 1316-1329.
- [8] T. Kokubo, Bioactive Glass Ceramics: Properties and Applications, *Biomaterials* 12(2) (1991) 155-163.
- [9] T. Kokubo, et al., Ca,P-Rich Layer Formed on High-Strength Bioactive Glass-Ceramic A-W, *J Biomed Mater Res* 24(3) (1990) 331-343.
- [10] A.L. Escada, et al., Biomimetic Calcium Phosphate Coating on Ti-7.5Mo Alloy for Dental Application, *J Mater Sci Mater Med* 22(11) (2011) 2457-2465.
- [11] T. Reiner, I. Gotman, Biomimetic Calcium Phosphate Coating on Ti Wires Versus Flat Substrates: Structure and Mechanism of Formation, *J Mater Sci Mater Med* 21(2) (2010) 515-523.
- [12] T. Kokubo, et al., Novel Bioactive Materials with Different Mechanical Properties, *Biomaterials* 24(13) (2003) 2161-2175.
- [13] T. Kawai, et al., Coating of an Apatite Layer on Polyamide Films Containing Sulfonic Groups by a Biomimetic Process, *Biomaterials* 25(19) (2004) 4529-4534.
- [14] A.C. Tas, Rapid Biomimetic Calcium Phosphate Coating on Metals, Bioceramics and Biopolymers at Room Temperature with 10× SBF, *Advances in Bioceramics and Porous Ceramics III* (2010) 63-75.
- [15] F. Barrere, et al., Biomimetic Coatings on Titanium: A Crystal Growth Study of Octacalcium Phosphate, *J Mater Sci Mater Med* 12(6) (2001) 529-534.
- [16] Y. Liu, et al., Biomimetic Coprecipitation of Calcium Phosphate and Bovine Serum Albumin on Titanium Alloy, *J Biomed Mater Res* 57(3) (2001) 327-335.
- [17] Y. Liu, et al., Delivery Mode and Efficacy of BMP2 in Association with Implants, *J Dent Res* 86(1) (2007) 84-89.
- [18] Y. Liu, et al., The Influence of BMP2 and Its Mode of Delivery on the Osteoconductivity of Implant Surfaces During the Early Phase of Osseointegration, *Biomaterials* 28(16) (2007) 2677-2686.

- [19] Y. Liu, et al., BMP2 Liberated from Biomimetic Implant Coatings Induces and Sustains Direct Ossification in an Ectopic Rat Model, *Bone* 36(5) (2005) 745-757.
- [20] Y. Liu, et al., Bone Morphogenetic Protein 2 Incorporated into Biomimetic Coatings Retains Its Biological Activity, *Tissue Eng* 10(1-2) (2004) 101-108.
- [21] Y. Liu, et al., Osteoinductive Implants: The Mise-En-Scène for Drug-Bearing Biomimetic Coatings, *Ann Biomed Eng* 32(3) (2004) 398-406.
- [22] G. Wu, et al., Functionalization of Deproteinized Bovine Bone with a Coating-Incorporated Depot of BMP2 Renders the Material Efficiently Osteoinductive and Suppresses Foreign-Body Reactivity, *Bone* 49(6) (2011) 1323-1330.
- [23] T. Liu, et al., Deproteinized Bovine Bone Functionalized with the Slow Delivery of BMP2 for the Repair of Critical-Sized Bone Defects in Sheep, *Bone* 56(1) (2013) 110-118.
- [24] G. Wu, et al., Biomimetic Coating of Organic Polymers with a Protein-Functionalized Layer of Calcium Phosphate: The Surface Properties of the Carrier Influence Neither the Coating Characteristics nor the Incorporation Mechanism or Release Kinetics of the Protein, *Tissue Eng Part C Methods* 16(6) (2010) 1255-1265.
- [25] G. Wu, et al., The Effect of a Slow Mode of BMP2 Delivery on the Inflammatory Response Provoked by Bone-Defect-Filling Polymeric Scaffolds, *Biomaterials* 31(29) (2010) 7485-7493.
- [26] T. Liu, et al., Cell-Mediated BMP2 Release from a Novel Dual-Drug Delivery System Promotes Bone Formation, *Clin Oral Implants Res* 25(12) (2014) 1412-1421.
- [27] X. Yu, et al., Incorporation of Bovine Serum Albumin into Biomimetic Coatings on Titanium with High Loading Efficacy and Its Release Behavior, *J Mater Sci Mater Med* 20(1) (2009) 287-294.
- [28] H.J. Gundersen, E.B. Jensen, The Efficiency of Systematic Sampling in Stereology and Its Prediction, *J Microsc* 147(Pt 3) (1987) 229-263.
- [29] A. Nakahira, et al., Synthesis and Evaluation of Various Layered Octacalcium Phosphates by Wet-Chemical Processing, *J Mater Sci Mater Med* 12(9) (2001) 793-800.
- [30] Y. Liu, et al., Biomimetic Coatings for Bone Tissue Engineering of Critical-Sized Defects, *J R Soc Interface* 7 Suppl 5 (2010) S631-647.
- [31] Y.F. Chou, et al., The Effect of PH on the Structural Evolution of Accelerated Biomimetic Apatite, *Biomaterials* 25(22) (2004) 5323-5331.
- [32] X. Wang, et al., Tissue-Engineered Endothelial Cell Layers on Surface-Modified Ti for Inhibiting *in Vitro* Platelet Adhesion, *Sci Technol Adv Mater* 14(3) (2013) 035002.
- [33] M. Yan, et al., TEM and XRD Characterisation of Commercially Pure A-Ti Made by Powder Metallurgy and Casting, *Materials Letters* 72 (2012) 64-67.
- [34] C.Y. Zhang, et al., Biomimetic Mineralization of Zein/Calcium Phosphate Nanocomposite Nanofibrous Mats for Bone Tissue Scaffolds, *CrystEngComm* 16(40) (2014) 9513-9519.
- [35] H. Yamamoto, et al., Mechanical Strength of Calcium Phosphate Cement *in Vivo* and *in Vitro*, *Biomaterials* 19(17) (1998) 1587-1591.
- [36] B.R. Constantz, et al., Histological, Chemical, and Crystallographic Analysis of Four Calcium Phosphate Cements in Different Rabbit Osseous Sites, *J Biomed Mater Res* 43(4) (1998) 451-461.
- [37] J. Chou, et al., Bioresorbable Zinc Hydroxyapatite Guided Bone Regeneration Membrane for Bone Regeneration, *Clin Oral Implants Res* 27(3) (2016) 354-360.

## CHAPTER 5

3D printed TCP scaffolds functionalized with polydopamine-immobilized BMP2 to construct prefabricated biomimetic bone grafts

Shuyi Li, Fen Zhang, Fidel Hugo Perera, Tim Forouzanfar, Gang Wu, Pedro Miranda, Miao Zhou

Submitted.

## ABSTRACT

The repair of large mandibular bone defects remains challenging for clinicians. As a viable treatment option, prefabrication technique is adopted in clinics to construct biomimetic bone grafts with mandibular curvatures by implanting superficially adsorbed bone morphogenetic protein-2 (rhBMP2)-functionalized bone-filling materials in *in-vivo* ectopic bioreactors, such as latissimus dorsi muscle. However, thereby delivered BMP2 may result in a burst release, causing various side effects and compromising its osteoinductive efficacy. One viable solution is polydopamine (pDA) coating, which can simply and biomimetically immobilize growth factors on various biomaterials. The purpose of this work was to prove the principle that 3D printed tricalcium phosphate (TCP) scaffolds functionalized by pDA-immobilized BMP2 were superior in prefabricating biomimetic bone grafts than the 3D printed TCP scaffolds functionalized by the superficially adsorbed one in latissimus dorsi muscle. Field emission scanning electron microscope was used to analyze the time-dependent morphologies of pDA-coating on TCP (TCP/pDA) scaffolds. The loading efficiency and release kinetics of BMP2 in TCP and TCP/pDA scaffolds were assessed. The bioactivity of released BMP2 was evaluated both *in vitro* and *in vivo*. Through these studies, we found that the content of pDA coating increased with the incubation time. TCP/pDA scaffolds bore 1.7 times higher loading efficiency of BMP2 than pure TCP scaffolds. TCP/BMP bore 2.3 times higher burst release of BMP2 than TCP/pDA/BMP on day 1. Furthermore, TCP/pDA/BMP scaffolds bore significantly higher expression levels of osteogenesis-related genes (ALP, Osx, and COL I) than TCP/BMP. When being implanted in the latissimus dorsi muscle of rats, TCP/pDA/BMP scaffolds bore about 2.1 times higher new bone area than TCP/BMP. These results suggested that the 3D printed TCP scaffolds functionalized with pDA-immobilized BMP2 were promising to prefabricate biomimetic bone grafts to repair large mandibular bone defects.

**Keywords:** 3D printing; Polydopamine; Prefabrication; BMP2; Bone grafts.

## 1. INTRODUCTION

Large mandibular bone defects due to malignant tumor resection often result in discontinuity of the mandible, loss of functions (e.g., mastication and articulation), and compromised appearance, causing great suffering to patients [1, 2]. As a combined treatment for malignant tumors, radiotherapy may compromise the blood supply in defect sites and thereby severely impair the outcome of orthotopic bone regenerative therapy [2]. Therefore, both autogenous vascularized and non-vascularized bone grafts, such as fibular, scapula, and iliac crest have been applied in clinics to restore the bone volume, contours and functions of the mandible [2]. The usage of non-vascularized bone grafts (NVBGs) is limited by uncontrolled resorption and may require a second-stage bone augmentation surgery [3]. NVBGs are not suitable for long bone defects (> 6 cm) with soft tissue loss and radiotherapy [4]. In contrast, vascularized bone grafts (VBGs) can repair most of large mandibular bone defects with a significantly higher success rate (96%) than NVBGs (69%) [5]. Furthermore, VBGs not only ensure sufficient blood and soft tissue supply, but also bear low risks of graft resorption and infection. However, the usage of VBGs is also restricted by limited availability, severe donor site morbidity, and difficulty to fit the irregular shape of bone defects [6]. Hitherto, the repair of large mandibular bone defects remains highly challenging for clinicians [7].

As a viable treatment option, prefabrication technique has been developed, involving the implantation of bone-filling materials (e.g., deproteinized bovine bone and tricalcium phosphate (TCP)) into an *in-vivo* ectopic bioreactor (e.g., gastrocolic omentum and latissimus dorsi muscle), which undergo a neovascularization and bone regeneration period to form biomimetic bone grafts. The 3D geometry of the bone-filling materials is usually shaped using a customized titanium mesh to ensure a rough fit to the curvatures of mandibular bones [2, 8]. Recombinant human bone morphogenetic protein-2 (rhBMP2) is often absorbed onto the materials to achieve sufficient bone formation [9]. After the ectopic prefabrication for about 2 to 3 months, the vascularized biomimetic bone grafts can be transferred with/without pedicle to repair large mandibular bone defects [2, 8]. Gastrocolic omentum and latissimus dorsi muscle are the most commonly used bioreactors to prefabricate biomimetic bone grafts for patients [2, 8] because these anatomic sites bear abundant blood

vessels to provide nutrients and oxygen to the prefabricated bone grafts, thereby facilitating a thorough vascularization. Besides, these sites also bear abundant native musculoskeletal progenitor cells, which can differentiate into osteoblasts to promote bone regeneration [7]. Furthermore, the implantation-caused injury of the muscles will also trigger the release of pro-osteogenic growth factors, such as BMPs and transforming growth factor- $\beta$ 1 (TGF- $\beta$ 1) [10]. Latissimus dorsi muscle contains the thoracodorsal artery and vein, which can be transferred with adjacent bone grafts to provide continuous blood supply [9]. Therefore, the survival and regenerative property of these pedicled biomimetic bone grafts will not be compromised when being implanted in irradiated bone defect sites.

With the development of computer-aided design and computer-aided manufacturing technologies, 3D printing has shown a promising application potential to directly fabricate customized biomedical constructs [11, 12]. As one of the most widely used 3D printing techniques, robocasting enables the fabrication of calcium phosphate (CaP)-based biomimetic constructs with controlled and customized structures [13]. Besides, the printed scaffolds bear good mechanical properties and osteoconductivity, and the slowly degraded calcium and phosphate ions contribute to bone metabolism and regeneration [13]. In our previous study, we had implanted 3D printed TCP scaffolds functionalized with absorbed BMP2 in the latissimus dorsi muscle of rhesus monkeys to prefabricate biomimetic bone grafts, which were later transferred with the muscle pedicle (containing the thoracodorsal artery and vein) to repair mandibular bone defects of the monkeys [9]. The prefabricated bone grafts facilitate a much faster osseointegration with host bone and a better 3D outcome than the directly orthotopically implanted grafts [2, 8, 9, 13]. On the other hand, it is well-established that the absorption of BMP2 is always associated with a burst release, thus needing a supra-physiological dose to adequately induce new bone formation. And thereby-generated transiently higher concentration of BMP2 may cause a series of side effects, such as inflammation and swelling, jeopardizing new bone formation [14-16].

As a viable approach to simply and biomimetically immobilize growth factors, polydopamine (pDA)-mediated surface modification has been widely applied to increase surface bioactivity and osteoinductivity of various biomaterials, such as

titanium, polymeric, composite, and CaP-based scaffolds [17-20]. As a precursor of pDA, dopamine (DA) with functional groups of catechol and phenethylamine can self-polymerize in a weak alkaline environment to form the pDA coating, thus covalently or non-covalently bonding to various matrices [21]. The pDA coating is biocompatible and can immobilize growth factors via Michael addition and Schiff-base reactions [22]. Previous study shows that the total amount of pDA coating-immobilized BMP2 is significantly higher than the directly adsorbed one on poly(lactic-co-glycolic acid) (PLGA)/hydroxyapatite (HA) scaffolds [23]. Besides, pDA can significantly increase cell adhesion to the hydrophobic matrix by adjusting surface energy [24].

In this study, we wished to prove the principle that the 3D printed TCP scaffolds functionalized by pDA-immobilized BMP2 were superior in prefabricating biomimetic bone grafts than the 3D printed TCP scaffolds functionalized by the superficially adsorbed one in latissimus dorsi muscle. Scanning electron microscopy (SEM) and micro-CT were applied to observe the hierarchical structure of 3D printed TCP scaffolds. Field emission scanning electron microscope (FESEM) was used to analyze the time-dependent morphologies of pDA-coating on TCP (TCP/pDA) scaffolds. Afterwards, the loading efficiency and release kinetics of BMP2 in TCP and TCP/pDA scaffolds were assessed using enzyme-linked immunosorbent assay (ELISA). The bioactivity of released BMP2 was examined through examining alkaline phosphatase (ALP) activity and the expression levels of osteogenic genes. Finally, the latissimus dorsi muscle model of rats was used to evaluate the osteogenic efficacy of such prefabricated biomimetic bone grafts, aiming to provide a novel bone graft to repair large mandibular bone defects.

## 2. MATERIALS AND METHODS

### 2.1 Fabrication of the TCP scaffolds

A stable suspension of 40%  $\beta$ -TCP (outer diameter of 30 nm, Whitlockite OD, Plasma Biotol Limited, UK) ink was prepared by dispersing the powder in deionized water containing Darvan<sup>®</sup> C (R.T. Vanderbilt, Norwalk, CT). The powder was added gradually under vigorously shaking at 2000 rpm for 20 s after each addition until a stable and homogeneous mixture was obtained. Previously dissolved



hydroxypropyl methylcellulose (Methocel F4M, Dow Chemical Company, Midland, MI) was added to increase the viscosity, followed by the polyethylenimine (Sigma-Aldrich, USA) to increase agglomeration. Finally, the ink's printability was assessed which could extrude continuously without clogging from a syringe.

By Robocad 4.2.9 (3D inks, Stillwater, OK, USA), the scaffold was designed to be 5 mm × 5 mm in the tetragonal mesh. The center to center spacing between the adjacent rods was 900 μm within one layer and the layer height was 322 μm. The printing speed was set as 20 mm/s. After the ink was loaded in the syringe and the bubbles were removed, a conical nozzle with an inner diameter of 410 μm was used for printing under the control of the computer robotic system of a robocasting device (A3200, 3D inks, Stillwater, OK, USA). To ensure the uniform drying of the scaffolds during assembly, the deposition process was conducted within a paraffin oil bath. After printing, the scaffolds were left in the oil bath for 24 h, followed by drying at room temperature for another 24 h. Finally, the scaffolds were sintered at 1200 °C for 1 h.

## 2.2 Surface modification

To immobilize rhBMP2 (PeproTech, USA), a pDA (Sigma-Aldrich, USA) coating was introduced to the TCP scaffolds. At room temperature, the TCP scaffolds were immersed in the DA solution (2 mg/mL in 10 mM Tris-HCl, pH 8.5) and maintained on the shaker for 3 h, 6 h, 12 h, and 24 h. After that, the TCP/pDA scaffolds were rinsed with deionized water for 3 times to remove the unattached pDA and dried for subsequent studies. As to the cell culture and animal studies, the scaffolds were autoclaved and DA solution was sterilized by the membrane filter.

## 2.3 Characterization of the scaffolds

The gross views of both TCP and TCP/pDA were captured. Besides, the structures of the struts were investigated by SEM (S3400N, Japan) and micro-CT (SkyScan1172, Bruker, Belgium). The time-dependent morphology changes of TCP/pDA scaffolds were explored by FESEM (Merlin, Germany). Furthermore, the elemental compositions were analyzed by EDS (550i, IXRF System, USA).

## 2.4 RhBMP2 immobilization

Lyophilized powder of rhBMP2 (PeproTech, USA) was dissolved in recombinant cytokine dissolution to obtain rhBMP2 solution under sterilized

conditions. For *in-vitro* studies, sterile TCP and TCP/pDA scaffolds were incubated in rhBMP2 solution (1 μg/mL) at 37 °C for 12 h. Afterwards, the scaffolds were harvested and the remnant rhBMP2 solution was used to assess the loading efficiency (n = 3). For the animal study, 100 μg/mL rhBMP2 solution was applied to construct TCP/BMP and TCP/pDA/BMP scaffolds.

## 2.5 Release kinetics

To observe the initial release kinetics of the immobilized rhBMP2, the TCP/pDA/BMP and TCP/BMP scaffolds (n = 3) were incubated in 2 mL 10% phosphate-buffered saline (PBS) at 37 °C, 120 rpm for 4 days. In the due time points of 1 h, 3 h, 6 h, 1 d, and 4 d, the supernatant was harvested and 2 mL fresh 10% PBS was added. The amount of rhBMP2 in the collected supernatant was measured by a commercially available ELISA kit (PeproTech, USA) according to the manufacturer's instructions. The optical density (OD) was measured by a microplate reader (Thermo Fisher Scientific, Inc.). The cumulative percentage of released BMP2 was calculated by dividing the values of coated BMP2.

## 2.6 Cytocompatibility and morphology

Pre-osteoblast MC3T3-E1 cells were cultured in  $\alpha$ -minimum essential medium ( $\alpha$ -MEM) with 10% fetal bovine serum (FBS) and 1% penicillin-streptomycin (Gibco, Invitrogen, USA) at 37 °C, 5% CO<sub>2</sub> humidified condition. When the cells reached 70–80% confluence, they were digested, counted, and re-suspended in fresh culture medium. The cell suspension ( $4 \times 10^5$ /mL) was added onto sterile TCP and TCP/pDA scaffolds in a 24-well culture plate. After cell adhesion of 3 h, the cell-laden scaffolds were transferred to new wells with fresh culture medium. After 24 h, the viability, adhesion, and spreading of cells on the scaffolds were evaluated live/dead staining and SEM. A live/dead staining kit (BestBio, China) was applied to stain the live cells green with calcine AM and dead cells red with propidium iodide (PI) according to the manufacturer's instructions. The final images were captured by a confocal laser scanning microscope (CLSM, Leica, Germany). Before SEM observation, the cell-laden scaffolds were fixed in 4% paraformaldehyde for 30 min. After that, the samples were washed gently with 10% PBS twice and dehydrated in gradient concentrations of ethanol. Finally, the dried cell-laden scaffolds were sputter-coated with Au–Pd plasma.

## 2.7 ALP activity and osteogenic genes expression

The bioactivity of rhBMP2 released from TCP/BMP and TCP/pDA/BMP was assessed by determining the ability to induce osteogenic differentiation of C2C12 cells. Pure TCP scaffolds were set as the control group. C2C12 cells were cultured in high glucose Dulbecco's modified Eagle medium (DMEM) containing 10% FBS and 1% penicillin-streptomycin at 37 °C, 5% CO<sub>2</sub> humidified condition. When the cells reached 70–80% confluence, they were digested, counted, and re-suspended. The cell suspension ( $1 \times 10^6$ /mL) was seeded on the scaffolds and incubated for 3 h before they were transferred to new wells containing fresh culture medium. The culture medium was refreshed every 3 days. After a continuous culture for 14 days, the cells were harvested for ALP and osteogenic genes expression assays.

### 2.7.1 ALP activity assay

The intracellular ALP activities were tested according to the manufacturers' instructions for ALP assay (Jiancheng Bioengineering Institute, China) (n = 3). 1% Triton X-100 was used to increase the permeability for 30 min. After that, the lysed cells were centrifuged at 12000 rpm for 5 min. The supernatant of each sample was mixed with the working reagent. The absorbance of each sample was measured at 520 nm by the microplate reader. For normalization, the protein concentration was detected by a BCA assay (Jiancheng Bioengineering Institute, China). The activity of ALP was calculated as U/g protein.

### 2.7.2 Osteogenic genes expression

Quantitative reverse transcription-polymerase chain reaction (qRT-PCR) assay was conducted to detect the mRNA expression levels of ALP, collagen type I (Col I), and osterix (Osx) (n = 3). The mouse primers used in this study were listed in table 1. Total RNA was isolated using TRIzol Reagent (Invitrogen, USA). The concentration and purity of total RNA were measured by a spectrophotometer (NanoDrop 2000, Thermo Fisher Scientific, Inc.). Furthermore, cDNA synthesis and PCR analysis were performed. The genes expression levels were finally normalized by the housekeeping gene of GAPDH. The  $2^{-\Delta\Delta C_t}$  formula was used to calculate the fold changes.

**Table 1.** The sequences of primers used for qRT-PCR analysis.

No.	Primer name	Sequences
1	ALP	sense: GCTGATCATCCCCACGTTTT antisense: CTGGGCCTGGTAGTTGTTGT
2	Osx	sense: ACTCATCCCTATGGCTCGTG antisense: GGTAGGGAGCTGGGTTAAGG
3	COL I	sense: ACTGGTACATCAGCCCCGAAC antisense: TACTCGAACGGGAATCCATC
4	GAPDH	sense: AAGAAGGTGGTGAAGCAGG antisense: GAAGGTGGAAGAGTGGGAGT

## 2.8 Prefabrication of bioactive bone grafts

All procedures were approved by the Ethical Committee of Guangzhou Medical University (2014091). 3 adult male Sprague-Dawley rats (weight of 200–300 g) were included and randomly divided into 2 groups: TCP/BMP and TCP/pDA/BMP (n = 6). Under general anesthesia with 2% pentobarbital sodium, the back of the rats was shaved and sterilized. A 1-cm vertical incision was made on the back to expose the latissimus dorsi muscle. By a careful dissection, a muscular pouch was created and the prepared scaffolds were implanted into the pouch. Every rat received 4 implants and there was a 1-cm distance between the adjacent scaffolds and the spine. After implantation, the wounds were closed with layered sutures. The samples were harvested 4 weeks post-implantation and fixed in 4% paraformaldehyde for 24 h. After fixation, the samples were continuously washed overnight. 10% EDTA was applied for decalcification. All the samples were washed, dehydrated, and embedded in paraffin. 5- $\mu$ m sections of each sample were stained by hematoxylin and eosin (H&E) staining. Representative sides of each sample were photographed and analyzed to calculate the percentage of new bone area by Image Pro Plus 6.0 (Media Cybernetics, Silver Spring, MD, USA).

## 2.9 Statistical analysis

All data were presented as mean  $\pm$  standard deviation (SD). Statistical analysis was performed using IBM SPSS 22.0 version (IBM Corp, Armonk, NY, USA). Statistical differences among two groups were evaluated by Student's t-test while

the differences among three groups were assessed by one-way ANOVA. A value of  $P < 0.05$  was considered to be statistically significant.

### 3. RESULTS AND DISCUSSION

#### 3.1 Characterization and surface modification of the scaffolds

Pore size is a key parameter during the fabrication of scaffolds for optimal bone regeneration as it directly influences cell migration, tissue infiltration, and mineralized matrix formation [25]. Generally, an average pore size larger than 300  $\mu\text{m}$  is recommended to achieve adequate vascularization and bone ingrowth [26]. Besides, the presence of micro-pores with a diameter less than 10  $\mu\text{m}$  on scaffold surfaces may increase surface area to facilitate cell attachment and the penetration of bodily fluids [27], thereby benefiting the osseointegration of macro-porous scaffolds [28]. In this study, micro-CT analysis showed that our 3D printed TCP scaffolds bore an interconnected and hierarchically porous structure (Figure 1A, B) with a high porosity of  $66.5 \pm 0.8\%$ . SEM images showed that the average macro-pore diameter was  $314.8 \pm 8.8 \mu\text{m}$  (Figure 1C). At a magnification of 1000 $\times$ , SEM observations showed that micro-pores of  $1.0 \pm 0.3 \mu\text{m}$  in diameter scattered on the surfaces of the scaffolds (Figure 1D). These results suggested that the 3D printed TCP scaffolds bore favorable macro- and micro-structures for bone regeneration.

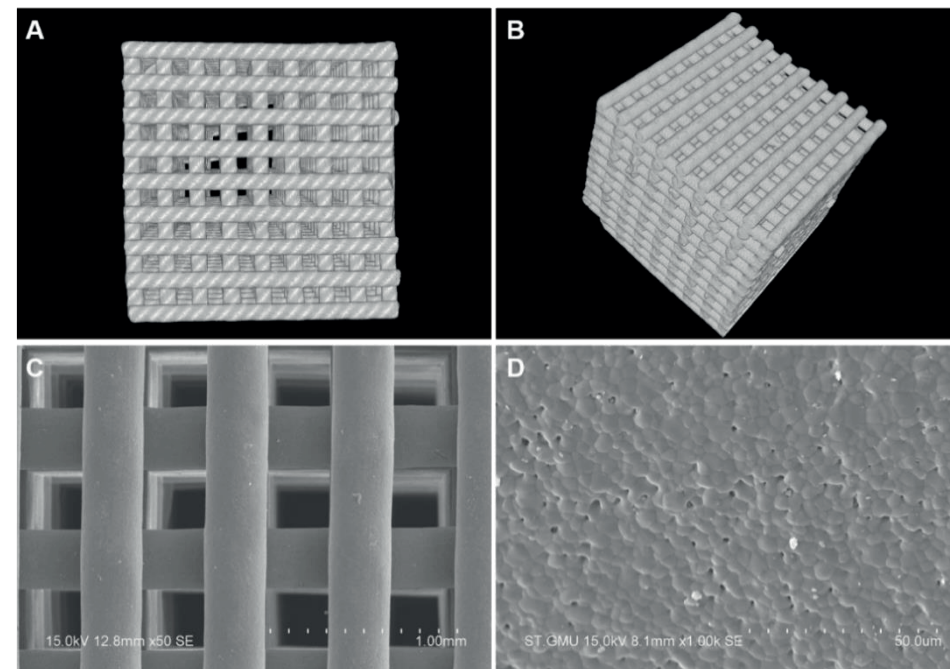


**Figure 1.** 3D hierarchical structure of 3D printed TCP scaffolds. A & B: Micro-CT images of the TCP scaffolds. C & D: SEM images of the macro- and micro-porous structures of the scaffolds.

Different from other surface modification methods, such as plasma treatment, pDA coating is a simple, safe, and effective method to modify scaffolds [21, 29]. Shin et al. find that the amount of pDA coating on polymeric films is highly dependent on the incubation time (from 5 min to 16 h) of the films in DA solution. It takes 4 h until pDA particles cover the whole surface of the film. Besides, the size of pDA particles increases from nanoscale (30 min) to microscale (16 h) [29]. Hitherto, there is still a lack of study to report the time-dependent morphological changes of pDA coating on 3D printed TCP scaffolds. In our study, with the increase of incubation time (3 h, 6 h, 12 h and 24 h), the color of the scaffolds gradually turned from white to dark brown (at 24 h) due to the oxidative polymerization of dopamine (Figure 2A). EDS analysis demonstrated the occurrence of a new element of N in pDA-modified TCP scaffolds, which was due to the amine groups of the pDA coating [30]. The atomic percentage of nitrogen increased from  $2.1 \pm$



0.4 % at 3 h to  $3.9 \pm 0.4$  % at 24 h (Figure 2B). This was consistent with another study where the atomic percentage of N on poly( $\epsilon$ -caprolactone)/pDA scaffolds is 3.49% after a 16-h incubation in DA solution [31].

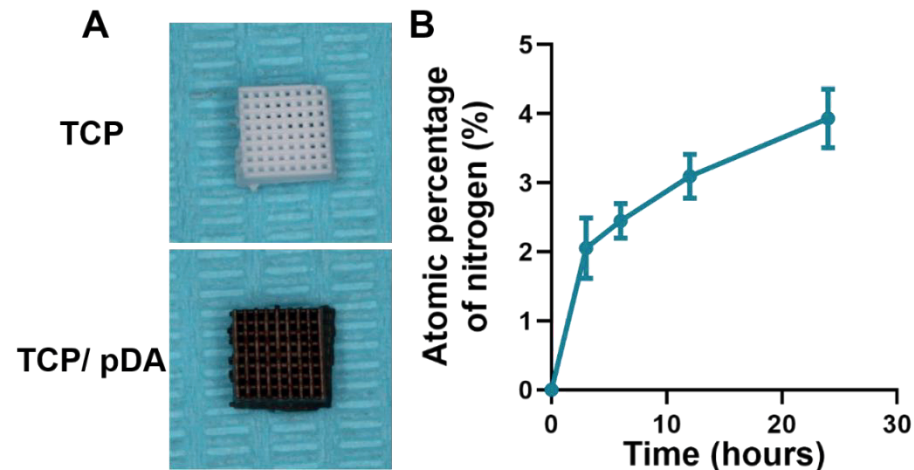


**Figure 2.** Gross view of (A), and the atomic percentage of nitrogen (B) on TCP/pDA scaffolds with an incubation time for 3 h, 6 h, 12 h, and 24 h.

FESEM was applied to observe the pDA coating. At a magnification of 10,000 $\times$ , the pentagonal crystal structures of TCP could be observed from 3 h to 12 h (Figure 3) while TCP/pDA at 24 h was covered with a thick layer of pDA particles. At a magnification of 30,000 $\times$ , the pDA particles uniformly aligned on the surface of the scaffolds after the incubation from 3 h to 6 h. After 12 h, the size of pDA particles increased, which might increase the surface roughness of the scaffolds. After 24 h, a thicker layer of pDA coating was observed on TCP. These findings were consistent with the study of Shin et al. [29]. Based on these results, pDA coating after a 12-h incubation was chosen for the subsequent studies.

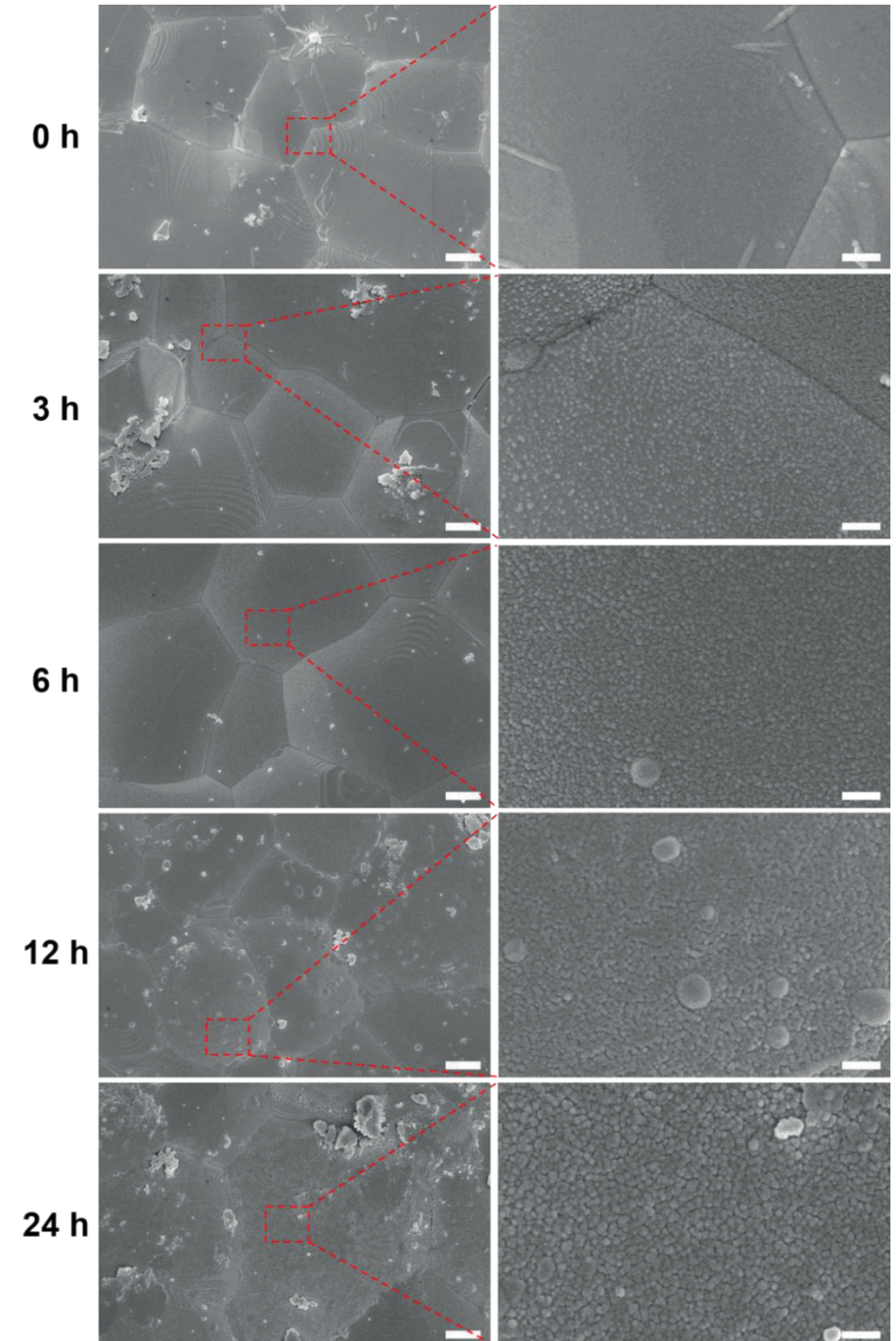




**Figure 3.** FESEM images at lower (left column) and higher (right column) magnifications depicting the surface morphologies of 3D printed TCP scaffolds incubated in DA solution for 0 h, 3 h, 6 h, 12 h, and 24 h. Scale bar = 1  $\mu\text{m}$  in the left column. Scale bar = 200 nm in the right column.

### 3.2 Cytocompatibility and cell morphology observation

MC3T3-E1 cells were selected to evaluate cell viability, attachment, migration, and proliferation on the scaffolds. Live/dead staining showed green-stained live MC3T3-E1 cells attached and aligned along the struts of the scaffolds (Figure 4A a1–b1). Some cells crossed the pores and anchored to the struts tightly. No red-stained dead cells were observed, which indicated that both TCP and TCP/pDA scaffolds bore excellent biocompatibility. Significantly higher fluorescence intensity was detected on TCP/pDA struts than TCP struts, which indicated that TCP/pDA was more favorable for cell attachment and spreading ( $p < 0.01$ ) (Figure 4B). SEM results further validated a favorable biocompatibility of TCP/pDA scaffolds. Multiple cells stretched out to anchor to the scaffolds (Figure 4A a2–b2). The increased cell adhesion on the pDA-coated surface may be attributed to the immobilized serum proteins by pDA [24, 29]. Besides, pDA bears abundant hydrophilic groups, such as  $\text{OH}^-$  and  $\text{NH}_2^-$ , which can increase the hydrophilicity of TCP scaffolds, thus benefiting cellular adhesion and spreading [32].

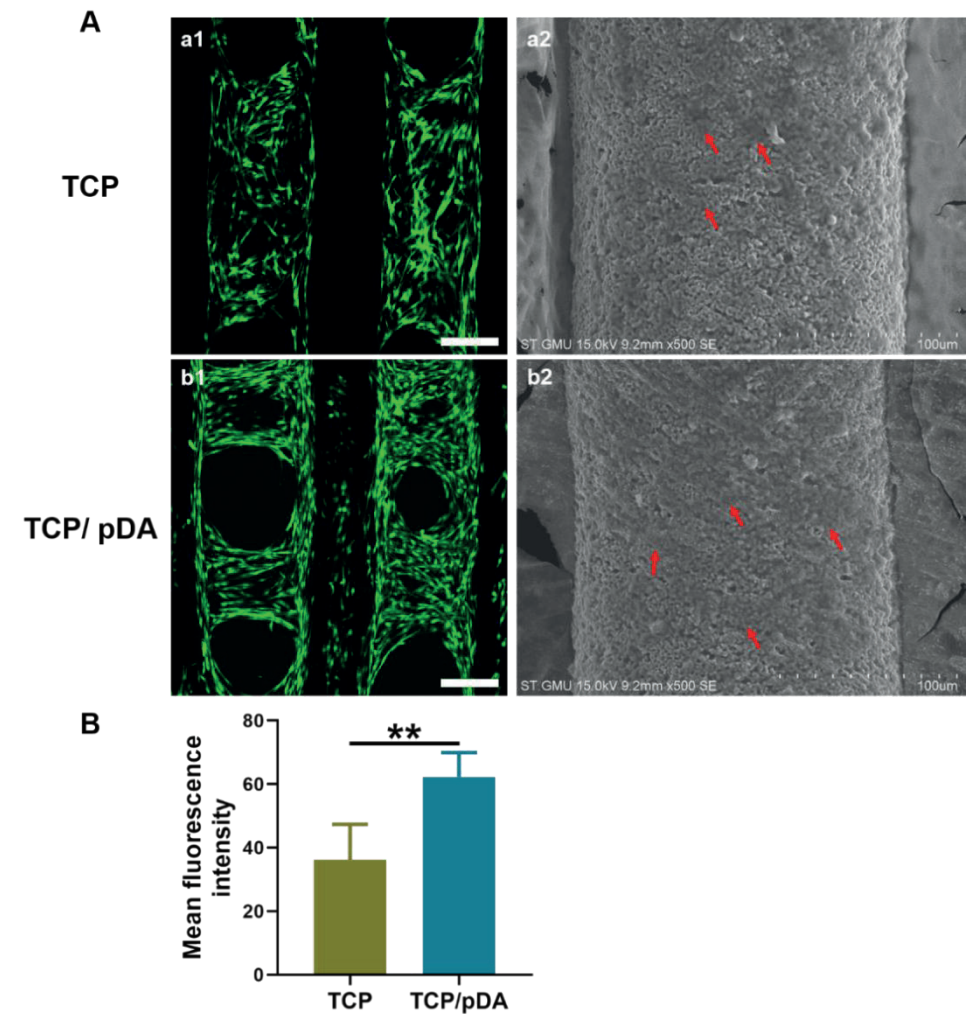


**Figure 4.** A: Live/dead staining and SEM analysis showed excellent biocompatibility of TCP and TCP/pDA scaffolds, on which MC3T3-E1 cells attached and spread along the struts. Red arrows refer to the attached cells. B: Mean fluorescence intensity of live/dead staining. a1–b1, Scale bar = 200  $\mu\text{m}$ . \*\*  $p < 0.01$ .

### 3.3 Immobilization and release kinetics of BMP2

With a prominent osteoinductivity, BMP2 together with absorbable collagen membrane has been used in clinics to promote the repair of bone non-union and spinal fusion in patients [33–35]. Due to a short half-life and rapid dissolution in the

physiological environment, a sustained release profile without burst release of BMP2 is highly needed to increase its osteoinductive efficacy and reduce the dosage. It is well-established that the immobilized BMP2 shows significantly higher osteoinductivity due to the slow delivery than the superficially absorbed BMP2 [36-38]. In our study, the BMP2 loading efficiency of TCP and TCP/pDA scaffolds was  $51.8\% \pm 10.4\%$  and  $89.9\% \pm 3.9\%$ , respectively ( $p < 0.01$ ) (Figure 5A). Besides, TCP/BMP bore a significantly higher release (Figure 5B), of which  $19.8\% \pm 2.1\%$  and  $38.3\% \pm 3.3\%$  BMP2 was released in the first 3 h and 1 day; in contrast, only  $4.3\% \pm 1.1\%$  and  $16.9\% \pm 1.8\%$  BMP2 was released from TCP/pDA/BMP scaffolds. Our result indicated that pDA coating could efficiently immobilize growth factors on TCP scaffolds and significantly reduce the burst release. The loading efficiency and release kinetics were consistent with pDA-coated biphasic calcium phosphate (BCP) granules, where 87% BMP2 is retained on the granules and releases continuously for 30 days [18]. It has been proved that the controlled release of BMP2 shows a significantly lower soft tissue edema when implanted subcutaneously and intramuscularly than the burst release of BMP2 [39, 40]. Therefore, the pDA coating would be beneficial for reducing BMP2-induced edema.

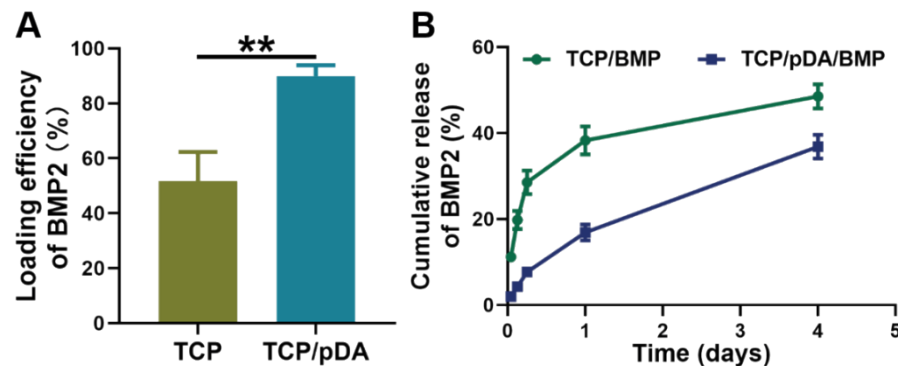


**Figure 5.** The loading efficiency (A) and release kinetics of BMP2 on TCP/pDA and TCP scaffolds (B). \*\*  $p < 0.01$ .

### 3.4 ALP activity and osteogenic genes expression

ALP activity and qRT-PCR assay were conducted to test the bioactivity of

released BMP2. ALP is secreted by osteoblasts and regarded as an early marker of osteogenic differentiation [41]. The TCP/BMP and TCP/pDA/BMP scaffolds bore significantly higher (1.4 and 2.9 times, respectively) ALP activities than pure TCP scaffolds ( $p < 0.01$ ). And the ALP activity of TCP/pDA/BMP scaffolds was also significantly higher (2.1 times) than that of TCP/BMP ( $p < 0.001$ ) (Figure 6A). Meanwhile, the mRNA expression levels of ALP in TCP/BMP and TCP/pDA/BMP scaffolds were significantly higher (2.3 and 4.6 times) than that of pure TCP ( $p < 0.05$ ). And the ALP gene expression of TCP/pDA/BMP scaffolds was also significantly higher (about 2.0 times) than that of TCP/BMP ( $p < 0.01$ ) (Figure 6B). *Osx* is a crucial transcription factor for osteogenic differentiation and bone formation, which is mainly expressed in osteoblasts and osteocytes [42]. *Osx* can induce the expression of mature osteogenic genes, such as COL I and osteocalcin [42]. The mRNA expression levels of *Osx* in TCP/BMP and TCP/pDA/BMP scaffolds were significantly higher (2.2 and 3.3 times, respectively) than in pure TCP scaffolds. TCP/pDA/BMP scaffolds bore a significantly higher (1.5 times) *Osx* expression than TCP/BMP ( $p < 0.05$ ) (Figure 6C). Moreover, COL I plays a key role in the formation of mineralized matrix and constitutes the extracellular matrix of bone tissue [43]. The mRNA expression levels of COL I in TCP/BMP and TCP/pDA/BMP scaffolds were significantly higher (1.4 and 1.6 times, respectively) than in pure TCP scaffolds ( $p < 0.01$ ). TCP/pDA/BMP scaffolds bore a significantly higher (1.2 times) COL I expression than TCP/BMP ( $p < 0.05$ ) (Figure 6D). The significantly higher expression levels of ALP, *Osx*, and COL I mRNAs indicated that TCP/pDA/BMP scaffolds were more advantageous in inducing the osteogenic differentiation of C2C12 than TCP/BMP.

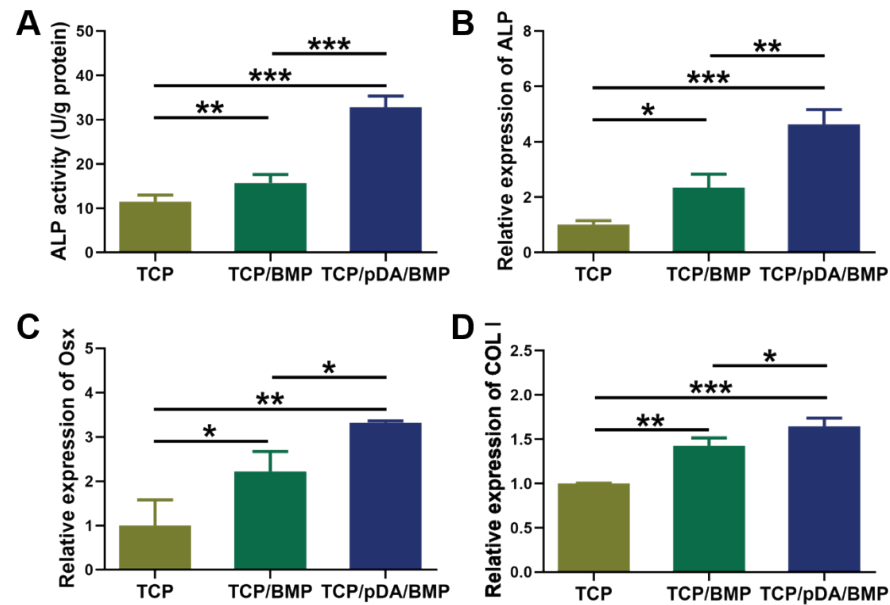


**Figure 6.** Osteogenic differentiation of C2C12 cells after being co-cultured with TCP, TCP/BMP and TCP/pDA/BMP scaffolds for 14 days. A: ALP activity. B–D: Osteogenesis-related genes (ALP, Osx, and COL I) expression levels of TCP, TCP/BMP, and TCP/pDA/BMP scaffolds. \*  $p < 0.05$ , \*\*  $p < 0.01$ , \*\*\*  $p < 0.001$ .

### 3.5 Ectopic new bone formation

Latissimus dorsi muscle is a commonly used bioreactor to prefabricate biomimetic bone grafts for patients [8]. It bears a rich capillary network and blood vessels, which can induce neovascularization of the implanted bone-filling materials. Latissimus dorsi muscle contains the thoracodorsal artery and vein, which can be transferred with bone grafts to provide continuous blood supply [9]. Besides, the abundant musculoskeletal progenitor cells can differentiate into osteoblasts to promote bone regeneration [7]. Furthermore, the implantation-caused injury of muscles will also enable the release of pro-osteogenic growth factors to support the construction of prefabricated biomimetic bone grafts [10]. In our study, new bone tissues formed along the straight struts in both TCP/BMP and TCP/pDA/BMP scaffolds. Plenty of bone lacunae scattered in the pink-stained new

bone tissues (Figure 7A). The quantitative study showed that TCP/pDA/BMP bore significantly higher bone surface area in the inter-strut spaces (2.1 times) than TCP/BMP (Figure 7B), suggesting that prefabricated TCP/pDA/BMP bore a much stronger osteoinductivity than TCP/BMP.

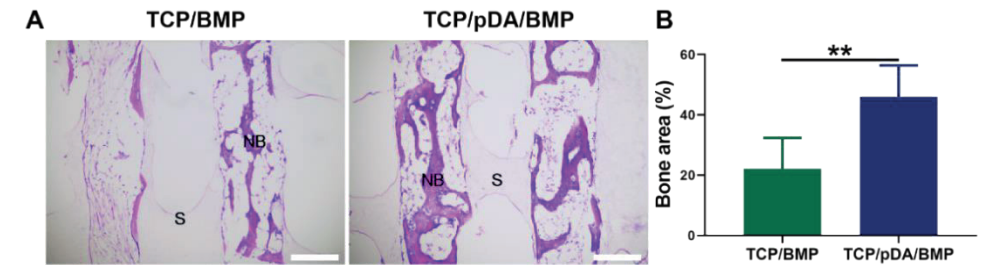


**Figure 7.** Histological analysis of prefabricated biomimetic bone grafts. A: Representative images of H&E staining. B: Quantitative analysis of the percentage of new bone area in inter-strut spaces. NB: New bone. S: Scaffold. Scale bar = 200  $\mu\text{m}$ . \*\*  $p < 0.01$ .

## 4. CONCLUSION

Our study demonstrated that pDA coating was an efficacious method to improve the loading efficacy of BMP2 on 3D printed TCP scaffolds, which could also ensure a slow release profile of the loaded BMP2. Besides, pDA-immobilized BMP2 could significantly promote the osteogenic differentiation of C2C12 and the *in-vivo* bone formation during the prefabrication of biomimetic bone grafts in latissimus dorsi muscle. Our data suggested that the 3D printed TCP scaffolds functionalized with pDA-immobilized BMP2 were promising to prefabricate biomimetic bone grafts to repair large mandibular bone defects.



## REFERENCES

- [1] L.B. Moura, et al., Autogenous Non-Vascularized Bone Graft in Segmental Mandibular Reconstruction: A Systematic Review, *Int J Oral Maxillofac Surg* 45(11) (2016) 1388-1394.
- [2] J. Wiltfang, et al., Man as a Living Bioreactor: Prefabrication of a Custom Vascularized Bone Graft in the Gastrocolic Omentum, *Tissue Eng Part C Methods* 22(8) (2016) 740-746.
- [3] A. Stricker, et al., Resorption of Retromolar Bone Grafts after Alveolar Ridge Augmentation — Volumetric Changes after 12 Months Assessed by CBCT Analysis, *Int J Implant Dent* 7(1) (2021) 7.
- [4] R.D. Foster, et al., Vascularized Bone Flaps Versus Nonvascularized Bone Grafts for Mandibular Reconstruction: An Outcome Analysis of Primary Bony Union and Endosseous Implant Success, *Head Neck* 21(1) (1999) 66-71.
- [5] P.K. Gadre, et al., Nonvascularized Bone Grafting for Mandibular Reconstruction: Myth or Reality?, *J Craniofac Surg* 22(5) (2011) 1727-1735.
- [6] C.E. Zimmermann, et al., Donor Site Morbidity after Microvascular Fibula Transfer, *Clin Oral Investig* 5(4) (2001) 214-219.
- [7] R.L. Huang, et al., Bone Graft Prefabrication Following the *in Vivo* Bioreactor Principle, *EBioMedicine* 12 (2016) 43-54.
- [8] P.H. Warnke, et al., Growth and Transplantation of a Custom Vascularised Bone Graft in a Man, *Lancet* 364(9436) (2004) 766-770.
- [9] M. Zhou, et al., Primate Mandibular Reconstruction with Prefabricated, Vascularized Tissue-Engineered Bone Flaps and Recombinant Human Bone Morphogenetic Protein-2 Implanted *in Situ*, *Biomaterials* 31(18) (2010) 4935-4943.
- [10] M.A. Scott, et al., Brief Review of Models of Ectopic Bone Formation, *Stem Cells Dev* 21(5) (2012) 655-667.
- [11] E.S. Bishop, et al., 3D Bioprinting Technologies in Tissue Engineering and Regenerative Medicine: Current and Future Trends, *Genes Dis* 4(4) (2017) 185-195.
- [12] Y. Bozkurt, E. Karayel, 3D Printing Technology; Methods, Biomedical Applications, Future Opportunities and Trends, *J Mater Res Technol* 14 (2021) 1430-1450.
- [13] S.S. Cao, et al., Prefabricated 3D Printed Tissue-Engineered Bone for Mandibular Reconstruction: A Preclinical Translational Study in Primate, *ACS Biomater Sci Eng* 7(12) (2021) 5727-5738.
- [14] S. Vukicevic, et al., The Clinical Use of Bone Morphogenetic Proteins Revisited: A Novel Biocompatible Carrier Device Osteogrow for Bone Healing, *Int Orthop* 38(3) (2014) 635-647.
- [15] E. Gibon, et al., Inflammation, Ageing, and Bone Regeneration, *J Orthop Translat* 10 (2017) 28-35.
- [16] S. Han, et al., Programmed BMP2 Release from Biphasic Calcium Phosphates for Optimal Bone Regeneration, *Biomaterials* 272 (2021) 120785.
- [17] M. Godoy-Gallardo, et al., Immobilization of BMP2 and VEGF within Multilayered Polydopamine-Coated Scaffolds and the Resulting Osteogenic and Angiogenic Synergy of Co-Cultured Human Mesenchymal Stem Cells and Human Endothelial Progenitor Cells, *Int J Mol Sci* 21(17) (2020) 6418.
- [18] G.H. Lee, et al., Development of BMP2 Immobilized Polydopamine Mediated Multichannelled Biphasic Calcium Phosphate Granules for Improved Bone Regeneration, *Materials Letters* 208 (2017) 122-125.
- [19] J.S. Lee, et al., Polydopamine-Assisted BMP2 Immobilization on Titanium Surface Enhances the Osteogenic Potential of Periodontal Ligament Stem Cells Via Integrin-Mediated Cell-Matrix Adhesion, *J Cell Commun Signal* 12(4) (2018) 661-672.
- [20] S.J. Lee, et al., Surface Modification of 3D Printed Porous Scaffolds Via Mussel-Inspired Polydopamine and Effective Immobilization of rhBMP2 to Promote Osteogenic Differentiation for Bone Tissue Engineering, *Acta Biomater* 40 (2016) 182-191.
- [21] S. Huang, et al., Polydopamine-Assisted Surface Modification for Bone Biosubstitutes, *Biomed Res Int* 2016 (2016) 2389895.
- [22] J. Fan, et al., Polydopamine Meets Porous Membrane: A Versatile Platform for Facile Preparation of Membrane Adsorbers, *J Chromatogr A* 1448 (2016) 121-126.
- [23] X. Zhao, et al., BMP2 Immobilized PLGA/Hydroxyapatite Fibrous Scaffold Via Polydopamine Stimulates Osteoblast Growth, *Mater Sci Eng C Mater Biol Appl* 78 (2017) 658-666.
- [24] S.H. Ku, et al., General Functionalization Route for Cell Adhesion on Non-Wetting Surfaces, *Biomaterials* 31(9) (2010) 2535-2541.
- [25] N. Abbasi, et al., Porous Scaffolds for Bone Regeneration, *J Sci Adv Mater Devices* 5(1) (2020) 1-9.
- [26] C.M. Murphy, F.J. O'Brien, Understanding the Effect of Mean Pore Size on Cell Activity in Collagen-Glycosaminoglycan Scaffolds, *Cell Adh Migr* 4(3) (2010) 377-381.
- [27] Z. Tang, et al., The Material and Biological Characteristics of Osteoinductive Calcium Phosphate Ceramics, *Regen Biomater* 5(1) (2018) 43-59.
- [28] S.K. Lan Levegood, et al., Multiscale Osteointegration as a New Paradigm for the Design of Calcium Phosphate Scaffolds for Bone Regeneration, *Biomaterials* 31(13) (2010) 3552-3563.
- [29] Y.M. Shin, et al., Time-Dependent Mussel-Inspired Functionalization of Poly(L-Lactide-Co-ε-Caprolactone) Substrates for Tunable Cell Behaviors, *Colloids Surf B Biointerfaces* 87(1) (2011) 79-87.
- [30] H. Lee, et al., Mussel-Inspired Surface Chemistry for Multifunctional Coatings, *Science* 318(5849) (2007) 426-430.
- [31] S. Jo, et al., Enhanced Adhesion of Preosteoblasts inside 3D PCL Scaffolds by Polydopamine Coating and Mineralization, *Macromol Biosci* 13(10) (2013) 1389-1395.
- [32] C. Wu, et al., Mussel-Inspired Bioceramics with Self-Assembled CaP/Polydopamine Composite Nanolayer: Preparation, Formation Mechanism, Improved Cellular Bioactivity and Osteogenic Differentiation of Bone Marrow Stromal Cells, *Acta Biomater* 10(1) (2014) 428-438.
- [33] R. Aryal, et al., Bone Morphogenetic Protein-2 and Vascular Endothelial Growth Factor in Bone Tissue Regeneration: New Insight and Perspectives, *Orthop*



Surg 6(3) (2014) 171-178.

[34] M.C. Simmonds, et al., Safety and Effectiveness of Recombinant Human Bone Morphogenetic Protein-2 for Spinal Fusion: A Meta-Analysis of Individual-Participant Data, *Ann Intern Med* 158(12) (2013) 877-889.

[35] P. Haubruck, et al., Comparison of the Clinical Effectiveness of Bone Morphogenetic Protein (BMP) -2 and -7 in the Adjunct Treatment of Lower Limb Nonunions, *Orthop Traumatol Surg Res* 104(8) (2018) 1241-1248.

[36] Y. Liu, et al., Delivery Mode and Efficacy of BMP2 in Association with Implants, *J Dent Res* 86(1) (2007) 84-89.

[37] T. Liu, et al., Deproteinized Bovine Bone Functionalized with the Slow Delivery of BMP2 for the Repair of Critical-Sized Bone Defects in Sheep, *Bone* 56(1) (2013) 110-118.

[38] G. Wu, et al., The Effect of a Slow Mode of BMP2 Delivery on the Inflammatory Response Provoked by Bone-Defect-Filling Polymeric Scaffolds, *Biomaterials* 31(29) (2010) 7485-7493.

[39] K.B. Lee, et al., Bone Morphogenetic Protein-Binding Peptide Reduces the Inflammatory Response to Recombinant Human Bone Morphogenetic Protein-2 and Recombinant Human Bone Morphogenetic Protein-7 in a Rodent Model of Soft-Tissue Inflammation, *Spine J* 11(6) (2011) 568-576.

[40] C.E. Taghavi, et al., Bone Morphogenetic Protein Binding Peptide Mechanism and Enhancement of Osteogenic Protein-1 Induced Bone Healing, *Spine (Phila Pa 1976)* 35(23) (2010) 2049-2056.

[41] S. Trivedi, et al., A Quantitative Method to Determine Osteogenic Differentiation Aptness of Scaffold, *J Oral Biol Craniofac Res* 10(2) (2020) 158-160.

[42] Q. Liu, et al., Recent Advances of Osterix Transcription Factor in Osteoblast Differentiation and Bone Formation, *Front Cell Dev Biol* 8 (2020) 601224.

[43] M. Farea, et al., Synergistic Effects of Chitosan Scaffold and TGF- $\beta$ 1 on the Proliferation and Osteogenic Differentiation of Dental Pulp Stem Cells Derived from Human Exfoliated Deciduous Teeth, *Arch Oral Biol* 59(12) (2014) 1400-1411.

## CHAPTER 6

Development and fabrication of co-axially electrospun biomimetic periosteum with a decellularized periosteal ECM shell/PCL core structure to promote the repair of critical-sized bone defects

Shuyi Li<sup>#</sup>, Rongli Deng<sup>#</sup>, Xuenong Zou, Qiong Rong, Jiali Shou, Zilong Rao, Wanqiu Wu, Gang Wu, Daping Quan, Miao Zhou, Tim Forouzanfar

*Composites Part B: Engineering*, 2022, 234:109620.

## ABSTRACT

Periosteum is crucial to the initial healing of bone defects because it provides a stable periosteum-specific microenvironment and abundant osteogenic cells towards bone repair. However, the usage of autologous periosteum is restricted by limited availability. Xenogeneic decellularized periosteum (DP) preserves periosteum-specific cues, but the hardly-controlled physicochemical properties make it inconvenient to use widely. Our study aimed to fabricate a tissue-engineered periosteum (TEP) with a continuous periosteum-specifically bioactive surface and tailored physicochemical properties by co-axial electrospinning of poly( $\epsilon$ -caprolactone) (PCL)/periosteal decellularized extracellular matrix (dECM) to promote bone defects healing. Initially, DP was confirmed for effective removal of residual DNA and well preservation of biological components, e.g., collagen and glycosaminoglycans. After optimization of fabrication processes, PCL/dECM co-axially electrospun membrane (PEC) bore an exquisite core-shell structure, which was effectively equipped with composite advantages of dECM and PCL. Notably, PEC stood out in terms of tensile strength and long-term durability within a physiological environment compared to that of the dECM uniaxial electrospun membrane (ECM). Besides, PEC bore significantly higher cell proliferation, bio-mineralization, and osteogenic properties than the PCL membrane. Moreover, PEC-TEP could significantly enhance the recovery of critical-sized bone defects in rats than that of PCL-TEP. To the best of our knowledge, biomimetic PEC-TEP was fabricated and used for the first time to repair bone defects. This novel strategy was promising to fabricate a dECM-based advanced membrane for tissue engineering and regenerative medicine.

**Keywords:** Tissue-engineered periosteum; Co-axially structured fibers; Decellularized extracellular matrix; Poly( $\epsilon$ -caprolactone); Critical-sized bone defect.

## 1. INTRODUCTION

Periosteum is a fibrous connective tissue membrane covering most of the outer surface of bone and is responsible for regulating bone development, regeneration, and remodeling [1, 2]. Periosteum is comprised of two distinct layers: a superficial fibrous layer and an inner cambium layer. The fibrous layer consists of highly organized and directionally aligned collagen and elastin fibers, which form the biological basis for the mechanical stability of periosteum [3] and possesses extracellular matrix (ECM) of fibroblasts [4]. The cambium layer serves as a reservoir of osteogenic cells, such as skeleton stem cells and osteoprogenitor cells [2, 4], which bear a comparable bone-forming efficiency with bone marrow mesenchymal stem cells (BMSCs) [5]. Furthermore, the ECM in the cambium layer provides a three-dimensional (3D) microenvironment with tissue-specific paracrine growth factors, which coordinately regulate many biological functions of periosteum-derived cells (PDCs) [6, 7]. For example, as a major biological event of the periosteal response to acute bone fracture, PDCs proliferate, migrate and differentiate into osteoblasts and chondrocytes to promote callus formation and bone healing by intramembranous and endochondral ossification [8]. The importance of periosteum for bone regeneration is further highlighted by the fact that the absence of periosteum significantly attenuates the healing efficacy of not only bone fractures [9] but also critical-sized diaphyseal defects [10]. Consequently, autologous transplantation of free periosteum has been adopted to accelerate bone regeneration and re-union of rabbit's segmental bone defect [11]. Consistently, a series of clinical trials have revealed that periosteal flaps can significantly enhance the healing of bone defects and the integration of bone graft to host bone tissue [12]. However, the usage of autologous periosteum is restricted by its limited availability and donor site morbidity. Therefore, continuous efforts have been taken to develop a tissue-engineered periosteum (TEP) to promote the healing of critical-sized bone defects [7, 13, 14].

An ideal TEP for promoting the osseous healing of bone defects should largely bio-mimic the major biological functions of periosteum. Firstly, TEP should bear certain mechanical stiffness to cover bone defects and stabilize bone grafts for a certain period (> 1 month) so as to provide a mechanically stable microenvironment

for bone regeneration [15, 16]. Secondly, TEP should also act as a reservoir to accommodate stem cells that can migrate, proliferate and differentiate into osteoblasts [7]. Thirdly, TEP should provide biocompatible and bioactive niches to stimulate osteogenic activities of the stem cells. One of the promising engineering techniques to synthesize TEP is electrospinning, which can produce periosteum-like membranes with controllable and even individualized shape and size. Furthermore, electrospun membranes bear micro- to nano-sized fibers, presenting a structurally-biomimetic and hierarchically-porous structure to facilitate cell migration and proliferation. Its high surface-to-volume ratio avails cell attachment and nutrition transportation [17]. In order to fabricate electrospun periosteum with sufficient mechanical strength, it is common to adopt synthetic polymeric materials, such as poly( $\epsilon$ -caprolactone) (PCL), poly(lactic-co-glycolic acid) (PLGA) [18], and poly(lactic acid) (PLA) [19]. Among them, PCL shows good biocompatibility, adjustable biodegradability, excellent mechanical ability, high tailorability as well as good rheological and viscoelastic properties. Furthermore, PCL has been approved by the US Food and Drug Administration (FDA) to be used in humans. These properties make PCL a very promising electrospinning material for biomedical applications [20-22]. However, PCL is hydrophobic and bears neither intrinsic adhesion motifs to enhance cell attachment, nor bioactive agents to promote osteogenic differentiation [23, 24]. Consequently, natural bioactive polymers (e.g., collagen, gelatin, and chitosan) and bioceramic biomaterials (e.g., hydroxyapatite and tricalcium phosphate) have been incorporated in PCL to improve its surface activities [25-27]. Collagen/gelatin can increase the hydrophilicity of PCL membrane and provide binding sites for cell attachment [28]. Meanwhile, the bioceramic materials which mimic components of bone tissue can provide essential ions for bone regeneration [29]. Though these composite membranes have improved physicochemical properties and osteoconductivity, they lack periosteum-specific niches to regulate cellular activities and are hard to realize genuine biomimetic periosteum in composition.

Tissue-derived ECM consists of multiple natural polymers (e.g., collagen, elastin, and fibrinogen) and various active macromolecules (e.g., growth factors, peptides, glycoproteins, and proteoglycans), which can interact with receptors on

the cell surface [30] and mitigate foreign body response [31]. It can be used as a vascular/bone graft [32], promoting regeneration of cardiac tissue, skeletal muscle, and skin [33]. ECMs from different sources have unique structures and compositions, which can provide a tissue-specific microenvironment for cells with biological and chemical cues to regulate cellular activities [34]. Decellularized ECM (dECM) from xenogeneic decellularized periosteum (DP) can maximally (more than 50%) preserve periosteum's ultrastructure and biological compositions [35, 36]. These preserved biological compositions are capable of accelerating the healing efficacy of critical-sized bone defects [37] and inducing bio-mineralization thereon-seeded MSCs ectopically in nude mice [38]. DECM can provide periosteum-specific niches for cells. However, as other natural materials, the hardly-controlled shape, intactness, uniformity, and size render DP inconvenient to fit various bone defects in clinics. DECM from DP needs to be modified especially the mechanical property and degradability [33]. Thus, to develop a TEP with biomimetic periosteal compositions and properties, it's necessary to study 1) whether dECM from DP can be used for electrospinning to overcome the aforementioned drawbacks; 2) whether it can be used with PCL to adjust the resultant TEP's physicochemical and biological properties.

ECM that is derived from decellularized tissues [39-41] and cells [42, 43] is usually blended with PCL for electrospinning to achieve biomimetic and bioactive tissue-engineered constructs to promote regeneration of various tissues. ECM from decellularized muscle has been reported to be electrospun alone or combined with PCL to build tissue-engineered muscle tissue [40]. The PCL/ECM-blended electrospun membrane shows both dramatically improved tensile strength than pure ECM-electrospun membrane and significantly enhanced bioactivity than pure PCL-electrospun membrane [40, 41]. Albeit so, the PCL/ECM compositions-blended electrospinning also bears a series of drawbacks in both the fabrication process and biological properties. For example, blended electrospinning frequently suffers from phase separation of PCL and ECM compositions, leading to deteriorated fiber morphology, non-uniform structure, and weak strength [44-46]. Although PCL is a biocompatible material, its bioinert composition may negatively affect cell viability due to the presence of PCL on the surface of blended electrospun

materials [47]. Consequently, an ideal electrospun TEP should bear a fiber surface with maximal ECM component and synthetic polymeric material being wrapped inside, so as to achieve optimal mechanical strength, biocompatibility, and bioactivity. In contrast to blended electrospinning, co-axial electrospinning fabricates core-shell structured fibers by separate channels, avoiding the contact and immiscibility of different compositions. The core and shell materials can mutually promote the electrospinnabilities of each other, extending the range of biomaterials and solvents used for electrospinning [48]. Besides, different characteristics of the core and shell materials endow the final core-shell fiber with a combination of their physicochemical properties, which can also be regulated separately by their respective channels. For example, the composite layered fiber has a bioactive shell reinforced by a core material [49], or a biodegradable shell stabilized by a core material [50]. So far, co-axial electrospinning hasn't been used to fabricate TEP using dECM. The electrospinnability and necessity of combining synthetic polymers with dECM remain to be validated.

We hypothesized that the adoption of co-axial electrospinning using dECM from DP as shell material and PCL as core material could ensure the fabrication of TEP with both a complete periosteum-specifically bioactive surface to recruit MSCs and regulate their bioactivities and a tailored core to regulate mechanical strength and degradation rate. In this study, biological safety and preservation of functional components in DP were examined initially, followed by an optimization study to fabricate the PCL/dECM co-axially electrospun membrane (PEC) and dECM uniaxial electrospun membrane (ECM), while electrospun PCL membrane was as a control. Subsequently, the physicochemical and biological properties of the membranes were evaluated by a series of *in-vitro* and *in-vivo* studies to determine the feasibility of the biomimetic periosteum to repair bone defects.

## 2. MATERIALS AND METHODS

### 2.1 Harvest and decellularization of porcine periosteum

Fresh adult porcine legs were collected from a local slaughterhouse. Periosteum were harvested from femoral bones and the harvested tissues were thoroughly washed by ultrapure water before being subjected to decellularization under

sterilized conditions. The periosteal tissues were successively treated with 1% Triton X-100 for 10 h, 1% sodium dodecyl sulfate (SDS, Sigma-Aldrich, USA) for 2 h, and 50 U/mL DNase (Sigma-Aldrich, USA) overnight under 100 rpm oscillation at room temperature. After each step, the tissues were rinsed three times with ultrapure water. The resultant DPs were sent for characterization before being used to fabricate TEP.

### 2.2 Characterization of the decellularized periosteum

For histological and immunohistochemistry (IHC) analyses, the specimens were fixed in 10% neutral buffered formalin solution for 24 h, followed by dehydration in a gradient series of dehydrating solvents, embedding in paraffin and microtome (5- $\mu$ m slices). Hematoxylin and eosin (H&E) staining was performed to observe the overall structure and cellular components within the decellularized tissues.

#### 2.2.1 Total DNA content analysis

DAPI staining was performed to qualitatively detect a successful removal of nuclei. Total DNA content was quantitatively estimated to satisfy the limits of the residual DNA content (< 50 ng/mg) of the decellularized tissue [51]. DNA contents in periosteum and DPs were examined by Quant-iT™ PicoGreen™ dsDNA Reagent (Invitrogen, USA) according to the manufacturer's instructions (n = 3). Briefly, the lyophilized periosteum and DP tissues of constant weight were digested with Proteinase K at 56 °C until no visible materials were left. The samples were thereby purified with the TIANamp Genomic DNA kit (Tiangen, China) and incubated with Picogreen for 5 min. Total DNA content was estimated by a microplate reader (Synergy™ HTX, Biotek, USA) (excitation wavelength: 485 nm; emission wavelength: 528 nm).

#### 2.2.2 Assessment of collagen

The specimens were subjected to Masson trichrome staining and IHC of collagen type I (COL I) to evaluate the residual collagen and its ultrastructure. For IHC staining, mouse anti-collagen type I primary antibody (1:1000, Abcam, Cambridge, MA) and goat anti-mouse secondary antibody (1:200, Servicebio, China) were used.

Collagen content was quantitatively assessed on the basis of standard



collagen bearing a collagen (mg dry weight) to hydroxyproline (Hyp) ratio of 7.2:1 [36]. The Hyp content was estimated by a hydroxyproline assay kit (Nanjing Jiancheng Bioengineering Institute, China) according to the manufacturer's instructions ( $n = 3$ ). Briefly, lyophilized periosteum and DP of equivalent weights were separately mixed with 1 mL hydrolysate and incubated at 95 °C for 4 h. Indicator solution (10  $\mu$ L) and solution A (1 mL) were added and the color of the mixed solution turned red. PH of the solution was then adjusted with solution B progressively until the red color turned yellow-green. The aforementioned solutions were diluted with ultrapure water until the final volume was 10 mL. After centrifugation, 1 mL of the supernatant was sent to test and the absorbance was measured at 550 nm by the microplate reader.

### 2.2.3 Evaluation of glycosaminoglycans (GAGs)

Safranin O staining was performed for the qualitative detection of GAGs. For quantitative detection, 1, 9-dimethyl methylene blue (DMMB) (Genmed, USA) colorimetric assay was performed ( $n = 3$ ) according to the manufacturer's protocol. Equivalent weights of periosteum and DP were digested and extracted with Genmed extraction solution, followed by an incubation at 56 °C for 16 h and 90 °C for 10 min. The mixed solutions were further incubated with a staining solution for 30 min. Final supernatants were harvested and reacted with the dissociation solution for 5 min. The absorbance was measured at 656 nm by the microplate reader. The standard curve was established with serial dilutions of the Genmed standard solution.

### 2.2.4 Evaluation of fibronectin

IHC staining of fibronectin was carried out using rabbit polyclonal fibronectin primary antibody (1:500, Abcam Cambridge, MA) and goat anti-rabbit secondary antibody (1:200, Servicebio, China).

## 2.3 Fabrication of TEPs

After lyophilization, milk-white DP tissues were milled and sieved to harvest DP powder of particle diameter of less than 425  $\mu$ m. 5% (w/v) DECM shell solution was prepared by dissolving 500 mg DP powder in 10 mL hexafluoroisopropanol (HFIP) (Aladdin, China) under magnetic stirring for 6 days at 4 °C (Figure 1A). The resultant dECM solution had no visible particles. Similarly, the core solution of PCL

was prepared by dissolving PCL ( $M_w = 80,000$ ) granules in HFIP with a final concentration of 12% (w/v). To prepare the PEC, the aforementioned solutions were transferred to two separate 10 mL syringes loaded on a syringe pump. Electrospinning was carried out through a co-axial spinneret (outer: 16 G, inner: 22 G) at a 1 mL/h constant flow rate of PCL solution and 1, 1.5, 2, 2.5, 3, 3.5 mL/h gradient flow rates of dECM solution (i.e., dECM1, dECM1.5, dECM2, dECM2.5, dECM3, dECM3.5). Different voltages were applied to optimize the fabrication parameters of PEC (Figure 2A). DECM solution was used to fabricate ECM with a voltage of 12.4 kV and a flow rate of 2.5 mL/h. PCL membrane (voltage: 12.18 kV; flow rate: 2 mL/h) was also fabricated for comparison.

During the electrospinning process (25 °C, 40–50% humidity), the fibers were collected at a distance of 10 cm from the spinneret and the collector which was wrapped by aluminum foil. A deposition time of 1.5 h was maintained for all the membranes to ensure similar thickness. For *in-vitro* analysis, the electrospun membranes were collected on glass coverslips of different sizes to fit into 48-, 24- and 6-well culture plates. After fabrication, the membranes were vacuum-dried for 24 h and crosslinked by 25% glutaraldehyde vapor for 48 h. For further aseptic studies, the membranes were soaked in 75% ethanol for 3 h followed by an overnight UV sterilization.

## 2.4 Characterizations of the TEPs

### 2.4.1 Microstructure and chemical analyses

The microstructures and cross-sectional images of PCL, ECM, and PEC were examined using scanning electron microscopy (SEM, S3400N, Hitachi, Japan). Before observation, the specimens were lyophilized and sputter-coated with Au-Pd plasma. Core-shell configurations of PEC fibers were analyzed using transmission electron microscopy (TEM, JEM-1400, JEOL, Japan). Average diameters (AD) of PEC fibers prepared at various conditions were analyzed using SEM by the measurement of total 80 fibers in each group. In addition, an elemental profile of dECM shell of PEC was analyzed using X-ray photoelectron spectroscopy (XPS, ESCALAB 250, Thermo-VG Scientific, England). The presence of collagen and GAGs after electrospinning was analyzed using H&E, Masson trichrome, and Safranin O staining. Furthermore, the wettability of the samples was evaluated by

water contact angle (WCA) measurement using the sessile drop technique ( $n = 5$ ).

#### **2.4.2 Mechanical properties**

Uniaxial tensile strength of the electrospun membranes (dry and wet) was measured by a universal mechanical machine (MTS CMT6103, USA) at a load of 50 N. Periosteum and electrospun membranes ( $n = 3$ ) were cut into a dumbbell-like shape. Samples for mechanical tests in wet conditions were immersed in 10% phosphate-buffered saline (PBS) for 24 h. After that, the samples were clamped at a 2-cm distance and pulled longitudinally at a 2 mm/min rate until rupture. The stress-strain curve was obtained from the load-displacement measurements and Young's modulus was calculated from the slope. Ultimate tensile strength (UTS) and elongation at break were also analyzed.

#### **2.4.3 Degradation study**

PCL, ECM, and PEC ( $n = 3$ ) were incubated in 10% PBS statically at 37 °C for 4 weeks under aseptic conditions. The degradation medium was changed every 3 days. At the predetermined time points (0.5, 1, 2, 3, 7, 14, and 28 d), the medium was removed gently and the membranes went through a thorough wash to remove the absorbed ions. Finally, the membranes were lyophilized and weighed. The degradation kinetics curve was obtained by plotting the percentage ratio of the final weight to the initial weight at different time points. Furthermore, morphological changes were observed using SEM.

#### **2.4.4 Acellular mineralization**

To evaluate the mineralization potential of the electrospun membranes, modified simulated body fluid (mSBF) was prepared as a mineralization medium [32]. PCL, ECM, and PEC were immersed in mSBF for 20 days with a medium change every alternative day. SEM and energy dispersive X-ray spectroscopy (EDS) were used to assess morphological changes and elemental analyses. The extent of mineralization was also evaluated by alizarin red S staining (ARS). Briefly, the samples were fixed in 4% paraformaldehyde solution before being incubated with ARS solution (0.2%, pH 8.3) for 15 min. After that, the samples were washed with ultrapure water to remove non-specific staining. The final images were captured by a stereomicroscope (Leica, Germany).

### **2.5 In-vitro cell culture study**

#### **2.5.1 Isolation and characterization of human bone marrow mesenchymal stem cells (hBMSCs)**

The bone marrow blood was kindly provided by Prof. Xuenong Zou (The First Affiliated Hospital of Sun Yat-sen University) [52]. Informed consent was obtained from the patients for bone marrow blood collection and all the procedures were conducted in accordance with the approval of the Ethics Committee at the First Affiliated Hospital of Sun Yat-sen University (2016130). Bone marrow blood was collected from the drilling holes of the pedicle during the internal spine fixation operations of 3 patients (male, age of  $44 \pm 10$ ) with lumbar spondylolisthesis. After centrifugation (500 g, 5 min), the upper layer of serum and fat was removed and the residual bone marrow was mixed with Ficoll-Paque separation medium. After another centrifugation at 800 g for 30 min, a cells' layer like white mist was observed between the upper and middle layer, which was transferred and centrifuged again for cell pelletization. The pellets were cultured in a specialized hBMSCs culture medium (Cyagen Biosciences, USA) and transferred to a T25 flask for culturing at 37 °C with 5% CO<sub>2</sub>. The medium was changed after 3 days to remove unattached cells and twice a week thereafter. When the cells reached a confluence of 80–90%, they were trypsinized, counted, and passaged at a density of  $2-3 \times 10^5$  per T25 flask. Cells from passage 4–5 were used for subsequent studies.

For identification of hBMSCs,  $6 \times 10^5$  cells dispersed in 10% PBS (containing 5% fetal bovine serum (FBS)) were incubated with monoclonal antibodies CD73, CD90, CD45, and CD34 and analyzed by flow cytometry (BD FACSCanto II, USA) according to a protocol reported elsewhere [53].

#### **2.5.2 Cytocompatibility study and cell proliferation**

To validate whether there was toxic residue left affecting the viability and metabolic activity of hBMSCs, a live/dead staining and Alamarblue assay were performed. For live/dead staining,  $2 \times 10^5$  hBMSCs were seeded on the membranes and cultured for 3 days. The cell-laden samples were incubated with a live/dead staining kit (BestBio, China) according to the manufacturer's instructions. The final images were captured by a confocal laser scanning microscope (CLSM, Leica, Germany).

Alamarblue assay was performed to assess the metabolic activity of cultured hBMSCs. Briefly,  $2 \times 10^4$  hBMSCs were seeded on the membranes in 48-well culture plates and incubated with 5% CO<sub>2</sub> at 37 °C. The culture medium was replaced every 3 days. On the 1<sup>st</sup>, 3<sup>rd</sup>, 5<sup>th</sup>, and 7<sup>th</sup> day, Alamarblue solution was added to the culture medium at the ratio of 1:10 (v/v). After the incubation at 37 °C for 3.5 h, the optical density (OD) was measured at 570 nm and 600 nm by the microplate reader. The rate of cell proliferation was estimated according to the manufacturer's protocol.

### 2.5.3 Cytoskeletal staining

$1.3 \times 10^4$  hBMSCs were seeded on the membranes and cultured for 3 days. After that, the cells were fixed in 4% paraformaldehyde solution for 15 min followed by PBS washing. The samples were further incubated with 0.1% Triton X-100 solution for permeabilization and rhodamine phalloidin-labeled FITC solution (Cytoskeleton, USA) for 30 min. After PBS washing, the samples were incubated with DAPI solution for 5 min to stain the nuclei. The final images were captured by the CLSM. The cell morphologies on various membranes was also observed using SEM.

## 2.6 In-vitro osteogenic activity

### 2.6.1 Alkaline phosphatase (ALP) activity and ARS test

ALP and ARS tests were performed to evaluate early and mature osteogenesis of the cultured hBMSCs on electrospun membranes. When the cells reached 80% confluence, the culture medium was replaced with osteogenic medium (OM), which was composed of high glucose Dulbecco's modified Eagle medium (DMEM), 10% FBS, 1% penicillin-streptomycin, 100 nmol/L dexamethasone, 10 mmol/L  $\beta$ -glycerophosphate, and 50  $\mu$ g/mL L-ascorbic acid. After 3 days' co-culture, ALP activity was evaluated by an ALP quantification kit (Nanjing Jiancheng Bioengineering Institute, China) and normalized by the protein content. After 21 days' co-culture, an ARS test was performed with the aforementioned procedures. For quantification analysis, 10% hexadecyl pyridinium chloride monohydrate (CPC) was applied to dissolve the mineralized nodules. The colorimetric absorbance was measured at 562 nm by the microplate reader.

### 2.6.2 Quantitative reverse transcription-polymerase chain reaction (qRT-PCR)

After being cultured in OM for 14 days, the total RNA of the cells was extracted by TRIzol (Invitrogen, USA) and quantified by Nanodrop 2000 Spectrophotometer (Thermo Fisher Scientific, USA). Furthermore, cDNA synthesis and RT-PCR analysis were performed according to the protocol reported elsewhere [53]. The expression levels of osteogenesis-related genes (bone morphogenetic protein-2/BMP2, runt-related transcription factor 2/RUNX2, ALP, and COL I) were calculated by  $2^{-\Delta\Delta C_t}$  and normalized by the housekeeping gene of GAPDH. The gene-specific primer sequences were listed in Supplemental Table 1.

**Supplemental table 1.** The sequences of primers used for qRT-PCR analysis.

No.	Primer name	Sequences
1	BMP2	sense: GGGAGAAGGAGGAGGCAAAGAA antisense: CTGGGGAAGCAGCAACGCTA
2	RUNX2	sense: TACTATGGCACTTCGTCAGGA antisense: GATTCATCCATTCTGCCACTA
3	ALP	sense: GGCTGTAAGGACATCGCCTA antisense: GGGTCAAGGGTCAGGAGTTC
4	COL I	sense: CGATGGATTCCAGTTCGATGTGGT antisense: TGTTCTTGCAAGTGGTAGGTGATG
5	GAPDH	sense: GCACCGTCAAGGCTGAGAAC antisense: TGGTGAAGACGCCAGTGGA

## 2.7 Recovery of critical-sized bone defects

Before *in-vivo* implantation study, the aseptic membranes ( $\phi = 8$  mm) were seeded with  $2 \times 10^5$  hBMSCs and cultured for 3 days in OM with 5% CO<sub>2</sub> at 37 °C. The animal study was performed according to the principles and procedures of the National Institutes of Health Guide for the care and use of laboratory animals. The experimental protocol was approved by the Ethics Committee of Guangdong Institute of Medical Devices (JL03303).

Nine male Sprague-Dawley rats (12 weeks, weight of 250-300 g) were included for the *in-vivo* study. Before the study, the skull hair was removed and the skin was sterilized after general anesthesia by giving pentobarbital sodium (30 mg/kg) injection intraperitoneally. The soft tissue was cut along the middle line and

bluntly separated to completely expose the operation area. After removal of the periosteum, critical-sized bone defects were made bilaterally using a trephine burr ( $\varphi = 5$  mm). PCL, ECM, and PEC ( $n = 6$ ) were overlaid on the defect regions with the hBMSCs-laden surfaces facing bone defects (Figure 7A). Finally, the wound was closed by a layer-by-layer strict closure. Penicillin 400 000U was injected intramuscularly for 3 days post-operatively and cyclosporine (10 mg/kg) was fed with water continuously. Four weeks post-implantation, the animals were euthanized with isoflurane (Yipin, China). The harvested calvarial specimens were fixed in 10% neutral buffered formalin solution for 24 h before radiographic and histological examinations.

### 2.7.1 Micro-CT

The radiographic raw data of the calvarial specimens were obtained from micro-CT (SkyScan1172, Bruker, Belgium). The scanning parameters were as follows: the aluminum filter of 1-mm thickness, a spatial resolution of  $2000 \times 1332$ , and pixel size of 9  $\mu\text{m}$ . The obtained data were reconstructed by NRecon 1.0 and analyzed by CTAn 1.13 software after selecting the region of interest (ROI) by Dataviewer. New bone volume and mineralization volume of the membranes were calculated and compared.

### 2.7.2 Histological analysis

The calvarial specimens were decalcified with 10% EDTA solution at 37 °C for nearly 2 months. H&E, Masson trichrome, and IHC staining of osteopontin (OPN) (1:500, Servicebio, China) were performed to evaluate new bone formation as well as the structures of the residual membranes. Imaging of histological specimens after staining was performed using an optical microscope (Leica, Germany). Membrane breakage and average thickness were analyzed by ImageJ (National Institutes of Health, USA) while the percentage of the bone area was calculated by Image Pro Plus (Media Cybernetics, Silver Spring, MD). Six areas were randomly selected for quantification.

### 2.8 Statistical analysis

Data were presented as mean  $\pm$  standard deviation (SD). The difference between two studied groups was assessed by Student's t-test. And significant difference among three groups was detected by one-way ANOVA via IBM SPSS

Statistics (version 20.0, SPSS Inc., IL, USA). A value of  $P < 0.05$  was considered to be statistically significant.

## 3. RESULTS

### 3.1 Characterizations of the decellularized periosteum

In histological images, periosteum (Figure 1B a1) displayed distinct fibrous and cambium layers (divided by a dark dotted line). In contrast, DP exhibited similar structures with loose and porous morphology (Figure 1B b1). The nuclei components in periosteum appeared as blue-black spots after H&E staining and they were absent in DP samples. Further evidence of immunofluorescent staining of DAPI showed no visible blue-stained nucleic acid in DP (Figure 1B b2) when compared with periosteum (Figure 1B a2). There was a significant decrease of DNA content from  $780.94 \pm 63.50$  ng/mg dry weight of periosteum to  $36.17 \pm 10.03$  ng/mg dry weight of DP ( $p < 0.001$ ), indicating elimination of over 95% DNA from DP samples (Figure 1C) and it satisfies the FDA standard for the decellularized tissue [51].

As the main functional components in ECM, collagen and GAGs were qualitatively and quantitatively analyzed. The majority of collagen fibrils remained intact as revealed from Masson trichrome staining and IHC of COL I in both periosteum and DP samples (Figure 1B & Figure S1). There was no significant difference ( $p > 0.05$ ) in collagen content between DP and periosteum ( $351.58 \pm 43.12$   $\mu\text{g}/\text{mg}$  and  $359.38 \pm 21.85$   $\mu\text{g}/\text{mg}$ , respectively) (Figure 1D). A similar result was also found in the case of another bioactive molecule, fibronectin (Figure S1). Safranin O staining and GAGs quantification (Figure 1B & E) revealed that there was some loss of GAGs in DP ( $9.24 \pm 0.71$   $\mu\text{g}/\text{mg}$  of periosteum and  $5.45 \pm 0.78$   $\mu\text{g}/\text{mg}$  of DP) ( $p < 0.01$ ).



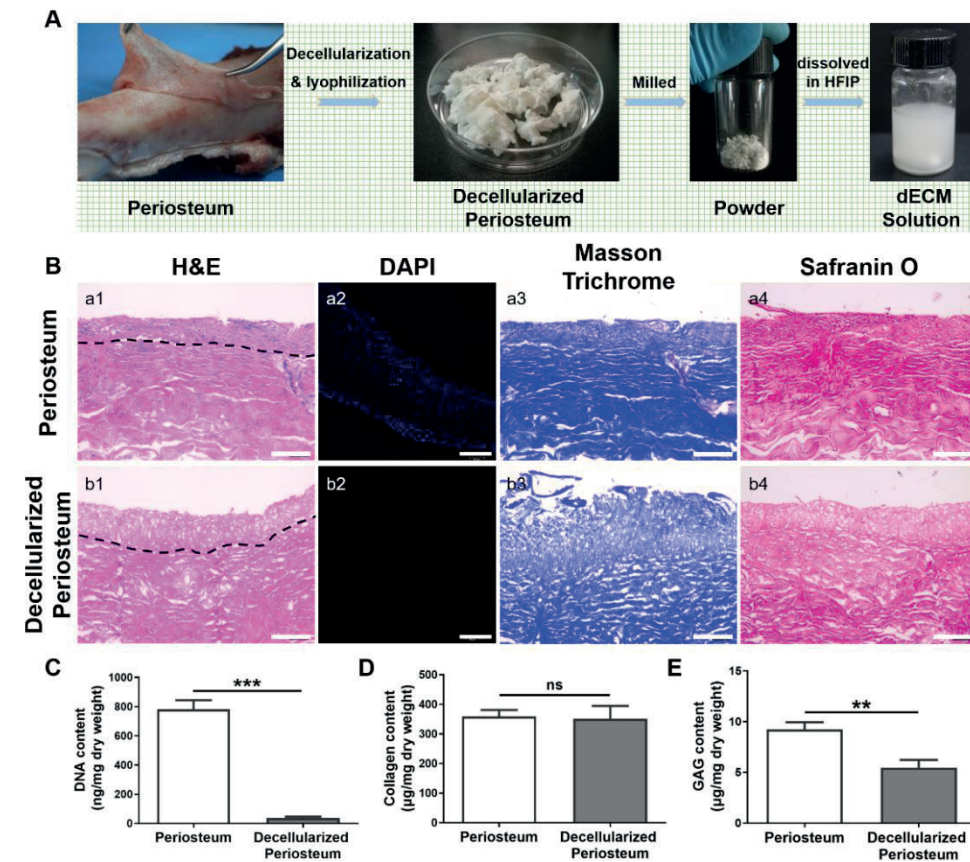
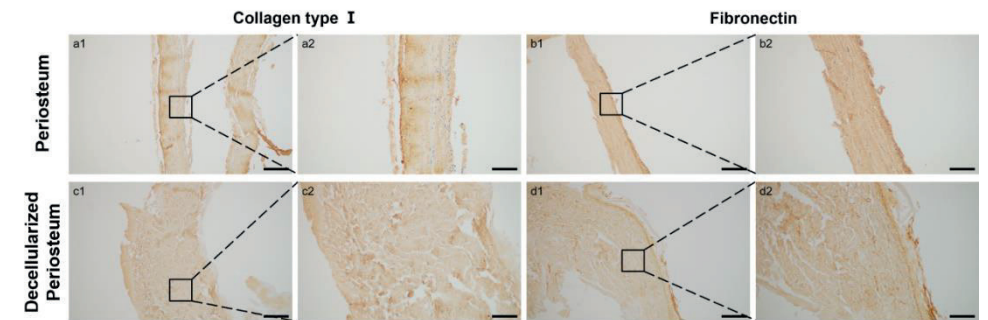


**Figure 1.** A: Schematic representation of harvesting periosteum and preparing decellularized extracellular matrix (dECM) solution from decellularized periosteum for electrospinning. B: Comparative study of periosteum and decellularized periosteum by histological analyses. H&E staining (a1–b1) and (a2–b2) DAPI staining demonstrated a successful removal of cellular components, which was further validated by (C) DNA content quantification. Black dotted lines in a1 and b1 indicate the boundary between the fibrous layer (top) and the cambium layer (bottom). a3–b4: Distributions of collagen and GAGs through Masson trichrome and Safranin O staining, respectively, and (D–E) their quantitative analyses. B: a1–b1, a3–b4, scale bar = 100 µm. a2–b2, scale bar = 200 µm. ns, no significance, \*\*  $p < 0.01$ , \*\*\*  $p < 0.001$ .



**Supplemental figure 1.** Characterization of collagen type I and fibronectin in periosteum and decellularized periosteum by IHC staining. a1–d1, scale bar = 200 µm; a2–d2, scale bar = 100 µm.

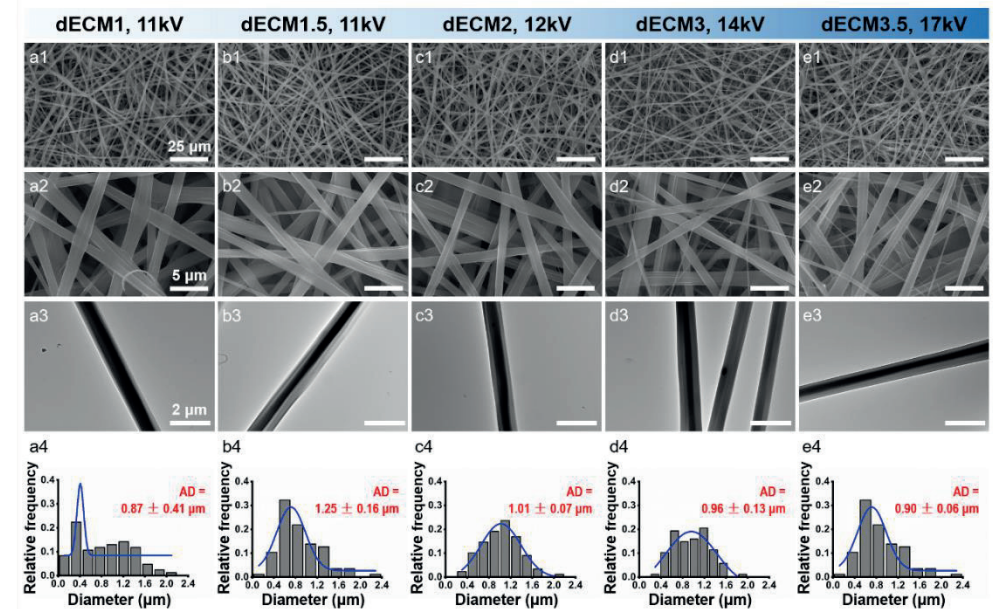
### 3.2 Physicochemical characterizations of PCL/dECM co-axial electrospinning

To optimize the co-axial electrospinning conditions, different flow rates and voltages were evaluated. Microstructural analysis of different PECs under SEM showed randomly orientated microfibrils of different diameters (Figure 2B & S2). There were distinct variations of fiber diameters at various conditions: dECM1, 11kV ( $0.87 \pm 0.41 \mu\text{m}$ ), dECM1.5, 11kV ( $1.25 \pm 0.16 \mu\text{m}$ ), dECM2, 12kV ( $1.01 \pm 0.07 \mu\text{m}$ ), dECM3, 14kV ( $0.96 \pm 0.13 \mu\text{m}$ ), and dECM3.5, 17kV ( $0.90 \pm 0.06 \mu\text{m}$ ) (Figure S2). Under all the conditions, the microfibrils consisted of a core-shell structure, of which the grey shell and black core represented dECM and PCL, respectively. Notably, dECM2.5 with a voltage of 12.9 kV displayed a favorable gross view (Figure 2A), more uniform fiber ( $1.10 \pm 0.04 \mu\text{m}$ ), and core-shell structures than the other conditions (Figure 2B a & b), suggesting this fabrication condition ensured a reproducibility to fabricate exquisite PEC.

The elemental profile of dECM shell in the PEC was analyzed by XPS (Figure 2B c). PCL is composed of carbon, hydrogen, and oxygen, among which hydrogen can't be detected by XPS. DECM consists of carbon, hydrogen, oxygen, and nitrogen [50]. The carbon and oxygen peaks of both PEC and ECM overlapped with that of PCL. Oxygen 1s binding energies between 530.08 eV to 536.08 eV and carbon 1s binding energies between 283.08 eV to 290.08 eV corresponded to oxygen and carbon in amine, amide, or peptide. Nitrogen presence was identified by the nitrogen 1s with a peak at 400.08 eV due to its presence in amide or peptide

of ECM and PEC, which was typically lacking in PCL.

Electrospun PCL, ECM, and PEC shared similar porous hierarchical structures ranging from micro- to nano-size, with average fiber diameters of  $0.86 \pm 0.22 \mu\text{m}$ ,  $0.89 \pm 0.52 \mu\text{m}$ , and  $1.00 \pm 0.38 \mu\text{m}$  (Figure S3). PCL and PEC fibers were uniformly distributed while some fibers in ECM had bead-like structures. Cross-sectional images of electrospun PCL ( $235.52 \pm 8.10 \mu\text{m}$ ), ECM ( $218.61 \pm 12.42 \mu\text{m}$ ), and PEC ( $205.77 \pm 1.46 \mu\text{m}$ ) also bore similar appearance and thickness (Figure S3). ECM and PEC were deeply stained after H&E, Masson trichrome staining, and Safranin O staining, while no staining was observed in PCL. PEC displayed more regular and aligned features than ECM. Blue-stains observed in Masson trichrome staining were due to the presence of collagen, whereas homogeneous pink-red stains in Safranin O staining were due to the presence of GAGs in the membranes (Figure S4). In the wettability study, PCL presented to be a hydrophobic surface with the WCA of over  $90^\circ$ , while both ECM and PEC possessed a hydrophilic surface with the WCA of less than  $90^\circ$ . The WCA of PCL didn't change much from 0 s to 30 s (from  $115.31 \pm 7.10^\circ$  to  $113.75 \pm 6.00^\circ$ ), while the WCA of ECM sharply decreased from  $109.81 \pm 7.20^\circ$  at 0 s to  $72.82 \pm 4.02^\circ$  at 15 s and  $66.32 \pm 4.21^\circ$  at 30 s. Significant differences in hydrophilicity between ECM and PCL were detected ( $p < 0.01$ ). The presence of dECM shell in PEC introduced a more hydrophilic character as its WCA was reduced by 53.96% at 15 s (from  $114.68 \pm 4.27^\circ$  to  $52.80 \pm 13.05^\circ$ ) ( $p < 0.001$ ), and by 60.70% at 30 s (from  $113.75 \pm 6.00^\circ$  to  $44.69 \pm 10.56^\circ$ ) ( $p < 0.001$ ) with respect to the values of PCL in each time point (Figure 2C & D). Furthermore, the WCA of PEC was also significantly less than that of ECM at 30 s ( $p < 0.05$ ).



**Supplemental figure 2.** SEM and TEM were applied to screen an optimal condition to fabricate PEC. a1–e1 & a2–e2: Randomly orientated and interconnected fiber distributions with no beads showed by SEM. a2–e2 were magnified views. a3–e3: TEM showed distinct characters of core-shell structures of PEC, of which the grey shell represents dECM and the black core is PCL. a4–e4: Average diameter (AD) and distributions of the electrospun fibers under different conditions.



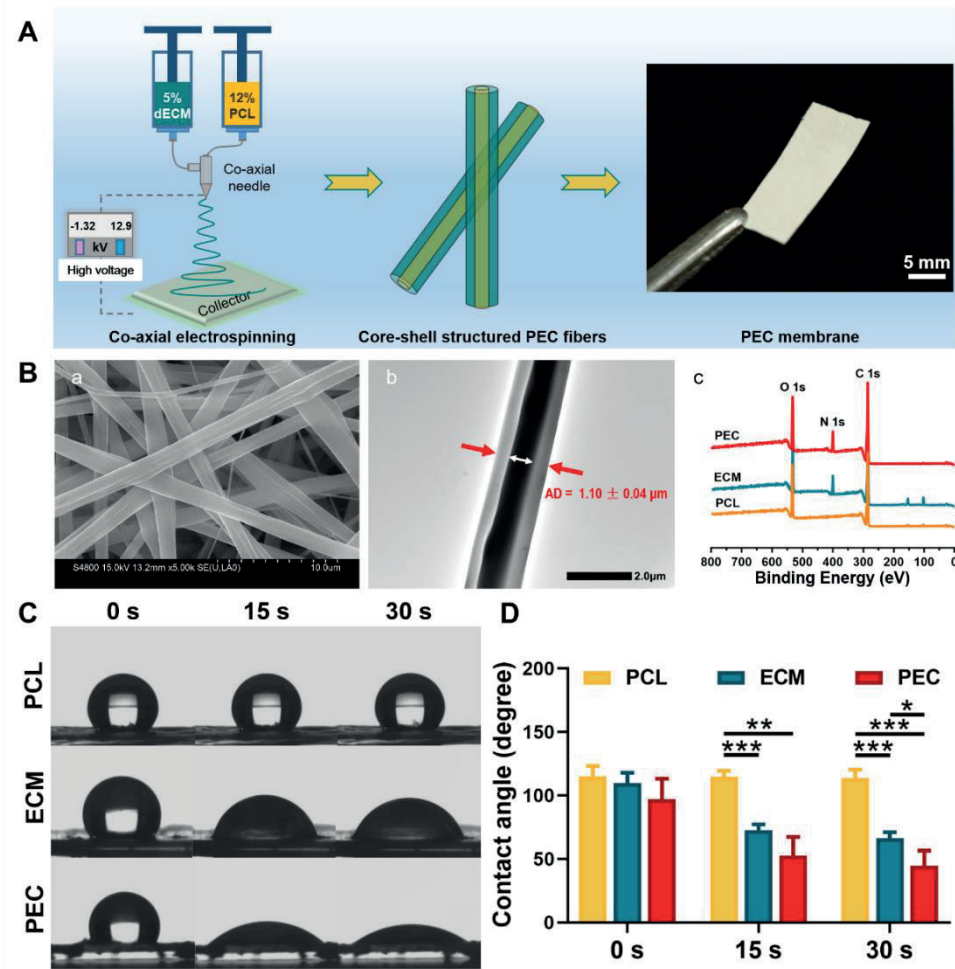
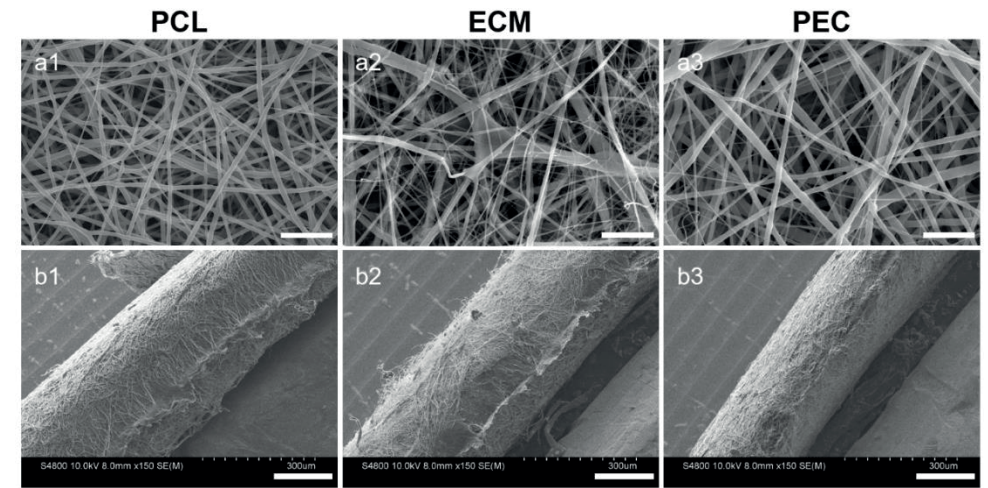
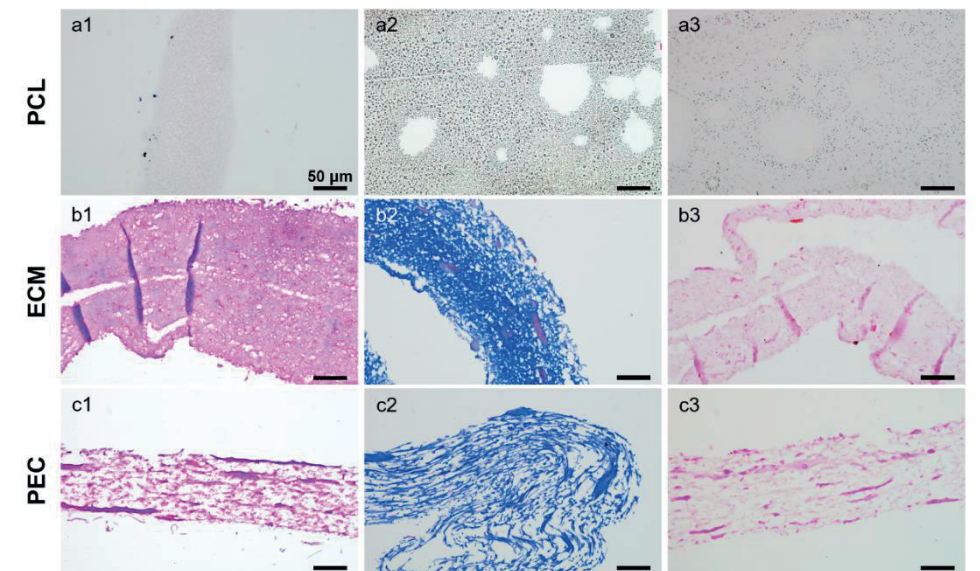


**Figure 2.** A: Schematic illustration of PEC fabrication and its gross view. B: Physicochemical characterizations of optimized PEC fibers using (a) SEM, (b) TEM (the red and white arrows refer to the dECM shell and the PCL core, respectively), and (c) XPS. C & D: Wettability test to assess the hydrophilicity of PCL, ECM, and PEC. \*  $p < 0.05$ , \*\*  $p < 0.01$ , \*\*\*  $p < 0.001$ .



**Supplemental figure 3.** Cross-sectional images of electrospun membranes by SEM. a1–a3, scale bar = 10  $\mu\text{m}$ ; b1–b3, scale bar = 150  $\mu\text{m}$ .



**Supplemental figure 4.** H&E staining (a1–c1), Masson trichrome staining (a2–c2), and Safranin O (a3–c3) staining of the electrospun membranes.

Representative uniaxial tensile stress-strain curves were obtained for PCL, ECM, and PEC under dry and wet conditions (Figure 3A). Dry ECM showed a

steeper slope than both PCL and PEC, while this phenomenon reversed when the membranes were in wet condition, which was detailed with an inset image. Young's modulus, UTS, and the percentage of elongation at break were calculated (Figure 3A b–d). Under dry condition, the Young's modulus of ECM ( $E = 0.23 \pm 0.03$  MPa) was significantly higher ( $p < 0.01$ ) than that of PCL ( $E = 0.05 \pm 0.004$  MPa) and PEC ( $E = 0.10 \pm 0.02$  MPa). UTS of PCL ( $2.02 \pm 0.10$  MPa) was significantly higher ( $p < 0.001$ ) than that of ECM ( $0.89 \pm 0.06$  MPa) and PEC ( $1.01 \pm 0.05$  MPa). In addition, the elongation at break of PCL ( $454.68\% \pm 52.07\%$ ) was significantly higher ( $p < 0.05$ ) than that of PEC ( $118.73\% \pm 9.51\%$ ) and ECM ( $10.67\% \pm 0.85\%$ ) ( $p < 0.05$ ). There was also a significant difference between PEC and ECM in elongation at break ( $p < 0.05$ ). Under wet condition, the Young's modulus of ECM ( $E = 0.004 \pm 0.0001$  MPa) decreased significantly and was lower than that of PCL ( $E = 0.05 \pm 0.003$  MPa) and PEC ( $E = 0.03 \pm 0.004$  MPa) ( $p < 0.001$ ). UTS of PCL ( $1.89 \pm 0.11$  MPa) was significantly higher ( $p < 0.001$ ) than that of ECM ( $0.75 \pm 0.11$  MPa) and PEC ( $1.12 \pm 0.01$  MPa) while PEC had a significantly higher Young's modulus and UTS than ECM ( $p < 0.05$ ). In addition, the elongation at break of PCL ( $600.43\% \pm 126.31\%$ ) was significantly higher than that of PEC ( $262.42\% \pm 26.52\%$ ) and ECM ( $186.15\% \pm 26.66\%$ ) ( $p < 0.05$ ). Compared with the dry condition, Young's modulus of wet ECM and PEC significantly declined ( $p < 0.05$ ), while the elongation at break of wet ECM and PEC significantly increased ( $p < 0.05$ ). UTS of PEC also increased when in wet status ( $p < 0.05$ ). Under dry and wet conditions, no significant changes were observed in the PCL membrane. The mechanical properties of periosteum under wet conditions were also tested. Its Young's modulus, UTS, and elongation at break were  $0.097 \pm 0.02$  MPa,  $4.24 \pm 0.90$  MPa, and  $179.49\% \pm 8.47\%$ . Periosteum had significantly higher Young's modulus and UTS than wet ECM and PEC ( $p < 0.05$ ) while bore similar elongation at break.

### 3.3 Degradation study

*In-vitro* degradation profiles of PCL, ECM, and PEC could be the indicator of *in-vivo* stability of the scaffolds. Though PCL, ECM, and PEC shared similar appearances before the degradation study, there was a distinct color change in ECM on day 1 and the membrane cracked on day 3. Only a few remnants of ECM could be harvested on day 14. After 28 days, only ECM crumbs dispersed in PBS

and could hardly be harvested for weight and image. No detectable changes were observed in the gross views of PCL and PEC over the study period (Figure 3B a). ECM showed a significant weight loss on day 7 ( $64.64\% \pm 6.34\%$ ), while PEC displayed a steady decrease in weight. On the 14<sup>th</sup> day, the mass weight of ECM and PEC remained to be  $15.04\% \pm 4.88\%$  and  $68.86\% \pm 2.81\%$ , respectively. Till the end of the study, PEC and PCL still retained  $56.97\% \pm 1.32\%$  and  $98.73\% \pm 0.62\%$  of their original weight, respectively (Figure 3B b). Microstructural analysis of the membranes under SEM revealed similar findings (Figure S5). After 7 days' degradation study, PCL could maintain its original fiber morphologies with insignificant swelling. However, dramatic changes occurred in topographic characteristics of ECM with an onset of swelling and fiber integration just after 12 h and part of the membrane disintegrated. On day 7, its hierarchical structure disappeared with a fusion of fibers. Only limited layers of fibers existed in ECM. A slight amount of ECM samples were harvested on day 14, which were not observed under SEM. In contrast, the long-duration property of the PCL core facilitated the maintenance of the PEC fiber profile. The dECM shell of PEC slowly swelled and part of its fibers fused on day 14.



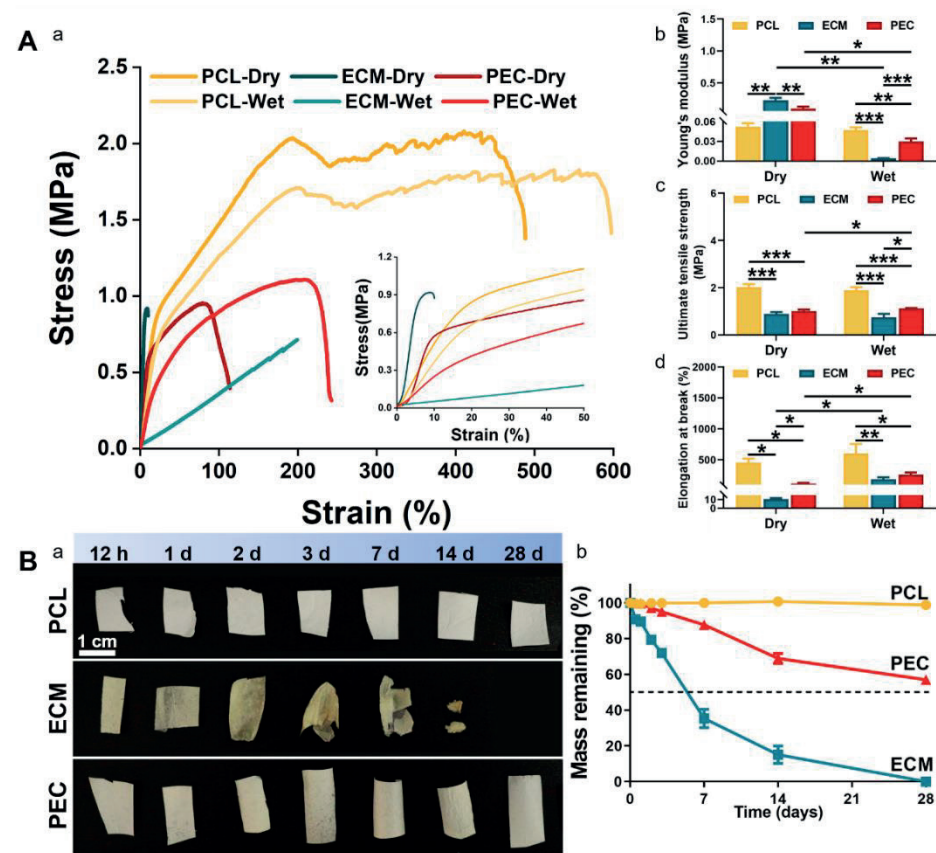
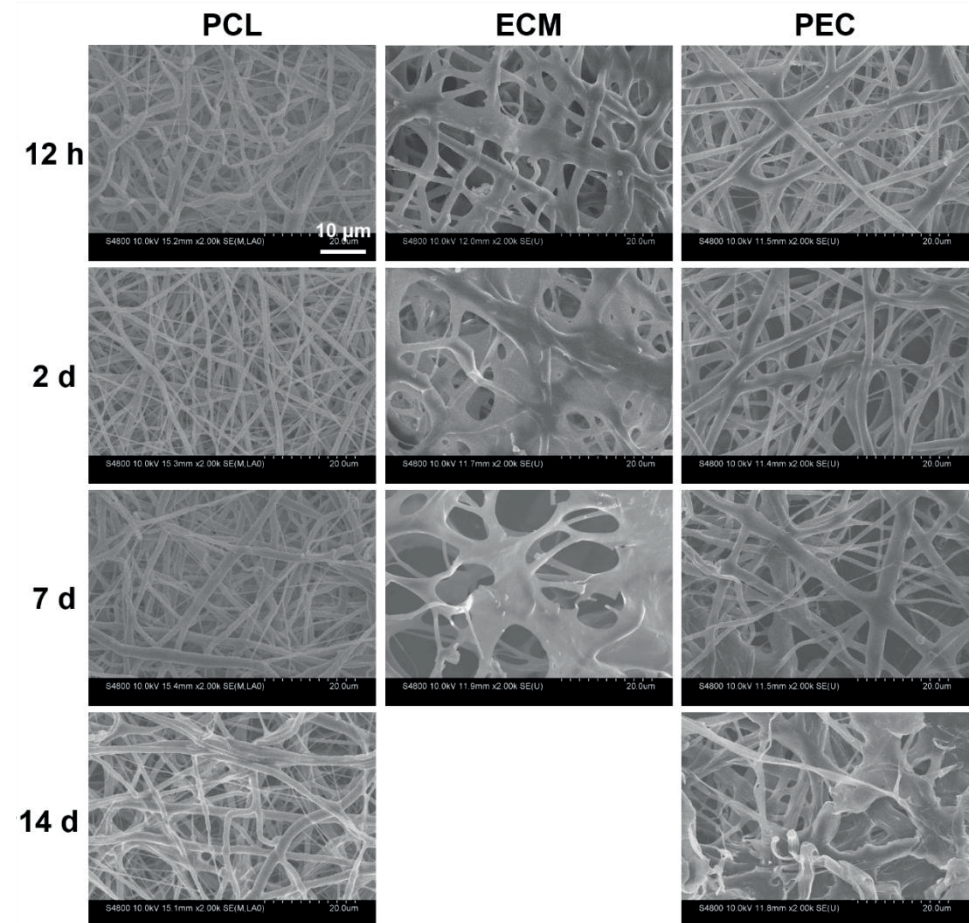


**Figure 3.** A: Mechanical properties of the electrospun membranes in dry and wet conditions. Plots representing (a) stress-strain curves obtained from tensile strength measurement (plot in the inset represents the range of strain (%) from 0 to 50), (b) Young's modulus, (c) ultimate tensile strength (UTS), and (d) elongation at break. B: Gross view (a) and weight remaining (b) of the residual membranes at different time points when the membranes were incubated in 10% PBS at 37 °C statically. \*  $p < 0.05$ , \*\*  $p < 0.01$ , \*\*\*  $p < 0.001$ .



**Supplemental figure 5.** Degradation analysis of PCL, ECM, and PEC from 12 h to day 14 using SEM.

### 3.4 Acellular mineralization

SEM images of ECM and PEC revealed deposition of mineralized crystals as compared to PCL membrane with no obvious mineralization (Figure 4A). From EDS analyses, calcium concentration and atomic percentages were significantly higher ( $p < 0.05$ ) in ECM and PEC as compared to those of PCL. No significant difference was detected between ECM and PEC (Figure 4B & C). Furthermore, compared with untreated membranes, mSBF-treated ECM and PEC showed prominent red-stained minerals depositing on their surfaces by ARS staining, while less red-

staining was observed in PCL (Figure 4D).

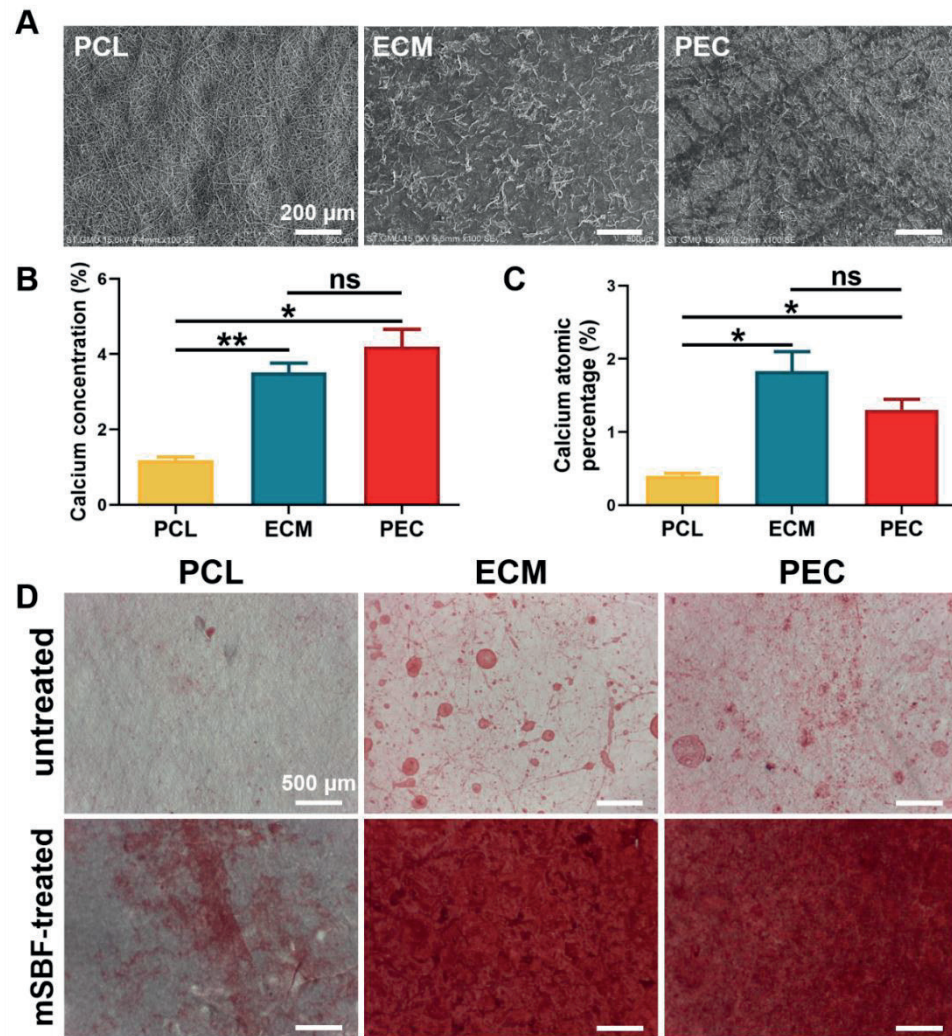


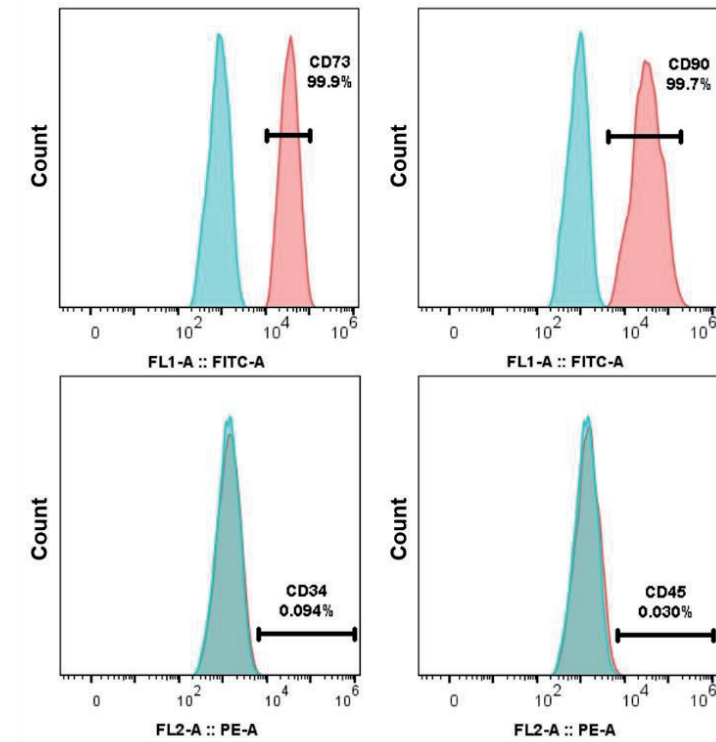
**Figure 4.** Acellular mineralization study of electrospun membranes using modified simulated body fluid (mSBF) at 37 °C for 20 days. A: Microstructural features of the mineralized membrane under SEM. B & C: Calcium concentration and atomic percentages showed by EDS. D: Calcium deposition by ARS. ns, no significance, \*  $p < 0.05$ , \*\*  $p < 0.01$ .

### 3.5 In-vitro cell culture study

#### 3.5.1 Characterization of hBMSCs

hBMSCs expressed typical MSC-related surface markers: CD73 (99.9%) and

CD90 (99.7%), without expression of peripheral blood cells associated surface markers: CD45 (0.030%) and CD34 (0.094%), indicating a pure hBMSCs population free from blood cells (Figure S6).



**Supplemental figure 6.** Flow cytometry study of hBMSCs.

#### 3.5.2 Cytocompatibility study

As shown in Figure 5A, hBMSCs firmly adhered to the membrane surfaces of PCL, ECM, and PEC, which were predominately viable (green) with few red-stained dead cells, indicating that electrospun membranes were adequately cyto-compatible. In addition, hBMSCs of polygonal shapes with pseudopodia and distinct red-stained  $\beta$ -actin cytoskeleton dominated on ECM (Figure 5A b2) and PEC (Figure 5A b3). On the contrary, hBMSCs could not spread on the surface of the PCL membrane with less cell spreading area and the cytoskeleton was not as obvious as that of ECM and PEC (Figure 5A b1). The results were also supported by SEM images. MSCs migrated into the porous structure of ECM and PEC, whereas the cells were



restricted to limited superficial space on PCL (Figure 5A c1–c3). Illustration images (Figure 5B) vividly showed that MSCs being cultured on dECM surface had more filopodia and cellular stretch area and could spread to the sub-superficial surface of the membrane (Figure 5B b), while MSCs displayed limited pseudopodia and couldn't spread themselves on the surface of PCL (Figure 5B a).

There was a steady increase in metabolic activity of cultured hBMSCs from day 1 to 7 as evidenced from Alamarblue study (Figure 6A). hBMSCs population on ECM was persistently higher than that on PCL from day 1 to day 7. Significantly higher metabolic activity of hBMSCs on PEC than that on PCL was noticed on day 3 and 5 ( $p < 0.001$ ). hBMSCs on ECM showed the highest proliferation rate over the study period.

### 3.5.3 *In-vitro* osteogenic activity

In terms of osteogenic activity, osteogenic markers of different stages were tested. As an early marker of osteogenesis, ALP activities of hBMSCs on ECM and PEC were significantly higher ( $p < 0.001$ ) than that of PCL. ALP activities of ECM showed the highest (Figure 6B). The same pattern was found in mRNA expression of ALP, while no significant difference was observed between ECM and PEC (Figure 6C). As crucial osteogenic genes, BMP2, RUNX2, and COL I were also analyzed. BMP2 expression levels in ECM and PEC were at a significantly higher quantity ( $p < 0.05$ ) than that of PCL (Figure 6D). RUNX2 expression in PCL was higher ( $p > 0.05$ ) than ECM but was dramatically lower than that on PEC ( $p < 0.05$ ) (Figure 6E). PEC showed the highest expression levels of both BMP2 and RUNX2. As to mRNA expression of COL I, both ECM and PEC were significantly higher than that of PCL ( $p < 0.05$ ) (Figure 6F). *In-vitro* mineralization nodule formation was regarded as the final osteogenic differentiation marker, of which PEC reached the same level of ECM, and was significantly higher than that of PCL ( $p < 0.001$ ) (Figure 6G & H).

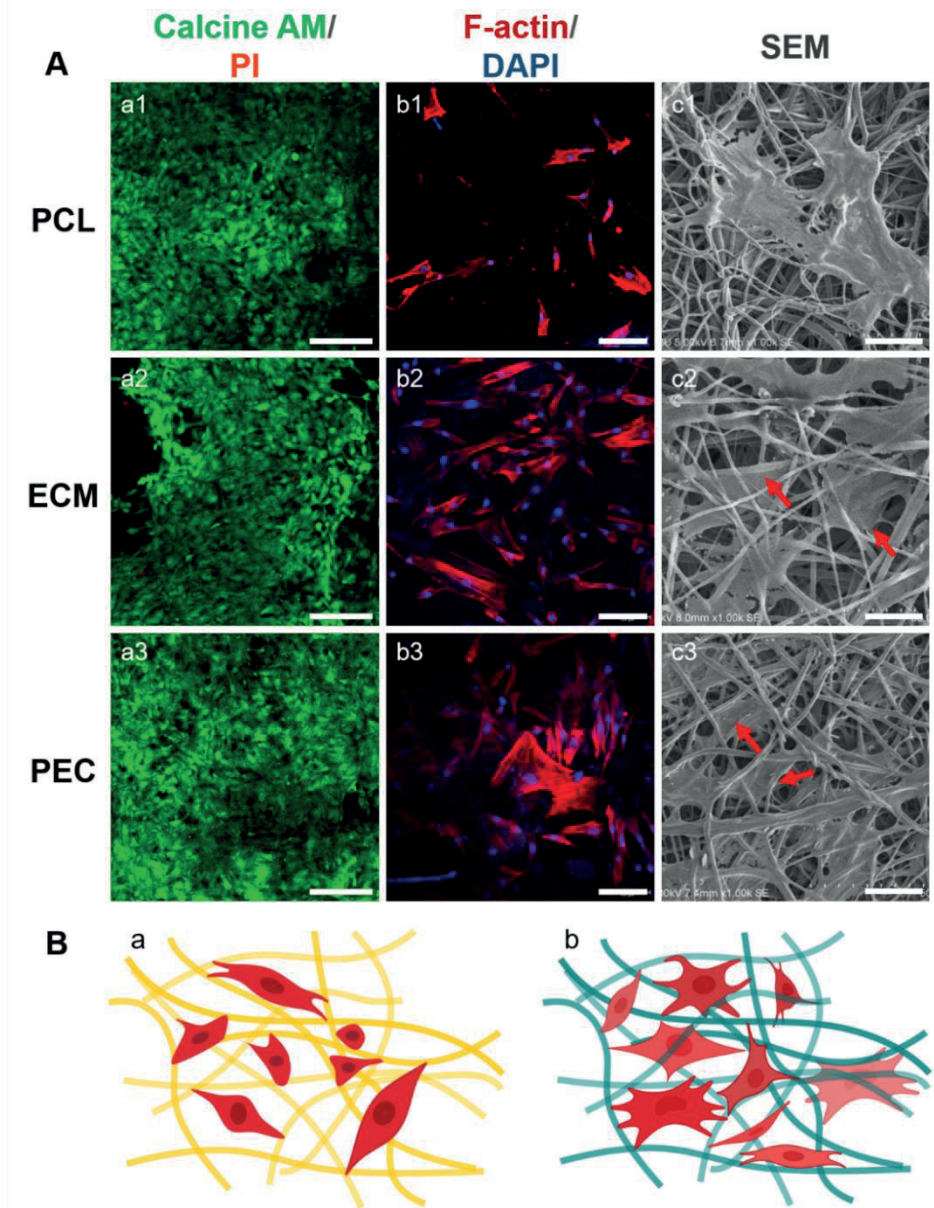


**Figure 5.** A: Live/dead staining, cytoskeletal staining, and SEM of PCL, ECM, and PEC. a1–a3: Green color of calcine AM represented live cells while the red color of propidium iodide (PI) referred to dead cells. b1–b3: Red-stained F-actin cytoskeleton and blue-stained DAPI showed the adhesion and spreading of hBMSCs on electrospun membranes. c1–c3:

Representative SEM images of MSCs co-cultured with electrospun membranes. Red arrows show hBMSCs migrated into the porous structure of ECM and PEC. B: Illustration images of hBMSCs' morphologies on the electrospun PCL (a) and membranes with dECM surface (b).

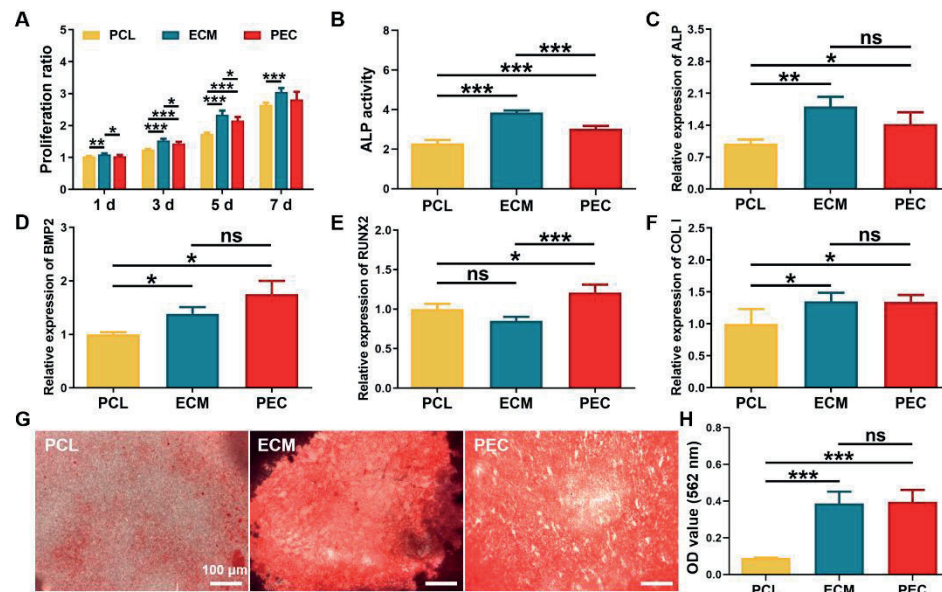


**Figure 6.** Metabolic activities and osteogenesis of hBMSCs cultured on PCL, ECM, and PEC. A: Alamarblue staining assay. B: ALP activity. C–F: Osteogenesis-related genes (ALP, BMP2, RUNX2, and COL1) expression levels. G & H: ARS and related quantitative analysis. ns, no significance, \*  $p < 0.05$ , \*\*  $p < 0.01$ , \*\*\*  $p < 0.001$ .

### 3.6 Recovery of critical-sized bone defects

The membranes were implanted on the critical-sized calvarial bone defects in rats to evaluate their comparative efficacy for promoting new bone formation (Figure 7A). Neo-bone regeneration was quantitatively assessed by micro-CT analysis 4 weeks post-implantation. For better visualization, micro-CT images at different rotational views were displayed in Figure 7B. Unlike PCL which was invisible in micro-CT, both ECM and PEC bore mineralized membranes like shields of higher density covering bone defects. Interestingly, membrane shape was successfully maintained in PEC, while ECM disseminated into the defects in a flake-like manner. Strip-like newly formed bone successfully bridged the two

opposite edges of the defect region as evidenced in ECM and PEC. However, only discrete bone islands were found in the periphery of the defect in PCL. The extent of membrane mineralization, as well as neo-bone formation (calculated as volume), were significantly higher in ECM and PEC than those in PCL (Figure 7C–D). No significant difference was detected between PEC and ECM.

From the images of histological analysis, PCL maintained intact and was encircled with multinuclear macrophages (indicated by red arrows) (Figure 8A). PEC almost kept its original shape with only mild breakage, while ECM was almost degraded with flake-like morphology, which was also embraced with connected tissues and macrophages. Both the breakage and average thickness of residual ECM was significantly higher than that of PCL and PEC ( $p < 0.01$ ) (Figure 8B & C). As to the repair of bone defects, the defect area was mainly filled with connective tissue apart from an insignificant amount of new bone formation in PCL, while large strip-like new bone formation was observed in cases of ECM and PEC. Woven bone structures were found in ECM and PEC around their membranes. Dark-blue staining of Masson trichrome implied collagen fibers in bone tissue, ECM, and PEC. Additionally, as an important non-collagenous protein during bone formation, dark-brown stained OPN was observed in the ECM and PEC, while it was absent in the PCL. Osteoblasts-mediated new bone formation was observed in the periphery of ECM and PEC. Osteoblasts could effectively migrate into the dECM matrix and progressively form mineralization (Figure 8A b5 & c5). Quantitative analysis also testified the pronounced new bone formation in ECM ( $10.13\% \pm 5.35\%$ ) and PEC ( $10.54\% \pm 4.52\%$ ) than in PCL ( $1.27\% \pm 0.77\%$ ) (Figure 8D).



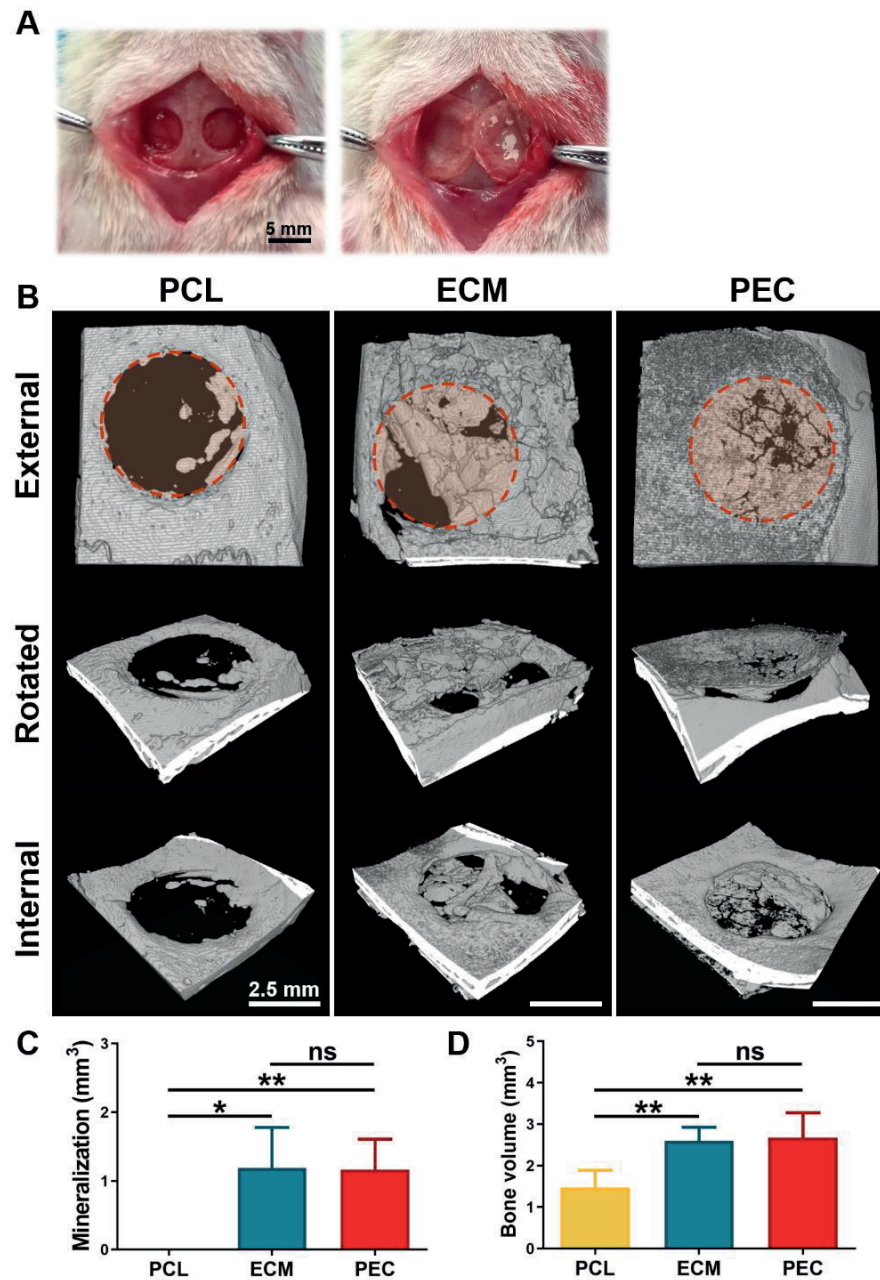


**Figure 7.** Micro-CT analysis to evaluate the repair of critical-sized bone defects using PCL, ECM, and PEC. A: Critical-sized calvarial bone defects in rats and implantation of membranes. B: Micro-CT images of the retrieved specimens at different angles for

visualizing the mineralization of membranes and neo-bone formation. C–D: Quantitative analysis of membrane mineralization and new bone formation. ns, no significance, \*  $p < 0.05$ , \*\*  $p < 0.01$ .

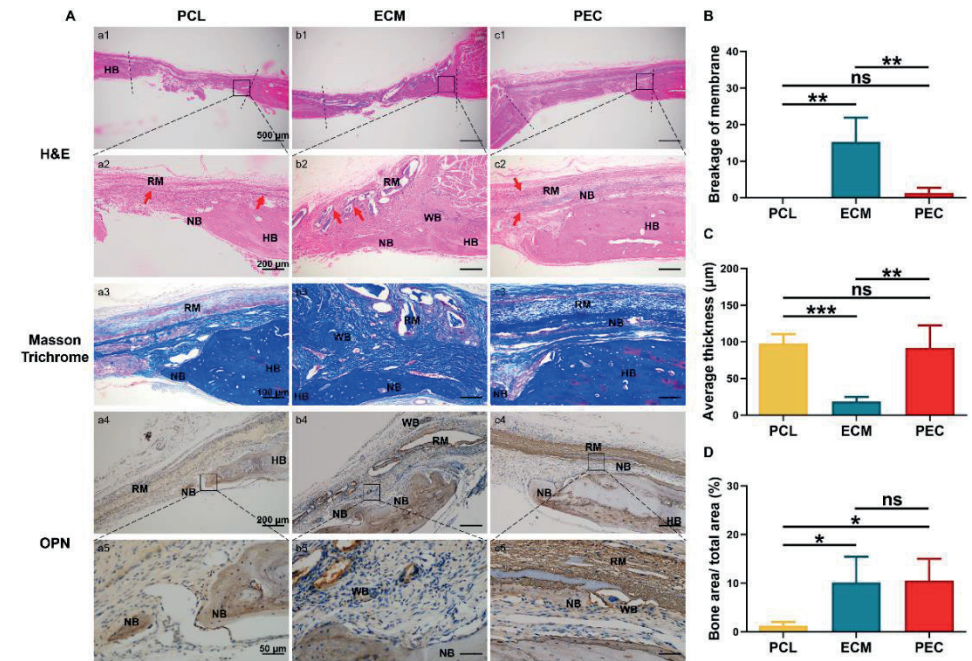


**Figure 8.** Histological analysis of the retrieved specimens for membrane degradation and new bone formation. A a1–c1: H&E staining, a2–c2: Magnified images. a3–c3: Masson trichrome staining. a4–c5: OPN staining. B–D: Quantitative study of membrane breakage, residual thickness, and percentage of new bone area. HB: Host bone; RM: Residual materials; NB: New bone; WB: Woven bone. Red arrows: Multinuclear macrophages. ns, no significance, \*  $p < 0.05$ , \*\*  $p < 0.01$ , \*\*\*  $p < 0.001$ .

#### 4. DISCUSSION

The development of biofunctional TEP has been recognized as a promising strategy to accelerate and promote the osseous repair of large bone defects. In this study, we, for the first time, adopted the co-axial electrospinning technique to fabricate a novel biomimetic TEP with PCL-core/dECM-shell-structured microfibers, with an aim to provide a mechanically stable and periosteum-specific microenvironment to promote the osteogenic activities of thereon-adhered stem cells and thus bone regeneration in the critical-sized bone defect. We showed that the novel PEC maximally resembled the mechanical strength of the PCL membrane. Meanwhile, the novel PEC also bore dECM-like hydrophilicity and bioactivity to promote cell spreading, proliferation, and osteogenic activities, which was far more advantageous than the pure PCL membrane. In the subsequent *in-vivo* repair of calvarial bone defects, the novel PEC bore a comparable healing efficacy as the pure ECM, which was significantly higher than the pure PCL membrane. Furthermore, the *in-vivo* retention of PEC was significantly higher than the ECM. These findings showed a promising application potential of the novel PEC-TEP in promoting the repair of bone defects.

One of the desired essential functions of TEP is to provide a mechanically stable microenvironment in bone defects to facilitate continuous osteogenic activities. For this purpose, TEP should bear certain mechanical stiffness so as to avoid membrane collapse, thereby maintaining the space for bone regeneration. Furthermore, it should maintain its structural integrity for at least 1–6 months *in vivo*, especially the initial 2–3 weeks [16, 54, 55] to prevent the invasion of fibroblasts into bone defects, thereby conferring osteoblasts sufficient time to repopulate the defect. Although natural polymers (e.g., collagen and gelatin) can provide a biomimetic niche for bone regeneration, their single application as TEP is limited by their low tensile strength and high degradation rate [56]. Therefore, synthetic polymers (e.g., PCL) that bear much higher tensile strength, mechanical stability, and relatively long-term degradation rate are adopted to improve the physicochemical properties of the electrospun membrane through either blended [25] or co-axial electrospinning [57]. The blended technique involves a thorough mixture of natural and synthetic polymers in a certain ratio to form a homogenous

hybrid solution for electrospinning. However, when the mass ratio of gelatin or collagen/PCL reaches 30/70 or above, the blended solution gradually separates into different phases after 3 hours, rendering it difficult for massive electrospinning processes and to harvest membranes with a stable and uniform quality [58, 59]. In addition, this demixing phenomenon results in nonuniform and coarse fiber morphology as well as large splash defects, which may severely compromise the mechanical strength and degradation properties of the electrospun membranes [58, 59]. Furthermore, the generated inhomogeneous distributions of gelatin and PCL in the resultant electrospun membranes lead to the clustering of cells in the gelatin-rich areas and difficulties in spreading to the surrounding PCL areas [44], which may impair their proliferation and metabolic activities [59].

In contrast, co-axial electrospinning offers separate channels for a respective solution without the need of premixing dissimilar polymers, thereby avoiding the aforementioned morphological and compositional inhomogeneity. As a consequence, co-axially electrospun membranes bear a homogenous and continuous structure of a PCL core and natural polymer shell, which contribute to a significantly improved stability in the biological microenvironment. For example, after soaking in 10% PBS at 37 °C, a co-axially electrospun PCL/gelatin membrane maintains its porous structure, while a blended electrospun PCL/gelatin membrane degrades much faster and loses its porous structure [60]. Such stability of the co-axially electrospun membrane is favorable to maintain its integrity so as to prevent the invasion of surrounding fibrous tissues. Furthermore, the co-axially electrospun PCL/gelatin membrane bears significantly higher Young's modulus (4.3-fold) and tensile strength (10.6-fold) than the blended electrospun PCL/gelatin membrane [60], which is highly important for ensuring a stable mechanical microenvironment for bone regeneration. Apart from these advantages in physicochemical properties, co-axial electrospinning provides a complete and continuous shell surface of natural polymers, which results in significantly higher cellular adhesion and metabolism on co-axially electrospun PCL/gelatin membranes than the blended ones [47]. Furthermore, the core-shell structure of co-axial electrospinning can also be used to realize a stepwise and controlled release pattern of bioactive agents [57, 61]. These properties indicate that co-axial electrospinning technique bears a

promising application potential for fabricating an ideal TEP. However, hitherto, most of these studies adopt gelatin as the natural polymer, which is insufficient to provide a periosteum-biomimetic niche for bone regeneration. Therefore, in this study, we planned to fabricate a biomimetic TEP by co-axial electrospinning of PCL and dECM.

One critical step for fabricating a co-axial electrospinning PCL/dECM membrane is to make an injectable solution with certain viscoelastic properties from periosteal dECM. After decellularization, there are two major techniques to obtain a homogenous dECM solution: 1) enzymatic digestion before dissolution in organic solvents [41, 62, 63] and 2) direct dissolution in organic solvents. The enzymatic digestion involves extra digestion of dECM with pepsin in acidic conditions (pH 2.0) for hours (12–72 h) followed by pH neutralization [64]. It shows that pepsin-digested ECMs lose the ability to promote the differentiation of MSCs [65]. Therefore, this method may be difficult to maintain the biomimetic property of the periosteal ECM. The dissolution of dECM involves soaking of dECM in HFIP for varied periods, such as overnight [39, 66, 67], 24 h [68] and 2 days [69]. In our study, we modified the dissolution protocol to ensure a homogenous solution of dECM. After milling and sieving, dECM (diameter less than 425  $\mu\text{m}$ ) was added into HFIP at the final concentration of 5% (w/v) with constant stirring for 6 days at 4 °C. Right after adding into HFIP, the dECM solution appeared to be cloudy-white and highly viscous with dispersed dECM particles. The density of dECM particles gradually decreased with time and the solution showed a semitransparent and homogenous morphology with a much lower viscosity, which suggested that 6 days are necessary to ensure the dissolution of dECM in HFIP. After dissolution, the solutions were further cleared by removing the residual undissolved components through centrifugation. These procedures facilitated the electrospinnability of dECM without clogging the needle or inducing bead formation of the fibers. The analyses of SEM, TEM, and XPS corroborated a uniform fiber distribution with a delicate PCL core/dECM shell structure. The fibers of PEC and ECM were positively stained by Masson trichrome and Safranin O staining, indicating uniformly distributed collagen and GAGs from dECM.

In this study, we found that the PEC bore more biomimetic physicochemical

and biological properties than the electrospun PCL and ECM. For example, in terms of mechanical properties, the ECM had the highest Young's modulus ( $0.23 \pm 0.03$  MPa) in dry conditions, while it significantly decreased ( $0.004 \pm 0.0001$  MPa) when in contact with PBS, indicating dry ECM bears high stiffness and will exhibit significant softness if in contact with blood or other body fluids. Besides, the elongation percentage at break of dry ECM ( $10.67\% \pm 0.85\%$ ) was too low. These characteristics render ECM difficult to manipulate during operation. On the contrary, the dECM shell endowed dry PEC a double Young's modulus compared with PCL membrane and enhanced elongation percentage at break ( $118.73\% \pm 9.51\%$ ) than ECM. Besides, wet PEC still maintained a certain stiffness ( $0.03 \pm 0.004$  MPa), an improved UTS ( $1.12 \pm 0.01$  MPa) and elongation percentage at break ( $262.42\% \pm 26.52\%$ ). Though its UTS was lower than that of periosteum ( $4.24 \pm 0.90$  MPa), it resembled a typical barrier membrane (Bio-Gide®,  $1.68 \pm 0.54$  MPa) [70]. The wet PEC had a similar elongation percentage at break to the native periosteum ( $179.49\% \pm 8.47\%$ ). These results indicated that PEC-TEP possessed a biomimetic stiffness and tunability to provide a favorable mechanical microenvironment for bone regeneration. Furthermore, PEC showed a prolonged biodegradability with its 57% retained after a 4-week incubation in PBS. In contrast, the ECM displayed a high rate of degradability, which was implied by the significant swelling, disappearance of its hierarchical structure, and over 65% material even after incubation of 7 days. Four weeks post-incubation, no membrane structure of ECM could be found. Such a high degradability of ECM may significantly compromise the desired functions of TEP, such as the mechanical stabilization of grafting materials and barrier function to prevent the invasions of surrounding fibrous tissues. As another extreme, PCL was too pliable since it bore a half Young's modulus ( $0.05 \pm 0.004$  MPa), but much higher (about 3.8 times) elongation percentage at break ( $454.68\% \pm 52.07\%$ ) in comparison with PEC. PCL bore a long half-life and showed no obvious morphological changes and mass loss after 4 weeks, which may cause slow replacement and risks of infections.

In addition to the physicochemical properties, the biological properties of PEC more resembled ECM, which were significantly advantageous over PCL. First of all, PEC bore a significantly lower WCA ( $44.69 \pm 10.56^\circ$ ) than not only PCL ( $113.75 \pm$



6.00°) but also ECM ( $66.32 \pm 4.21^\circ$ ), which indicated its superior hydrophilicity. Such a phenomenon was highly interesting since it could not be only attributed to the dECM shell composition. The high surface-to-volume ratio of PEC may be another contributing factor, which still needs to be further investigated. Secondly, the PEC and ECM supported a comparable level of *in-vitro* bio-mineralization when being soaked in mSBF (without any cellular components) for 20 days, while dramatically less mineralization formed in PCL, which indicated that the dECM shell conferred PEC a bioactive surface property. Such induction of bio-mineralization on dECM may be attributed to that polyanionic GAGs can mediate the mineralization process and bind cations like  $\text{Ca}^{2+}$ , thus regulating extracellular cation homeostasis [71, 72]. Besides, collagen type I in dECM also contributes to the bio-mineralization by serving as a template for the binding of calcium and phosphate ions and subsequent nucleation of apatite crystals. Thirdly, cell adhesion and spreading will influence cellular interactions, cell-matrix communication, and finally its behaviors and functions [73]. HBMSCs bore prominent actin cytoskeleton, occupied more spreading area, and tended to migrate into the sub-superficial fiber layers on PEC and ECM though the pore size of the membrane was smaller than that of MSCs, while hBMSCs always stayed in the superficial fiber layer with a limited cellular stretch area when being seeded on PCL. This may be attributed to that ECM and PEC bear an active dECM surface, which has abundant cell-ECM-recognition molecules (e.g., RGD sequence) and growth factors. Wang et al. show that decellularized BMSCs sheets can significantly promote BMSCs' migration in a Transwell model (3.0- $\mu\text{m}$  pore) compared with the control group without dECM [74]. This chemotactic effect is also observed in decellularized chondrocyte sheets [75]. Besides, due to the interconnected porous structure, high surface area, and low stiffness, we supposed that BMSCs could enter the membrane by amoeboid movement, which can be supported by a study from Song et al. They find when cultured on electrospun hyaluronic acid (HA)-based fibrous membrane (Young's modulus of about 0.12 GPa), cells can spread and migrate into the porous network by deforming adjacent fibers and expanding the pores [76]. Compared with membranes with large pores (20  $\mu\text{m}$ ), MSCs on 5- $\mu\text{m}$  pore PLA honeycomb film extend between several pores with long pseudopodia and can form a thicker

cartilage layer due to firm adherence to the film [77]. We supposed there would be a synergistic effect of superficial and sub-superficial BMSCs on ECM and PEC.

On days 3 and 5, the proliferation ratio of hBMSCs on PEC was significantly higher than that on PCL, suggesting that the dECM shell significantly enhanced cell proliferation. A similar pattern was also found in the mRNA expression levels of ALP, an early osteogenic differentiation marker, representing osteoblasts' activities in mineralization [61, 78], which were 1.8-fold and 1.4-fold higher in ECM and PEC groups than that in the PCL group. Thereafter, we also checked the mRNA expression levels of two crucial osteogenic differentiation markers — BMP2 and RUNX2 on the three types of TEPs. BMP2 is the main factor that differentiates MSCs into osteoblasts by binding to type I and type II serine/threonine kinase receptors of MSCs, activating downstream Smad and non-Smad signaling pathways, which ultimately activate osteogenic genes expression levels such as RUNX2 [79, 80]. RUNX2 is a key transcription factor for MSCs differentiation. It can upregulate the expression levels of ALP and COL I in the initial stage when MSCs differentiate into preosteoblasts and immature osteoblasts. However, the expression of RUNX2 will decrease in mature osteoblasts [81, 82]. Our data showed that mRNA expression levels of BMP2 and RUNX2 were the highest in the PEC group, which indicated the favorable property of PEC in inducing osteogenic differentiation. That RUNX2 expression in ECM was lower than in PEC may be attributed to the cells on ECM were gradually turning to mature osteoblasts. Collagen type I involves the initial osteoblasts differentiation, non-collagenous proteins deposition, and the final mineralization process for the formation of bone matrix [83, 84]. PEC and ECM induced a comparable level of COL I, which was significantly higher than that of PCL. Consistently, a comparable level of the *in-vitro* mineralization nodule formation was also found on the ECM and PEC, which was also significantly higher than that on the PCL. These data indicated that PEC was superior in promoting cell proliferation, early differentiation marker, and crucial osteogenic genes expression levels in comparison with PCL. More importantly, PEC induced the same level of final osteogenic differentiation marker — *in-vitro* mineralization nodule formation, as ECM, thus suggesting that PEC could provide a biomimetic microenvironment to facilitate osteogenesis.



One month post-implantation, micro-CT analysis was performed to analyze the *in-vivo* bone regeneration. In the group of PEC, 3D reconstruction showed that an intact mineralized membrane-like structure was found covering the bone defects, which suggested that PEC could keep its integrity within one month and induced a strong osteogenic activity right on its surface. In contrast, no membrane-like structure was found in PCL, which indicated no osteogenic activities on its surface. Interestingly, only an irregular fragment-like structure was found in the ECM, which suggested that ECM degraded fast and broke into pieces. Quantitative analysis confirmed that the ECM and PEC bore a comparable level of membrane-associated osteogenesis, while no such mineralization was found in the PCL. Furthermore, the bone volumes within the bone defects in the groups of ECM and PEC were comparable, but significantly higher (1.8-fold) than that in PCL. Consistent with the micro-CT findings, the histological analysis also corroborated that ECM broke into many pieces with only 19% thickness retained, while only mild breakage or no breakage was found in the PEC and PCL. This result was consistent with the *in-vitro* degradation property of the three membranes. The too rapid degradation rate of the ECM may raise the concern of fibrous tissue invasion into bone defects. Furthermore, more new bone volume was also formed in ECM and PEC than that in PCL. OPN, as an important non-collagenous protein, is involved in bone remodeling and bio-mineralization. It concentrates in the mineralized collagen matrix during bone formation and increases adhesion of cells [85]. The intense OPN staining at the boundaries between ECM or PEC and tissues suggested an inductive function of dECM in promoting bone regeneration, while no dark-brown staining was formed in the peripheral of the PCL membrane, indicating it couldn't induce osteoblastic differentiation. These data validated that PEC and ECM had more osteogenesis-related cues for bone regeneration than PCL.

The dECM decorated PEC brought encouraging results in both physicochemical and biological properties and is promising in repairing bone defects. For bone defects in non-load-bearing areas, this dECM/PCL composite can be fabricated in PCL-reinforced dECM hydrogel as an injected bone graft or a scaffold [33] to guide bone regeneration. As to segmental or large volume bone defects, dECM can be used as a bioactive coating material or a carrier for drug

delivery (e.g., anti-inflammation, anti-tumor, and growth factors) [34] in combination with load-bearing materials (e.g., tricalcium phosphate and hydroxyapatite) [86]. TEP can then promote the initial osseointegration of bone-filling materials and host bone. Nevertheless, to obtain an efficacious bone repairing outcome, further investigations are necessary to reveal the fate of MSCs on the PEC. The underlying mechanism of osteogenic property of PEC also needs to be explored. As periosteum also has excellent angiogenic capacity, whether the biomimetic PEC can promote vascularization in the host site remains to be analyzed in our future research.

## 5. CONCLUSION

Our study successfully fabricated a novel PEC-TEP from dECM and PCL by the co-axial electrospinning technique. The exquisite core-shell structured PEC bore advantages acting as TEP: 1) compared with the pure PCL, dECM shell endowed PEC a periosteum-specific osteogenic microenvironment for MSCs, which rendered PEC a superior bioactive surface for promoting cell proliferation, matrix mineralization, and bone formation; besides, the favorable biodegradation rate of PEC avoided the risks of infection and slow tissue replacement; a certain stiffness of PEC made it resistant to tissue collapse and kept a stable environment for osteogenesis; 2) compared with the pure ECM, the PCL core conferred PEC a biomimetic tensile strength and long degradation rate for guiding bone regeneration. Overall, these findings indicated that the newly developed biomimetic periosteum of PEC holds great application potential to repair bone defects.

## REFERENCES

- [1] M.R. Allen, et al., Periosteum: Biology, Regulation, and Response to Osteoporosis Therapies, *Bone* 35(5) (2004) 1003-1012.
- [2] S.J. Roberts, et al., Uncovering the Periosteum for Skeletal Regeneration: The Stem Cell That Lies Beneath, *Bone* 70 (2015) 10-18.
- [3] S.H. McBride, et al., Anisotropic Mechanical Properties of Ovine Femoral Periosteum and the Effects of Cryopreservation, *J Biomech* 44(10) (2011) 1954-1959.
- [4] N. Li, et al., Periosteum Tissue Engineering — a Review, *Biomater Sci* 4(11) (2016) 1554-1561.
- [5] P. Stockmann, et al., Guided Bone Regeneration in Pig Calvarial Bone Defects Using Autologous Mesenchymal Stem/Progenitor Cells — a Comparison of Different Tissue Sources, *J Craniomaxillofac Surg* 40(4) (2012) 310-320.
- [6] Y.M. Ryu, et al., Osteogenic Differentiation of Human Periosteal-Derived Cells in a Three-Dimensional Collagen Scaffold, *Mol Biol Rep* 38(5) (2011) 2887-2894.
- [7] M.D. Hoffman, D.S. Benoit, Emulating Native Periosteum Cell Population and Subsequent Paracrine Factor Production to Promote Tissue Engineered Periosteum-Mediated Allograft Healing, *Biomaterials* 52 (2015) 426-440.
- [8] T. Wang, et al., Osteogenic Differentiation of Periosteal Cells During Fracture Healing, *J Cell Physiol* 232(5) (2017) 913-921.
- [9] S.E. Utvag, et al., Effects of Periosteal Stripping on Healing of Segmental Fractures in Rats, *J Orthop Trauma* 10(4) (1996) 279-284.
- [10] S. Karaoglu, et al., Experimental Repair of Segmental Bone Defects in Rabbits by Demineralized Allograft Covered by Free Autogenous Periosteum, *Injury* 33(8) (2002) 679-683.
- [11] M.L. Knothe Tate, et al., Testing of a New One-Stage Bone-Transport Surgical Procedure Exploiting the Periosteum for the Repair of Long-Bone Defects, *J Bone Joint Surg Am* 89(2) (2007) 307-316.
- [12] F. Soldado, et al., Vascularized Fibular Periosteal Graft: A New Technique to Enhance Bone Union in Children, *J Pediatr Orthop* 32(3) (2012) 308-313.
- [13] Y. Yang, et al., Biomimetic, Stiff, and Adhesive Periosteum with Osteogenic-Angiogenic Coupling Effect for Bone Regeneration, *Small* 17(14) (2021) e2006598.
- [14] L. Wu, et al., Hierarchical Micro/Nanofibrous Membranes of Sustained Releasing VEGF for Periosteal Regeneration, *Biomaterials* 227 (2020) 119555.
- [15] A. Hasuike, et al., Pedicle Periosteum as a Barrier for Guided Bone Regeneration in the Rabbit Frontal Bone, *In Vivo* 33(3) (2019) 717-722.
- [16] D. Hutmacher, et al., A Review of Material Properties of Biodegradable and Bioresorbable Polymers and Devices for GTR and GBR Applications, *Int J Oral Maxillofac Implants* 11(5) (1996) 667-678.
- [17] F. Berton, et al., A Critical Review on the Production of Electrospun Nanofibres for Guided Bone Regeneration in Oral Surgery, *Nanomaterials (Basel)* 10(1) (2019) 16.
- [18] L. Jiang, et al., Effect of Component and Surface Structure on Poly(L-Lactide-Co- $\epsilon$ -Caprolactone) (PLCA)-Based Composite Membrane, *Composites Part B: Engineering* 174 (2019) 107031.
- [19] S. Chahal, et al., Development of Biomimetic Electrospun Polymeric Biomaterials for Bone Tissue Engineering. A Review, *J Biomater Sci Polym Ed* 30(14) (2019) 1308-1355.
- [20] J.M. Miszuk, et al., Functionalization of PCL — 3D Electrospun Nanofibrous Scaffolds for Improved BMP2-Induced Bone Formation, *Appl Mater Today* 10 (2018) 194-202.
- [21] Y. Lin, et al., *In Vitro* Behavior of Tendon Stem/Progenitor Cells on Bioactive Electrospun Nanofiber Membranes for Tendon-Bone Tissue Engineering Applications, *Int J Nanomedicine* 14 (2019) 5831-5848.
- [22] F.J. Chaparro, et al., Sintered Electrospun Polycaprolactone for Controlled Model Drug Delivery, *Mater Sci Eng C Mater Biol Appl* 99 (2019) 112-120.
- [23] A.O. Lobo, et al., Electrospun Nanofiber Blend with Improved Mechanical and Biological Performance, *Int J Nanomedicine* 13 (2018) 7891-7903.
- [24] Y.S. Kim, et al., Applications of Decellularized Extracellular Matrix in Bone and Cartilage Tissue Engineering, *Bioeng Transl Med* 4(1) (2019) 83-95.
- [25] T. Wang, et al., Layer-by-Layer Nanofiber-Enabled Engineering of Biomimetic Periosteum for Bone Repair and Reconstruction, *Biomaterials* 182 (2018) 279-288.
- [26] M. Masoudi Rad, et al., Fabrication and Characterization of Two-layered Nanofibrous Membrane for Guided Bone and Tissue Regeneration Application, *Mater Sci Eng C Mater Biol Appl* 80 (2017) 75-87.
- [27] M. Gong, et al., Icarin-Loaded Electrospun PCL/Gelatin Nanofiber Membrane as Potential Artificial Periosteum, *Colloids Surf B Biointerfaces* 170 (2018) 201-209.
- [28] L. Ghasemi-Mobarakeh, et al., Electrospun Poly( $\epsilon$ -Caprolactone)/Gelatin Nanofibrous Scaffolds for Nerve Tissue Engineering, *Biomaterials* 29(34) (2008) 4532-4539.
- [29] S.L. Bee, Z.A.A. Hamid, Characterization of Chicken Bone Waste-Derived Hydroxyapatite and Its Functionality on Chitosan Membrane for Guided Bone Regeneration, *Compos B Eng* 163 (2019) 562-573.
- [30] S. Politi, et al., Smart ECM-Based Electrospun Biomaterials for Skeletal Muscle Regeneration, *Nanomaterials (Basel)* 10(9) (2020) 1781.
- [31] H. Xing, et al., Extracellular Matrix-Derived Biomaterials in Engineering Cell Function, *Biotechnol Adv* 42 (2020) 107421.
- [32] P. Qiu, et al., Periosteal Matrix-Derived Hydrogel Promotes Bone Repair through an Early Immune Regulation Coupled with Enhanced Angio- and Osteogenesis, *Biomaterials* 227 (2020) 119552.
- [33] S. Krishtul, et al., Processed Tissue-Derived Extracellular Matrices: Tailored Platforms Empowering Diverse Therapeutic Applications, *Adv Funct Mater* 30(18) (2020) 1900386.
- [34] Q. Yao, et al., Recent Development and Biomedical Applications of Decellularized Extracellular Matrix Biomaterials, *Mater Sci Eng C Mater Biol Appl* 104 (2019) 109942.
- [35] S.J. Rapp, et al., Repairing Critical-Sized Rat Calvarial Defects with Progenitor Cell-Seeded Acellular Periosteum: A Novel Biomimetic Scaffold, *Surgery* 152(4) (2012) 595-605.
- [36] K. Chen, et al., Decellularized Periosteum as a Potential Biologic Scaffold for

Bone Tissue Engineering, *Acta Biomater* 19 (2015) 46-55.

[37] J. He, et al., Preparation and Evaluation of Acellular Sheep Periosteum for Guided Bone Regeneration, *J Biomed Mater Res A* 108(1) (2020) 19-29.

[38] J. Zhang, et al., Preparation and Evaluation of Tibia- and Calvarium-Derived Decellularized Periosteum Scaffolds, *ACS Biomater Sci Eng* 3(12) (2017) 3503-3514.

[39] J. Fernandez-Perez, et al., Characterization of Extracellular Matrix Modified Poly( $\epsilon$ -Caprolactone) Electrospun Scaffolds with Differing Fiber Orientations for Corneal Stroma Regeneration, *Mater Sci Eng C Mater Biol Appl* 108 (2020) 110415.

[40] K.H. Patel, et al., Aligned Nanofibers of Decellularized Muscle ECM Support Myogenic Activity in Primary Satellite Cells *in Vitro*, *Biomed Mater* 14(3) (2019) 035010.

[41] R. Sobreiro-Almeida, et al., Extracellular Matrix Electrospun Membranes for Mimicking Natural Renal Filtration Barriers, *Mater Sci Eng C Mater Biol Appl* 103 (2019) 109866.

[42] R. Junka, et al., Acellular Polycaprolactone Scaffolds Laden with Fibroblast/Endothelial Cell-Derived Extracellular Matrix for Bone Regeneration, *J Biomed Mater Res A* 108(2) (2020) 351-364.

[43] M.S. Carvalho, et al., Co-Culture Cell-Derived Extracellular Matrix Loaded Electrospun Microfibrous Scaffolds for Bone Tissue Engineering, *Mater Sci Eng C Mater Biol Appl* 99 (2019) 479-490.

[44] B. Feng, et al., Effect of Inhomogeneity of the Electrospun Fibrous Scaffolds of Gelatin/Polycaprolactone Hybrid on Cell Proliferation, *J Biomed Mater Res A* 103(2) (2015) 431-438.

[45] X. Jing, et al., Electrospinning Homogeneous Nanofibrous Poly(propylene carbonate)/Gelatin Composite Scaffolds for Tissue Engineering, *Ind Eng Chem Res* 53(22) (2014) 9391-9400.

[46] J.J. Stankus, et al., Hybrid Nanofibrous Scaffolds from Electrospinning of a Synthetic Biodegradable Elastomer and Urinary Bladder Matrix, *J Biomater Sci Polym Ed* 19(5) (2008) 635-652.

[47] B.N. Blackstone, et al., Tunable Engineered Skin Mechanics Via Coaxial Electrospun Fiber Core Diameter, *Tissue Eng Part A* 20(19-20) (2014) 2746-2755.

[48] Y. Wakuda, et al., Native Collagen Hydrogel Nanofibres with Anisotropic Structure Using Core-Shell Electrospinning, *Sci Rep* 8(1) (2018) 6248.

[49] N. Nagiah, et al., Highly Compliant Vascular Grafts with Gelatin-Sheathed Coaxially Structured Nanofibers, *Langmuir* 31(47) (2015) 12993-13002.

[50] N. Nagiah, et al., Development and Characterization of Coaxially Electrospun Gelatin Coated Poly(3-Hydroxybutyric Acid) Thin Films as Potential Scaffolds for Skin Regeneration, *Mater Sci Eng C Mater Biol Appl* 33(7) (2013) 4444-4452.

[51] P.M. Crapo, et al., An Overview of Tissue and Whole Organ Decellularization Processes, *Biomaterials* 32(12) (2011) 3233-3243.

[52] M. Gong, et al., Gene Expression Profiling: Identification of Gene Expression in Human MSC Chondrogenic Differentiation, *Am J Transl Res* 10(11) (2018) 3555-3566.

[53] Q. Rong, et al., A Novel Method to Improve the Osteogenesis Capacity of

Hucmscs with Dual-Directional Pre-Induction under Screened Co-Culture Conditions, *Cell Prolif* 53(2) (2020) e12740.

[54] E. Calciolari, et al., Degradation Pattern of a Porcine Collagen Membrane in an *in Vivo* Model of Guided Bone Regeneration, *J Periodontal Res* 53(3) (2018) 430-439.

[55] D. Buser, et al., Localized Ridge Augmentation with Autografts and Barrier Membranes, *Periodontol* 2000 19 (1999) 151-163.

[56] J. Behring, et al., Toward Guided Tissue and Bone Regeneration: Morphology, Attachment, Proliferation, and Migration of Cells Cultured on Collagen Barrier Membranes. A Systematic Review, *Odontology* 96(1) (2008) 1-11.

[57] M. Gong, et al., Core-Sheath Micro/Nano Fiber Membrane with Antibacterial and Osteogenic Dual Functions as Biomimetic Artificial Periosteum for Bone Regeneration Applications, *Nanomedicine* 17 (2019) 124-136.

[58] B. Feng, et al., Acetic-Acid-Mediated Miscibility toward Electrospinning Homogeneous Composite Nanofibers of GT/PCL, *Biomacromolecules* 13(12) (2012) 3917-3925.

[59] H.M. Powell, S.T. Boyce, Engineered Human Skin Fabricated Using Electrospun Collagen-PCL Blends: Morphogenesis and Mechanical Properties, *Tissue Eng Part A* 15(8) (2009) 2177-2187.

[60] D. Kai, et al., Mechanical Properties and *in Vitro* Behavior of Nanofiber-Hydrogel Composites for Tissue Engineering Applications, *Nanotechnology* 23(9) (2012) 095705.

[61] W.T. Su, et al., Differentiation Potential of SHEDs Using Biomimetic Periosteum Containing Dexamethasone, *Mater Sci Eng C Mater Biol Appl* 58 (2016) 1036-1045.

[62] T.H. Kim, et al., Nanofibrous Electrospun Heart Decellularized Extracellular Matrix-Based Hybrid Scaffold as Wound Dressing for Reducing Scarring in Wound Healing, *Tissue Eng Part A* 24(9-10) (2018) 830-848.

[63] X. Wang, et al., Harnessing Electrospun Nanofibers to Recapitulate Hierarchical Fibrous Structures of Meniscus, *J Biomed Mater Res B Appl Biomater* 109(2) (2021) 201-213.

[64] R.A. Pouliot, et al., Porcine Lung-Derived Extracellular Matrix Hydrogel Properties Are Dependent on Pepsin Digestion Time, *Tissue Eng Part C Methods* 26(6) (2020) 332-346.

[65] B.B. Rothrauff, et al., Tissue-Specific Bioactivity of Soluble Tendon-Derived and Cartilage-Derived Extracellular Matrices on Adult Mesenchymal Stem Cells, *Stem Cell Res Ther* 8(1) (2017) 133.

[66] J.A. Reid, A. Callanan, Hybrid Cardiovascular Sourced Extracellular Matrix Scaffolds as Possible Platforms for Vascular Tissue Engineering, *J Biomed Mater Res B Appl Biomater* 108(3) (2020) 910-924.

[67] M.M. Smoak, et al., Fabrication and Characterization of Electrospun Decellularized Muscle-Derived Scaffolds, *Tissue Eng Part C Methods* 25(5) (2019) 276-287.

[68] B.M. Young, et al., Electrospun Decellularized Lung Matrix Scaffold for Airway Smooth Muscle Culture, *ACS Biomater Sci Eng* 3(12) (2017) 3480-3492.

[69] Y. Zhu, et al., Biomimetic Hybrid Scaffold of Electrospun Silk Fibroin and

Pancreatic Decellularized Extracellular Matrix for Islet Survival, *J Biomater Sci Polym Ed* 32(2) (2021) 151-165.

[70] P. Raz, et al., Tensile Properties of Three Selected Collagen Membranes, *Biomed Res Int* 2019 (2019) 5163603.

[71] L. Chen, et al., Refinement of Collagen–Mineral Interaction: A Possible Role for Osteocalcin in Apatite Crystal Nucleation, Growth and Development, *Bone* 71 (2015) 7-16.

[72] J. Salbach, et al., Regenerative Potential of Glycosaminoglycans for Skin and Bone, *J Mol Med (Berl)* 90(6) (2012) 625-635.

[73] B. Geiger, et al., Transmembrane Crosstalk between the Extracellular Matrix — Cytoskeleton Crosstalk, *Nat Rev Mol Cell Biol* 2(11) (2001) 793-805.

[74] Z. Wang, et al., Extracellular Matrix Derived from Allogenic Decellularized Bone Marrow Mesenchymal Stem Cell Sheets for the Reconstruction of Osteochondral Defects in Rabbits, *Acta Biomater* 118 (2020) 54-68.

[75] Z. Wang, et al., Cartilaginous Extracellular Matrix Derived from Decellularized Chondrocyte Sheets for the Reconstruction of Osteochondral Defects in Rabbits, *Acta Biomater* 81 (2018) 129-145.

[76] K.H. Song, et al., Influence of Fiber Stiffness on Meniscal Cell Migration into Dense Fibrous Networks, *Adv Healthc Mater* 9(8) (2020) e1901228.

[77] M. Yagi, et al., Optimal Pore Size of Honeycomb Polylactic Acid Films for *in Vitro* Cartilage Formation by Synovial Mesenchymal Stem Cells, *Stem Cells Int* 2021 (2021) 9239728.

[78] C. Zhang, et al., 3D-Printed Pre-Tapped-Hole Scaffolds Facilitate One-Step Surgery of Predictable Alveolar Bone Augmentation and Simultaneous Dental Implantation, *Compos B Eng* 229 (2022) 109461.

[79] D. Halloran, et al., Bone Morphogenetic Protein-2 in Development and Bone Homeostasis, *J Dev Biol* 8(3) (2020).

[80] D. Chen, et al., Bone Morphogenetic Proteins, *Growth Factors* 22(4) (2004) 233-241.

[81] T. Komori, Regulation of Osteoblast Differentiation by RUNX2, *Adv Exp Med Biol* 658 (2010) 43-49.

[82] Z. Maruyama, et al., RUNX2 Determines Bone Maturity and Turnover Rate in Postnatal Bone Development and Is Involved in Bone Loss in Estrogen Deficiency, *Dev Dyn* 236(7) (2007) 1876-1890.

[83] M.F. Young, Bone Matrix Proteins: Their Function, Regulation, and Relationship to Osteoporosis, *Osteoporos Int* 14 (2003) S35-S42.

[84] M. Farea, et al., Synergistic Effects of Chitosan Scaffold and TGF- $\beta$ 1 on the Proliferation and Osteogenic Differentiation of Dental Pulp Stem Cells Derived from Human Exfoliated Deciduous Teeth, *Arch Oral Biol* 59(12) (2014) 1400-1411.

[85] C.M. Giachelli, S. Steitz, Osteopontin: A Versatile Regulator of Inflammation and Biomineralization, *Matrix Biology* 19(7) (2000) 615-622.

[86] Y. Kang, et al., The Osteogenic Differentiation of Human Bone Marrow MSCs on HUVEC-Derived ECM and  $\beta$ -TCP Scaffold, *Biomaterials* 33(29) (2012) 6998-7007.

## CHAPTER 7

### General Discussion



The repair of large-volume bone defects (LVBDs) remains challenging in clinical practice due to the respective limitations of the clinically available bone-defect-filling materials, such as autografts, allografts, xenografts, and synthetic materials. Therefore, continuous efforts have been made to develop novel biomaterials with advanced properties for bone tissue engineering (BTE). One of the major strategies to develop such biomaterials for BTE is “biomimetic”, which refers to the resemblance of a BTE construct’s fabrication condition, geometries, physicochemical properties, and biological functions to natural bone or periosteum tissues. The main objectives of this thesis were to 1) develop novel biomimetic bone and periosteum constructs and 2) investigate their physicochemical properties and promoting effects on the healing of LVBDs, with a final goal to provide efficacious treatment options.

#### **HUCMSC-based biomimetic bone constructs**

MSCs are widely used to functionalize BTE scaffolds with pro-osteogenic properties. HUCMSCs bear self-renewal capacity and can differentiate into various types of cells [1]. Unlike hBMSCs, hUCMSCs are primitive and possess a non-invasive harvesting procedure, an abundant source, and a high cell yield [2], which secure a sufficient number of cells for BTE. HUCMSCs also have a significantly higher proliferation capacity than hBMSCs and maintain a high activity after multiple passages [3, 4]. Furthermore, hUCMSCs bear lower expression levels of HLA I/II and a higher production of tolerogenic IL-10, TGF- $\beta$ , and HLA-G than BMSCs, which indicate that hUCMSCs have low immunogenicity and a strong immunosuppressive capacity, facilitating the application of allogenic hUCMSCs [5]. These characteristics make hUCMSCs promising MSCs for BTE. However, a series of *in-vitro* studies have shown that hUCMSCs form less mineralized extracellular matrix — the final osteogenic differentiation marker — than that of hBMSCs in osteogenic differentiation medium [4, 6, 7], which suggests a relatively lower osteogenic capacity of hUCMSCs. In this thesis, to enhance the osteogenic efficacy of hUCMSCs and fabricate hUCMSC-based biomimetic bone constructs with potent osteogenic efficacy, we put forward two biomimetic strategies: 1) the co-culture of osteogenically- and angiogenically-committed hUCMSCs, and 2) using

decellularized periosteal ECM-derived hydrogels as pro-osteogenic carriers of hUCMSCs.

#### **Co-culture of osteogenically- and angiogenically-committed hUCMSCs**

Angiogenesis is a prerequisite of the healing of bone defects, which can facilitate the transportation of nutrients and oxygen as well as promote the migration, survival, and differentiation of MSCs to repair bone defects [8]. In BTE, a biomimetic strategy of co-culturing osteogenic and angiogenic cells is often applied to improve the osteogenic efficacy of BTE constructs [9-11]. We hypothesized that the biomimetic strategy of co-culturing osteogenically-committed hUCMSCs and angiogenically-committed hUCMSCs could significantly promote the osteogenic efficacy of hUCMSCs. In **Chapter 2**, hUCMSCs were pre-treated in respective induction media to produce osteogenically- and angiogenically-committed cells. We further screened the optimal mixing ratios of both cells and culture media by assessing their *in-vitro* osteogenic differentiation efficacies. Furthermore, after such a pre-treatment for 3 days, the osteogenically- and angiogenically-committed cells were loaded onto customized TCP scaffolds to repair bone defects. Our study found that the 3:1 ratio of osteogenically- and angiogenically-committed cells co-cultured in a 3:1 ratio of osteogenic medium (OM) and endothelial cell induction medium (EIM) bore dramatically higher osteogenic properties than the hUCMSCs that were only osteogenically-committed cells, thus providing a novel strategy to fabricate hUCMSC-based biomimetic BTE constructs with significantly enhanced osteogenic efficacy.

The biomimetic strategy of co-culturing osteogenic cells (e.g., BMSCs and osteogenic cells) and angiogenic cells (e.g., endothelial progenitor cells (EPCs) and endothelial cells (ECs)) represents a viable strategy in fabricating MSC-based BTE constructs, which not only facilitates the survival and bioactivities of the transplanted MSCs, but also promotes the angiogenic and osteogenic activities of the BTE constructs [9, 12]. However, the widely used co-culture of cells, such as BMSCs and EPCs, involve an invasive harvesting process, which brings pain to patients and increases the risks of infection. Besides, it’s difficult to harvest a sufficient number of human EPCs or ECs as the proliferation rate of mature ECs is relatively low [13-15]. The co-cultured cells in our study were from a single origin,

which bore abundant sources, a non-invasive harvest, rapid proliferation, and multilineage differentiation, thus avoiding the aforementioned problems.

The crosstalk between ECs and osteoblasts remarkably promotes vascularization and bone formation. Such synergistic effects may be mediated by both paracrine growth factors and direct cell-cell interactions. For example, osteogenic cells produce high amounts of VEGF, which can regulate the viability and functions of ECs; and then ECs can release growth factors, such as BMP2 and insulin-like growth factor (IGF-1), to modulate osteogenic differentiation [16, 17]. Besides, the direct contact of the co-cultured BMSCs/ECs can mediate early osteogenic differentiation by membrane proteins or intercellular gap junctions to exchange ions and small molecules, such as  $\text{Ca}^{2+}$  and cAMP [18, 19]. Therefore, the mixing ratio of osteoblasts and ECs can significantly influence cellular behaviors and osteogenic/angiogenic efficacies. On the other hand, the optimal mixing ratios of osteogenic cells and angiogenic cells show large inconsistency in different studies. In most studies, a mixing ratio of 1:1 is directly applied, which significantly promotes the final osteogenic differentiation by 1.5-fold compared with mono-culture osteogenic cells [9, 20]. Some studies have compared different co-culture ratios and found the optimal mixing ratio is 1:1, which results in a significant enhancement in final osteogenic differentiation by 1.5 to 6.5-fold [21, 22]. Few studies show that the optimal mixing ratio is 2:1 [23] or 1:3 [24, 25]. In addition to the mixing ratio of cells, the compositions of the co-culture media seem also to play an important role. Ma et al. report that extracellular matrix mineralization — the final osteogenic differentiation marker is only detected in OM, but not in proliferation medium (PM), or endothelium medium (EM), or the 1:1 mixture of OM and EM [21]. Other studies have directly used a 1:1 mixture of OM/PM and EM [20, 23, 24]. In our study, we found that the combination of 3:1-mixed cells and 3:1-mixed media resulted in dramatically enhanced extracellular matrix mineralization by 5.1-fold in comparison with hUCMSCs in OM. In contrast, the combination of 2:2-mixed cells and 2:2-mixed media only enhanced this parameter by 2.0-fold. The other combinations showed no significant effects. Such an inconsistency may be partially attributed to the differences in cell types and experimental set-ups. Therefore, the optimal mixing ratio of co-cultured osteogenic and angiogenic cells and respective

culture media should be thoroughly screened for each co-culture-based BTE construct.

### ***Decellularized periosteal ECM-derived hydrogels***

A hydrogel that is comprised of a single ECM-derived component, such as collagen or gelatin, is widely used as a 3D scaffold for tissue engineering. This type of hydrogel contains abundant cell-binding motifs (e.g., RGD sequence) to promote cell adhesion, spreading, and migration [26]. However, this type of hydrogel lacks many important bioactive components in ECM, such as hyaluronic acid, GAGs, and growth factors. Thus, they are suboptimal in promoting cell differentiation to the intended directions. One feasible approach is to extract ECM components from soft tissues so as to develop a bio-functional hydrogel with various ECM-derived components. One of the most commonly used ECM hydrogels is Matrigel, which is derived from the basement membrane of murine Engelbreth-Holm-Swarm (EHS) tumors and contains a mixture of ECM proteins, such as laminin, collagen type IV, perlecan, entactin, and growth factors [27]. It has been extensively applied to culture cells in 2D/3D ways or spheroids/organoid and promote cell growth and differentiation [28]. As a non-bone-specific hydrogel, Matrigel primarily functions to provide a 2D/3D culture platform for adipose tissue-derived MSCs, which is associated with a significantly enhanced extracellular matrix mineralization in comparison with polystyrene culture plate [29]. It has already been established that ECM hydrogel bears a tissue-specific induction property. For example, ECM hydrogels from decellularized nucleus pulposus (NP) induce BMSCs to differentiate into NP-like cells while the hydrogels from decellularized annulus fibrosus (AF) induce AF-like cells [30]. Similarly, ECM hydrogels from peripheral nerve matrix are more effective in supporting myelination, whereas hydrogels from spinal cord support synapse formation [31]. Therefore, we hypothesized that ECM hydrogels derived from decellularized periosteum could maintain the pro-osteogenic function of periosteum to expedite the osteogenic efficacy of hUCMSCs. In **Chapter 3**, decellularized periosteum-derived hydrogels (dPH) were fabricated, characterized, and compared with the non-periosteum/bone-specific ECM hydrogel, Matrigel.

In our study, we adopted the most widely used method to prepare ECM hydrogels — pepsin-mediated ECM digestion. Pepsin can selectively remove non-

helical telopeptides to unravel collagen fibrils [32, 33]. During this process, pepsin can be dissolved in 0.5 M acetic acid or 0.01–0.1 M hydrochloric acid (HCl) to obtain the desired concentration for digestion. After thorough digestion, ECM gelation can be induced by pH neutralization, salt concentration balance, and physiological temperature [33]. The physicochemical and biological properties of the final ECM hydrogels are largely influenced by the digestion degree and ECM concentrations. The digestion duration varies in different tissues (ranging from hours to days) and the minimal time when the solution is homogenous with no visible particles can be regarded as a favorable digestion time for a specific tissue [33]. Pouliot et al. find significant digestion time-dependent changes in protein concentrations, gelation kinetics, mechanical properties, and cellular behaviors. Long digestion time results in both increases of small soluble proteins, gelation duration, and decreases of gelation speed, mechanical properties, structural complexity, and the ability to support cells [34]. Therefore, it is essential to elucidate the critical time, which benefits both the physical and biological properties of ECM hydrogels. Besides, the types and concentrations of acidic solutions can significantly influence the degree of digestion, the final osmotic pressure, and stiffness of ECM hydrogels. Zhao et al. find that 0.1 M HCl of low pH value (about 1.6) accelerates the digestion process of tendon tissues and results in soft ECM hydrogels, which facilitate the exchange of nutrients and oxygen, as well as cell spreading and proliferation. In contrast, 0.5 M acetic acid with a relatively higher pH value (about 3.7) compromises pepsin activities and leads the hydrogel to a hyperosmotic state, which has a negative effect on cellular viability [35]. To fabricate ECM hydrogels from decellularized periosteum, we adopted 0.01 M HCl (pH 2) to dissolve pepsin (1 mg) and the periosteal powder was almost digested after 7 h. In contrast, when using the 0.5 M acetic acid as the solution for pepsin digestion, more pepsin (6.5 mg) and longer digestion time (24 h) are required [36]. Therefore, we suggested that 0.01 M HCl was favorable as the solution for pepsin digestion when making dPH hydrogels.

When dPH and Matrigel were co-cultured with hUCMSCs, a significantly higher initial cell spreading surface area (1.47-fold), cell spreading length (1.45-fold), and growth (1.05–1.13-fold) were observed in dPH compared with those in Matrigel. This may be attributed to the following mechanisms: first, we showed that dPH was

more hydrophilic than Matrigel. Second, periosteal ECM hydrogels contain various cell adhesion-related proteins, such as fibronectin, fibrillin-1, vitronectin, and thrombospondin 4 [36], while Matrigel lacks these proteins [27, 37]. Furthermore, we showed that dPH was more favorable for cell migration and mineralized matrix formation (9.74-fold) than Matrigel, which might be due to the soluble bioactive agents (e.g., insulin-like growth factor-binding 5 and periostin) in dPH [36, 38]. Our study showed that dPH could provide a favorable osteogenic microenvironment for hUCMSCs, indicating a promising application potential of biomimetic hUCMSCs/dPH constructs in repairing bone defects.

### BioCaP coating

Apart from the direct fabrication of biomimetic BTE constructs, BioCaP coating has long been used to confer BTE constructs an osteoconductive surface and enhanced scaffold-cell interactions in recipient sites [39–41]. However, its biomedical application is limited by the low coating yield efficiency and protein-incorporation rate of the current coating procedure using 1× supersaturated CaP solution (SCPS) [42]. We hypothesized that by increasing the concentrations of major ions in SCPS to lower the coating solution volume, the coating yield efficiency and protein incorporation rate could increase. In **Chapter 4**, a new biphasic biomimetic coating procedure (4.5× SCPS) was established and compared with 1× SCPS.

Our study showed that both 1× SCPS and 4.5× SCPS bore volume-dependent efficiency. There was a positive linear correlation between the coating thickness and the solution volume of 1× SCPS, indicating that the coating thickness could be increased proportionally by increasing the volume of the 1× SCPS solution. In contrast, a biphasic pattern was found in the relationship between the volume of 4.5× SCPS and the thickness of the produced coating. The initial rapid increase in coating thickness was detected when the volume of 4.5× SCPS ranged from 0.1 to 1 mL, which was followed by a relatively slower increase pattern at higher solution volumes (2–6 mL). The coating thickness formed in 6 mL of 4.5 × SCPS reached  $136 \pm 6 \mu\text{m}$ , which was 1.9 times than that of 6 mL 1× SCPS ( $71 \pm 8 \mu\text{m}$ ). Besides, the topographic pattern of amorphous CaP was still visible when the 1× SCPS

coating solution volume was increased to 2 mL [24]. In contrast, the morphology of amorphous CaP was not visible even after incubation in 0.1 mL of 4.5× SCPS. Instead, a crystalline structure was observed. These results suggested the coating yield efficiency of 4.5× SCPS was significantly higher than that of 1× SCPS.

By X-ray diffraction analysis, the new coating formed in 4.5× SCPS had characteristic peaks of dicalcium-phosphate dehydrate (DCPD) and hydroxyapatite [43], in contrast to the apatite-only peak of the 1× SCPS-coating. DCPD is biocompatible, biodegradable, and osteoconductive, and can be converted into dicalcium-phosphate anhydrous (DCPA) (pH < 6), octacalcium-phosphate (OCP) (pH = 6–7), or precipitated hydroxyapatite (pHAp) (pH > 7) [39]. In medicine, DCPD is used in the production of CaP cement [44]. It has been observed that DCPD can either be converted into hydroxyapatite [45] or be degraded and replaced by bone *in vivo*. The *in-vivo* biocompatibility of the novel coating will be further tested.

An acidic solution was selected to imitate a surgical site (where the initial environment could be acidic) as well as the effect of osteoclasts (which degrade bone by acid secretion) [37]. When the pH was 4.5, the 4.5× SCPS-coating released significantly less Ca<sup>2+</sup> (about 45%) than the 1× SCPS-coating. This could be explained by the solid architecture and higher amounts of BioCaP deposited onto the discs. The faster dissolution rate of the 1× SCPS group was due to the free H<sup>+</sup>, which affected the nucleation of apatite with a loose structure. This finding suggested that BioCaP-coatings fabricated in 4.5× SCPS demonstrated acid-resistant properties against osteoclastic resorption, which may indicate slow degradation *in vivo*. The final analysis of protein incorporation demonstrated that due to the reduced solution volume and enhanced coating yield, FITC-BSA incorporation was significantly higher (3.7-fold) than in the 1× SCPS-coating. Therefore, this modified coating procedure holds promise for biomedical applications.

#### **Prefabricated biomimetic TCP/pDA/BMP bone grafts**

Prefabrication technique bears a promising potential to repair LVBDs for patients [46, 47]. It can construct biomimetic bone grafts with mandibular curvatures by implanting superficially adsorbed BMP2-functionalized bone-filling materials in *in-*

*vivo* ectopic bioreactors, such as latissimus dorsi muscle. After ectopic prefabrication of about 2 to 3 months, the vascularized biomimetic bone grafts can be transferred with/without pedicle to repair large mandibular bone defects [46, 47]. The prefabricated bone grafts bear faster osseointegration with host bone and a better 3D outcome than the directly orthotopically implanted grafts [46-49]. Nevertheless, it is well-established that the absorption of BMP2 is always associated with a burst release, thus needing a supra-physiological dose to adequately induce new bone formation. In addition, the thereby-generated transiently higher concentration of BMP2 may cause a series of side effects, such as inflammation and swelling, jeopardizing new bone formation [50-52].

As a viable approach to immobilize growth factors, polydopamine (pDA)-mediated surface modification has been widely applied to increase surface bioactivity and osteoinductivity of various biomaterials, such as titanium, polymeric, composite, and CaP-based scaffolds [53-56]. Therefore, we hypothesized that 3D printed tricalcium phosphate (TCP) scaffolds functionalized by pDA-immobilized BMP2 were superior in prefabricating biomimetic bone grafts than the 3D printed TCP scaffolds functionalized by the superficially adsorbed one in latissimus dorsi muscle. In **Chapter 5**, pDA-coated TCP (TCP/pDA) scaffolds were fabricated and characterized. The loading efficiency and release kinetics of BMP2 in TCP/pDA scaffolds were compared with pure TCP scaffolds. The latissimus dorsi muscle model of rats was used to assess the osteogenic efficacy of prefabricated biomimetic TCP/pDA/BMP bone grafts.

Different from other surface modification methods, such as plasma treatment, pDA coating is a simple, safe, and effective method to modify scaffolds [57, 58]. Shin et al. find that the amount of pDA coating on polymeric films is highly dependent on the incubation time (from 5 min to 16 h) of the films in DA solution. It takes 4 h until pDA cover the whole surface of the film. Besides, the size of pDA particles increases from nanoscale (30 min) to microscale (16 h) [58]. Consistently, our study found the occurrence of a new element of N in pDA-modified TCP scaffolds, which was due to the amine groups of the pDA coating [59]. The atomic percentage of N increased with the incubation time. By field emission scanning electron microscope, the pDA particles were uniformly layered on the surface of the



3D printed TCP scaffolds after the incubation from 3 h to 6 h. After 12 h, the size of pDA particles increased, which might increase the surface roughness of the scaffolds. After 24 h, a thick layer of pDA coating was observed on the 3D printed TCP scaffolds.

It is well-established that the immobilized BMP2 shows significantly higher osteoinductive ability due to the slow delivery than the superficially absorbed BMP2 [60-62]. The BMP2 loading efficiency of TCP/pDA scaffolds was about 1.7 times higher than that of pure TCP scaffolds. Besides, TCP/BMP bore 2.3 times higher burst release of BMP2 than TCP/pDA/BMP on day 1. It has been proved that the controlled release of BMP2 shows a significantly lower soft tissue edema when implanted subcutaneously and intramuscularly than the burst release of BMP2 [63, 64]. Therefore, the pDA coating would be beneficial for reducing BMP2-induced edema. Moreover, as a commonly used *in-vivo* bioreactor, latissimus dorsi muscle bears a rich capillary network and blood vessels, which can induce neovascularization of the implanted bone-filling materials. It contains the thoracodorsal artery and vein, which can be transferred with bone grafts to provide continuous blood supply [48]. Besides, the abundant musculoskeletal progenitor cells can differentiate into osteoblasts to promote bone regeneration [65]. The implantation-caused injury of muscles will also release pro-osteogenic growth factors to support the construction of prefabricated biomimetic bone grafts [66]. Our *in-vitro* and *in-vivo* studies found that pDA-immobilized BMP2 could significantly promote the osteogenic differentiation of C2C12 and the prefabrication of biomimetic bone grafts, suggesting that the pDA modified 3D printed TCP scaffolds were promising to prefabricate biomimetic bone grafts to repair large mandibular bone defects.

#### **DECM-based biomimetic periosteum construct**

The development of biomimetic tissue-engineered periosteum (TEP) has been recognized as a promising strategy to accelerate the osseous repair of LVBDs. One of the desired essential functions of TEP is to provide a mechanically stable microenvironment in bone defects to facilitate continuous osteogenic activities. For this purpose, TEP should bear certain mechanical stiffness so as to avoid

membrane collapse, thereby maintaining the space for bone regeneration. Besides, it should maintain its structural integrity for at least 1–6 months *in vivo*, especially the initial 2–3 weeks [67-69] to prevent the invasion of fibroblasts into bone defects, thereby conferring osteoblasts sufficient time to repopulate the defect. Furthermore, TEP should also act as a reservoir to accommodate stem cells [70] and provide biocompatible and bioactive niches to stimulate the osteogenic activities of these cells. Although natural polymers (e.g., collagen and gelatin) can provide a biomimetic niche for bone regeneration, their single application as TEP is limited by their low tensile strength and high degradation rate [71]. Therefore, synthetic polymers (e.g., PCL) that bear much higher tensile strength, mechanical stability, and relatively long-term degradation rate are often adopted to improve the physicochemical properties of the electrospun TEP membranes through blended [72] or co-axial electrospinning [73]. The blended technique involves a thorough mixture of natural and synthetic polymers in a certain ratio to form a homogenous hybrid solution for electrospinning. However, when the mass ratio of gelatin or collagen/PCL reaches 30/70 or above, the blended solution gradually separates into different phases after 3 hours, rendering it difficult for massive electrospinning processes and to harvest membranes with a stable and uniform quality [74, 75]. In addition, this demixing phenomenon results in non-uniform and coarse fiber morphology as well as large splash defects, which may severely compromise the mechanical strength and degradation properties of the electrospun membranes [74, 75]. Furthermore, the thereby generated inhomogeneous distributions of gelatin and PCL in the resultant electrospun membranes lead to the clustering of cells in the gelatin-rich areas and difficulties in spreading to the surrounding PCL areas [76], which may impair their proliferation and metabolic activities [75]. In contrast, co-axial electrospinning offers separate channels for a respective solution without the need of premixing dissimilar polymers, thereby avoiding the aforementioned morphological and compositional inhomogeneity. As a consequence, co-axially electrospun membranes bear a homogenous and continuous structure of a PCL core and natural polymer shell, which contribute to significantly improved stability in the biological microenvironment. For example, after soaking in 10% PBS at 37 °C, a co-axially electrospun PCL/gelatin membrane maintains its porous structure,

while a blended electrospun PCL/gelatin membrane degrades much faster and loses its porous structure [77]. Such stability of the co-axially electrospun membrane is favorable to maintain its integrity so as to prevent the invasion of surrounding fibrous tissues. Furthermore, the co-axially electrospun PCL/gelatin membrane bears significantly higher Young's modulus (4.3-fold) and tensile strength (10.6-fold) than the blended electrospun PCL/gelatin membrane [77], which is highly important for ensuring a stable mechanical microenvironment for bone regeneration. Apart from these advantages in physicochemical properties, co-axial electrospinning provides a complete and continuous shell surface of natural polymers, which results in significantly higher cellular adhesion and metabolism on co-axially electrospun PCL/gelatin membranes than blended ones [78]. These properties indicate that the co-axial electrospinning technique bears a promising application potential for fabricating an ideal TEP.

However, the previously developed TEPs still lack periosteum-specific niches to regulate cellular activities and are hard to realize genuine biomimetic periosteum in composition. dECM from xenogeneic periosteum can maximally (more than 50%) preserve periosteum's ultrastructure and biological compositions [79, 80]. These preserved biological compositions are capable of accelerating the healing efficacy of critical-sized bone defects [81]. We hypothesized that co-axially electrospun dECM/PCL could possess a suitable mechanical strength, long-term biological integrity, and a continuous periosteum-specific surface to promote bone regeneration. In **Chapter 6**, we, for the first time, adopted the co-axial electrospinning technique to fabricate a novel biomimetic TEP with PCL-core/dECM-shell-structured microfibers.

By a series of *in-vitro* and *in-vivo* studies, we found that the novel PCL/dECM co-axially electrospun membrane (PEC) bore more biomimetic physicochemical and biological properties than the electrospun PCL and ECM. In terms of mechanical properties, the ECM had the highest Young's modulus in dry conditions, while it significantly decreased when in contact with PBS, indicating dry ECM bears high stiffness and will exhibit high softness if it contacts blood or other body fluid. And the elongation percentage at break of dry ECM was too low. These characteristics render ECM difficult to manipulate during operation. On the contrary,

the dECM shell endowed dry PEC a double Young's modulus compared with PCL membrane. Furthermore, the PCL core conferred PEC an improved UTS and elongation percentage at break. Though its UTS was lower than that of the native periosteum, it resembled a typical barrier membrane (Bio-Gide®) [82]. Besides, the wet PEC had a similar elongation percentage at break to the native periosteum. These results indicated that PEC-TEP possessed a biomimetic stiffness and tunability to provide a favorable mechanical microenvironment for bone regeneration.

Moreover, PEC showed a prolonged biodegradability with its 57% retained after a 4-week incubation in PBS. In contrast, the ECM displayed a high rate of degradability that no ECM could be found 4 weeks post-incubation. Such a high degradability of the ECM may significantly compromise the desired functions of TEP, such as the mechanical stabilization of grafting materials and barrier function to prevent the invasions of surrounding fibrous tissues. As another extreme, PCL bore a long half-life and showed no obvious morphological changes and mass loss after 4 weeks, which may cause slow replacement and risks of infections.

Furthermore, with the biomimetic dECM surface, both PEC and ECM facilitated the spreading and migration of BMSCs, while BMSCs always stayed in the superficial fiber layer with a limited cellular stretch area when being seeded on PCL. This may be attributed to that the active dECM surface has abundant cell-ECM-recognition molecules (e.g., RGD sequence) [83] and growth factors [84, 85]. Moreover, the proliferation ratio of hBMSCs on PEC was significantly higher than that on PCL on day 3 and day 5, suggesting that the dECM shell significantly enhanced cell proliferation. A similar pattern was also found in the mRNA expression of ALP, which were 1.8-fold and 1.4-fold higher in ECM and PEC groups than in the PCL group. Furthermore, the mRNA expression levels of BMP2 and RUNX2 were the highest in the PEC group. PEC and ECM induced a comparable level of COL I, which was significantly higher than that of PCL. Consistently, a comparable level of the *in-vitro* mineralized matrix formation was also found on the ECM and PEC, which was also significantly higher than that on the PCL. The *in-vivo* studies further validated that PEC bore a slow degradation rate with the membrane covering bone defects after one month, prominent mineralization, and

new bone regeneration. Our study indicated that the biomimetic dECM surface rendered PEC superior in promoting cell proliferation, early differentiation marker, and crucial osteogenic genes expression levels in comparison with PCL. More importantly, PEC induced the same level of the mineralized matrix formation and new bone formation to those of ECM, thus suggesting that PEC could provide a biomimetic microenvironment to facilitate osteogenesis.

## REFERENCES

- [1] D.C. Ding, et al., Human Umbilical Cord Mesenchymal Stem Cells: A New Era for Stem Cell Therapy, *Cell Transplant* 24(3) (2015) 339-347.
- [2] H. Zhang, et al., Isolation and Characterization of Mesenchymal Stem Cells from Whole Human Umbilical Cord Applying a Single Enzyme Approach, *Cell Biochem Funct* 30(8) (2012) 643-649.
- [3] G. La Rocca, et al., Isolation and Characterization of Oct-4+/HLA-G+ Mesenchymal Stem Cells from Human Umbilical Cord Matrix: Differentiation Potential and Detection of New Markers, *Histochem Cell Biol* 131(2) (2009) 267-282.
- [4] C. Capelli, et al., Minimally Manipulated Whole Human Umbilical Cord Is a Rich Source of Clinical-Grade Human Mesenchymal Stromal Cells Expanded in Human Platelet Lysate, *Cytotherapy* 13(7) (2011) 786-801.
- [5] T. Deuse, et al., Immunogenicity and Immunomodulatory Properties of Umbilical Cord Lining Mesenchymal Stem Cells, *Cell Transplant* 20(5) (2011) 655-667.
- [6] D. Kouroupis, et al., Assessment of Umbilical Cord Tissue as a Source of Mesenchymal Stem Cell/Endothelial Cell Mixtures for Bone Regeneration, *Regen Med* 8(5) (2013) 569-581.
- [7] C. Mennan, et al., Isolation and Characterisation of Mesenchymal Stem Cells from Different Regions of the Human Umbilical Cord, *Biomed Res Int* 2013 (2013) 916136.
- [8] K. Hu, B.R. Olsen, Osteoblast-Derived VEGF Regulates Osteoblast Differentiation and Bone Formation During Bone Repair, *J Clin Invest* 126(2) (2016) 509-526.
- [9] J. Chen, et al., Angiogenic and Osteogenic Synergy of Human Mesenchymal Stem Cells and Human Umbilical Vein Endothelial Cells Co-Cultured on a Nanomatrix, *Sci Rep* 8(1) (2018) 15749.
- [10] W.L. Dissanayaka, et al., Co-Culture of Dental Pulp Stem Cells with Endothelial Cells Enhances Osteo-/Odontogenic and Angiogenic Potential *in Vitro*, *J Endod* 38(4) (2012) 454-463.
- [11] S. Shanbhag, et al., Cell Cotransplantation Strategies for Vascularized Craniofacial Bone Tissue Engineering: A Systematic Review and Meta-Analysis of Preclinical *in Vivo* Studies, *Tissue Eng Part B Rev* 23(2) (2017) 101-117.
- [12] Y. Deng, et al., 3D Printed Scaffolds of Calcium Silicate-Doped  $\beta$ -TCP Synergize with Co-Cultured Endothelial and Stromal Cells to Promote Vascularization and Bone Formation, *Sci Rep* 7(1) (2017) 5588.
- [13] P. Simara, et al., Reprogramming of Adult Peripheral Blood Cells into Human Induced Pluripotent Stem Cells as a Safe and Accessible Source of Endothelial Cells, *Stem Cells Dev* 27(1) (2018) 10-22.
- [14] J.M. Melero-Martin, et al., *In Vivo* Vasculogenic Potential of Human Blood-Derived Endothelial Progenitor Cells, *Blood* 109(11) (2007) 4761-4768.
- [15] H. Hagiwara, et al., Effectiveness of Endothelial Progenitor Cell Culture under Microgravity for Improved Angiogenic Potential, *Sci Rep* 8(1) (2018) 14239.
- [16] C.E. Clarkin, et al., Evaluation of VEGF-Mediated Signaling in Primary Human Cells Reveals a Paracrine Action for VEGF in Osteoblast-Mediated Crosstalk to

- Endothelial Cells, *J Cell Physiol* 214(2) (2008) 537-544.
- [17] Y.N. Jiang, et al., Tension-Loaded Bone Marrow Stromal Cells Potentiate the Paracrine Osteogenic Signaling of Co-Cultured Vascular Endothelial Cells, *Biol Open* 7(6) (2018) bio032482.
- [18] B.N. Giepmans, Gap Junctions and Connexin-Interacting Proteins, *Cardiovasc Res* 62(2) (2004) 233-245.
- [19] F. Villars, et al., Effect of Human Endothelial Cells on Human Bone Marrow Stromal Cell Phenotype: Role of VEGF?, *J Cell Biochem* 79(4) (2000) 672-685.
- [20] D. Kaigler, et al., Endothelial Cell Modulation of Bone Marrow Stromal Cell Osteogenic Potential, *FASEB J* 19(6) (2005) 665-667.
- [21] J. Ma, et al., Co-Culture of Osteoblasts and Endothelial Cells: Optimization of Culture Medium and Cell Ratio, *Tissue Eng Part C Methods* 17(3) (2011) 349-357.
- [22] H. Yang, et al., Differentiated Adipose-Derived Stem Cell Co-cultures for Bone Regeneration in Rada16-1 *in Vitro*, *J Cell Physiol* 233(12) (2018) 9458-9472.
- [23] J. Peng, et al., Bone Marrow Mesenchymal Stem Cells and Endothelial Progenitor Cells Co-Culture Enhances Large Segment Bone Defect Repair, *J Biomed Nanotechnol* 15(4) (2019) 742-755.
- [24] W.L. Fu, et al., Co-Culture of Peripheral Blood-Derived Mesenchymal Stem Cells and Endothelial Progenitor Cells on Strontium-Doped Calcium Polyphosphate Scaffolds to Generate Vascularized Engineered Bone, *Tissue Eng Part A* 21(5-6) (2015) 948-959.
- [25] L. Li, et al., Enhanced Bone Tissue Regeneration of a Biomimetic Cellular Scaffold with Co-Cultured MSCs-Derived Osteogenic and Angiogenic Cells, *Cell Prolif* 52(5) (2019) e12658.
- [26] N. Davidenko, et al., Evaluation of Cell Binding to Collagen and Gelatin: A Study of the Effect of 2D and 3D Architecture and Surface Chemistry, *J Mater Sci Mater Med* 27(10) (2016) 148.
- [27] E.A. Aisenbrey, W.L. Murphy, Synthetic Alternatives to Matrigel, *Nat Rev Mater* 5(7) (2020) 539-551.
- [28] H.K. Kleinman, G.R. Martin, Matrigel: Basement Membrane Matrix with Biological Activity, *Semin Cancer Biol* 15(5) (2005) 378-386.
- [29] B.J. Kang, et al., Effect of Matrigel on the Osteogenic Potential of Canine Adipose Tissue-Derived Mesenchymal Stem Cells, *J Vet Med Sci* 74(7) (2012) 827-836.
- [30] Y. Peng, et al., Decellularized Disc Hydrogels for HBMSCs Tissue-Specific Differentiation and Tissue Regeneration, *Bioact Mater* 6(10) (2021) 3541-3556.
- [31] J.L. Zou, et al., Peripheral Nerve-Derived Matrix Hydrogel Promotes Remyelination and Inhibits Synapse Formation, *Adv Funct Mater* 28(13) (2018) 1705739.
- [32] D.J.S. Hulmes, Collagen Diversity, Synthesis and Assembly, in: P. Fratzl (Ed.), *Collagen: Structure and Mechanics*, Springer US, Boston, MA, 2008, pp. 15-47.
- [33] L.T. Saldin, et al., Extracellular Matrix Hydrogels from Decellularized Tissues: Structure and Function, *Acta Biomater* 49 (2017) 1-15.
- [34] R.A. Pouliot, et al., Porcine Lung-Derived Extracellular Matrix Hydrogel Properties Are Dependent on Pepsin Digestion Time, *Tissue Eng Part C Methods* 26(6) (2020) 332-346.
- [35] F. Zhao, et al., Comparison of Three Different Acidic Solutions in Tendon Decellularized Extracellular Matrix Bio-Ink Fabrication for 3D Cell Printing, *Acta Biomater* 131 (2021) 262-275.
- [36] P. Qiu, et al., Periosteal Matrix-Derived Hydrogel Promotes Bone Repair through an Early Immune Regulation Coupled with Enhanced Angio- and Osteogenesis, *Biomaterials* 227 (2020) 119552.
- [37] T.L. Sellaro, et al., Maintenance of Human Hepatocyte Function *in Vitro* by Liver-Derived Extracellular Matrix Gels, *Tissue Eng Part A* 16(3) (2010) 1075-1082.
- [38] Y. Tang, et al., Periostin Promotes Migration and Osteogenic Differentiation of Human Periodontal Ligament Mesenchymal Stem Cells Via the Jun Amino-Terminal Kinases (Jnk) Pathway under Inflammatory Conditions, *Cell Prolif* 50(6) (2017) e12369.
- [39] N. Eliaz, N. Metoki, Calcium Phosphate Bioceramics: A Review of Their History, Structure, Properties, Coating Technologies and Biomedical Applications, *Materials (Basel)* 10(4) (2017) 334.
- [40] P. Sun, et al., BMP2/7 Heterodimer Is a Stronger Inducer of Bone Regeneration in Peri-Implant Bone Defects Model Than BMP2 or BMP7 Homodimer, *Dent Mater J* 31(2) (2012) 239-248.
- [41] P. Kazimierczak, A. Przekora, Osteoconductive and Osteoinductive Surface Modifications of Biomaterials for Bone Regeneration: A Concise Review, *Coatings* 10(10) (2020) 971.
- [42] G. Wu, et al., Functionalization of Deproteinized Bovine Bone with a Coating-Incorporated Depot of BMP2 Renders the Material Efficiently Osteoinductive and Suppresses Foreign-Body Reactivity, *Bone* 49(6) (2011) 1323-1330.
- [43] C.Y. Zhang, et al., Biomimetic Mineralization of Zein/Calcium Phosphate Nanocomposite Nanofibrous Mats for Bone Tissue Scaffolds, *CrystEngComm* 16(40) (2014) 9513-9519.
- [44] H. Yamamoto, et al., Mechanical Strength of Calcium Phosphate Cement *in Vivo* and *in Vitro*, *Biomaterials* 19(17) (1998) 1587-1591.
- [45] B.R. Constantz, et al., Histological, Chemical, and Crystallographic Analysis of Four Calcium Phosphate Cements in Different Rabbit Osseous Sites, *J Biomed Mater Res* 43(4) (1998) 451-461.
- [46] J. Wilffang, et al., Man as a Living Bioreactor: Prefabrication of a Custom Vascularized Bone Graft in the Gastrocolic Omentum, *Tissue Eng Part C Methods* 22(8) (2016) 740-746.
- [47] P.H. Warnke, et al., Growth and Transplantation of a Custom Vascularised Bone Graft in a Man, *Lancet* 364(9436) (2004) 766-770.
- [48] M. Zhou, et al., Primate Mandibular Reconstruction with Prefabricated, Vascularized Tissue-Engineered Bone Flaps and Recombinant Human Bone Morphogenetic Protein-2 Implanted *in Situ*, *Biomaterials* 31(18) (2010) 4935-4943.
- [49] S.S. Cao, et al., Prefabricated 3D Printed Tissue-Engineered Bone for Mandibular Reconstruction: A Preclinical Translational Study in Primate, *ACS Biomater Sci Eng* 7(12) (2021) 5727-5738.
- [50] S. Vukicevic, et al., The Clinical Use of Bone Morphogenetic Proteins Revisited:



A Novel Biocompatible Carrier Device Osteogrow for Bone Healing, *Int Orthop* 38(3) (2014) 635-647.

[51] E. Gibon, et al., Inflammation, Ageing, and Bone Regeneration, *J Orthop Translat* 10 (2017) 28-35.

[52] S. Han, et al., Programmed BMP2 Release from Biphasic Calcium Phosphates for Optimal Bone Regeneration, *Biomaterials* 272 (2021) 120785.

[53] M. Godoy-Gallardo, et al., Immobilization of BMP2 and VEGF within Multilayered Polydopamine-Coated Scaffolds and the Resulting Osteogenic and Angiogenic Synergy of Co-Cultured Human Mesenchymal Stem Cells and Human Endothelial Progenitor Cells, *Int J Mol Sci* 21(17) (2020) 6418.

[54] G.H. Lee, et al., Development of BMP2 Immobilized Polydopamine Mediated Multichannelled Biphasic Calcium Phosphate Granules for Improved Bone Regeneration, *Materials Letters* 208 (2017) 122-125.

[55] J.S. Lee, et al., Polydopamine-Assisted BMP2 Immobilization on Titanium Surface Enhances the Osteogenic Potential of Periodontal Ligament Stem Cells Via Integrin-Mediated Cell-Matrix Adhesion, *J Cell Commun Signal* 12(4) (2018) 661-672.

[56] S.J. Lee, et al., Surface Modification of 3D Printed Porous Scaffolds Via Mussel-Inspired Polydopamine and Effective Immobilization of rhBMP2 to Promote Osteogenic Differentiation for Bone Tissue Engineering, *Acta Biomater* 40 (2016) 182-191.

[57] S. Huang, et al., Polydopamine-Assisted Surface Modification for Bone Biosubstitutes, *Biomed Res Int* 2016 (2016) 2389895.

[58] Y.M. Shin, et al., Time-Dependent Mussel-Inspired Functionalization of Poly(L-Lactide-Co- $\epsilon$ -Caprolactone) Substrates for Tunable Cell Behaviors, *Colloids Surf B Biointerfaces* 87(1) (2011) 79-87.

[59] H. Lee, et al., Mussel-Inspired Surface Chemistry for Multifunctional Coatings, *Science* 318(5849) (2007) 426-430.

[60] Y. Liu, et al., Delivery Mode and Efficacy of BMP2 in Association with Implants, *J Dent Res* 86(1) (2007) 84-89.

[61] T. Liu, et al., Deproteinized Bovine Bone Functionalized with the Slow Delivery of BMP2 for the Repair of Critical-Sized Bone Defects in Sheep, *Bone* 56(1) (2013) 110-118.

[62] G. Wu, et al., The Effect of a Slow Mode of BMP2 Delivery on the Inflammatory Response Provoked by Bone-Defect-Filling Polymeric Scaffolds, *Biomaterials* 31(29) (2010) 7485-7493.

[63] K.B. Lee, et al., Bone Morphogenetic Protein-Binding Peptide Reduces the Inflammatory Response to Recombinant Human Bone Morphogenetic Protein-2 and Recombinant Human Bone Morphogenetic Protein-7 in a Rodent Model of Soft-Tissue Inflammation, *Spine J* 11(6) (2011) 568-576.

[64] C.E. Taghavi, et al., Bone Morphogenetic Protein Binding Peptide Mechanism and Enhancement of Osteogenic Protein-1 Induced Bone Healing, *Spine (Phila Pa 1976)* 35(23) (2010) 2049-2056.

[65] R.L. Huang, et al., Bone Graft Prefabrication Following the *in Vivo* Bioreactor Principle, *EBioMedicine* 12 (2016) 43-54.

[66] M.A. Scott, et al., Brief Review of Models of Ectopic Bone Formation, *Stem Cells Dev* 21(5) (2012) 655-667.

[67] E. Calciolari, et al., Degradation Pattern of a Porcine Collagen Membrane in an *in Vivo* Model of Guided Bone Regeneration, *J Periodontal Res* 53(3) (2018) 430-439.

[68] D. Buser, et al., Localized Ridge Augmentation with Autografts and Barrier Membranes, *Periodontol* 2000 19 (1999) 151-163.

[69] D. Huttmacher, et al., A Review of Material Properties of Biodegradable and Bioresorbable Polymers and Devices for GTR and GBR Applications, *Int J Oral Maxillofac Implants* 11(5) (1996) 667-678.

[70] M.D. Hoffman, D.S. Benoit, Emulating Native Periosteum Cell Population and Subsequent Paracrine Factor Production to Promote Tissue Engineered Periosteum-Mediated Allograft Healing, *Biomaterials* 52 (2015) 426-440.

[71] J. Behring, et al., Toward Guided Tissue and Bone Regeneration: Morphology, Attachment, Proliferation, and Migration of Cells Cultured on Collagen Barrier Membranes. A Systematic Review, *Odontology* 96(1) (2008) 1-11.

[72] T. Wang, et al., Layer-by-Layer Nanofiber-Enabled Engineering of Biomimetic Periosteum for Bone Repair and Reconstruction, *Biomaterials* 182 (2018) 279-288.

[73] M. Gong, et al., Core-Sheath Micro/Nano Fiber Membrane with Antibacterial and Osteogenic Dual Functions as Biomimetic Artificial Periosteum for Bone Regeneration Applications, *Nanomedicine* 17 (2019) 124-136.

[74] B. Feng, et al., Acetic-Acid-Mediated Miscibility toward Electrospinning Homogeneous Composite Nanofibers of GT/PCL, *Biomacromolecules* 13(12) (2012) 3917-3925.

[75] H.M. Powell, S.T. Boyce, Engineered Human Skin Fabricated Using Electrospun Collagen-PCL Blends: Morphogenesis and Mechanical Properties, *Tissue Eng Part A* 15(8) (2009) 2177-2187.

[76] B. Feng, et al., Effect of Inhomogeneity of the Electrospun Fibrous Scaffolds of Gelatin/Polycaprolactone Hybrid on Cell Proliferation, *J Biomed Mater Res A* 103(2) (2015) 431-438.

[77] D. Kai, et al., Mechanical Properties and *in Vitro* Behavior of Nanofiber-Hydrogel Composites for Tissue Engineering Applications, *Nanotechnology* 23(9) (2012) 095705.

[78] B.N. Blackstone, et al., Tunable Engineered Skin Mechanics Via Coaxial Electrospun Fiber Core Diameter, *Tissue Eng Part A* 20(19-20) (2014) 2746-2755.

[79] S.J. Rapp, et al., Repairing Critical-Sized Rat Calvarial Defects with Progenitor Cell-Seeded Acellular Periosteum: A Novel Biomimetic Scaffold, *Surgery* 152(4) (2012) 595-605.

[80] K. Chen, et al., Decellularized Periosteum as a Potential Biologic Scaffold for Bone Tissue Engineering, *Acta Biomater* 19 (2015) 46-55.

[81] J. He, et al., Preparation and Evaluation of Acellular Sheep Periosteum for Guided Bone Regeneration, *J Biomed Mater Res A* 108(1) (2020) 19-29.

[82] P. Raz, et al., Tensile Properties of Three Selected Collagen Membranes, *Biomed Res Int* 2019 (2019) 5163603.

[83] B.S. Kim, et al., Decellularized Extracellular Matrix-Based Bioinks for

Engineering Tissue- and Organ-Specific Microenvironments, Chem Rev 120(19) (2020) 10608-10661.

[84] I. Ullah, et al., VEGF — Supplemented Extracellular Matrix is Sufficient to Induce Endothelial Differentiation of Human iPSC, Biomaterials 216 (2019) 119283.

[85] J. Zhang, et al., Preparation and Evaluation of Tibia- and Calvarium-Derived Decellularized Periosteum Scaffolds, ACS Biomater Sci Eng 3(12) (2017) 3503-3514.

## CHAPTER 8

### General Summary

The repair of large-volume bone defects remains challenging in clinical practice due to the respective limitations of the clinically available bone-defect-filling materials. Therefore, continuous efforts have been made to develop new bone and periosteum substitutes to enhance bone regeneration.

HUCMSCs are promising stem cells for bone tissue engineering, which have a non-invasive harvesting process, high cell yield, rapid proliferation capacity, and low immunogenicity. However, a series of *in-vitro* studies have shown that the osteogenic efficacy of hUCMSCs is relatively lower than that of BMSCs. Therefore, in **Chapter 2**, we adopted a biomimetic strategy of co-culturing osteogenically- and angiogenically-committed hUCMSCs in various mixing ratios and culture media so as to promote the osteogenic efficacy of hUCMSCs. We found that hUCMSCs bore a relatively lower osteogenic efficacy and could differentiate into angiogenic cells after induction. Compared with mono-cultured osteogenically-committed hUCMSCs in OM, a 3:1 ratio of osteogenically- and angiogenically-committed cells co-cultured in a 3:1 ratio of osteogenic medium and endothelial cell induction medium bore dramatically higher osteogenic properties both *in vitro* and *in vivo*, thus providing a novel strategy to fabricate hUCMSC-based biomimetic BTE constructs with significantly enhanced osteogenic efficacy.

Moreover, it has already been established that ECM hydrogels bear a tissue-specific induction property. Therefore, in **Chapter 3**, decellularized periosteum-derived hydrogels (dPH) were fabricated, characterized, and compared with the non-periosteum/bone-specific ECM hydrogel, Matrigel. Our *in-vitro* data showed that dPH exhibited a prominent effect on promoting the initial cellular spreading, migration, and proliferation. Moreover, the dPH group was associated with the enhanced osteogenesis-related genes expression and mineralized matrix formation of hUCMSCs than that of Matrigel. Our study indicated that dPH could provide a favorable osteogenic microenvironment for hUCMSCs, indicating a promising application potential of biomimetic hUCMSCs/dPH constructs to repair bone defects.

Apart from the direct fabrication of biomimetic BTE constructs, BioCaP coating has long been used to confer BTE constructs an osteoconductive surface and enhanced scaffold-cell interactions in recipient sites. However, its biomedical

application is limited by the low coating yield efficiency and protein-incorporation rate of the current coating procedure using 1× supersaturated CaP solution (SCPS). Therefore, in **Chapter 4**, we developed a highly concentrated 4.5× SCPS solution to harvest BioCaP coating. The thereby produced coating had shown a series of advantages over the original coating, such as a significantly higher coating yield efficiency and protein-incorporating rate. Furthermore, the new coating was identified as DCPD/apatite crystalline and showed a strong acid-resistant property, which enabled a slow coating dissolution, and thus, a slow delivery of bioactive agents in acidic environments. These properties conferred the new coating a promising potential in the functionalization of titanium implants for biomedical applications.

Additionally, polydopamine (pDA) coating is a simple, safe, and effective method to modify scaffolds, thus covalently immobilizing growth factors and increasing surface bioactivity. Whether 3D printed TCP scaffolds functionalized by pDA-immobilized BMP2 were superior in prefabricating biomimetic bone grafts than the 3D printed TCP scaffolds functionalized by the superficially adsorbed one in latissimus dorsi muscle remained to be studied. Therefore, in **Chapter 5**, pDA-coated TCP (TCP/pDA) scaffolds were fabricated and characterized. Our study demonstrated that pDA coating was an efficacious method to improve the loading efficacy of BMP2 on 3D printed TCP scaffolds, which could also ensure a slow release profile of the loaded BMP2. Besides, pDA-immobilized BMP2 significantly promoted the osteogenic differentiation of C2C12 and the *in-vivo* bone formation during the prefabrication of biomimetic bone grafts in latissimus dorsi muscle. Our data suggested that the 3D printed TCP scaffolds functionalized with pDA-immobilized BMP2 were promising to prefabricate biomimetic bone grafts for repairing large mandibular bone defects.

The development of biomimetic tissue-engineered periosteum (TEP) has been recognized as a promising strategy to accelerate the osseous repair of bone defects. However, the previously developed TEPs lack periosteum-specific niches to regulate cellular activities, and are hard to realize genuine biomimetic periosteum in composition. Therefore, in **Chapter 6**, we adopted the co-axial electrospinning technique to fabricate a novel biomimetic TEP with PCL-core/dECM-shell-

structured microfibers. The novel PEC resembled the mechanical strength of the PCL membrane. Besides, the PEC bore dECM-like hydrophilicity and bioactivity to promote cell spreading, proliferation, and osteogenic activities, which was far more advantageous than the pure PCL membrane. Moreover, PEC bore a comparable healing efficacy in repairing bone defects to the pure ECM, which was significantly higher than that in the pure PCL membrane. The *in-vivo* retention of PEC was also significantly higher than that of the pure ECM. These findings indicated a promising application potential of the novel PEC-TEP in promoting the repair of bone defects.

## APPENDICES

Contributing Authors

Acknowledgments

Curriculum Vitae



**Contributing authors****Chapter 2 was published as:**

A novel method to improve the osteogenesis capacity of hUCMSCs with dual-directional pre-induction under screened co-culture conditions

**Authors:**

Qiong Rong, Shuyi Li, Yang Zhou, Yuanming Geng, Shangbin Liu, Wanqiu Wu, Tim Forouzanfar, Gang Wu, Zhiyong Zhang, Miao Zhou

**Authors' contributions:**

Qiong Rong and Shuyi Li carried out, analyzed and wrote the manuscript draft, contributing equally to this study and shared the first authorship.

Yang Zhou, Yuanming Geng, Shangbin Liu and Wanqiu Wu assisted in performing part of the *in-vitro* and *in-vivo* studies.

Tim Forouzanfar and Gang Wu helped to revise the manuscript.

Miao Zhou and Zhiyong Zhang designed the experiments and revised the manuscript.

**Chapter 3 was published as:**

Decellularized periosteum-derived hydrogels promote the proliferation, migration, and osteogenic differentiation of human umbilical cord mesenchymal stem cells

**Authors:**

Shuyi Li, Rongli Deng, Tim Forouzanfar, Gang Wu, Daping Quan, Miao Zhou

**Authors' contributions:**

Shuyi Li: Investigation, conceptualization, methodology, analysis and writing.

Rongli Deng: Methodology and analysis. Shuyi Li and Rongli Deng contributed equally and shared the first authorship.

Tim Forouzanfar: Conceptualization and supervision.

Gang Wu: Supervision, data curation, draft review and editing.

Daping Quan: Conceptualization, resources and data curation.

Miao Zhou: Supervision, validation and funding acquisition.

**Chapter 4 was published as:**

Highly efficient biphasic calcium-phosphate coating procedure with an enhanced

coating yield and protein incorporation rate

**Authors:**

Ping Sun, Shuyi Li, Jianhua Niu, Min Yi, Weixing Xu, Liyong Wu, Gang Wu

**Authors' contributions:**

Ping Sun: Investigation, analysis and financial support.

Shuyi Li: Investigation and writing. Ping Sun and Shuyi Li contributed equally and shared the first authorship.

Jianhua Niu and Min Yi: Assisted in performing part of the study.

Weixing Xu: Conceptualization, designed the experiments and financial support.

Liyong Wu: Conceptualization and resources.

Gang Wu: Designed the experiments and revised the manuscript.

**Chapter 5 to be published as:**

3D printed TCP scaffolds functionalized with polydopamine-immobilized BMP2 to construct prefabricated biomimetic bone grafts

**Authors:**

Shuyi Li, Fen Zhang, Fidel Hugo Perera, Tim Forouzanfar, Gang Wu, Pedro Miranda, Miao Zhou

**Authors' contributions:**

Shuyi Li: Investigation, methodology, analysis and writing.

Fen Zhang and Fidel Hugo Perera: Investigation.

Tim Forouzanfar: Conceptualization and supervision.

Gang Wu: Supervision, data curation, draft review and editing.

Pedro Miranda: Resources and data curation.

Miao Zhou: Supervision, validation and funding acquisition.

**Chapter 6 was published as:**

Development and fabrication of co-axially electrospun biomimetic periosteum with a decellularized periosteal ECM shell/PCL core structure to promote the repair of critical-sized bone defects

**Authors:**

Shuyi Li, Rongli Deng, Xuenong Zou, Qiong Rong, Jiali Shou, Zilong Rao, Wanqiu

Wu, Gang Wu, Daping Quan, Miao Zhou, Tim Forouzanfar

**Authors' contributions:**

Shuyi Li: Investigation, conceptualization, methodology, analysis and writing.

Rongli Deng: Investigation, methodology and analysis. Shuyi Li and Rongli Deng contributed equally to this work and shared the first authorship.

Xuenong Zou: Conceptualization and methodology.

Qiong Rong and Jiali Shou: Investigation.

Zilong Rao: Methodology and investigation.

Gang Wu: Supervision, data curation, draft review and editing.

Daping Quan: Conceptualization, resources and data curation.

Miao Zhou: Supervision, validation and funding acquisition.

Tim Forouzanfar: Conceptualization and supervision.

**Acknowledgments**

The experience of studying at ACTA as a PhD student has been momentous and unforgettable, and will forever be cherished in my life. I have gained many friendships, much knowledge, support, and happiness here. The successful completion of my PhD study relied on continuous guidance from all promoters, tremendous help from all colleagues and collaborators, and substantial support from my friends, family, CSC scholarship, and the project grants. It is difficult to express the sincere gratitude in my heart. I could not have achieved this without all of you!

My deepest gratitude goes firstly to **Prof. Dr. Tim Forouzanfar**: Dear Tim, I appreciate that you offered me the valuable opportunity to study in Amsterdam. You are always so kind and considerate whenever I come to you for help. Your professional and continuous guidance helped me master many skills and knowledge. Your encouragement always inspired me and gave me hope whenever I was frustrated.

Special appreciation to **Dr. Gang Wu**: Dear Wu, it was an honor to have you as my co-promotor. You are always so energetic and optimistic, showing positive energy to those around you. Your sophistication in a broad range of knowledge and critical thinking greatly influenced me and helped me develop a new perspective on my academic career. Your rigorous and prudent attitude towards research and writing pushed me to learn and improve. I appreciate all your efforts in helping me construct research concepts, in offering me chances to learn new skills, and in revising every word and figure. Thank you for always supporting me!

Special appreciation to **Dr. Miao Zhou**: Dear Zhou, thank you for the valuable instructions and support. Your persistent attitude to work deeply influences me. Without your constant help and professional guidance, I could not have finished this thesis and the PhD study. Your motivation inspired me to progress and keep moving. You also taught me many clinical skills and offered me chances to learn from other masters. Thank you for always supporting me!

To **Dr. Marco N. Helder**: Dear Marco, thank you so much for offering me this valuable opportunity to finish my PhD study at VU. You are always so gentle and kind. Your profound knowledge of stem cells and tissue engineering helped me

substantially.

To **Dr. Astrid D. Bakker**: Dear Astrid, thank you so much for creating such a friendly and positive atmosphere for work and study. You are always so supportive, caring, and patient. You give us practical suggestions not only for research and studies, but also daily life. Thank you for organizing the tour in the city center, which enabled me to learn more about Amsterdam. Thank you for searching and providing us with valuable information about the courses and conferences we could attend.

To **Prof. Dr. Jenneke Klein-Nulend**: Dear Jenneke, you are always with a gentle voice and a big smile. Thank you for your selfless help, timely message about the conference, and the kind reminders of the skills that I could improve. Thank you so much for welcoming me to your warm and artistic house!

To **Dr. Yuelian Liu**: Dear Liu, thank you so much for the warm welcome and considerate reminder of all the precautions during the pandemic. You are always so kind, amiable, and elegant.

To **Dr. Behrouz Zandieh Doulabi**: Dear Behrouz, thank you so much for reminding me of the knowledge loophole in electrospinning and lending me the book for further study. You are always so helpful, kind, and positive.

To **Dr. Jianfeng Jin**: Dear Jin, thank you so much for your consistent help! You are always so kind and friendly! You can always arrange everything in perfect order. There are so many good characteristics that I would love to learn from you.

To my dear colleagues **Jolanda, Cor, Ton, Inneke, Teun, Cees, Sue, Jan Harm, Kamran, Jacqueline, Tineke** and **Victor**: I appreciate all your kindness, help, and care. Thank you! Special thanks to **Jolanda, Cor,** and **Kamran**. Dear **Jolanda**, thank you so much for helping me do the biological tests, and for ordering experimental materials for me. Your smile is so bright that it brings tremendous energy to the whole lab. I hope you always stay with a smile. Dear **Cor**, thank you so much for showing me around the lab and explaining everything that I need to pay attention to. You are always so gentle and equipped with lots of skills that can repair everything in the lab. Dear **Kamran**, thank you so much for helping me lyophilize the samples!

To my friends **Naichuan, Andi, Yan, Gaoli, Cuicui, Xiaoxuan, Rongli, Rui Li, Qiong Rong, Wei Cao, Wei Sun, Yiwu, Menghong, Lei Wang, Chen Zhang,**

**Shanlin, Yaling, Xumin,** and **Jiayi**: I sincerely thank all of you! Without your help and encouragement, I would not be where I am today. I hope all of you reach your dreams and stay happy!

To my family: Thank you for the constant, unconditional support. There are millions of words that I want to say, but the most important thing is that I will love you always and forever!

**Curriculum Vitae**

Name Shuyi Li  
Date of birth 02 May 1989  
Place of birth Lianyungang, Jiangsu, China  
Email [s.li@acta.nl](mailto:s.li@acta.nl), [592180096@qq.com](mailto:592180096@qq.com)

**Education background**

01. 2018 – Now PhD student, Department of Oral and Maxillofacial Surgery/Pathology and Department of Oral and Cell Biology, Academic Centre for Dentistry Amsterdam (ACTA), Vrije University Amsterdam
09. 2014 – 06. 2017 Master's degree in Stomatology, Guangzhou Medical University
09. 2007 – 06. 2012 Bachelor's degree in Stomatology, Southern Medical University

**Publications**

1. **Shuyi Li**<sup>#</sup>, Rongli Deng<sup>#</sup>, Xuenong Zou, et al. Development and fabrication of co-axially electrospun biomimetic periosteum with a decellularized periosteal ECM shell/PCL core structure to promote the repair of critical-sized bone defects. *Composites Part B: Engineering*. 2022, 234:109620.
2. **Shuyi Li**<sup>#</sup>, Rongli Deng<sup>#</sup>, Qiong Rong, et al. Decellularized periosteum-derived hydrogels promote the proliferation, migration, and osteogenic differentiation of human umbilical cord mesenchymal stem cells. *Gels*. 2022, 8(5):294.
3. **Shuyi Li**, Fen Zhang, Fidel Hugo Perera, et al. 3D printed TCP scaffolds functionalized with polydopamine-immobilized BMP2 to construct prefabricated biomimetic bone grafts. *Submitted*.



4. Qiong Rong<sup>#</sup>, **Shuyi Li<sup>#</sup>**, Yang Zhou, et al. A novel method to improve the osteogenesis capacity of hUCMSCs with dual-directional pre-induction under screened co-culture conditions. *Cell Proliferation*. 2020, 53:e12740.
5. Ping Sun<sup>#</sup>, **Shuyi Li<sup>#</sup>**, Jianhua Niu, et al. Highly efficient biphasic calcium-phosphate coating procedure with an enhanced coating yield and protein incorporation rate. *Materials Express*. 2021, 11:1428-1437.
6. **Shuyi Li<sup>#</sup>**, Ming Gao<sup>#</sup>, Miao Zhou, et al. Bone augmentation with autologous tooth shell in the esthetic zone for dental implant restoration: a pilot study. *International Journal of Implant Dentistry*. 2021, 7:108.
7. Shuaishuai Cao<sup>#</sup>, **Shuyi Li<sup>#</sup>**, Yuanming Geng<sup>#</sup>, et al. Prefabricated 3D-printed tissue-engineered bone for mandibular reconstruction: a preclinical translational study in primate. *ACS Biomaterials Science & Engineering*. 2021, 7(12):5727-5738.
8. Miao Zhou, **Shuyi Li**, Hendrik Terheyden, et al. Particulate coral hydroxyapatite sheltered by titanium mesh for localized alveolar rehabilitation after onlay graft failure: a case report. *Journal of Oral Implantology*. 2018, 44(2):147-152.
9. Miao Zhou, Xiaobin Yang, **Shuyi Li**, et al. Bioinspired channeled, rhBMP2-coated  $\beta$ -TCP scaffolds with embedded autologous vascular bundles for increased vascularization and osteogenesis of prefabricated tissue-engineered bone. *Materials Science and Engineering: C*. 2021, 118: 111389.
10. Miao Zhou<sup>#</sup>, Yuanming Geng<sup>#</sup>, **Shuyi Li**, et al. Nanocrystalline hydroxyapatite-based scaffold adsorbs and gives sustained release of osteoinductive growth factor and facilitates bone regeneration in mice ectopic model. *Journal of Nanomaterials*. 2019, 2019:1-10.
11. Yuanming Geng<sup>#</sup>, Dongni Ren<sup>#</sup>, **Shuyi Li**, et al. Hydroxyapatite-incorporation improves bone formation on endosseous PEEK implant in canine tibia. *Journal of Applied Biomaterials & Functional Materials*. 2020, 18:1-9.
12. Miao Zhou, Hui Zhou, **Shuyi Li**, et al. Dental implant location via surface scanner: A pilot study. *BMC Oral Health*. 2020, 20:306.
13. Miao Zhou, Hui Zhou, **Shuyi Li**, et al. Accuracy of implant placement guided with surgical template: an *in vitro* and *in vivo* study. *International Journal of Periodontics and Restorative Dentistry*. 2021, 41(2):e55-e62.
14. **Shuyi Li**, Miao Zhou. Recent advancement on the carriers and controlled-release systems of bone morphogenetic proteins. *Journal of Biomedical Engineering*. 2016, 33(4):812-815. (Chinese)
15. **Shuyi Li**, Miao Zhou, Yuxiao Lai, et al. Biological evaluation of three-dimensional printed co-poly lactic acid/glycolic acid/tri-calcium phosphate scaffold for bone reconstruction. *Chinese Journal of Stomatology*. 2016, 51(11):661-666. (Chinese)

#### Other academic achievements

1. Miao Zhou, **Shuyi Li**, Yuanming Geng, Zhen Shen. Competition of the scientific research achievements commercialization of universities in Guangdong Province. 2019, the 3<sup>rd</sup> prize.
2. Miao Zhou, Qiong Rong, **Shuyi Li**, Yang Zhou, Shangbin Liu, Wanqiu Wu, Guanjie Lu. A method to enhance the osteogenic efficiency of human umbilical cord mesenchymal stem cells. No. 201911121302.3.
3. Miao Zhou, Yongqiang Yang, Guangyan Yu, **Shuyi Li**. A dental implant metal guide made by selective laser melting technology. No. 201520250684.0.
4. Miao Zhou, Yongqiang Yang, Guangyan Yu, **Shuyi Li**. A 3D printed mandibular prosthesis. No. 201520246396.8.